Stony Brook University

Designing a New Class of Electrocatalysts for Polymer Electrolyte Membrane Fuel Cells: Probing Size, Composition, and Structure Dependent Electrocatalytic Performance in High-Quality, One-Dimensional Noble Metal Nanostructures

A Dissertation Presented

by

Christopher Koenigsmann

to

The Graduate School

in Partial Fulfillment of the

Requirements

for the Degree of

Doctor of Philosophy

in

Chemistry

Stony Brook University

August 2013

Stony Brook University

The Graduate School

Christopher Koenigsmann

We, the dissertation committee for the above candidate for the

Doctor of Philosophy degree, hereby recommend

acceptance of this dissertation.

Dr. Stanislaus S. Wong – Dissertation Advisor
Professor, Department of Chemistry

Dr. Peter Khalifah – Chairperson of Defense
Assistant Professor, Department of Chemistry

Dr. Michael White – Third Member of Academic Committee
Professor, Department of Chemistry

Dr. Alan West – Outside Member
Samuel Ruben-Peter G. Viele Professor of Electrochemistry & Professor Chemical Engineering, Department of Chemical Engineering, Columbia University

This dissertation is accepted by the Graduate School

Charles Taber
Interim Dean of the Graduate School

Abstract of the Dissertation

Designing a New Class of Electrocatalysts for Polymer Electrolyte Membrane Fuel Cells: Probing Size, Composition, and Structure Dependent Electrocatalytic Performance in High-Quality, One-Dimensional Noble Metal Electrocatalysts

by

Christopher Koenigsmann

Doctor of Philosophy

in

Chemistry

Stony Brook University

2013

A key challenge in the practical commercialization of PEMFCs is the extremely high cost and relatively poor durability of carbon supported Pt nanoparticle (Pt NP/C) electrocatalysts utilized in both the anode and cathode half-cells. Herein, we synthesize and characterize a new class of high-quality one-dimensional noble metal nanostructures as a potentially new and promising structural paradigm for the next generation of electrocatalyst materials. Specifically, we investigate the nature of the complex interplay amongst size, chemical composition, and electrocatalytic performance in high-quality elemental and bimetallic 1D noble metal nanowire systems with an emphasis on achieving efficient and sustainable methods for catalyst preparation.

In terms of nanowire dimensions and composition, an interesting and measureable size-dependent enhancement in performance emerges in the case of elemental Pt, Pd, and $Pd_{1-x}Au_x$ nanowires possessing diameters ranging from the submicron (d = ~200 nm) to the ultrathin regime (d = ~1 nm). In a similar context, we have considered the role of chemical composition in 1D electrocatalysts and noted significant composition-dependent enhancements in activity and durability in high-quality, bimetallic $Pd_{1-x}Au_x$ and $Pd_{1-x}Pt_x$ NWs. A key finding that is apparent from these experimental results is that widely seen behavioral trends in the composition- and size-dependent performance for 0D nanoparticle-based catalysts do not hold in the case of 1D architectures, because of the patently unique structural and electronic effects, associated with their anisotropic structures. As a culmination of our efforts to take advantage of these intrinsic structure-activity correlations, our group has developed a morphology-, size-, and composition-optimized Pd_9Au NW possessing a Pt monolayer shell (Pt_{ML}~Pd_9Au NWs) electrocatalyst with an ultrathin 2 nm diameter, which yielded outstanding Pt mass and PGM activities of 2.56 A/mg_{Pt} and 0.64 A/mg_{PGM}, respectively, thereby surpassing the activity of conventional state-of-the-art Pt NP/C by more than ten-fold.

This dissertation is dedicated to my family, friends, and all of those who have supported me throughout my career. This dissertation is also dedicated to teachers, mentors, professors and all of those who inspire their students to pursue careers in chemistry.

Table of Contents

List of Figures

List of Abbreviations and Symbols

$	dollar
%	percent
°C	degree Celsius
0D	zero-dimensional
1D	one-dimensional
2D	two-dimensional
2θ	two theta
3D	three-dimensional
A	Ampere
Å	Angstrom
AAO	anodic aluminum oxide
AAS	atomic absorption spectroscopy
ABL	anode backing layer
ad-atom	added atoms
AEL	anode electrocatalyst layer
A_g	geometric area of electrode
Ag/AgCl	silver/silver chloride reference electrode
B	electron transfer constant
BA	n-Butylamine
C	Coulombs
CA	chronoamperometry
CBL	cathode backing layer
CEL	cathode electrocatalyst layer
cm	centimeter
CO	carbon monoxide
C_{O2}	concentration of dissolved oxygen
CV	cyclic voltammetry
d	diameter
DAFC	direct alcohol fuel cell
DCM	dichloromethane
DEFC	direct ethanol fuel cell
DFT	density functional theory
DMF	dimethylformamide
DMFC	direct methanol fuel cell
DNA	deoxyribonucleic acid
D_{O2}	diffusion coefficient of oxygen
DOE	U.S. Department of Energy

DP	diffraction pattern
DTAB	dodecyltrimethylammonium bromide
E	potential
e^-	electron
$E°$	standard reduction potential
EDAX	energy dispersive X-ray spectroscopy
electrodeposition	electrochemical deposition
electroxidation	electrochemical oxidation
EOR	ethanol oxidation reaction
ESA	electrochemically accessible surface area
EtOH	ethanol
F	Faraday's constant
FAOR	formic acid oxidation reaction
FCC	face centered cubic
FESEM	field emission scanning electron microscopy
g	gram
GC	glassy carbon
GCE	glassy carbon electrode
GC-RDE	glassy carbon rotating disk electrode
GD	galvanic displacement
h	hours
HAADF	high-angle annular dark field detector
H_{ads}	hydrogen adsorption
H_{des}	hydrogen desorption
HFC	hydrogen fuel cell
HP	high performance
HRTEM	high resolution transmission electron microscopy
I	current
$I_{0.9\ V}$	current at 0.9 V
ICE	internal combustion engine
ICP	inductively coupled plasma
ICP-AES	inductively coupled plasma atomic emission spectroscopy
ICP-MS	inductively coupled plasma mass spectrometry
I_D	diffusion limited current
I_K	kinetic current
IPA	isopropyl alcohol
J	current density
JCPDS	Joint Committee on Powder Diffraction Standards
J_K	kinetic current density (specific activity)

J_K [MeOH]	specific activity in the presence of methanol
kg	kilogram
K-L	Koutecky - Levich
kV	kilovolts
kW	kilowatt
L	liter
LCA	low coordination atoms
LSV	linear sweep voltammogram
M	molar
MCFC	molten carbonate fuel cell
MEA	membrane electrode assembly
MEMS	micro electromechanical systems
MeOH	methanol
mg	milligram
mg_{PGM}	milligrams of platinum group metal
mg_{Pt}	milligrams of platinum
min	minute
mL	milliliter
mM	millimolar
MOR	methanol oxidation reaction
mV	millivolts
MΩ	megaohms
n	number of electrons transferred
nanomaterial	nanostructured material
nanoscale	nanometer scale
nm	nanometer
NP	nanoparticle
NP/C	carbon supported nanoparticles
NR	nanorod
NT	nanotube
NW	nanowire
NW/C	carbon supported nanowires
^{o}	degrees
ODA	octadecylamine
ORR	oxygen reduction reaction
PC	polycarbonate
PEM	polymer electrolyte membrane
PEMFC	polymer electrolyte membrane fuel cells
PGM	platinum group metal
Pt_{ML}	platinum monolayer

PVD	physical vapor deposition
PVP	polyvinyl pyrrolidone
RDE	rotating disk electrode
RHE	reversible hydrogen electrode
rpm	revolutions per minute
s	seconds
SAED	selected area electron diffraction
SEM	scanning electron microscopy
SI	international system of units
SOFC	solid oxide fuel cell
SOM	small organic molecule
STEM	scanning transmission electron microscopy
T	temperature
TEA	triethylamine
TEM	transmission electron microscopy
TGA	thermogravimetric analysis
UPD	under potential deposition
UV	ultraviolet
UV/vis	ultraviolet/visible
V	volts
W	watt
XPS	X-ray photoelectron spectroscopy
XRD	X-ray powder diffraction
Z	atomic number
α	lattice parameter
μC	micro-Coulombs
μm	micrometer
ν	kinetic viscosity of solution
χ	mole fraction
Ω	Ohms
ω	rotation speed of rotating disk electrode

Acknowledgements

First and foremost, I would like to acknowledge and thank Dr. Stanislaus Wong for his outstanding efforts as a research advisor, over the course of my doctoral course work and research. His unceasing support, expert guidance, motivation and dedication to my success have been a key foundation to my training and his advice will be indispensable as I move forward in my career. I would also to express my deepest gratitude to Dr. Radoslav Adzic for his mentorship, advice, and tutelage. His expertise and commitment to training me in the fields of electrochemistry and catalysis has provided me with a new dimension of experience that will be helpful to me throughout my career. I would also like to thank him for supporting my research efforts and providing access to his research facilities over the course of my Ph.D. research. I would like to thank my academic committee include my committee chair Dr. Peter Khalifah and my third member Dr. Michael White for their insightful guidance and support. I am also grateful to Dr. Alan West for his time, consideration, and expertise, while serving as the outside member on my academic committee.

I also acknowledge and thank all of my fellow colleagues and group members especially Dr. Alexander Santulli, Dr. Amanda Tiano, Dr. Jonathan Patete, Dr. Xiaohui Peng, Dr. Fen Zhang, and Dr. Hongjun Zhou for their help at the start of my research career. I am especially grateful to Dr. Eli Sutter, Dr. Jim Quinn, and Susan Van Horn for their assistance, helpful discussion and guidance with electron microscopy. Many thanks to the members of Dr. Adzic's group including Dr. Kuanping Gong, Dr. Wei-Ping Zhou, Dr. Stoyan Bliznakov, Dr Miomir Vukmirovic, and Dr. Yun Cai for their insights into electrochemical experiments. I would like to especially acknowledge Dr. Miomir Vukmirovic for his expertise and training in

electrochemistry and also thank him for many interesting conversations. I am very grateful for the assistance and support of the faculty and staff of the Department of Chemistry at Stony Brook University as well as the Department of Condensed Matter Physics & Material Science, the Department of Chemistry, and the Center for Functional Nanomaterial at Brookhaven National Laboratory.

As a personal note, I would like to especially thank and acknowledge Mr. Marsilio Langella for his outstanding efforts as a high school chemistry teacher. His dedication and commitment to excellent teaching inspired me to pursue a career in chemistry and education and for that, I am forever grateful. I would also like gratefully acknowledge the chemistry faculty at Fairfield University, especially Dr. Amanda Harper-Leatherman, my undergraduate research advisor, for providing me with a superb foundation in chemistry, supporting my research efforts, and inspiring me to continue my training at the graduate level.

Finally, I would like to express my deepest gratitude to my family and friends, especially my parents, Dr. Carl Koenigsmann & Dr. Denise Sepe, sister, Jenna Koenigsmann, and fiancé, Dr. Erin Culbert, for their continuous love and support throughout my life and during my Ph.D. career.

List of Publications

1. **Koenigsmann, C.**; Wong S. S., Tailoring Chemical Composition to Achieve Enhanced Methanol Oxidation Reaction and Methanol-Tolerant Oxygen Reduction Reaction Performance in Palladium-Based Nanowire Systems. *ACS Catalysis* ASAP.

2. **Koenigsmann, C.**; Semple, D. B.; Sutter, E.; Tobierre, S. E.; Wong, S. S., Ambient Synthesis of High-Quality Ruthenium Nanowires and the Morphology-Dependent Electrocatalytic Performance of Platinum-Decorated Ruthenium Nanowires and Nanoparticles in the Methanol Oxidation Reaction. *ACS Applied Materials & Interfaces* **2013**, *5*, 5518-5530.

3. **Koenigsmann, C.**; Tan, Z.; Peng, H.; Sutter, E.; Jacobskind, J.; Wong, S. S., Multifunctional Nanochemistry: Ambient, Electroless, Template-Based Synthesis & Characterization of Segmented Bimetallic Bimetallic Pd/Au and Pd/Pt Nanowires as High-Performance Electrocatalysts and Nanomotors. *Israeli Journal of Chemistry* (Invited Article) **2012**, *52*, 1090-1103.

4. **Koenigsmann, C.**; Scofield, M. E.; Liu, H.; Wong, S. S., Designing Enhanced One-Dimensional Electrocatalysts for the Oxygen Reduction Reaction: Probing Size- and Composition-Dependent Electrocatalytic Behavior in Noble Metal Nanowires. *Journal of Physical Chemistry Letters* (Invited Perspective & Cover Article) **2012**, *3* (22), 3385-3398.

5. **Koenigsmann, C.**; Sutter, E.; Adzic, R. R.; Wong, S. S., Size- and Composition-Dependent Enhancement of Electrocatalytic Oxygen Reduction Performance in Ultrathin Palladium–Gold ($Pd_{1-x}Au_x$) Nanowires. *Journal of Physical Chemistry C* **2012**, *116* (25), 15297-15306.

6. **Koenigsmann, C.**; Sutter, E.; Chiesa, T. A.; Adzic, R. R.; Wong, S. S., Highly Enhanced Electrocatalytic Oxygen Reduction Performance Observed in Bimetallic Palladium-Based Nanowires Prepared under Ambient, Surfactantless Conditions. *Nano Letters* **2012,** *12* (4), 2013-2020.

7. Zhou, W.-P.; Li, M.; **Koenigsmann, C.**; Ma, C.; Wong, S. S.; Adzic, R. R., Morphology-Dependent Activity of Pt Nanocatalysts for Ethanol Oxidation in Acidic Media: Nanowires Versus Nanoparticles. *Electrochimica Acta* **2011,** *56* (27), 9824-9830.

8. **Koenigsmann, C.**; Santulli, A. C.; Sutter, E.; Wong, S. S., Ambient, Surfactantless Synthesis, Growth Mechanism, and Size-Dependent Electrocatalytic Behavior of High-Quality, Single Crystalline Palladium Nanowires *ACS Nano* **2011,** *5* (9), 7471-7487.

9. Tiano, A. L.; Santulli, A. C.; **Koenigsmann, C.**; Feygenson, M.; Aronson, M. C.; Harrington, R.; Parise, J. B.; Wong, S. S., Toward a Reliable Synthesis of Strontium Ruthenate: Parameter Control and Property Investigation of Submicrometer-Sized Structures. *Chemistry of Materials* **2011,** *23* (14), 3277-3288.

10. **Koenigsmann, C.**; Santulli, A. C.; Gong, K.; Vukmirovic, M. B.; Zhou, W.-p.; Sutter, E.; Wong, S. S.; Adzic, R. R., Enhanced Electrocatalytic Performance of Processed, Ultrathin, Supported Pd–Pt Core–Shell Nanowire Catalysts for the Oxygen Reduction Reaction. *Journal of the American Chemical Society* **2011,** *133* (25), 9783-9795.

11. Santulli, A.C.; **Koenigsmann, C.**; Tiano, A. L.; DeRosa, D.; Wong, S. S., Correlating Titania Morphology and Chemical Composition with Dye-Sensitized Solar Cell Performance. *Nanotechnology* **2011,** *22* (24), 245402.

12. **Koenigsmann, C.**; Wong, S. S., One-Dimensional Noble Metal Electrocatalysts: A Promising Structural Paradigm for Direct Methanol Fuel Cells. *Energy & Environmental Science* (Invited Perspective & Cover Article) **2011,** *4* (4), 1161-1176.

13. Patete, J. M.; Peng, X.; **Koenigsmann, C.**; Xu, Y.; Karn, B.; Wong, S. S., Viable Methodologies for the Synthesis of High-Quality Nanostructures. *Green Chemistry* (Invited Review) **2011,** *13* (3), 482-519.

14. Chen, P.; Xu, X.; **Koenigsmann, C.**; Santulli, A. C.; Wong, S. S.; Musfeldt, J. L., Size-Dependent Infrared Phonon Modes and Ferroelectric Phase Transition in $BiFeO_3$ Nanoparticles. *Nano Letters* **2010,** *10* (11), 4526-4532.

15. Tiano, A. L.; **Koenigsmann, C.**; Santulli, A. C.; Wong, S. S., Solution-Based Synthetic Strategies for One-Dimensional Metal-Containing Nanostructures. *Chemical Communications* (Invited Review) **2010,** *46* (43), 8093-8130.

16. **Koenigsmann, C.**; Zhou, W.-p.; Adzic, R. R.; Sutter, E.; Wong, S. S., Size-Dependent Enhancement of Electrocatalytic Performance in Relatively Defect-Free, Processed Ultrathin Platinum Nanowires. *Nano Letters* **2010,** *10* (8), 2806-2811

Chapter 1. Nanostructured, One-Dimensional Noble Metal Electrocatalysts: A Promising Structural Paradigm for Polymer Electrolyte Membrane Fuel Cells

1.1 A Brief Introduction to "Nano" and Nanostructured Materials

The prefix "nano" is derived from the international system of units (SI) and refers to the unit of measurement that is 1 x 10^{-9} that of the base unit. Therefore, nanostructured materials or so called "nanomaterials" have been defined by the National Nanotechnology Initiative as materials, which possess at least one geometric dimension (*e.g.* length, diameter or thickness) that is between 1 and 100 nanometers (nm). To place the nanometer length scale in perspective, the diameter of a double-helix strand of deoxyribonucleic acid (DNA) is essentially equivalent to 1 nm. Thus, nanomaterials are characterized by their small dimensions and high surface area to volume ratios.

In the context of the definition of nanomaterials, the potential combinations of size and shapes are nearly endless. From a practical perspective however, the number of dimensions that are confined to the nanoscale has served as a useful tool for categorizing nanomaterial into four broad categories including, zero-dimensional (0D), one-dimensional (1D), two-dimensional (2D) or three-dimensional (3D).[1-5] In 0D nanostructures, all of the dimensions are confined to the nanoscale and therefore, common manifestations of 0D particles include spherical nanoparticles (NPs),[5] nanocubes, nanooctahedra, nanopyramids, and as well as many other isotropic-shapes. By contrast, 1D nanostructures are defined as structures with two-dimensions that are confined to the nanoscale. Thus, the 1D structures such as nanowires (NWs), nanotubes (NTs) and nanorods (NRs) maintain two-dimensions that are confined to the nanoscale (*e.g.* the diameter), while the length of the structure can vary to lengths on the macroscopic scale.[2-4] In a similar context, 2D structures require only one-dimension that is confined to the nanoscale and therefore common

2D morphologies are defined by their thickness such as in the case of nanoplates, nanodisks or nanosheets, for example. Although not a true nanomaterial, three-dimensional nanomaterials are defined as materials, which are composed of ensembles of 0D, 1D, or 2D nanostructured materials forming a composite heterostructure. Relevant examples of hierarchical 3D structures include dendritic "sea-urchin" like structures composed of multiple NW dendrites fused at the core[6,7] and particulate superstructures[8] formed from the three-dimensional aggregations of NPs.

The distinctively small size of these materials and the ability to tailor their morphology impart a broad spectrum of characteristic optical,[9] electromagnetic,[10] catalytic,[11,12] and thermal[13] properties in nanomaterials that are different from macroscopic or so-called "bulk" analogs.[9] In many cases, the properties of nanomaterials are inherently linked to the dimensions and physicochemical properties of the nanostructure itself, which renders these materials as exciting candidates in a broad range of practical applications including biotechnology, sensors, catalysis, electromagnetic devices, photovoltaic devices, energy storage, and many more. The observed size- and shape-dependent properties has led to a veritable explosion in the literature, involving the synthesis and characterization of nanomaterials, wherein control over size, morphology (*e.g.* shape), composition, crystallinity, surface structure, and homogeneity can be predictably controlled.[1-3] For example, Figure 1.1 demonstrates the shape-dependent synthesis of palladium nanostructures utilizing preformed 0D NPs as seeds.[4] In this case, the production of a range of morphologies such as 0D faceted particles, 2D plates, or anisotropic 1D rods and bars, can be realized by tailoring synthetic parameters such as the either reaction kinetics, the presence of shape directing agents in the reaction solution, or the morphology of the pre-formed seed employed in the synthesis.

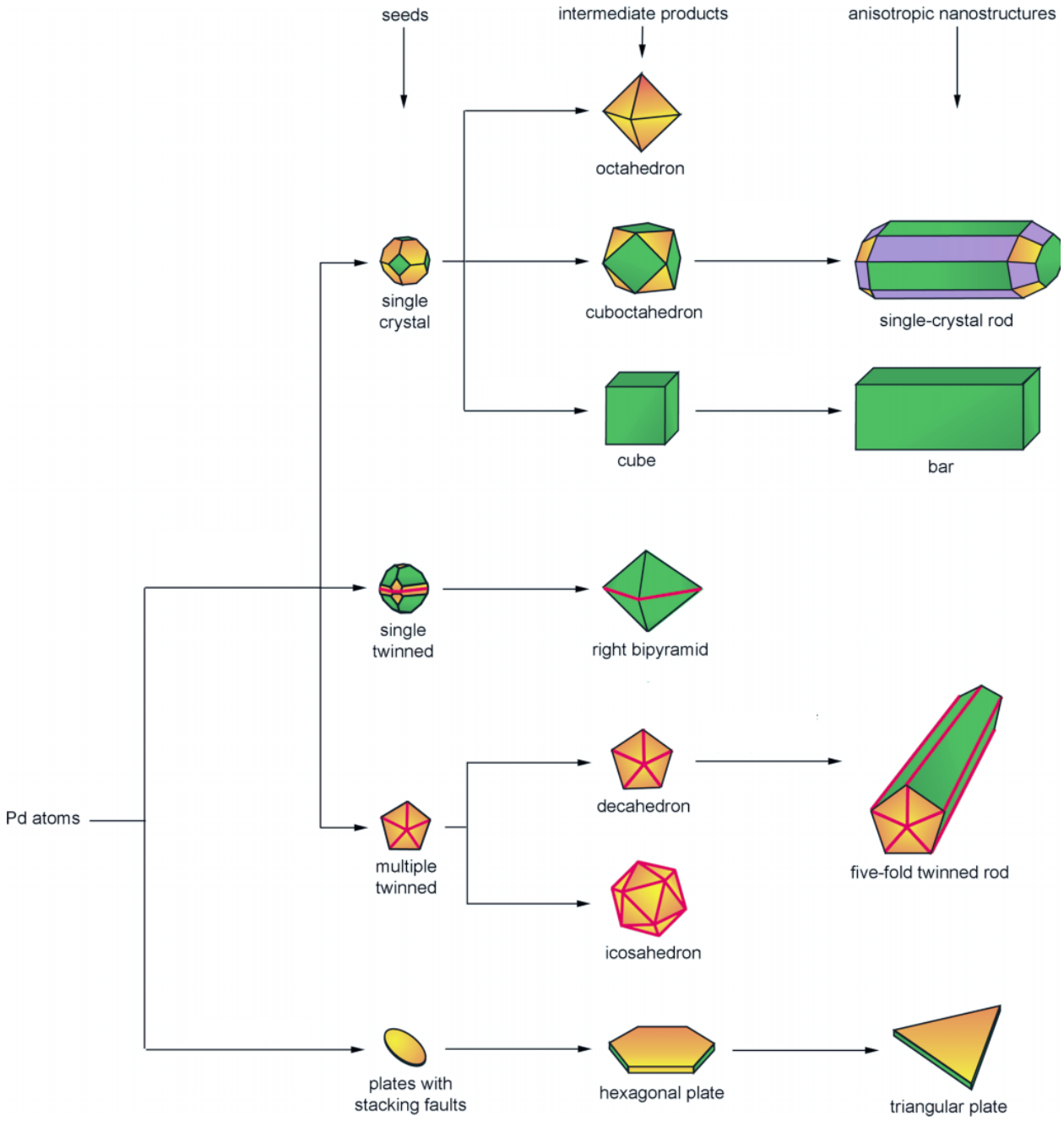

Figure 1.1 A schematic illustration of the reaction pathways that lead to Pd nanostructures with different shapes. (Adapted with permission from Ref. 4. Copyright © 2007 WILEY-VCH Verlag GmbH & Co. KGaA, Weinheim)

Although a complete and detailed discussion of all of the properties and applications of nanomaterials is beyond the scope of this dissertation, the development of nanostructured materials has led to advances in the commercial development of several technologies and these efforts have been summarized in several relevant reviews.[14-20] In this dissertation, we focus specifically on the application of nanostructured materials in the role of electrocatalysts within polymer electrolyte membrane fuel cells (PEMFCs).[12,21-25] PEMFCs represent a key developing technology with direct and practical applications in the portable power and automotive industries with the potential for greatly improving upon efficiency. In addition, PEMFCs also represent a promising paradigm in the progression towards the ubiquitous use of renewable energy sources to meet our future power needs. Despite their promise, their commercialization has been hindered by the long-standing challenges associated with the fabrication of uniform, high performance nanostructured precious metal electrocatalysts that are at the core of this electrochemical device. Specifically, commercially available, state-of-the-art nanoparticulate catalysts maintain low overall performance and poor long-term durability, which contributes to high capital costs for PEMFC device production.

In light of the challenges associated with electrocatalyst development, the following sections provide a concise introduction to electrocatalysis in PEMFCs. Specifically, we first provide a concise introduction to PEMFCs in Section 1.2, including the challenges associated with their commercialization. In Section 1.3, we consider the operational principles of a PEMFC with an emphasis on elaborating upon the role of electrocatalysts in both the anode and cathode half-reactions. Subsequently, the technological challenges and shortfalls associated with commercial electrocatalysts are outlined in Section 1.4 with a focus on understanding correlations between the structure of the catalyst and the corresponding performance. In the

context of the technological shortfalls associated with commercial catalysts, 1D noble metal nanostructures are highlighted in Section 1.5 as a new and potentially promising structural paradigm for the development of highly active and durable electrocatalysts. Specifically, we emphasize the importance of structural anisotropy in 1D nanostructures in terms of electrocatalytic performance.

In this chapter, we also present in Section 1.6 the objectives of the current work, which includes the development of a novel class of 1D noble metal nanostructured materials, wherein a rational correlation of size, composition, structure, and morphology with electrocatalytic performance has led to considerable enhancements in both activity and durability as both anode and cathode electrocatalysts.[11,12,26-34] The enhancement of these physicochemical parameters has led to the development of size, composition, and structure-optimized ultrathin Pt monolayer (Pt_{ML}) shell supported on a Pd_9Au NW core (Pt_{ML}~Pd_9Au NW) electrocatalysts that display significant enhancements over commercial NP analogs for the oxygen reduction reaction (ORR).[29] Collectively, our efforts demonstrate that coupling rational design principles with ambient, scalable synthesis can lead to practical, highly active 1D catalytic architectures that can achieve activities in excess of commercial, state-of-the-art analogs.

1.2 A Concise Guide to Polymer Electrolyte Membrane Fuel Cells

The growing demand for low-cost, renewable energy sources has sparked the commercial development of several energy conversion and storage devices including batteries, solar cells, fuel cells, supercapacitors, thermoelectronic devices and many others.[35] At the core of this effort, is the need for practical devices that are not only inexpensive and efficient but also portable for applications in electronic devices and automobiles.[11,12] Of the multitude of technologies

available, PEMFCs have been highlighted as a promising alternative energy source for portable power applications, particularly in the context of replacing the internal combustion engine (ICE) for vehicular applications.[21-25] PEMFCs operate on the principle of electrochemical conversion of chemical energy from fuels to electrical current, which is utilized to operate the intended device.[36,37] In principle, PEMFC technology is advantageous, because theoretical efficiencies of up to 30 – 50% can be achieved, whereas analogous ICEs are limited by the Carnot cycle with an efficiency approaching ~30%.[22,38] In addition, the ability to extract chemical energy from a fuel source can circumvent the need for extensive recharge cycles required for lithium ion batteries, for instance and provide for longer operational ranges in vehicular applications, when compared with supercapacitors.[14,39]

In the spectrum of fuel cell technologies, PEMFCs are distinctive from other fuel cell architectures because of their low operating temperature, which can span from near ambient temperatures (30 – 80°C) to as high as 120°C in static designs.[22,23] This architecture renders them uniquely suited in the role of portable power generation for automotive and electronics applications.[37] Other fuel cell designs such as the solid oxide fuel cell (SOFC) and molten carbonate fuel cell (MCFC) operate at significantly higher temperatures of up to 700°C – 900°C in order to maintain sufficiently high conductivity through the solid or molten electrolytes, respectively.[40,41] High temperature SOFCs and MCFCs have found promising applications as static power sources because of their ability to utilize a broad range of fuels including natural gas.[41] However, the high temperature and considerable external equipment necessary for their operation render them less suited for mobile or portable applications.

From a practical perspective, PEMFCs can operate on a variety of fuels including gaseous hydrogen in hydrogen fuel cells (HFCs) and small organic molecules (SOMs) such as

methanol, formic acid, or ethanol in direct alcohol fuel cells (DAFCs).[42] The use of elemental hydrogen (H_2) as a fuel source is advantageous in the context of achieving a zero-carbon emission power source, since the exhaust consists only of water.[43] Cells based on hydrogen also have higher practical efficiencies (40 – 50%) since the oxidation of hydrogen is facile on platinum catalysts.[38] However, the commercialization of HFCs has been largely hindered by the technological shortfalls that are associated with the practical production, storage and transportation of hydrogen.[37] Although considerable work is underway on the efficient production of hydrogen from solar energy, the production of effective water splitting catalysts has not yet been commercially realized at a scale that is sufficiently practical for the commercialization of hydrogen fuel cells.[44,45] In addition, the development of HFCs is hindered by the challenges associated with storage and transport of hydrogen both for vehicular and portable power applications.[35] Thus, significant advances are necessary at many levels of technological development and engineering in order to practically commercialize HFCs.

By contrast with HFCs, the fuel sources in DAFCs are either liquids or aqueous solutions containing the liquid fuel.[24,46] This is advantageous, since the inherent technological challenges associated with transportation and storage of hydrogen are inherently circumvented. From an engineering perspective, liquid fuels are also compatible with existing fuel storage and feed devices for automotive applications, thereby rendering them as better candidates with direct applications for automobiles.[47] In addition, liquid fuels such as methanol maintain significantly higher energy densities, especially as compared with hydrogen. For example, under ambient conditions, methanol and ethanol maintain energy densities of approximately 4.3 kW h L^{-1} and 6.7 kW h L^{-1}, which are several orders of magnitude higher than gaseous hydrogen (2.4×10^{-4} kW h L^{-1}).[23] Although ethanol can be readily prepared from renewable sources such as

biomass,[48] the oxidation of ethanol requires the catalytic breakage of a C–C bond, which greatly hinders the performance of the overall device.[49] By contrast, the complete oxidation of methanol is generally more facile. However, the production of methanol is most readily realized through the reformation of natural gas, which is an abundant but non-renewable energy source.[48] Other fuels such as formic acid and sodium borohydride have gained some popularity although their high toxicity and corrosive nature render them less attractive for broad application.

The inherent advantages of liquid-based fuel cells and direct methanol fuel cells (DMFCs) in particular have already made some preliminary commercial inroads into portable power generation and for military and civilian transportation applications, particularly in Europe.[38] For example, Smart Fuel Cells of Germany has begun commercial production of light weight fuel cells (*e.g.* ~7 kg) with maximum power outputs that range from 40 W to 150 W at 12 V for use in portable power applications.[50] This basic design has been scaled up for military applications to include static energy production for powering mobile operations centers and miniaturized for hand-portable electronics and communication devices. Toshiba has also produced the Dynario™ DMFC with a weight of 280 g and a fuel capacity of 14 mL that is suitably portable for hand-held electronics, including cellular phones. Tentative commercialization efforts have also been made in the context of HFCs for automotive and military applications albeit at a considerably slower rate.[51] Collectively, these devices have not been as ubiquitous as expected, largely because of their prohibitive expense and concerns about their reliability.

Despite the initial commercialization of PEMFCs, the wide-spread commercial adoption of HFCs and DAFCs suffer from several technological challenges that continue to elevate production costs.[15] For example, capital costs for DMFCs continue to remain at nearly $1000 US

per kW largely due to their low efficiency (30 – 40%) and high materials costs. The shortfalls associated with PEMFC device designs are complex and require technical innovations at many levels including the polymer electrolyte membrane (PEM), the electrodes, and external components, such as humidifiers and fuel feed systems. However, it is critical to highlight that large portions of the cost associated with PMFCs arise from the poor performance and the high cost of the precious metal electrocatalysts that are necessary for the electrochemical conversion of energy in both the anode and cathode half cells.[52] In fact, the US Department of Energy (DOE) in a 2009 report,[53] has suggested that the cost of the electrocatalysts alone will represent ~20% of the total cost of a commercial fuel cell stack with a precious metal loading of 0.15 – 0.25 mg/cm^2 in the cathode, even when outlays associated with their manufacturing and development are included. On this basis, it is clear that significant innovations are required on the frontier of electrocatalyst development in order to achieve practical fuel cell designs. This challenge is particularly compounded in DMFC designs where catalyst poisoning from the methanol oxidation reaction (MOR) can contribute to even higher loading requirements in the anode, when compared with HFCs.

In Sections 1.3 – 1.5, we focus our discussion on the direct methanol fuel cell as a relevant example of a PEMFC, since the work within this dissertation is focused upon the development of electrocatalysts for MOR and ORR, which are inherent to this cell. However, we stress that the design principles, technological challenges, and advantages of 1D nanostructures presented in the context of the DMFC design can be generalized to all PEMFCs (*e.g.* HFCs and DEFCs) particularly in the case of ORR catalysis.

1.3 The Role of Nanostructured Noble Metal Electrocatalysts in the Electrochemical Conversion of Energy in PEMFCs

Fuel cells including PEMFCs generate power by coupling the electrochemical oxidation of a fuel with the reduction of molecular oxygen, thereby producing an electrical current through an external circuit.[54] In the context of PEMFCs, a variety of fuels exist. However, in this section, we consider the DMFC, which specifically utilizes methanol as a liquid fuel source. Equations (1) and (2) highlight the methanol oxidation and the oxygen reduction processes that occur at the anode and cathode half-cells, respectively. When these half-cell processes are combined in a functional DMFC, the overall cell reaction obtained is illustrated in Equation (3). In this case, the calculated theoretical operating potential is 1.21 V on the basis of the standard potentials for the anode process (E° = 0.02 V) and the cathode process (E° = 1.23 V), and closely approximates the value calculated for the HFC (1.23 V).

$$CH_3OH + H_2O \rightarrow CO_2 + 6H^+ + 6e^- \quad (1)$$

$$6H^+ + 6e^- + 3/2O_2 \rightarrow 3H_2O \quad (2)$$

$$CH_3OH + 3/2O_2 \rightarrow CO_2 + 2H_2O \quad (3)$$

The half-cell reactions are catalyzed by heterogeneous precious metal catalysts, which mutually facilitate the transfer of electrons and the multi-step reaction pathways for the oxidation and reduction processes.[55] State-of-the-art DMFC electrocatalysts primarily consist of platinum NPs (cathode) and platinum-ruthenium alloy NPs (anode) physisorbed onto mesoporous carbon supports, which are impregnated into gas diffusion media.[47,56-59] The diameter of commercial supported NPs (*e.g.* Pt NP/C) typically range between 2 – 4 nm, which significantly increases the

specific surface area and the utilization of the precious metal.[46,59] In the case of nanoparticulate catalysts, the carbon support serves as a three-dimensional substrate, which decreases the effects of particle ripening and aggregation under fuel cell conditions and promotes a higher three-dimensional dispersion of the particles on the electrode itself.[60-62] Despite the increased surface area and dispersion of these catalysts, there are several inherent challenges in the context of both catalytic activity and durability in these catalysts.[61] These technological shortfalls are discussed in detail in Section 1.4 in the context of both the MOR and ORR reactions.

In practical cell designs, the anodic and cathodic electrodes are incorporated into a single membrane electrode assembly (MEA), shown schematically in Figure 1.2, which serves as the heart of the functioning device. Within the MEA, the anode and cathode are mutually separated by a proton-conducting PEM, commercially referred to as Nafion®.[63] The electrodes themselves are comprised of an outer polymeric diffusion layer and an inner electrocatalytic layer, supported onto a carbon backing. Methanol or other liquid fuels can be transported to the anode passively by diffusion or actively by a fuel feed pump external to the MEA. The oxidation process results in the production of (i) protons, which are conducted to the cathode via the PEM, (ii) electrons, which are transferred to the cathode via an external circuit, and (iii) carbon dioxide, which is exhausted from the cell. At the cathode, molecular oxygen is provided either by means of passive convection or provided under pressure from an external compressor. The oxygen is combined with protons and reduced to form water, which is exhausted from the cell.

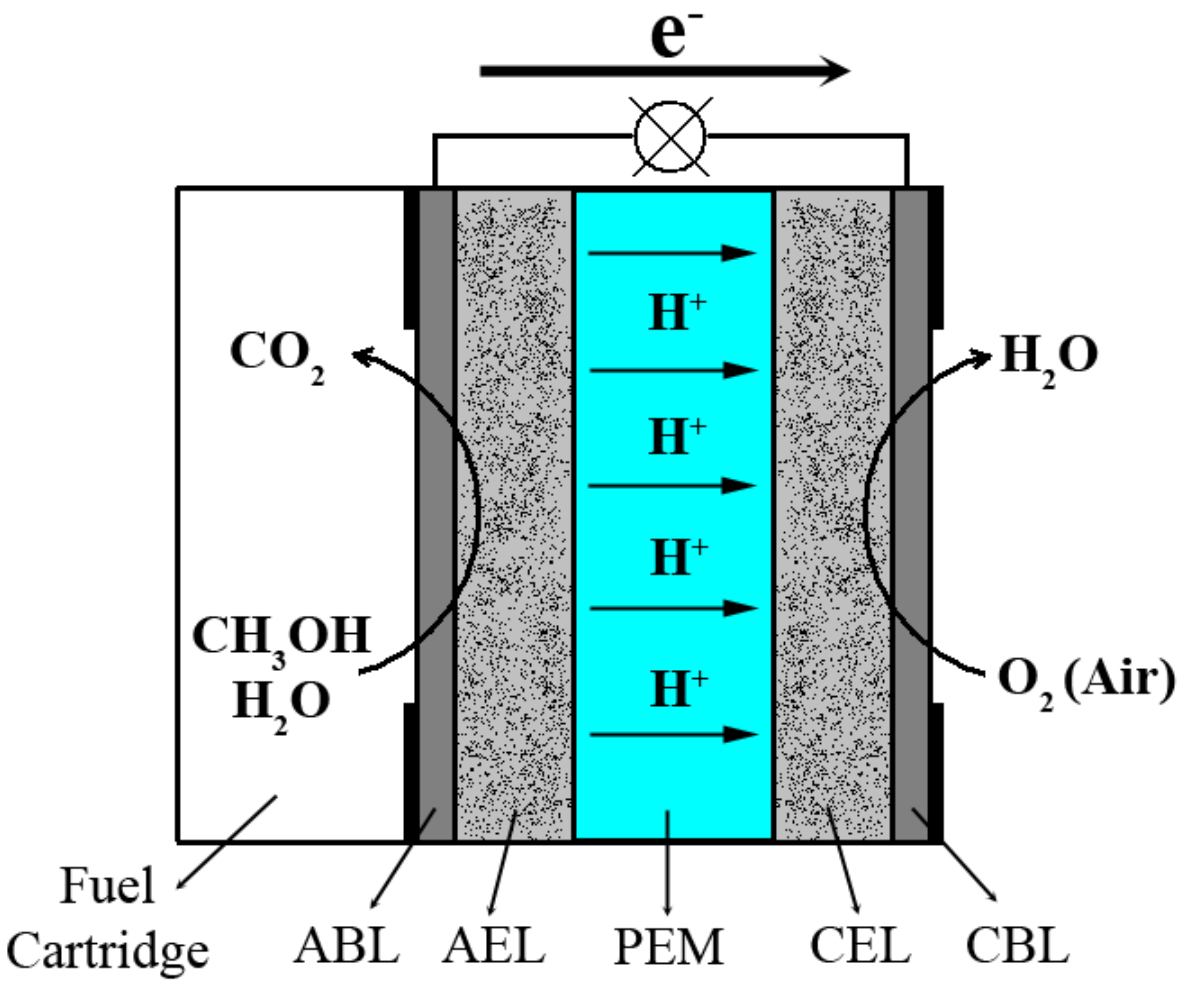

Figure 1.2 A simplified schematic representation of a membrane electrode assembly in a direct methanol fuel cell showing the anode and cathode backing layers (ABL and CBL), the anode and cathode electrocatalyst layers (AEL and CEL) and the polymer electrolyte membrane (PEM). (Reprinted with permission from Ref. 12, Copyright 2011 Royal Society of Chemistry)

In the broader sense, passive designs are relatively simple in the context of their production.[63] However, long term analysis of existing commercial models is required in order to understand their durability and performance, which has been a major concern amongst various manufacturers.[59,61] Moreover, these designs can be scaled up for larger power applications and miniaturized, utilizing micro electromechanical systems (MEMS) techniques.[47] The inherent performance and durability have in large part been attributed to the nanostructured precious metal electrocatalysts employed in both the anode and cathode of PEMFCs. Accordingly, we discuss the technological shortfalls of contemporary DMFC electrocatalysts in the context of the materials that are currently employed to catalyze the oxygen reduction and methanol oxidation reactions in the next section.

1.4 Technological Shortfalls of Contemporary PEMFC Electrocatalysts

Although PEMFC technology is definitely promising, contemporary PEMFCs and particularly DAFCs suffer from high production costs and relatively low efficiencies.[64] Utilizing the DMFC as an example, the maximum theoretical operating potentials is 1.21 V, which closely approximates the operating potential for HFCs (1.23 V). However, modern DMFCs maintain half-cell potentials of approximately 0.3 V and 0.7 V at the anode and cathode, respectively, thereby imparting a dramatically reduced practical cell potential of 0.4 V.[47] Significant overpotentials at both the anode and the cathode can be traced in large part to the precious metal catalysts that are employed at both the methanol oxidation anode[60-62,65] and the coupled oxygen reduction cathode.[66-68] These electrocatalysts possess slow kinetics, require high precious metal loadings between 2 – 4 mg/cm^2 to achieve suitable kinetics in the anode, and lack the necessary cost-efficiency for wide-spread commercialization.[38] In addition, typical electrocatalysts also

lack the durability for long term applications in fuel cells due to poisoning, metal dissolution, oxidation, and particle ripening. In Sections 1.4.1 and 1.4.2, we discuss the origin of the overpotential at both the cathode and anode of DMFCs, respectively.

1.4.1. Cathode Electrocatalysts

Contemporary commercial ORR electrocatalysts in PEMFCs typically rely on metallic platinum NPs physisorbed onto nanostructured carbon supports (Pt NP/C).[36,38,69] Despite the high specific surface area evinced by Pt NP/C, the measured ORR kinetics are relatively low and significant overpotentials are required to achieve suitable kinetics. Recently, a large number of theoretical studies, particularly those of Nørskov and co-workers, have been performed in order to explore the slow kinetics and high overpotentials of ORR occurring on Pt-based metal electrodes.[70-73] In particular, density functional theory (DFT) analysis has been particularly useful in studying the thermodynamics associated with the mechanism of ORR and correlating inherent structural and electronic properties of Pt catalyst with their corresponding ORR performance.[70]

Although Pt has long been considered as the best catalyst for ORR, the results of this analysis have demonstrated that there are two fundamental challenges that arise from utilizing nanostructured Pt as a catalyst. *First*, the oxygen affinity of elemental bulk Pt was found to be too high for optimum kinetics at low overpotentials.[72] The relatively high oxygen affinity is thought to prevent effective formation of O–H bonds, which is a critical step in the formation of water at the cathode. In essence, the catalytically active Pt (111) surface forms passivating layers of coordinated $O–H_{ads}$ and O_{ads} species at potentials comparable to the working potential (*i.e.* 0.7 – 0.9 V) of practical cathodes.[71,74] This effectively decreases the number of active catalytic Pt

sites and necessitates higher overpotentials to reduce the surface oxygen coverage and achieve suitable ORR kinetics. In terms of Pt NP/C, the problem of high oxygen affinity is compounded as the size of Pt catalysts is decreased to the nanoscale, thereby leading to lower overall ORR activity in Pt NP/C when compared with bulk analogs.[75,76] The lower performance in Pt NP/C is attributed to a combined size-dependent electronic effect as well as the high defect site density inherent to Pt NPs with diameters of less than 2 – 3 nm, which mutually increase the strength of the interaction with adsorbed oxygen species.[77-82]

Second, the strong interaction with oxygen and the high defect site density associated with Pt NP/C also contribute to significant challenges associated with the durability of these catalysts under fuel cell conditions.[60,61,83] Specifically, long term durability tests have demonstrated that Pt NP/C undergo significant irreversible oxidation, particle dissolution, and ripening, which leads to lower overall performance. Poor long term performance in carbon supported catalysts has also been linked to oxidation and corrosion of the carbon supports themselves, which leads to further loss of active Pt surface area.[61] Hence, a significant amount of research and optimization are required to address these intrinsic difficulties associated with nanostructured platinum catalysts, especially when the prohibitively high cost of platinum (more than $1,600 US per ounce)[84] is considered.

In addition to studying the origin of the overpotential on elemental Pt, DFT studies have also provided a useful direction to achieve enhanced performance towards ORR with precious metal electrocatalysts. Recently, Norskøv and co-workers have correlated the electronic structure of a large range of transition metals with relative ORR performance, and a distinctive "volcano-type" dependence was observed.[72] In effect, the most effective electrocatalysts should possess a weighted *d*-band center that is slightly lower in energy as compared with pure Pt, so as to

weaken the interaction between the Pt *d*-band and the π^* orbitals of oxygen and thereby facilitate ORR kinetics. This has sparked a great interest in tailoring the physicochemical properties of noble metal electrocatalysts to achieve higher activity and durability.

One successful strategy is to create distinctive structural alternatives to standard, spherical NPs. For example, improvements in activity have been achieved by tailoring the shape of symmetrical NPs in order to produce faceted cubes and octahedra composed of Pt and Pd, which maintain improved ORR activity.[85-88] Adzic and co-workers have also developed a new class of electrocatalysts based on a core-shell design, wherein a platinum monolayer (Pt_{ML}) is supported on either Pd or Pd-alloy NP cores.[66,67,89,90] These Pt_{ML}~Pd NP/C catalysts maintain significant improvements in performance over Pt NP/C, owing to the modulation of the electronic and structural properties of the Pt_{ML} by the Pd core. In a parallel effort, highly active catalysts have also been prepared by manipulating the chemical composition so as to include homogeneous alloy-type formulations[59,91-93] and hierarchical "Pt-skin" core-shell structures.[94,95] Although tangible gains have been achieved in the continued development of the NP motif, generating viable, permanent solutions to many of these inherent performance issues continues to remain elusive, particularly in the context of catalyst durability.

In addition to the intrinsic issues associated with effective ORR performance, the issue of fuel cross-over in DAFCs has also represented a key challenge in the development of cathode electrocatalysts. In DMFCs, for example, a fraction of the methanol that diffuses into the anode remains un-oxidized and continues to diffuse into the cathode half-cell, where it is oxidized by the cathode electrocatalyst.[96,97] This parasitic oxidation process contributes to a loss of potential in the cathode, thereby directly increasing the observed overpotential. Partial oxidation of the methanol can also contribute to the formation of oxidized carbon containing species including

carbon monoxide (CO).[73] The strong interaction of Pt active sites with CO can contribute to significant poisoning effects in the cathode, thereby decreasing the number of Pt active sites available and reducing performance. Recently, there has been a considerable effort to reduce the contribution of methanol crossover by optimizing the device parameters and the chemistry of the PEM itself.[98] These efforts have led to reductions in methanol crossover by nearly 50%. However, measurable effects on catalyst performance are still observed despite the tangible improvements. Collectively, it is clear that the issue of methanol crossover must be addressed from the perspective of the cathode electrocatalysts by reducing their sensitivity to methanol under operating conditions. This can be accomplished either by increasing the tolerance of cathode materials to adsorbed CO or by reducing their inherent ability to oxidize methanol in the potential window relevant for ORR.

1.4.2. Anode Electrocatalysts

By analogy with cathode electrocatalysts, PEMFC anode catalysts also rely upon carbon-supported Pt-based NPs.[61,62,65] The development of anode catalysts has been largely focused upon the corresponding fuel that is oxidized at the anode. Accordingly, the mechanism of hydrogen, methanol, ethanol, and formic acid oxidation are unique and necessitate different electrocatalyst design principles to achieve high performance. In this dissertation, we focus our efforts on the development of electrocatalysts for the oxidation of small organic molecules and in particular, methanol and ethanol, which represent two of the key reactions in DAFCs. In this section, we focus our discussion on the methanol oxidation reaction (MOR) as a useful example for the challenges that face the development of effective anode electrocatalysts.

The electrocatalytic oxidation of methanol on Pt, although very complex, can be simplified into four mechanistic steps, with the primary intermediate being CO.[57,99-103] Essentially, methanol is adsorbed onto the Pt surface and in a rapid $4e^-$ oxidation process occurring over several mechanistic steps, the carbon is dehydrogenated, producing adsorbed CO. The subsequent oxidation of CO proceeds relatively slowly at potentials close to the thermodynamic potential, due to a lack of adsorbed oxygen species, such as Pt-OH^*, which are believed to facilitate the oxidation process.[73] Therefore, the adsorbed CO, which is rapidly formed at low overpotentials, acts as a poisoning intermediate and blocks Pt active sites. The poisoning effect of the CO intermediate prevents high MOR kinetics at low potentials. In case of elemental Pt, defect sites on the Pt surface play a key role in the oxidation of CO, since these sites adsorb oxygen species at lower potentials and thereby facilitate the oxidation of CO.[104] Thus, the high defect site density associated with Pt NP/C by comparison with bulk analogs facilitates the oxidation of CO. However, the small size of the commercial Pt NP/C increases the relative interaction with CO. Collectively, it has been demonstrated that the poisoning effect of CO and the correspondingly low MOR kinetics at low overpotentials render elemental Pt as a poor candidate for practical MOR catalysts.

Significant enhancements in performance have been achieved by tailoring the chemical composition of Pt to include more oxophilic metals in homogeneous alloys. The most promising example has been nanostructured $Pt_{1-x}Ru_x$ alloys, which have demonstrated a shift in the onset potential of MOR by nearly ~100 mV to lower potentials.[15,56,105,106] Optimization of these alloys has shown that maximum efficiency can be obtained, when Ru concentrations range between x = 0.07 and 0.33 in $Pt_{1-x}Ru_x$ alloys. Specifically, when alloyed at low to moderate concentrations ($\chi_{Ru} = 0 – 0.6$), the PtRu alloy forms a solid solution with Ru atoms occupying sites within the

Pt's face-centered cubic structure.[56] In the context of the electrocatalytic oxidation of methanol, the more oxophilic Ru sites adsorb oxygen species (*e.g.* Ru-OH_{ads}) at significantly lower potentials than Pt. This facilitates the oxidation of CO to CO_2 in a process referred to as carbonyl spillover. Accordingly, PtRu alloys have also been demonstrated to improve the selectivity of the MOR process for the complete oxidation of methanol and to decrease the production of partially oxidized species, such as formic acid.

Despite the tangible improvements in the CO tolerance and activity of alloyed PtRu NPs, contemporary DMFCs continue to maintain high anodic overpotentials and suffer from considerable CO poisoning. Another issue that has become increasingly important in the development of anode catalysts has been the challenge of poor durability in PtRu NPs, which is readily attributed to the presence of Ru. The addition of more oxophilic metals, which are less stable toward permanent oxidation and dissolution, especially in the acidic and corrosive conditions of DMFCs.[107] Hence, continued research is necessary in order to develop more effective catalysts that are equally active, stable, and CO-tolerant for successful and wide spread commercialization.

1.5 Importance of One-Dimensionality – The Role of Structural Anisotropy in Electrocatalysis

In light of the shortfalls of contemporary DMFCs, the use of one-dimensional (1D) motifs in the development of fuel cell electrocatalysts has been highlighted as a new and promising paradigm with which to solve many of the technological challenges that face the development of DMFCs as a commercially viable portable power source. There are many existing reviews that already discuss the properties of 1D nanostructures in great detail.[2,3,108-110]

Since our Perspective in 2011 on the subject,[12] the number of publications involving 1D noble metal nanostructures has increased significantly owing to their advantageous properties as both cathode and anode electrocatalysts. Our group along with several others has recently reviewed the progress in this exciting and emerging field.[11,111-113] In this section, we summarize the advantages associated with 1D nanostructures, which has contributed to the significant and measureable increase in their application as electrocatalysts for PEMFCs.

From a structural perspective, 1D noble metal nanostructures are characterized by their geometric anisotropy and this anisotropy can impart several beneficial properties. For example, the anisotropic structure of 1D noble metal nanostructures has been shown to promote the exposure of largely pristine surfaces with long segments of crystalline planes, as compared with their associated 0D morphologies.[110] Additionally, the anisotropic growth of 1D structures typically results in the preferential display of low energy crystal facets in order to minimize the surface energy of the systems.[114] In the case of noble metal nanostructures, the use of basic amine-terminated surfactants has been widely shown to lead to the preferential display of (100) facets on the NW surface. In terms of platinum and palladium, the low energy (100) and (111) facets are most active for oxygen-reduction and thus, the preferential display of the low-energy facets are highly advantageous for catalysis.[36,115]

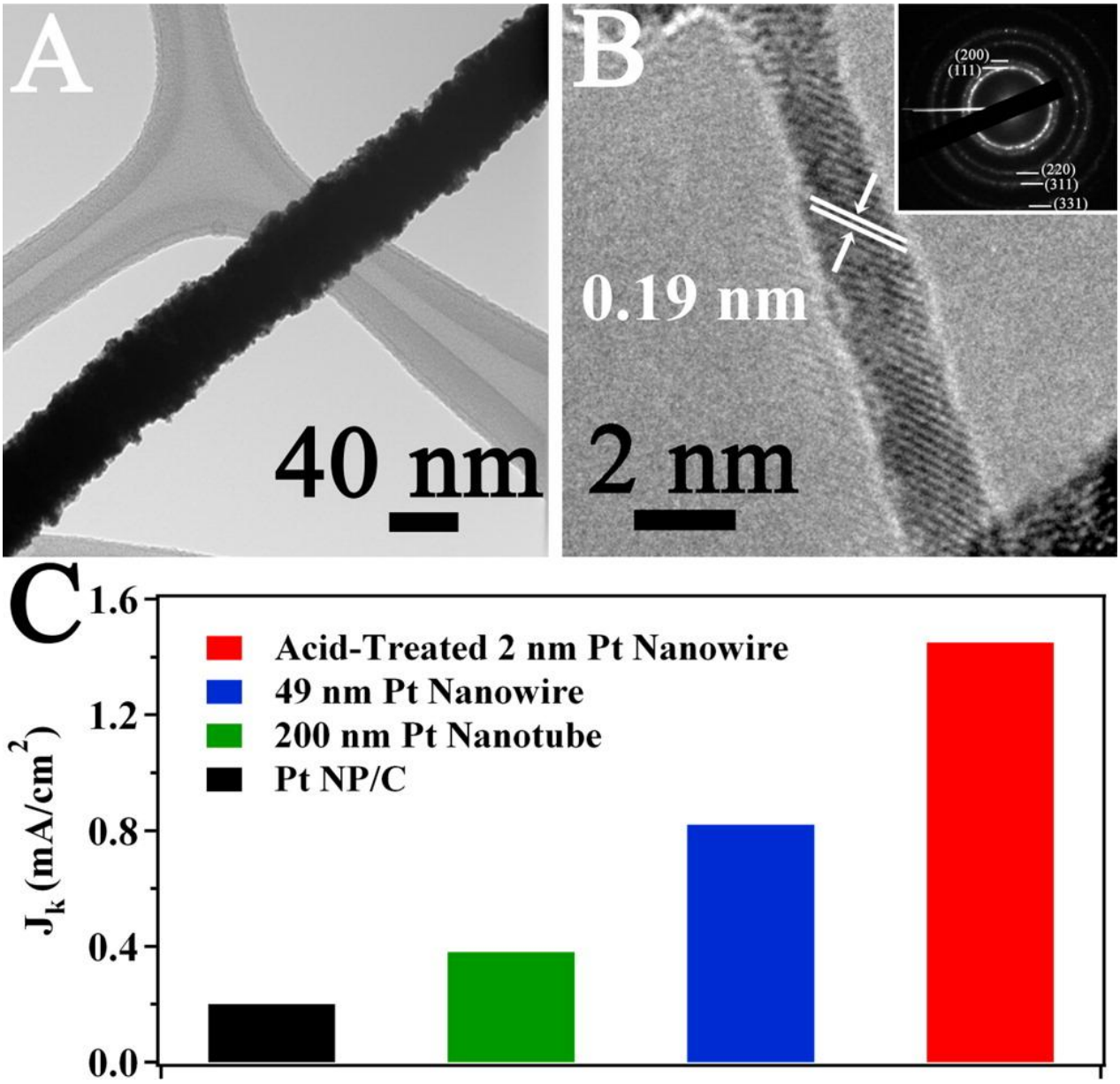

Figure 1.3 Comparison of electrocatalytic behavior between 1D platinum nanostructures and commercial Pt NP/C. Representative TEM images collected from individual isolated Pt NWs possessing diameters of 49 (A) and 2 nm (B). A representative selected area electron diffraction pattern collected from an ensemble of individual 2 nm NWs is shown as an inset. The size-dependent trend in 1D Pt nanostructures of specific ORR activity measured at 0.9 V with commercial Pt NP/C serving as a commercial reference system is illustrated in (C). (Reprinted with permission from Ref. 11. Copyright 2012 American Chemical Society)

In addition, it is also important to note that the recent literature has demonstrated that single-crystalline, 1D nanostructures generally maintain fewer surface defect sites as compared with 0D morphologies.[37] This arises from their structural anisotropy wherein growth in one dimension allows for the preferential exposure of lattice planes with fewer lattice boundaries.[3] In the context of ORR, the low defect site density associated with 1D noble metal nanostructures is expected to promote more facile kinetics by weakening the interaction with adsorbed oxygen species and delaying the passivation of the surface to higher potentials.[36] When taken together, these factors clearly demonstrate that 1D motifs can possess advantageous intrinsic structural aspects that would impart improved catalytic performance towards ORR at the interface in the cathode. For example, Figure 1.3 shows a comparison of the electrocatalytic behavior of a number of 1D Pt nanostructures including 200 nm Pt NTs, 45 nm Pt NWs (Figure 1.3A), and 1.3 nm Pt NWs (Figure 1.3B) with commercial Pt NP/C.[11] In all cases, the 1D Pt nanostructures maintained higher area-normalized or so-called "specific" ORR activity by comparison with a state-of-the-art, commercial Pt NP/C sample (Figure 1.3C), demonstrating the intrinsic advantages of 1D nanostructures.

In the case of MOR, the role of defect sites has been highlighted in previous literature and found to be advantageous, for example in the case of pure platinum.[104] However, it is unclear whether in the case of pure platinum if strictly anisotropic structures will serve to necessarily increase the intrinsic activity as defect sites become less available. By contrast, there has been less emphasis on the importance of defect sites in the case of the more effective and most commonly utilized PtRu alloy catalysts where the surface Ru sites act as the more oxophilic catalyst for the oxidation of adsorbed CO.[25] Thus, it is generally unknown in the case of MOR catalysis if anisotropy will necessarily increase the intrinsic activity. However, we have recently

demonstrated that processed, Pt NWs possess considerably better CO tolerance on the basis of the shift in the main CO stripping peak potential by 200 and 80 mV to lower potential, in ultrathin 1.3 nm NWs and 45 nm NWs, respectively.[32,34] This intrinsic property of ultrathin NWs has rendered them as excellent candidates for both the methanol and ethanol oxidation reactions and demonstrates that 1D morphologies are more tolerant to CO owing to their weaker interaction with adsorbed intermediates.[34,116] In addition, structural anisotropy may largely contribute to an increase in the stability of the catalysts by removing defect sites, which are susceptible to oxidation and decomposition.[46]

In terms of catalytic stability, lattice boundaries and defect sites are more susceptible to decomposition, because these regions evince surface Pt atoms with lower coordination numbers, which are more prone to irreversible oxidation.[61,117] The three primary "break-down" mechanisms of carbon-supported Pt and Pt alloy NPs are dissolution and ripening, support breakdown, and irreversible oxidation.[62,66] The structural nature of 1D nanostructures are thought to mitigate for all of these issues.[3] That is, the asymmetry of this structure suppresses physical ripening processes and thus, these nanomaterials are inherently stabilized from dissolution and Oswald ripening. [118,119] Therefore, 1D nanostructures would in theory be less apt to require a carbon support, because they do not suffer from the same propensity to ripen and aggregate.

Finally, anisotropic 1D nanostructures also possess advantageous path-directing effects, which greatly enhance their electron transport properties.[109,120] A previous study of metallic NWs in devices has shown that single-crystalline NWs can maintain resistivity values commensurate with that of their bulk counterparts.[121] Moreover, the resistance of metallic NWs can be reliably tuned as function of diameter, which is highly advantageous in terms of the nanoscale design of conductive systems. The growth mechanism and anisotropic structure may in essence reduce the

number of grain boundaries and particle interconnects, which thereby suppresses the electronic scattering and would therefore improve the overall electronic transport present in the half cells. This advantageous property would be particularly beneficial to vertically oriented, free-standing NW or NT arrays, since the 1D structure serves as both the catalyst and the conductive media.[27,30]

As a culmination of all of these advantages, 1D nanomaterials possess many of the key structural and electronic properties that can contribute to solving many of the technological challenges that are observed with 0D-based electrocatalysts. When taken together, these noteworthy advantages have the potential to reduce the inevitable material needs and processing costs associated with future cell designs. As such, in light of the advantages of 1D nanostructures, there has been a significant push towards the development of electrocatalysts, possessing 1D motifs. In the following section, we critically explore the recent progress in this area within the context of the correlation between structure and electrocatalytic performance.

1.6 Objectives of Current Work

Although 1D noble metal nanostructures have been widely demonstrated in recent literature to maintain significantly better activity and durability than commercial Pt NP/C, several critical challenges remain in their practical application as feasible commercial catalysts.[11] For example, 1D nanostructures possess inherently lower specific surface areas as compared with 0D spherical particles of the same diameter. Thus, the greatly enhanced specific activities observed in these anisotropic systems may not necessarily lead to corresponding enhancements in terms of mass-normalized performance. Although several promising examples in the literature have corroborated the reproducibility of enhanced platinum group metal (PGM) normalized

activities in 1D structures,[26,29,122] the mass activities typically observed in existing NW and NT electrocatalyst systems are actually similar to what has been correspondingly observed for Pt NP/C. Therefore, a key step in designing practical 1D catalysts will be to minimize the necessary precious metal loading, while simultaneously continuing to improve upon the inherent activity of these materials.[11,12] This strategy includes developing synthetic approaches (many of which are presented herein) for the production of high-quality so called "ultrathin" 1D nanostructures with diameters below 5 nm so as to maximize the surface area-to-volume ratio and correspondingly, minimize the precious metal content necessary for high performance.

Additionally, the goal of achieving enhanced performance in 1D nanostructures is further complicated by the fact that the origin of electrocatalytic enhancement, as a result of the anisotropic structure, remains elusive. This issue is particularly apparent in multi-metallic 1D catalysts, wherein both morphology and chemical composition mutually and synergistically contribute to improved performance. Therefore, a key step in terms of producing practical 1D electrocatalysts has been to probe ORR performance as a function of both particle size and composition. This endeavor is important not only to gain critical insights into the correlation between structure and activity but also, more practically, to establish a means of reducing Pt content and overall precious metal loading in functional electrocatalysts, since presumably both catalyst size and composition can be further optimized. For example, decreasing the diameter of a NW catalyst of a fixed length by a factor of two can more than double the effective specific surface area expected, thereby leading to plausibly greater improvements in PGM utilization.

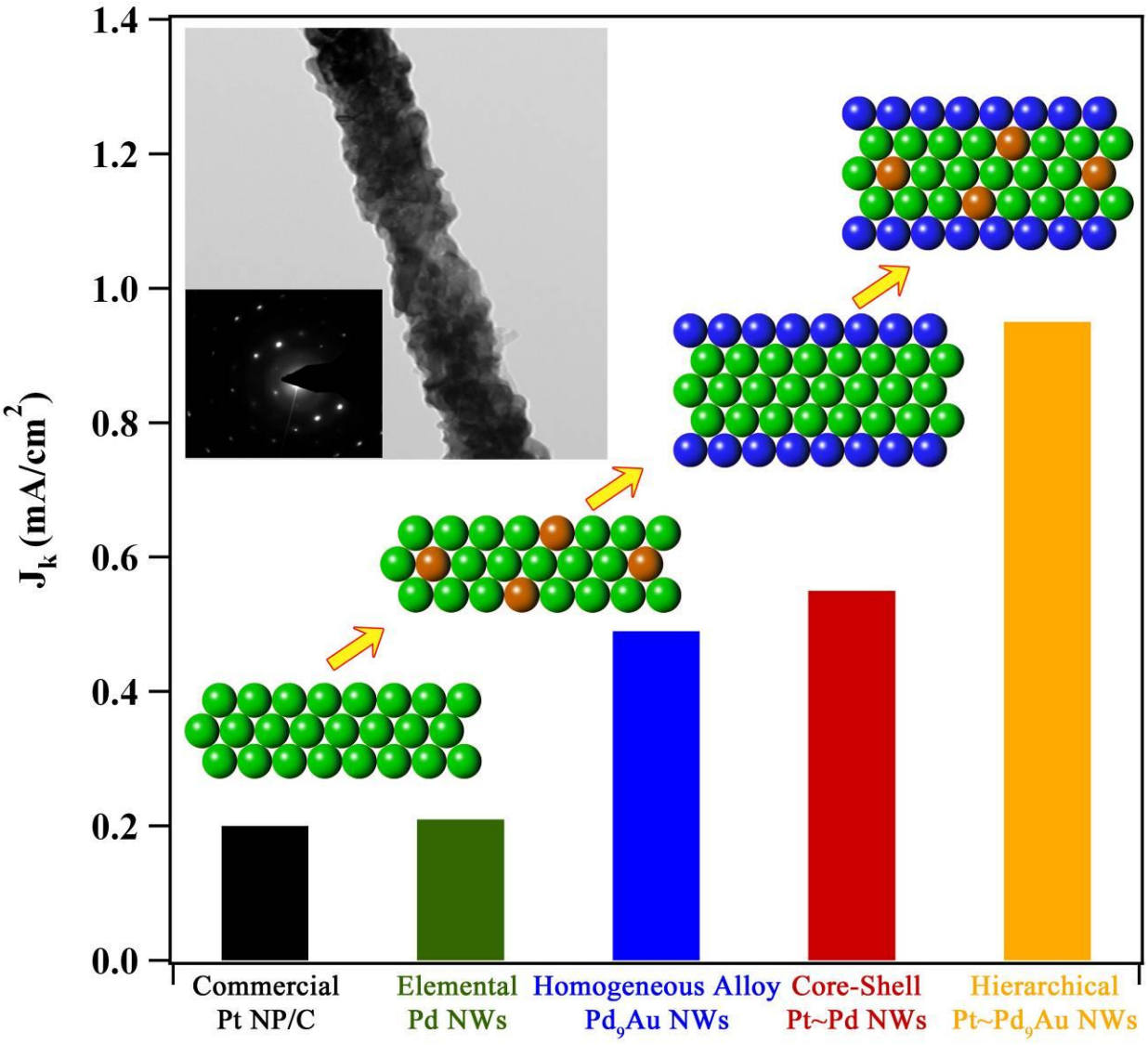

Figure 1.4 Rationally tailoring the size, composition, and structure of one-dimensional nanostructures represents a key step in moving towards active, cost-effective, and durable replacements for commercial Pt NP catalysts for oxygen reduction. (Reprinted with permission from Ref. 11. Copyright 2012 American Chemical Society)

In this dissertation, we focus our experimental efforts on precisely deducing the nature of the complex interplay amongst size, chemical composition, and electrocatalytic performance in high-quality elemental and bimetallic 1D noble metal NW systems with an emphasis on achieving efficient and sustainable methods for catalyst preparation. In terms of catalyst dimensions, an interesting and measureable size-dependent trend emerges in the case of elemental Pt and Pd[26,33] as well as in more complex hierarchical core-shell Pt_{ML}~Pd and Pt_{ML}~$Pd_{1-x}Au_x$ NWs.[27,29,30] In fact, outstanding enhancements in catalyst performance are measured, when the diameter of 1D NW electrocatalysts is purposefully decreased into the ultrathin size regime. In a similar context, we have considered the role of chemical composition in 1D electrocatalysts and noted significant composition-dependent enhancements in activity and durability in high-quality, bimetallic $Pd_{1-x}Au_x$ and $Pd_{1-x}Pt_x$ NWs.[29,30] A key finding that is apparent from these experimental results is that widely seen behavioral trends in the composition- and size-dependent performance for 0D NP-based catalysts do not necessarily hold in the case of 1D architectures, because of the structural and electronic effects, associated with their anisotropic structures.

As a culmination of our efforts to take advantage of these intrinsic structure-activity correlations, our group developed a morphology-, size-, and composition-optimized Pt_{ML}~Pd_9Au NW electrocatalyst with an ultrathin 2 nm diameter, which possessed outstanding Pt mass and PGM activities of 2.56 A/mg_{Pt} and 0.64 A/mg_{PGM}, respectively, surpassing the activity of conventional state-of-the-art Pt NP/C by more than ten-fold. The rational progression towards this fully optimized 1D electrocatalyst system (Figure 1.4) was achieved by combining several design principles including tailoring the composition and structure to achieve progressively enhanced performance. This exciting result has been highlighted in a recent editorial entitled

"The Magic of Electrocatalysts"[123] and demonstrates that the fundamental insights gained into the intimate correlation between size, shape, composition, and catalyst performance can lead to very practical improvements in terms of both catalyst efficiency and cost-effectiveness. On the basis of this progress, we divide this dissertation into chapters describing the synthesis, characterization, and investigation of morphology, size, and composition-dependent performance in high-quality 1D electrocatalysts. The following sections provide a concise outline of each chapter.

1.6.1. Experimental Methods for Characterizing Structure, Determining Electrocatalytic Performance and Depositing Surface Pt_{ML} on Novel 1D Noble Metal Nanostructures (Chapter 2)

A core set of experimental methods are employed to examine the structure and performance of novel, as-prepared, 1D nanostructures as a function of composition, size, structure and morphology. In this chapter, we discuss the experimental methods for evaluating catalyst crystallinity, structure, and morphology utilizing powder X-ray diffraction (XRD) and electron microscopy techniques including scanning electron microscopy (SEM), and transmission electron microscopy (TEM). In addition, we describe the methods for evaluating electrocatalyst performance under three-electrode conditions or so called "half-cell" conditions. This includes methods for preparing the working electrode, evaluating the surface structure of the electrocatalyst, and quantitative methods for determining electrochemically accessible surface area (ESA). In addition, common electrochemical characterization methods (*e.g.* cyclic voltammetry and CO stripping voltammetry) are discussed. The electrocatalytic performance towards the oxygen reduction reaction is measured, utilizing the thin-layer rotating disk electrode approach, and we describe in detail the methods for calculating surface area and mass-

normalized kinetic current densities. In addition, the synthetic protocol for depositing a homogeneous Pt_{ML} on the surface of noble metal nanostructures utilizing a copper underpotential deposition process (UPD) combined with a galvanic displacement protocol developed by Adzic and co-workers[124] is discussed. This process has been generalized to include Pt_{ML} deposition on elemental, bimetallic and segmented NW systems.

1.6.2. Size-Dependent Enhancement of Electrocatalytic Performance in Relatively Defect-Free, Processed, Ultrathin Platinum NWs (Chapter 3)

The synthesis, characterization, and size-dependent electrocatalytic performance of ultrathin Pt NWs with a diameter of less than 2 nm are described.[33] An acid-wash process was developed in order to suitably exfoliate and purify the crystalline nanostructures, in this case the Pt NWs of surface defect sites, thereby yielding processed NWs with diameters of 1.3 ± 0.4 nm. The electrocatalytic activity of these NWs toward ORR was studied in relation to commercial Pt NP/C and to analogously processed, unsupported Pt NP, which mutually demonstrate that the one-dimensional Pt NWs maintain a significant morphology-dependent enhancement in electrocatalytic performance. More importantly, we demonstrate for the first time that there is a significant and measureable size-dependent enhancement in specific ORR activity in 1D Pt nanostructures. Specifically, the ultrathin acid treated Pt NWs display a specific activity of 1.45 mA/cm^2, which is nearly a two-fold and four-fold enhancement over nanosized Pt wires (0.82 mA/cm^2) and submicron Pt tubes (0.38 mA/cm^2), respectively. This novel size-dependent phenomenon observed in 1D architectures starkly contrasts with the corresponding trend in 0D nanoparticulate catalysts, and represents a critical step in demonstrating the highly advantageous properties of 1D nanostructures for electrocatalysis.

1.6.2. Enhanced Electrocatalytic Performance in Processed, Ultrathin, Carbon Supported Pt_{ML}~Pd Core-Shell NW Catalysts for the Oxygen Reduction Reaction (Chapter 4)

In the context of our results with elemental Pt NWs, we develop for the first time a practical, one-dimensional core-shell electrocatalyst consisting of a Pt_{ML} shell supported onto a high quality, carbon supported ultrathin Pd NW core (Pt_{ML}~Pd NW/C).[26] Ultrathin Pd NWs were prepared with diameters of 2.0 ± 0.5 nm, utilizing a simple, scalable solution-based technique, and a method was developed for dispersing the as-prepared NWs onto a Vulcan XC-72R carbon support forming Pd NW/C composite structures. The Pd NW/C were purified of residual surfactant and activated for electrocatalysis utilizing a two-step process involving a pretreatment (*e.g.* acid wash or ozone oxidation) followed by a selective CO adsorption process. The Pt_{ML} was deposited onto the processed, purified Pd NW/C composites by means of a Cu UPD process followed by the galvanic displacement of the Cu ad-atoms by a platinum precursor. Extensive characterization of the NWs pretreated with either acid or UV generated ozone confirmed that the ozone pre-treatment leads to the production of purified NWs with an optimum dispersion of the catalyst on the carbon surface. Accordingly, the UV-ozone pre-treated Pt_{ML}~Pd NW/C catalyst was found to possess outstanding specific and mass-activities of 0.77 mA/cm^2 and 1.83 A/mg_{Pt}, which was significantly enhanced beyond that of commercial Pt NP/C and analogous core-shell Pt_{ML}~Pd NP/C. The ozone-treated Pt_{ML}~Pd NW/C composites also maintained excellent electrochemical durability under accelerated half-cell testing and it was confirmed that there was no measureable loss in mass-normalized activity after 30,000 electrochemical cycles.

1.6.3. Ambient Surfactantless Synthesis, Growth Mechanism and Size-Dependent Electrocatalytic Behavior of High-Quality, Single Crystalline Palladium NWs (Chapter 5)

In light of the distinctive size-dependent properties associated with 1D nanostructures, we undertake a systematic investigation of the diameter-dependent phenomena associated with elemental Pd NWs and hierarchical core-shell Pt_{ML}~Pd NWs. In this chapter, we develop an ambient, surfactantless methodology that employs commercially available filter membranes as templates for the produce high quality, single crystalline Pd NWs with direct and predictable control over the diameter and the aspect ratio.[27] The NWs grown within 200 and 15 nm polycarbonate membranes maintain homogeneous diameters of 270 ± 45 nm and 45 ± 9 nm, respectively, and can be isolated as either individual NWs or as vertically oriented, free-standing NWs arrays. To fully understand the potential of this novel synthetic technique, the growth mechanism of these NWs has been extensively explored and on the basis of a direct examination of individual NWs within the template pores, we have determined that a two-step growth mechanism predominates in the formation of the NWs within the template pore. As a culmination of our synthetic efforts, we also demonstrate the feasibility of preparing segmented or so called "A/B NWs", wherein predictable control over the composition of the NW is achieved along the axial dimension.[31]

The ability to predictably tailor the diameters of as-synthesized Pd NWs affords a unique opportunity to explore the diameter-dependent electrocatalytic ORR performance in elemental and core-shell NWs. As-prepared submicrometer (270 nm) and nanosized (45 nm) Pd NWs were studied by comparison with ultrathin 2 nm NWs described in Chapter 4 in order to elucidate systematic trends in ORR activity and durability. The specific and platinum mass activity was found to increase significantly from 0.40 mA/cm^2 and 1.01 A/mg_{Pt} to 0.74 mA/cm^2

and 1.74 A/mg_{Pt}, as the diameter was decreased from the submicrometer size regime to the ultrathin nanometer range. This exciting result demonstrated that the size-dependent phenomena associated with elemental Pt NWs can be further generalized to elemental Pd NWs and core-shell Pt_{ML}~Pd NW analogs.

1.6.4. Highly Enhanced Electrocatalytic Oxygen Reduction Performance in Bimetallic Palladium-Based NWs Prepared Under Ambient, Surfactantless, Conditions (Chapter 6)

In addition to considering particle dimensions, tailoring the chemical composition of nanostructured electrocatalysts has led to a veritable explosion of new catalytically active noble metal formulations and considerable improvements in performance have been realized. In this context, we employ our ambient, template-based technique described in Chapter 5 to prepare a series of bimetallic $Pd_{1-x}Au_x$ and $Pd_{1-x}Pt_x$ NWs with control over composition and size.[30] Extensive characterization of the as-prepared NWs demonstrates that our methodology can produce high-quality, crystalline NWs with homogeneous, alloy-type compositions. The ability to tailor chemical composition at the nanoscale, while maintaining nearly identical surface structure, crystallinity, purity and quality, highlights the U-tube synthesis technique as an ideal candidate for studying composition-dependent phenomena in 1D nanostructured systems. Accordingly, we examine the performance of as-synthesized $Pd_{1-x}Au_x$ NWs and $Pd_{1-x}Pt_x$ towards ORR, MOR, and formic acid oxidation (FAOR). In addition, we also consider the stability of highly activity Pd_9Au NWs toward ORR in the presence of SOMs such as methanol. Collectively, our results demonstrate that tailoring composition in 1D NWs can lead to considerable enhancements in electrocatalytic performance. As a tangible example, the core-shell Pt_{ML}~Pd_9 Au NWs were found to maintain a platinum and PGM mass normalized activities of

2.08 A/mg_{Pt} and 0.16 A/mg_{PGM}, respectively, representing significant improvements over elemental Pt_{ML}~Pd NW analogs.

1.6.5. Size- and Composition-Dependent Enhancement of Electrocatalytic Oxygen Reduction Performance in Ultrathin Palladium – Gold ($Pd_{1-x}Au_x$) NWs (Chapter 7)

Drawing upon our collective findings in Chapters 3 – 6, we have developed a hierarchical, ultrathin Pt_{ML}~Pd_9Au NW/C electrocatalyst that is optimized in terms of morphology, structure, size and composition.[29] The solution-based synthetic protocol described in Chapter 4 has been generalized to include the synthesis of ultrathin $Pd_{1-x}Au_x$ NWs, wherein composition is controlled simply by manipulating the ratio of precursors present within the reaction mixture. The as-synthesized Pd_9Au NW/C maintain a specific activity of 0.40 mA/cm^2, which is an improvement upon elemental Pd NW/C analogs (0.12 mA/cm^2) and commercial Pt NP/C (0.20 mA/cm^2). After Pt_{ML} deposition, a volcano-type composition dependence is observed in the ORR activity of the corresponding Pt_{ML}~$Pd_{1-x}Au_x$ NWs as the Au content is increased to 30% with the activity of the Pt_{ML}~Pd_9Au NWs (0.98 mA/cm^2, 2.54 A/mg_{Pt}) representing the optimum performance. The ultrathin size of the optimized Pt_{ML}~Pd_9Au NWs (0.64 A/mg_{PGM}) is highly advantageous and promotes a significant increase in the PGM normalized mass activity, especially when compared with 45 nm Pt_{ML}~Pd_9Au NWs (0.16 A/mg_{PGM}) and commercial Pt NP/C (0.1 – 0.2 A/mg_{PGM}). In fact, preliminary results have not only demonstrated that the synthetic protocol can be scaled to produce near gram-scale quantities of optimized NWs but also excellent performance within a MEA can be realized. Collectively, this result demonstrates that coupling rational design principles with ambient, scalable synthesis can lead to practical,

highly active 1D catalytic architectures that can achieve activities in excess of commercial, state-of-the-art analogs.

1.7 References

(1) Patete, J. M.; Peng, X.; Koenigsmann, C.; Xu, Y.; Karn, B.; Wong, S. S. *Green Chem.* **2011**, *13*, 482-519.
(2) Tiano, A. L.; Koenigsmann, C.; Santulli, A. C.; Wong, S. S. *Chem. Commun.* **2010**, *46*, 8093-8130.
(3) Xia, Y.; Yang, P.; Sun, Y.; Wu, Y.; Mayers, B.; Gates, G.; Yin, Y.; Kim, F.; Yan, H. *Adv. Mater.* **2003**, *15*, 353-389.
(4) Xiong, Y.; Xia, Y. *Adv. Mater.* **2007**, *19*, 3385-3391.
(5) Sau, T. K.; Rogach, A. L. *Adv. Mater.* **2010**, *22*, 1781-1804.
(6) Mao, Y.; Kanungo, M.; Hemraj-Benny, T.; Wong, S. S. *J. Phys. Chem. B* **2006**, *110*, 702-710.
(7) Mao, Y.; Park, T.-J.; Zhang, F.; Zhou, H.; Wong, S. S. *Small* **2007**, *3*, 1122-1139.
(8) Mao, Y.; Park, T.-J.; Wong, S. S. *Chem. Commun.* **2005**, 5721-5735.
(9) Murphy, C. J.; Sau, T. K.; Gole, A. M.; Orendorff, C. J.; Gao, J.; Gou, L.; Hunyadi, S. E.; Li, T. *J. Phys. Chem. B* **2005**, *109*, 13857-13870.
(10) Chen, J.; Wiley, B. J.; Xia, Y. *Langmuir* **2007**, *23*, 4120-4129.
(11) Koenigsmann, C.; Scofield, M. E.; Liu, H.; Wong, S. S. *J. Phys. Chem. Lett.* **2012**, *3*, 3385-3398.
(12) Koenigsmann, C.; Wong, S. S. *Energy Environ. Sci.* **2011**, *4*, 1161 - 1176.
(13) Kline, T. R.; Tian, M.; Wang, J.; Sen, A.; Chan, M. W. H.; Mallouk, T. E. *Inorg. Chem.* **2006**, *45*, 7555-7565.
(14) Armand, M.; Tarascon, J. M. *Nature* **2008**, *451*, 652-657.
(15) Steele, B. C. H.; Heinzel, A. *Nature* **2001**, *414*, 345-352.
(16) Zhao, X.; Sanchez, B. M.; Dobson, P. J.; Grant, P. S. *Nanoscale* **2011**, *3*, 839-855.
(17) Bruce, P. G.; Scrosati, B.; Tarascon, J.-M. *Angew. Chem. Int. Ed.* **2008**, *47*, 2930-2946.
(18) Slaoui, A.; Collins, R. T. *MRS Bull.* **2007**, *32*, 211-218.
(19) Hubbell, J. A.; Chilkoti, A. *Science* **2012**, *337*, 303-305.
(20) Parmon, V. *Mater. Res. Innovations* **2008**, *12*, 60-61.
(21) Hartnig, C.; Jorissen, L.; Lehnert, W.; Scholta, J. In *Materials for Fuel Cells*; Gasik, M., Ed.; Woodhead Publishing: Oxford, UK, 2008, p 185-208.
(22) Lamy, C. In *Carbons for Electrochemical Energy Storage and Conversion Systems* 1ed.; Beguin, F., Frackowiak, E., Eds.; CRC Press: Boca Raton, Fl, 2010, p 377-409.
(23) Narayan, S. R.; Valdez, T. I. *Electrochem. Soc. Interface* **2008**, *17*, 40-45.
(24) Shukla, A. K.; Ravikumar, M. K.; Gandhi, K. S. *J. Solid State Electrochem.* **1998**, *2*, 117-122.
(25) Wasmus, S.; Küver, A. *J. Electroanal. Chem.* **1999**, *461*, 14-31.
(26) Koenigsmann, C.; Santulli, A. C.; Gong, K.; Vukmirovic, M. B.; Zhou, W.-p.; Sutter, E.; Wong, S. S.; Adzic, R. R. *J. Am. Chem. Soc.* **2011**, *133*, 9783-9795.
(27) Koenigsmann, C.; Santulli, A. C.; Sutter, E.; Wong, S. S. *ACS Nano* **2011**, *5*, 7471-7487.

(28) Koenigsmann, C.; Semple, D. B.; Sutter, E.; Tobierre, S. E.; Wong, S. S. *ACS Appl. Mater. Interfaces* **2013**, *5*, 5518-5530.
(29) Koenigsmann, C.; Sutter, E.; Adzic, R. R.; Wong, S. S. *J. Phys. Chem. C* **2012**, *116*, 15297-15306.
(30) Koenigsmann, C.; Sutter, E.; Chiesa, T. A.; Adzic, R. R.; Wong, S. S. *Nano Lett.* **2012**, *12*, 2013-2020.
(31) Koenigsmann, C.; Tan, Z.; Peng, H.; Sutter, E.; Jacobskind, J.; Wong, S. S. *Isr. J. Chem.* **2012**, *52*, 1090-1103.
(32) Koenigsmann, C.; Wong, S. S. *ACS Catal.* **2013**, ASAP.
(33) Koenigsmann, C.; Zhou, W.-p.; Adzic, R. R.; Sutter, E.; Wong, S. S. *Nano Lett.* **2010**, *10*, 2806-2811.
(34) Zhou, W.-P.; Li, M.; Koenigsmann, C.; Ma, C.; Wong, S. S.; Adzic, R. R. *Electrochim. Acta* **2011**, *56*, 9824-9830.
(35) Chalk, S. G.; Miller, J. F. *J. Power Sources* **2006**, *159*, 73-80.
(36) *Fuel Cell Catalysts*; Koper, M. T. M., Ed.; Wiley Interscience: Hoboken, NJ, 2009.
(37) Williams, M. C. *Fuel Cells* **2001**, *1*, 87-91.
(38) He, C.; Desai, S.; Brown, G.; Bollepalli, S. *Electrochem. Soc. Interface* **2005**, *14*, 41-44.
(39) Simon, P.; Gogotsi, Y. *Nat Mater* **2008**, *7*, 845-854.
(40) Adams, T. A.; Nease, J.; Tucker, D.; Barton, P. I. *Ind. Eng. Chem. Res.* **2012**, *52*, 3089-3111.
(41) Cowin, P. I.; Petit, C. T. G.; Lan, R.; Irvine, J. T. S.; Tao, S. *Adv. Energy Mater.* **2011**, *1*, 314-332.
(42) Wang, Y.; Chen, K. S.; Mishler, J.; Cho, S. C.; Adroher, X. C. *Applied Energy* **2011**, *88*, 981-1007.
(43) Kordesch, K. V.; Simader, G. R. *Chem. Rev.* **1995**, *95*, 191-207.
(44) Bolton, J. R. *Solar Energy* **1996**, *57*, 37-50.
(45) Ni, M.; Leung, M. K. H.; Leung, D. Y. C.; Sumathy, K. *Renewable Sustainable Energy Rev.* **2007**, *11*, 401-425.
(46) Choi, W. C.; Jeon, M. K.; Kim, Y. J.; Woo, S. I.; Hong, W. H. *Catal. Today* **2004**, *93-95*, 517-522.
(47) Aricò, A. S.; Srinivasan, S.; Antonucci, V. *Fuel Cells* **2001**, *1*, 133-161.
(48) Xuan, J.; Leung, M. K. H.; Leung, D. Y. C.; Ni, M. *Renewable Sustainable Energy Rev.* **2009**, *13*, 1301-1313.
(49) Nonaka, H.; Matsumura, Y. *J. Electroanal. Chem.* **2002**, *520*, 101-110.
(50) *EFOY Comfort Series Fuel Cells: Technical Specifications*, Smart Fuel Cells Inc., 2013.
(51) *Multi-Year Research, Development and Demonstration Plan: Planned Program Activities for 2005-2015*, Department of Energy, 2009.
(52) *Platinum Availability and Economics for PEMFC Commercialization*, Tiax LLC & United States Department of Energy, 2003.
(53) Sinha, J.; Marcinkoski, J.; Randolph, K.; Benjamin, T. G. *Cost Analysis of Fuel Cell Stacks/Systems*, DOE Hydrogen Program Review, 2009.
(54) Scott, K.; Argyropoulos, P. *J. Power Sources* **2004**, *137*, 228-238.
(55) Wang, C.-Y. *Chem. Rev.* **2004**, *104*, 4727-4766.
(56) Wee, J.-H.; Lee, K.-Y. *J. Power Sources* **2006**, *157*, 128-135.
(57) Hamnett, A. In *Interfacial Electrochemistry: Theory, Experiment and Applications*; Wieckowski, A., Ed.; Marcel Dekker: New York, NY, 1999, p 843-879.

(58) Wang, H.; Alden, L. R.; DiSalvo, F. J.; Abruña, H. c. D. *Langmuir* **2009**, *25*, 7725-7735.
(59) Zhao, X.; Yin, M.; Ma, L.; Liang, L.; Liu, C.; Liao, J.; Lu, T.; Xing, W. *Energy Environ. Sci.* **2011**, *4*, 2736-2753.
(60) Yu, X.; Ye, S. *J. Power Sources* **2007**, *172*, 145-154.
(61) Shao, Y.; Yin, G.; Gao, Y. *J. Power Sources* **2007**, *171*, 558-566.
(62) Liu, H.; Song, C.; Zhang, L.; Zhang, J.; Wang, H.; Wilkinson, D. P. *J. Power Sources* **2006**, *155*, 95-110.
(63) Zhao, T. S.; Chen, R.; Yang, W. W.; Xu, C. *J. Power Sources* **2009**, *191*, 185-202.
(64) Joo, S. H.; Choi, S. J.; Oh, I.; Kwak, J.; Liu, Z.; Terasaki, O.; Ryoo, R. *Nature* **2001**, *412*, 169-172.
(65) Antolini, E.; Salgado, J. R. C.; Gonzalez, E. R. *Appl. Catal., B* **2006**, *63*, 137-149.
(66) Adzic, R.; Zhang, J.; Sasaki, K.; Vukmirovic, M.; Shao, M.; Wang, J.; Nilekar, A.; Mavrikakis, M.; Valerio, J.; Uribe, F. *Top. Catal.* **2007**, *46*, 249-262.
(67) Zhang, J.; Vukmirovic, M. B.; Xu, Y.; Mavrikakis, M.; Adzic, R. R. *Angew. Chem. Int. Ed.* **2005**, *44*, 2132-2135.
(68) Zhang, J.; Vukmirovic, M. B.; Sasaki, K.; Nilekar, A. U.; Mavrikakis, M.; Adzic, R. R. *J. Am. Chem. Soc.* **2005**, *127*, 12480-12481.
(69) Shukla, A. K.; Raman, R. K. *Ann. Rev. Mater. Res.* **2003**, *33*, 155-168.
(70) Nørskov, J. K.; Bligaard, T.; Rossmeisl, J.; Christensen, C. H. *Nat. Chem.* **2009**, *1*, 37-46.
(71) Nørskov, J. K.; Rossmeisl, J.; Logadottir, A.; Lindqvist, L.; Kitchin, J. R.; Bligaard, T.; Jonsson, H. *J. Phys. Chem. B* **2004**, *108*, 17886-17892.
(72) Greeley, J.; Nørskov, J. K. *J. Phys. Chem. C* **2009**, *113*, 4932-4939.
(73) Feibelman, P. J.; Hammer, B.; Nørskov, J. K.; Wagner, F.; Scheffler, M.; Stumpf, R.; Watwe, R.; Dumesic, J. *J. Phys. Chem. B* **2000**, *105*, 4018-4025.
(74) Adzic, R. R.; Wang, J. X. *J. Phys. Chem. B* **1998**, *102*, 8988-8993.
(75) Adzic, R. R.; Wang, J. X. *J. Phys. Chem. B* **2000**, *104*, 869-872.
(76) Markovic, N. M.; Schmidt, T. J.; Stamenkovi, V.; Ross, P. N. *Fuel Cells* **2001**, *1*, 105-116.
(77) Mavrikakis, M.; Hammer, B.; Nørskov, J. K. *Phys. Rev. Lett.* **1998**, *81*, 2819.
(78) Mayrhofer, K. J. J.; Blizanac, B. B.; Arenz, M.; Stamenkovic, V. R.; Ross, P. N.; Markovic, N. M. *J. Phys. Chem. B* **2005**, *109*, 14433-14440.
(79) Mukerjee, S.; McBreen, J. *J. Electroanal. Chem.* **1998**, *448*, 163-171.
(80) Shao, M.; Peles, A.; Shoemaker, K. *Nano Lett.* **2011**, *11*, 3714-3719.
(81) Tritsaris, G.; Greeley, J.; Rossmeisl, J.; Nørskov, J. *Catal. Lett.* **2011**, *141*, 909-913.
(82) Tsou, Y. M.; Cao, L.; Castro, E. D. *ECS Transactions* **2008**, *13*, 67-84.
(83) Shao-Horn, Y.; Sheng, W.; Chen, S.; Ferreira, P.; Holby, E.; Morgan, D. *Top. Catal.* **2007**, *46*, 285-305.
(84) *Monthly Average Commercial Price of Platinum*, Johnson & Matthey, February 2013.
(85) Lim, B.; Jiang, M.; Camargo, P. H. C.; Cho, E. C.; Tao, J.; Lu, X.; Zhu, Y.; Xia, Y. *Science* **2009**, *324*, 1302-1305.
(86) Shao, M.; Yu, T.; Odell, J. H.; Jin, M.; Xia, Y. *Chem. Commun.* **2011**, *47*, 6566-6568.
(87) Wang, C.; Daimon, H.; Onodera, T.; Koda, T.; Sun, S. *Angew. Chem. Int. Ed.* **2008**, *47*, 3588-3591.
(88) Wang, Q.; Geng, B.; Tao, B. *J. Power Sources* **2011**, *196*, 191-195.
(89) Zhang, J.; Lima, F. H. B.; Shao, M. H.; Sasaki, K.; Wang, J. X.; Hanson, J.; Adzic, R. R. *J. Phys. Chem. B* **2005**, *109*, 22701-22704.

(90) Zhang, J.; Mo, Y.; Vukmirovic, M. B.; Klie, R.; Sasaki, K.; Adzic, R. R. *J. Phys. Chem. B* **2004**, *108*, 10955-10964.
(91) Mazumder, V.; Lee, Y.; Sun, S. *Adv. Funct. Mater.* **2010**, *20*, 1224-1231.
(92) Shao, M.; Liu, P.; Zhang, J.; Adzic, R. *J. Phys. Chem. B* **2007**, *111*, 6772-6775.
(93) Wang, D.; Li, Y. *Adv. Mater.* **2011**, *23*, 1044-1060.
(94) Stamenkovic, V. R.; Markovic, N. M. In *Handbook of Fuel Cells*; John Wiley & Sons Ltd.: 2009; Vol. 5, p 18-29.
(95) Yang, H. *Angew. Chem. Int. Ed.* **2011**, *50*, 2674-2676.
(96) Heinzel, A.; Barragán, V. M. *J. Power Sources* **1999**, *84*, 70-74.
(97) Antolini, E.; Lopes, T.; Gonzalez, E. R. *J. Alloys Compd.* **2008**, *461*, 253-262.
(98) DeLuca, N. W.; Elabd, Y. A. *J. Polym. Sci., Part B: Polym. Phys.* **2006**, *44*, 2201-2225.
(99) Batista, E. A.; Hoster, H.; Iwasita, T. *J. Electroanal. Chem.* **2003**, *554-555*, 265-271.
(100) Shiroishi, H.; Ayato, Y.; Kunimatsu, K.; Okada, T. *J. Electroanal. Chem.* **2005**, *581*, 132-138.
(101) Kunimatsu, K.; Hanawa, H.; Uchida, H.; Watanabe, M. *J. Electroanal. Chem.* **2009**, *632*, 109-119.
(102) Shao, M. H.; Adzic, R. R. *Electrochim. Acta* **2005**, *50*, 2415-2422.
(103) Shao, M. H.; Warren, J.; Marinkovic, N. S.; Faguy, P. W.; Adzic, R. R. *Electrochem. Commun.* **2005**, *7*, 459-465.
(104) Housmans, T. H. M.; Koper, M. T. M. *J. Phys. Chem. B* **2003**, *107*, 8557-8567.
(105) Liu, P.; Nørskov, J. K. *Fuel Cells* **2001**, *1*, 192-201.
(106) Basnayake, R.; Li, Z.; Katar, S.; Zhou, W.; Rivera, H.; Smotkin, E. S.; Casadonte, D. J.; Korzeniewski, C. *Langmuir* **2006**, *22*, 10446-10450.
(107) Chu, D.; Gilman, S. *J. Electrochem. Soc.* **1996**, *143*, 1685-1690.
(108) Hu, J.; Odom, T. W.; Lieber, C. M. *Acc. Chem. Res.* **1999**, *32*, 435-445.
(109) Lieber, C. M. *Solid State Commun.* **1998**, *107*, 607-616.
(110) Kuchibhatla, S.; Karakoti, A. S.; Bera, D.; Seal, S. *Prog. Mater Sci.* **2007**, *52*, 699-913.
(111) Morozan, A.; Jousselme, B.; Palacin, S. *Energy Environ. Sci.* **2011**, *4*, 1238-1254.
(112) Antolini, E.; Perez, J. *J. Mater. Sci.* **2011**, *46*, 1-23.
(113) Li, H.-H.; Cui, C.-H.; Yu, S.-H. *ChemCatChem* **2013**, *5*, 1693-1695.
(114) Cademartiri, L.; Ozin, G. A. *Adv. Mater.* **2009**, *21*, 1013-1020.
(115) Subhramannia, M.; Pillai, V. K. *J. Mater. Chem.* **2008**, *18*, 5858-5870.
(116) Wang, S.; Jiang, S. P.; Wang, X.; Guo, J. *Electrochim. Acta* **2011**, *56*, 1563-1569.
(117) Yu, X.; Ye, S. *J. Power Sources* **2007**, *172*, 133-144.
(118) Chen, Z.; Waje, M.; Li, W.; Yan, Y. *Angew. Chem. Int. Ed.* **2007**, *46*, 4060-4063.
(119) Garbarino, S.; Ponrouch, A.; Pronovost, S.; Gaudet, J.; Guay, D. *Electrochem. Commun.* **2009**, *11*, 1924-1927.
(120) Wang, C.; Waje, M.; Wang, X.; Tang, J. M.; Haddon, R. C.; Yan *Nano Lett.* **2003**, *4*, 345-348.
(121) Tian, M.; Kumar, N.; Xu, S.; Wang, J.; Kurtz, J. S.; Chan, M. H. W. *Phys. Rev. Lett.* **2005**, *95*, 076802.
(122) Zhiyong, Z.; Li, M.; Wu, Z.; Li, W. *Nanotechnology* **2011**, *22*, 015602.
(123) Kamat, P. V. *J. Phys. Chem. Lett.* **2012**, *3*, 3404-3404.
(124) Vukmirovic, M. B.; Bliznakov, S. T.; Sasaki, K.; Wang, J. X.; Adzic, R. R. *Electrochem. Soc. Interface* **2011**, *20*, 33-40.

Chapter 2. Experimental Methods for Characterizing Morphology & Chemical Composition, Determining Electrocatalytic Performance and Depositing Surface Pt Monolayers on Novel 1D Noble Metal Nanostructures

2.1 Importance of Characterization in the Development of Effective Nanoscale Electrocatalysts

The optical, electromagnetic, thermal, catalytic, and mechanical properties of nanostructured materials depend highly upon the dimensions, morphology, crystallinity, chemical composition, surface texture, structure, and homogeneity of their structure.[1,2] Therefore, rigorous characterization of nanoscale materials is necessary in the context of designing functional nanoscale architectures and is necessary in order to investigate relevant structure-property correlations. This is particularly relevant to the design of nanoscale electrocatalysts, since the structure of the catalytic interface is necessarily dictated by the physical and chemical properties of the nanostructured catalyst itself.[3,4] For instance, we have recently prepared hierarchical, core-shell NWs consisting of Pt clusters supported on elemental Ru NWs, shown in Figure 2.1.[5] Extensive characterization of this heterostructured 1D system revealed that the structure of the Pt-Ru interface at the NW surface was essential in determining the catalytic performance toward MOR. Furthermore, the interpretation of catalytic performance in nanostructured catalysts is also highly dependent upon factors, such as three-dimensional dispersion on support materials, and surface area, for instance, all of which can contribute to the structure of the catalytic interface and the active sites available. Collectively, the challenge of correlating trends in electrocatalytic performance with morphology, chemical composition, and structure of the catalyst can be a significant problem, and requires rigorous efforts to characterize the physicochemical properties of as-synthesized catalyst materials both before and after catalytic operation.

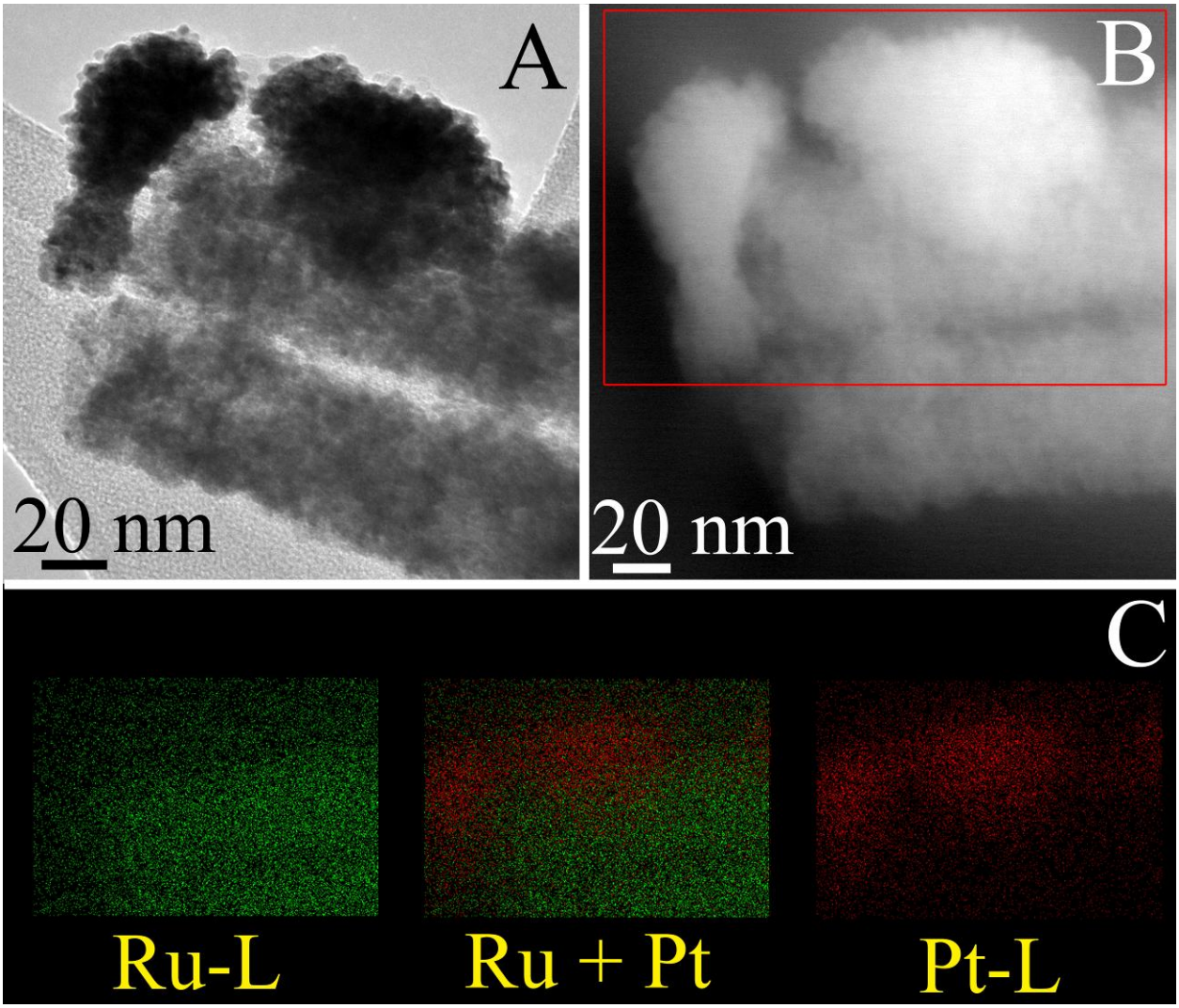

Figure 2.1 Characterization of Pt-Ru interface in Pt~Ru NWs consisting of Pt clusters supported on elemental Ru NWs. A TEM image (A) and an HAADF (B) of a representative Pt NP on the surface of the Ru NW. Spatially-resolved EDAX maps (C), highlighting the Ru L-edge signal (left) and the Pt L-edge signal (right), along with the composite image (center). (Reprinted with permission from Ref. 5. Copyright 2013 American Chemical Society)

In the first part of this Chapter, we provide a concise overview of the methodologies and instrumentation employed in the structural characterization of our novel as-synthesized 1D electrocatalyst materials. In terms of studying structure and chemical composition, we have employed X-ray powder diffraction (Section 2.2) as an effective technique to characterize the crystallinity and structure of as-synthesized and commercial catalyst materials. This is complemented by a broad suite of scanning (SEM) and transmission (TEM) electron microscopy techniques (Section 2.3), which provides direct characterization of not only catalyst morphology but also crystal structure, chemical composition, and homogeneity. For example, we can couple high resolution TEM (HRTEM) analysis with other *in situ* characterization techniques, such as energy dispersive X-ray spectroscopy (EDAX) and selected area electron diffraction (SAED), to deduce chemical composition and crystallinity in three-dimensional space. In addition, we have also combined electron microscopy with microtome cross-sectioning to examine the growth mechanism of 1D nanostructures directly within the spatial confines of the porous templates, within which they were grown.[6,7] In Chapter 5 and 6, for example, we examine the morphology, crystallinity, and composition of as-synthesized Pd[6] and $Pd_{1-x}Au_x$[7] NWs directly within the 1D pore channels of the polycarbonate filter membranes that served as templates for their growth.

In addition to characterizing the physical structure of the catalyst, the challenge of developing effective nanoscale catalysts also requires the development of electrochemical methods to study electrocatalytic performance. This endeavor is complicated by the fact that the activity and durability of catalysts under functional membrane electrode assembly (MEA) conditions differ from those of half-cell conditions with catalysts supported on glassy carbon electrodes (GCEs). Therefore, care must be taken when considering the activity and durability results obtained from novel electrocatalysts under half-cell conditions. Regardless, the objective

of our examination of performance herein is to identify relevant trends in the performance of high-quality 1D nanostructures as a function of physicochemical properties, such as size, chemical composition, structure, and crystallinity. From a fundamental perspective, these inherent structure-property correlations represent key insights into the potential of development and optimizing 1D noble metal nanostructures as an entirely new class of electrocatalysts.

From a practical perspective, we have also taken steps to mimic the conditions of operating MEAs, thereby enabling initial insights into the performance of 1D electrocatalysts under practical operating conditions. Our efforts to rigorously characterize and optimize the structure of 1D catalysts have led to a fully optimized, ultrathin Pt_{ML}~Pd_9Au NW/C catalyst.[3,8] In fact, recent preliminary testing of this optimized catalyst under true MEA conditions has demonstrated that the high performance observed under half-cell conditions is indeed observed in a practical device architecture. Not only does this highlight the importance of rigorously studying structure-property correlations but also it stresses the importance of rational design principles in the development of highly active catalyst materials.

In this dissertation, we have developed a core, commonly accepted set of electrochemical techniques to study the properties, structure, and catalytic performance of novel 1D structures. In Section 2.4, we describe our methods for preparing the working electrode, dispersing novel catalysts into so-called "catalyst inks", and depositing the catalysts onto the surfaces of the working electrode with uniform dispersions. The electrochemical properties have been studied by several traditional electrochemical methods, such as cyclic voltammetry (Section 2.5), in order to determine the electrochemically accessible surface area (ESA) and the surface structure. In addition, we also describe the methods (Section 2.7) for determining catalytic activity toward the oxygen reduction reaction (ORR) and the oxidation of small organic molecules such as

methanol (MOR). The key point is that this standardized portfolio of electrochemical techniques has enabled the direct correlation of performance amongst various catalysts, since each catalyst undergoes an identical set of electrochemical protocols. More importantly, we can employ a variety of state-of-the-art catalysts as internal standards throughout all of the testing protocols, so as to better understand the performance of our novel nanostructures in the context of the existing commercial benchmarks for PEMFC catalysts.

2.2 Methods for Structural Characterization: X-ray Powder Diffraction & Electron Microscopy

$$\chi_{\mathbf{Au}} = \frac{\left(a_{\mathbf{M}} - a_{\mathbf{Pd}}\right)}{\left(a_{\mathbf{Au}} - a_{\mathbf{Pd}}\right)} \qquad (1)$$

X-ray powder diffraction (XRD) is utilized to probe the crystallinity, crystalline structure, and chemical composition of as-synthesized 1D noble metal nanostructures. Powder diffraction samples were prepared by rendering the dried powders into slurries in ethanol after sonication for several minutes. The slurries were then air dried onto glass slides. XRD patterns were obtained from the as-prepared samples on a Scintag diffractometer, operating in the Bragg-Brentano configuration using Cu Kα radiation (λ = 1.54 Å) at a scan rate of 0.2 – 0.4° in 2θ per minute. Information regarding the crystalline structure was determined by comparing the experimental diffraction patterns with standard patterns obtained from the Joint Committee on Powder Diffraction Patterns (JCPDS).

In Chapter 6, we also employed XRD as a useful methodology for estimating the composition of alloy-type $Pd_{1-x}Au_x$ and $Pd_{1-x}Pt_x$ NWs.[7] The lattice parameters for elemental Pd and Au NWs and bimetallic $Pd_{1-x}Au_x$ NWs were determined from the experimental diffraction patterns, utilizing the peak positions of the (111), (200), and (220) reflections from the face-centered cubic structure. The chemical compositions of these as-synthesized $Pd_{1-x}Au_x$ and $Pd_{1-x}Pt_x$ NWs were calculated utilizing Vegard's Law, which assumes that there is a linear relationship between the lattice parameter and chemical composition in bimetallic metal alloys.

In Equation (1), for example, the mole fraction of Au ($\chi_{\mathbf{Au}}$) in $Pd_{1-x}Au_x$ NW is calculated from the measured lattice parameter of the as-synthesized alloy-type NW ($a_{\mathbf{M}}$) as well as the lattice parameters of the elemental Pd ($a_{\mathbf{Pd}}$) and Au ($a_{\mathbf{Au}}$) NWs. In both cases, we employed the measured lattice parameters from the elemental Pd and Au or Pd and Pt NWs, so as to account for any variations of the lattice parameter of the NWs from that reported in the JCPDS, associated with either the size or the morphology, for example. To validate this methodology, linear fits of the calculated lattice parameter with respect to the predicted composition, on the basis of the precursor solution contents, were highly correlated with the R^2 values of 0.991 and 0.995 for the $Pd_{1-x}Pt_x$ and $Pd_{1-x}Au_x$ NW systems, respectively. Additional details, including the experimental XRD patterns and calculated lattice parameters, as well as extra discussion can be found in Chapter 6.

2.3 Methods for Structural Characterization: Electron Microscopy

In addition to XRD, electron microscopy techniques represent a critical technique that enables direct examination of morphology, size, homogeneity, crystallinity, chemical composition, and surface structure at the nanoscale. Typically, the morphology and size of as-

synthesized 1D nanostructures were probed by means of scanning electron microscopy (SEM). SEM samples were prepared by drop casting the nanostructures dispersed into ethanol onto clean silicon wafers. Overview SEM images were obtained using either a Hitachi S4800 SEM instrument with an operating voltage of 5 kV or a Leo 1550 field emission SEM (FESEM instrument operating at 15 kV. The SEM technique can be coupled with energy dispersive X-ray spectroscopy (EDAX), which is capable of detecting elemental composition with spatial resolution. EDAX measurements and corresponding compositions were obtained on the Leo 1550 FESEM instrument to verify the composition and purity of individual nanostructures.

In addition to SEM, we have also extensively characterized our nanostructures, utilizing transmission electron microscopy (TEM). In all cases, TEM samples of individual NWs were prepared by dispersing the as-synthesized nanostructures into a solvent, typically ethanol or methanol, and evaporating a single drop onto a 300 mesh Cu grid, coated with a lacey carbon film. Initially, low magnification TEM images were obtained on a Technai12 BioTwinG^2 TEM instrument at 80 kV equipped with an AMT XR-60 CCD camera system to provide an overview of catalyst morphology and size. TEM images were analyzed in the ImageJ software package.[9]

Once the morphology and dimensions of the as-synthesized nanostructures were confirmed, high resolution TEM (HRTEM) was employed to examine the local structure, crystallinity, chemical composition, and homogeneity. HRTEM images were obtained on a JEOL 2100F instrument at 200 kV, which is equipped with a Gatan high-angle annular dark field (HAADF) detector for performing incoherent HAADF or *Z*-contrast imaging in scanning TEM (STEM) mode. The crystallinity of as-prepared structures was examined by combining HRTEM imaging with selected area electron diffraction (SAED) in order to study the local crystal structure and crystallinity of as-synthesized nanostructures at selected locations. In addition, the

chemical composition and homogeneity of as-synthesized elemental (*e.g.* Pt, Pd, Au, Ru, & Ag) and bimetallic (*e.g.* $Pd_{1-x}Pt_x$ & $Pd_{1-x}Au_x$) were studied by HAADF and EDAX in STEM mode. The contrast in HAADF is sensitive to the atomic number (*Z*) and the density of material present. Thus, HAADF imaging is a useful methodology for examining the spatial homogeneity of as-synthesized nanostructures. HAADF can be coupled with EDAX in STEM mode (0.2 nm beam size) in order to quantitatively study composition at a desired point in the HAADF image. The ability to couple EDAX with HAADF is crucial in determining if regions of high contrast in the HAADF image are a result of a corresponding variation in either the chemical composition or the density of material. More importantly, the JEOL 2100F is capable of obtaining spatially resolved EDAX composition maps, thereby further enabling the determination of the homogeneity and composition of novel nanostructured materials.

2.4 Preparation of Catalyst Inks and Glassy Carbon Rotating Disk Working Electrode

The electrochemical properties and catalytic performance of novel nanostructured materials were accessed by depositing thin catalyst layers onto a glassy carbon rotating disk electrode (GC-RDE, Pine Instruments, 5 mm disk diameter), serving as the working electrode. Recently, Kocha and co-workers have reviewed the methods for evaluating catalyst performance utilizing thin catalyst films on GC-RDEs and systematically investigating the effects of the uniformity of the catalyst film and methods for depositing catalyst films on the surface.[10] In this context, we have developed a methodology for preparing thin catalyst films of both supported ultrathin and unsupported noble metal NWs on GC-RDEs with excellent uniformity and reproducibility. Initially, the electrode is polished to a mirror finish with a micro-abrasive polishing cloth and alumina powder slurry (0.05 μm) prepared in water. The polished electrode is

then cleaned by periods of brief sonication in water and ethanol in order to remove inorganic salts and organic impurities. The clean electrode is subsequently allowed to dry under ambient conditions before the deposition of the catalyst can proceed.

Prior to deposition on the electrode, nanostructured catalysts and commercial catalysts are rendered into aqueous suspensions referred to herein as "catalyst inks." The optimization of the homogeneity and uniformity of catalyst inks is of critical importance, since this dictates the uniformity of the film after deposition on the GC-RDE. Herein, we have developed optimized ink formulations for (i) as-synthesized carbon-supported ultrathin noble metal NWs and (ii) as-prepared free-standing NWs. The extensive optimization process has enabled highly uniform catalyst films to be achieved.

Protocol 1: In the case of carbon-supported nanostructures, the dried composite powder is dispersed into a solution of 25% isopropyl alcohol (IPA) in water by means of sonication with a concentration of approximately 2 mg/mL. The dispersion of the catalyst in solution is essential and parameters, such as the sonication time, were optimized for the commercial Pt NP/C (E-Tek or BASF, 20% precious metal loading), Pd NP/C (E-Tek, 20% precious metal loading), Pd NW/C composites (Chapter 4),[6,11] and $Pd_{1-x}Au_x$ NW/C (Chapter 7)[8] systems in order to achieve catalyst inks that maintain stable dispersions for a minimum of 48 – 72 h. For each carbon supported catalyst ink, the GC-RDE was loaded with either one or two drops (5 μL each). Smooth, uniform catalyst films on the working electrode's surface were achieved for the Pd NWs and $Pd_{1-x}Au_x$ NWs by allowing the catalyst modified electrodes to dry under ambient conditions, and the film uniformity was confirmed by visual inspection with an optical microscope.

Protocol 2: In the case of unsupported noble metal NWs, the as-prepared powder consisting of Pd,[6] Pd-Au, Pd-Pt,[12] (Chapter 5), $Pd_{1-x}Au_x$, or $Pd_{1-x}Pt_x$[7] (Chapter 6) NWs were rendered into catalysts inks by dispersing the NWs into a solution of 25% IPA in water with a concentration of approximately 1 mg/mL. Prior to depositing the catalyst ink onto the electrode, the surface of GC-RDE was pre-modified by a thin-carbon layer. This was accomplished by depositing two drops of a carbon ink consisting of 1 mg/mL Vulcan XC-72R carbon dispersed into 25% IPA in water on the surface of the GC-RDE. When dried rapidly under vacuum, the carbon modified electrode forms a thin, uniform layer of carbon on the surface of the GC, which serves as a three-dimensional textured substrate for the deposition of the unsupported NWs. The purposeful pre-modification of the GCE surface has been previously demonstrated to be useful in approximating the textured carbon surfaces within practical functional devices, and can also contribute to an improved distribution of NWs over the geometric area of the electrode.[6,7] However, the addition of carbon to the electrode is not necessary to promote a uniform distribution of the individual isolated NWs, as homogeneous dispersions of NWs can be achieved directly on the GCE surface itself.[6] In fact, we demonstrate in a prior report that the deposition of Pd NWs directly onto the surface of the GC-RDE and onto a GC-RDE premodified with a thin carbon layer produces essentially identical activity results.[6] Finally, the GCE is then loaded with the catalyst by placing one 5 μL drop of the unsupported NW ink on the surface, and we noted that drying rapidly under vacuum can produce a uniform layer of NWs on the surface of the carbon substrate.

In both protocols, the as-prepared electrodes were sealed by adding one 5 μL drop of a 0.025 % Nafion solution prepared by diluting a 5% stock solution (Aldrich) with ethanol. The Nafion ionomer is added to improve upon the adhesion of the catalyst film to the electrode

surface and thereby prevent catalyst loss during rotating disk measurements.[10] However, the addition of Nafion is also useful in simulating the operating conditions of the fuel cell, since the catalyst layer on the electrode includes Nafion ionomers and is typically hot pressed to the Nafion PEM in order to form the functional MEA. Herein, a dilute solution (0.025%) of the Nafion ionomer is employed to prevent a significant contribution of the polymeric layer to the diffusion of O_2 during rotating disk electrode measurements (see Section 2.7).[13,14] After Nafion modification, the electrodes are immersed in ultrapure water in order to remove any residual inorganic impurities, such as salts that may have been present either in the catalyst ink or Nafion solution. The immersion in water is also useful in saturating the catalyst layer with water before electrochemical experiments.

In addition, a key aspect of evaluating catalyst performance is to normalize catalytic activity (*i.e.* current) to the mass of precious metal present on the electrode, thereby giving a so-called "mass activity." To achieve this goal, several methods have been employed to determine the concentration of precious metal present in typical catalyst inks including inductively coupled plasma (ICP) mass spectrometry, ICP atomic emission spectroscopy (ICPAES), and atomic absorption spectroscopy (AAS).[10] Herein, we utilize thermogravimetric analysis (TGA) to determine the relative precious metal content in a catalyst ink. This was accomplished by transferring a known quantity of catalyst ink consisting of either carbon supported or unsupported noble metal NWs to a Pt TGA boat. The quantity of liquid ink was adjusted to give approximately 1 – 3 mg of residue after drying to give an accurate TGA profile. The ink was allowed to dry for a period of 24 hours in a drying oven at 100°C, and rapidly transferred to the TGA to prevent moisture accumulation. The TGA profiles were obtained on a TGA Q500 (TA Instruments) from 100 - 900°C at a rate of 5°C/min. Organic residue (*e.g.* residual surfactant)

and carbon support material are decomposed at ~400°C, thereby leaving the precious metal content. The quantity of precious metal residue was then utilized to determine the concentration of precious metal in the catalyst ink. This method is advantageous over spectroscopic methods, since it is generally more reproducible. However, care must be taken when considering and comparing the mass values obtained by this method with those collected by other means. Essentially, the results presented herein are self-consistent, thereby enabling accurate comparisons to be made with respect to commercial standards like Pt NP/C, for instance.

2.5 Methods for Electrochemical Characterization and Determination of Electrochemically Accessible Surface Area

Electrochemical characterization including cyclic voltammetry, CO stripping voltammetry, linear sweep voltammetry, and chronoamperometry was performed, utilizing a three-electrode, half-cell configuration. The measurement of the electrochemical properties and corresponding catalytic activity of noble metal nanostructures is challenging, since these measurements are highly sensitive to both organic and inorganic impurities. For example, sulfate (SO_4^{2-}) and chloride (Cl^-) species even at very low concentrations can significantly impact performance, particularly in the context of catalytic oxygen reduction.[15] Extensive care has been utilized to prevent contamination of the electrolyte by impurities. Prior to use, a custom made glass electrochemical cell was cleaned of residual impurities by first filling the cell with sulfuric acid for a period of 24 h and subsequently treating it with steam for a period of 2 h in order to remove adsorbed sulfate species on the surfaces of the glass. Immediately prior to each measurement, the cleaned cell was washed with ultrapure water, possessing a resistivity of 18.2 MΩ·cm before adding the electrolyte to the cell.

Electrochemical measurements were performed in 0.1 M perchloric acid ($HClO_4$) electrolyte, prepared by diluting the acid concentrate (Fisher Scientific, Optima Grade) in ultrapure water with a measured resistivity of 18.2 MΩ·cm, unless otherwise noted. A silver/silver chloride (BASi, Ag/AgCl, 3 M Cl^-) electrode isolated in a double junction chamber (BASi) and Pt foil served as the reference and counter electrodes, respectively. The double junction chamber exists to isolate the Ag/AgCl reference electrode, thereby preventing the diffusion of Cl^- ions into the electrolyte of the cell. To minimize the diffusion of Cl^- ions, the electrolyte solution in the double junction chamber was changed periodically to prevent measureable contamination of the main cell by Cl^- ions. The Pt counter electrode was cleansed of residual impurities by undergoing the same purification process as the electrochemical cell before use. All electrodes were washed extensively with ultrapure water before immersion into the cell, and all of the potentials in this dissertation are reported with respect to the reversible hydrogen electrode (RHE), unless otherwise noted.

The first step in assessing the quality and electrochemical properties of our as-synthesized noble metal NW electrocatalysts was to perform cyclic voltammetry (CV). Typically, CVs of as-prepared catalysts are collected at a scan rate of 20 mV/s in 0.1 M $HClO_4$, which is deoxygenated by bubbling gaseous Argon (0.99998%) for a period of 20 minutes. Under these conditions, the CVs of noble metals, including Pt, Pd, and Ru, maintain characteristic features associated with reversible, interfacial processes that enable characterization of the surface structure, the active sites, as well as the relative interaction of the surface with adsorbates.[3,4] Therefore, we have also employed this powerful technique to probe the purity of the surface, including determining if residual inorganic or organic impurities are present.

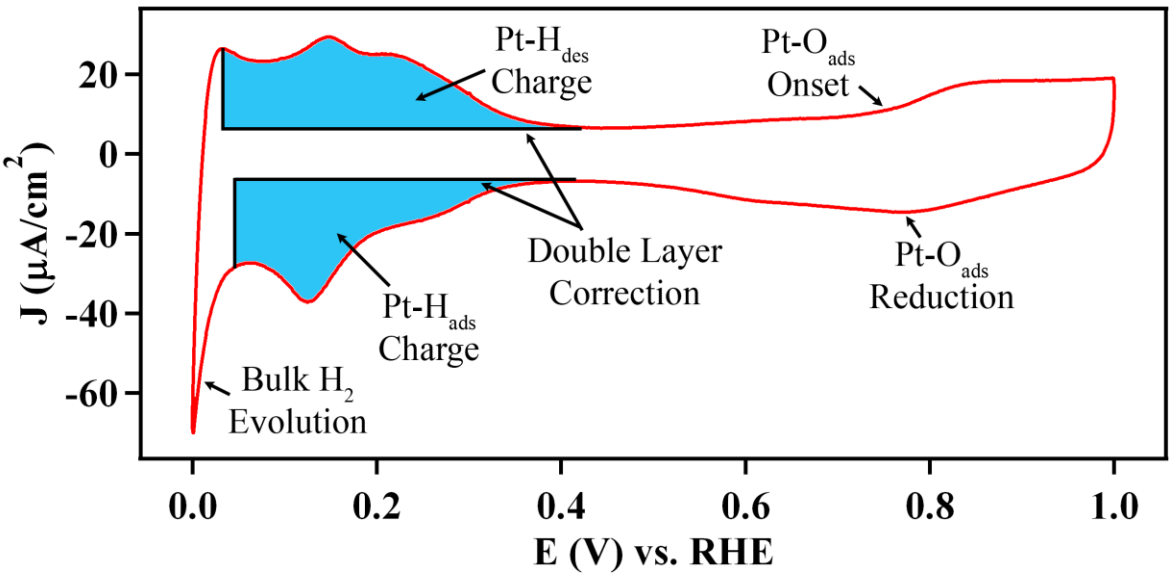

Figure 2.2 A representative CV obtained from commercial Pt NP/C is shown with the hydrogen underpotential adsorption/desorption and surface oxide regions denoted. The regions highlighted in blue indicate the area utilized to calculate the hydrogen adsorption (H_{ads}, cathodic sweep) and desorption (H_{des}, anodic sweep) charges. The horizontal and vertical black lines indicate the double layer correction and integration limit used to determine the integrated H_{ads} and H_{des} charge, respectively.

In a typical CV, there are two characteristic regions associated with reversible oxidation and reduction processes at the noble metal interface, which are shown in the case of commercial Pt NP/C, in Figure 2.2. Specifically, the first is the region of hydrogen adsorption/desorption (H_{ads}), which is in essence the reversible underpotential deposition (UPD) of a surface monolayer of hydrogen atoms. In addition, the H_{ads} region is particularly useful in probing the electrochemically accessible surface area (ESA) of noble metal electrocatalysts, since the charge associated with H_{ads} can be employed to calculate the geometric surface area in Pt catalysts. In the case of Pt and Pt_{ML} catalysts, we have employed this methodology and determined the ESA of our catalysts by first determining the average of the hydrogen adsorption and desorption charges. Figure 2.2 demonstrates the typical integration area employed for the determination of the adsorption and desorption charges including the correction for the double layer charge.[†] The average charge associated with the monolayer formation of adsorbed hydrogen is converted to a geometric surface area, utilizing 210 $\mu C/cm^2$ as the known conversion factor.[16] In addition to calculating the ESA, examination of the shape and structure of the H_{ads} and H_{des} regions provide for important information, regarding the type, structure, and availability of active sites, present at the catalytic surface. Further discussion relating to specific noble metal NW systems can be found in Chapters 3 – 7.

The second feature that is characteristic to the CV obtained from Pt and Pd nanostructures is the so called "surface oxide region," which is associated with the reversible oxidation of the surface sites and the corresponding adsorption of oxygen species (*e.g.* $Pt–OH_{ads}$ and $Pt–O_{ads}$). In the context of designing ORR electrocatalysts, this region is an important tool in

[†] The hydrogen adsorption and desorption processes are specified in Figure 2.2 as H_{ads} and H_{des}, respectively for the sake of clarity. In future chapters, the hydrogen adsorption/desorption process is referred to generally as "H_{ads}" for the sake of consistency with the relevant literature.

terms of understanding the relative interaction of the surface with oxygen adsorbates, which are crucial species present during oxygen reduction.[17] The formation and reduction features associated with the commercial Pt NP/C are highlighted in Figure 2.2. The shape and structure of the H_{ads} region and oxide region represent important diagnostic tools, since different active sites will adsorb/desorb hydrogen and oxygen at different potentials and the particular details regarding the interpretation of this region for each of our novel 1D catalysts are provided in Chapters 3 – 7.

In addition to CV measurements, we have also characterized our as-synthesized noble metal NWs, utilizing carbon monoxide (CO) stripping. The CO stripping measurement involves the oxidative stripping of monolayer of CO molecules forming CO_2. Typical CO stripping measurements were obtained by first immersing the electrode in 0.1 M $HClO_4$ solution saturated with gaseous CO by bubbling for a period of 30 minutes in order to ensure complete adsorption. The electrode was then transferred directly to the argon-saturated electrolyte for CO stripping experiments. CO stripping voltammograms were obtained by immersing the electrode into the electrolyte and sweeping the potential in the anodic direction at a rate of 20 mV/s. CO stripping voltammetry provides important information regarding the interaction of the surface with adsorbed intermediates, and these data are utilized in Chapters 3 – 7 to elucidate relative trends in electrochemical properties as a function of NW size, chemical composition, and structure. In the case of small molecule oxidation, CO stripping is an important tool in terms of evaluating the performance of a novel electrocatalyst toward the oxidation of CO, which has been identified as a poisoning intermediate in the methanol and ethanol oxidation reactions, for instance.

CO stripping is also an important methodology for determining ESA, since the oxidation of the CO monolayer is related to the geometric surface area in an analogous manner to H_{ads}. In

the case of Pd-based nanostructures, CO stripping is particularly advantageous since the determination of ESA from H_{ads} is often complicated by the additional contribution of hydrogen absorption in this potential window, thereby rendering the direct conversion factor as unreliable.[18] To avoid this inaccuracy, we have elected to utilize the carbon monoxide (CO) stripping peak charge of the as-prepared Pd NWs as an alternative, since this measurement of the surface area is not affected by the presence of hydrogen absorption. The method for calculating ESA from CO stripping measurements is described in detail elsewhere.[19] A comparison of the calculated ESA confirms that the ESA determined from CO stripping is systematically lower than that of the corresponding ESA obtained by H_{ads} which is consistent with the absorption of hydrogen by Pd. Hence, the ESA calculated from H_{ads} provides for an overestimate of surface area in Pd-based catalysts. Both methods (*i.e.* H_{ads} and CO_{ads}) yield numerically self-consistent results. However, care should be taken when making comparisons between the ESAs obtained here and those acquired in other reports by different methods, since the specific assumptions regarding the formation of CO monolayers can influence both the nature and magnitude of the ESA.

2.6 Deposition of Pt Monolayer Shells on Nanostructured 1D Electrocatalysts

Recently, considerable enhancements in electrocatalytic performance have been garnered by adopting core-shell geometries, wherein the Pt content is localized at the surface of the electrocatalyst.[20,21] This structural architecture promotes enhanced performance of the Pt through the structural and electronic interactions between the Pt shell and the core material and more importantly, reduces the necessary Pt content and associated cost. Therefore, a key objective of this dissertation is not only to develop a novel class of 1D electrocatalysts but also to couple this

structural paradigm with a core-shell motif in order to develop highly active 1D heterostructures.[3] Specifically, we have utilized a methodology developed by Adzic and co-workers that is capable of depositing a homogeneous, uniform Pt monolayer (Pt_{ML}) on the surface of noble metal nanostructures and we optimized this process for use with nanostructures possessing 1D morphologies.

$$Cu_{ML} + K_2PtCl_{4aq} \rightarrow Pt_{ML} + 2KCl_{aq} + CuCl_{2aq} \qquad (2)$$

The deposition of a Pt_{ML} onto 1D noble metal NWs was accomplished by initially electrodepositing a monolayer of Cu through a Cu underpotential deposition (UPD) process followed by galvanic displacement of the Cu ad-atoms by Pt^{2+}.[22,23] The details of the process have recently been reviewed.[24] All of these steps were performed in a custom-made two-chamber glass housing (Figure 2.3), thereby allowing for the transfer of the Cu modified electrode under an inert N_2 atmosphere so as to prevent the oxidation of the Cu ad-atoms. In the first step, the deposition of a Cu monolayer (Cu UPD) was achieved in a solution of 50 mM $CuSO_4$ in a 0.10 M H_2SO_4 electrolyte. In a typical experiment, the potential is scanned negatively at a rate of 1 mV/s and the potential is held prior to the onset for the bulk deposition of Cu, for a period of 5 minutes to ensure that a complete monolayer is formed.[25] The Cu modified electrode was then transferred under the protection of argon to a solution of 1.0 mM K_2PtCl_4 dissolved in 50 mM H_2SO_4. The Cu ad-atoms are galvanically displaced (Eqn. 2) by the Pt^{2+} ions within the precursor, thereby producing a uniform Pt_{ML} on the surface. The quantity of Pt deposited can be calculated from the integrated Cu UPD charge calculated from the UPD LSV. The quality and uniformity of the Pt_{ML} have been confirmed by cyclic voltammetry.

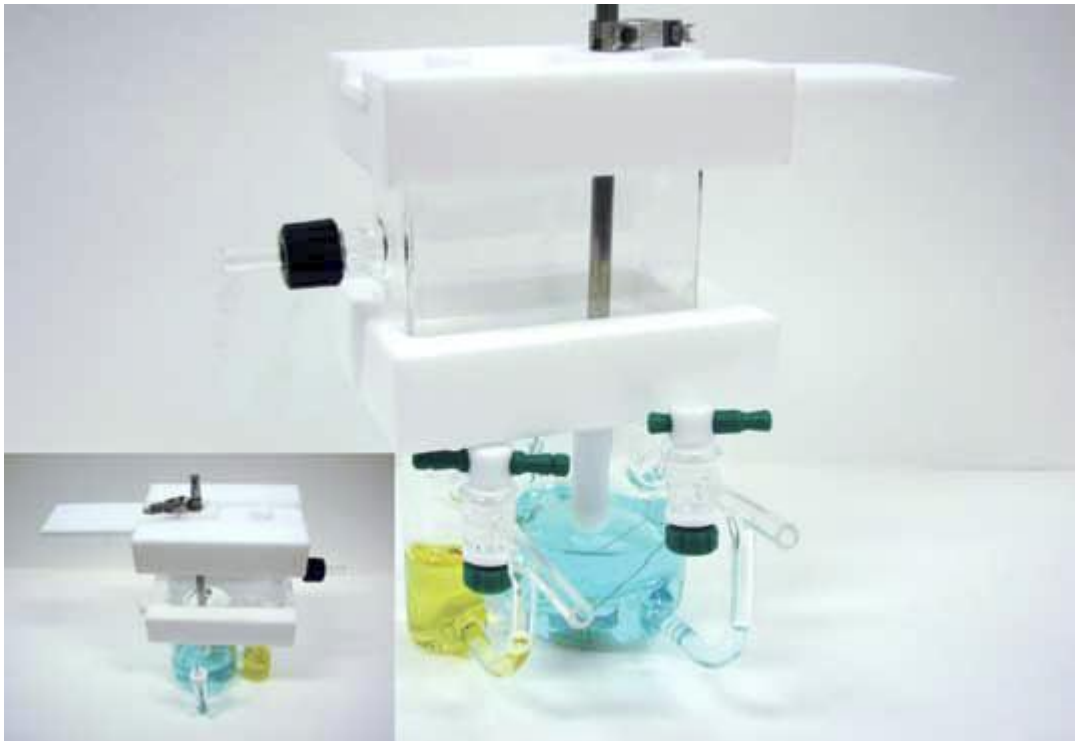

Figure 2.3 Cells and set-up for the deposition for Pt_{ML} deposition by displacement of a Cu UPD monolayer. (Reprinted with permission from Ref. 24. Copyright 2011 The Electrochemical Society)

The process has been generalized to include the deposition of a Pt_{ML} on (i) elemental Pd NWs[6,11] with diameters ranging from the submicron to the ultrathin size regime, (ii) bimetallic $Pd_{1-x}Au_x$ NWs[7,8], and (iii) segmented A/B NWs.[12] These as-prepared core-shell NWs maintain outstanding performance towards the oxygen reduction reaction, and the results are described in detail in Chapters 4 – 7. Recently, we have also explored the morphology-dependent deposition of Pt onto nanostructured Ru electrocatalysts.[5] The distinctive surface properties associated with elemental Ru promotes a unique structure of the Pt~Ru interface, when Ru NWs and Ru NP/C are employed as the substrate. The resulting materials maintain highly advantageous properties, that are suited for the methanol oxidation reaction, and these data have been described in a recent report.[5]

2.7 Measurement of Electrocatalytic Oxygen Reduction, Methanol Oxidation and Formic Acid Oxidation Performance and Electrocatalyst Durability

$$\frac{1}{I_{\mathbf{0.9\,V}}} = \left(\frac{1}{I_{\mathbf{K}}} + \frac{1}{I_{\mathbf{D}}} \right) \tag{3}$$

$$I_{\mathbf{K}} = \frac{I_{\mathbf{D}} - I}{I_{\mathbf{D}} I_{\mathbf{0.9\,V}}} \tag{4}$$

The measurement of electrocatalyst performance in Chapters 3 – 7 is accomplished in terms of both activity and durability, so as to examine the correlation between physicochemical properties and performance. The activity of the NWs toward ORR was measured by obtaining a linear sweep voltammogram or so called “polarization curves” in an oxygen-saturated 0.1 M $HClO_4$ electrolyte at 20°C with the electrode, rotating at a rate of 1600 rpm and at a scan rate of

10 mV/s.[10] The rotation of the electrode modified with a thin catalyst film is particularly advantageous in determining ORR activity, since the diffusion of oxygen to the electrode is largely defined by experimental parameters, such as the rate of rotation, the temperature, and the electrolyte employed. Utilizing this method, the Koutecky-Levich relationship (Eqn. 3) was employed to calculate the kinetic ORR current (I_K), which serves as an intrinsic measurement of ORR activity at a desired potential. The Koutecky-Levich relationship can be recast (Eqn. 4) such that $\boldsymbol{I_K}$ can be calculated at 0.9 V from the measured disk current ($\boldsymbol{I_{0.9\,V}}$) and the diffusion controlled current ($\boldsymbol{I_D}$), which are obtained from the polarization curve at 0.9 V and 0.4 V, respectively. The I_K is typically calculated at 0.9 V in accordance with the U.S. Department of Energy (DOE)[26] protocol and the existing precedent in the literature.[10] Once calculated, the measured $\boldsymbol{I_K}$ is then normalized to either the ESA, platinum mass, or platinum group metal mass (PGM) of the catalyst loaded onto the RDE, respectively, in order to obtain surface area or mass normalized kinetic current (J_K) densities.

An important parameter in evaluating practical catalyst performance is to examine the long-term durability and stability of novel 1D ORR electrocatalysts in the context of existing commercial standards. The catalyst durability has been tested by a protocol defined by the U.S. DOE for simulating a catalyst lifetime under MEA conditions. The procedure though has been modified for use with a thin catalyst layer supported on a GC-RDE under half-cell conditions.[26] Specifically, the electrode is cycled from 0.6 to 1.0 V at 50 mV/s in a 0.1 M $HClO_4$ solution, left open to the air for up to 30,000 cycles. The ESA and specific activity are measured incrementally after every 5,000 cycles. As internal standard, we have run the identical durability protocol on state-of-the-art Pt NP/C, so as to understand the durability in practical context.

In addition, we have also examined the stability of ORR performance in the presence of small organic molecule impurities. The testing protocol utilized herein is designed to simulate the effects of methanol crossover from the anode to the cathode in functional DMFC designs, which is a critical technological challenge in terms of the fabrication of electrocatalysts for DMFC cathodes. The stability of ORR performance in the presence of methanol was examined by obtaining a series of polarization curves in electrolytes with increasing methanol concentration. In the case of Pt-based catalysts including commercial Pt NP/C and $Pd_{1-x}Pt_x$ NWs, separate polarization curves were obtained in 0.1 M $HClO_4$ electrolytes, containing methanol concentrations of 0, 1, 2, 3, and 4 mM, respectively. In the case of the highly methanol-tolerant Pd-based catalysts, including Pd and Pd_9Au NWs, polarization curves were obtained in 0.1 M $HClO_4$ solutions, containing methanol concentrations of 0, 1, 2, 3, 4, 25, 50, 75, and 100 mM, respectively. The relative methanol tolerance was estimated by normalizing the measured specific activity in the presence of methanol (J_K [MeOH]) to the measured specific activity in a pure solution, containing no methanol (J_K). The measurement of the fraction of specific activity in the presence of methanol with respect to the activity in a pure electrolyte (*i.e.* J_K [MeOH] / J_K) provides for an accepted and useful metric of the level of methanol tolerance as a function of NW composition.

We have also examined the catalytic performance of novel 1D electrocatalysts toward the oxidation of small organic molecules, which is a relevant endeavor to developing anode catalysts for DEFCs. The catalytic MOR and formic acid oxidation reaction (FAOR) performance was measured by obtaining linear sweep voltammograms (LSVs) in the anodic sweep direction in a solution consisting of either 0.1 M methanol (Fisher Scientific, Optima Grade) or 0.1 M formic acid (Fisher Scientific, Optima Grade), respectively, supported in a 0.1 M $HClO_4$ electrolyte at

20 mV/s. The oxidation current, which is related to the kinetics of the oxidation process measured from the LSVs after double layer correction, can be normalized to the measured catalyst surface area, so as to provide for a specific MOR activity at a given potential. Additional details relating the measurement of the oxidation kinetics of small organic molecules can be found in Chapter 1 and Chapter 6.

2.8 References

(1) Tiano, A. L.; Koenigsmann, C.; Santulli, A. C.; Wong, S. S. *Chem. Commun.* **2010**, *46*, 8093-8130.
(2) Xia, Y.; Yang, P.; Sun, Y.; Wu, Y.; Mayers, B.; Gates, G.; Yin, Y.; Kim, F.; Yan, H. *Adv. Mater.* **2003**, *15*, 353-389.
(3) Koenigsmann, C.; Scofield, M. E.; Liu, H.; Wong, S. S. *J. Phys. Chem. Lett.* **2012**, *3*, 3385-3398.
(4) Koenigsmann, C.; Wong, S. S. *Energy Environ. Sci.* **2011**, *4*, 1161 - 1176.
(5) Koenigsmann, C.; Semple, D. B.; Sutter, E.; Tobierre, S. E.; Wong, S. S. *ACS Appl. Mater. Interfaces* **2013**, *5*, 5518-5530.
(6) Koenigsmann, C.; Santulli, A. C.; Sutter, E.; Wong, S. S. *ACS Nano* **2011**, *5*, 7471-7487.
(7) Koenigsmann, C.; Sutter, E.; Chiesa, T. A.; Adzic, R. R.; Wong, S. S. *Nano Lett.* **2012**, *12*, 2013-2020.
(8) Koenigsmann, C.; Sutter, E.; Adzic, R. R.; Wong, S. S. *J. Phys. Chem. C* **2012**, *116*, 15297-15306.
(9) Schneider, C. A.; Rasband, W. S.; Eliceiri, K. W. *Nat. Methods* **2012**, *9*, 671-675.
(10) Garsany, Y.; Baturina, O. A.; Swider-Lyons, K. E.; Kocha, S. S. *Anal. Chem.* **2010**, *82*, 6321-6328.
(11) Koenigsmann, C.; Santulli, A. C.; Gong, K.; Vukmirovic, M. B.; Zhou, W.-p.; Sutter, E.; Wong, S. S.; Adzic, R. R. *J. Am. Chem. Soc.* **2011**, *133*, 9783-9795.
(12) Koenigsmann, C.; Tan, Z.; Peng, H.; Sutter, E.; Jacobskind, J.; Wong, S. S. *Isr. J. Chem.* **2012**, *52*, 1090-1103.
(13) Watanabe, M.; Igarashi, H.; Yosioka, K. *Electrochim. Acta* **1995**, *40*, 329-334.
(14) Zecevic, S. K.; Wainright, J. S.; Litt, M. H.; Gojkovic, S. L.; Savinell, R. F. *J. Electrochem. Soc.* **1997**, *144*, 2973-2982.
(15) *Fuel Cell Catalysts*; Koper, M. T. M., Ed.; Wiley Interscience: Hoboken, NJ, 2009.
(16) Strmcnik, D.; Tripkovic, D.; van der Vliet, D.; Stamenkovic, V.; Markovic, N. M. *Electrochem. Commun.* **2008**, *10*, 1602-1605.
(17) Wang, J. X.; Markovic, N. M.; Adzic, R. R. *J. Phys. Chem. B* **2004**, *108*, 4127-4133.
(18) Kobayashi, H.; Yamauchi, M.; Kitagawa, H.; Kubota, Y.; Kato, K.; Takata, M. *J. Am. Chem. Soc.* **2008**, *130*, 1828-1829.
(19) Vidakovic, T.; Christov, M.; Sundmacher, K. *Electrochim. Acta* **2007**, *52*, 5606-5613.

(20) Adzic, R.; Zhang, J.; Sasaki, K.; Vukmirovic, M.; Shao, M.; Wang, J.; Nilekar, A.; Mavrikakis, M.; Valerio, J.; Uribe, F. *Top. Catal.* **2007**, *46*, 249-262.
(21) Stamenkovic, V. R.; Markovic, N. M. In *Handbook of Fuel Cells*; John Wiley & Sons Ltd.: 2009; Vol. 5, p 18-29.
(22) Zhang, J.; Mo, Y.; Vukmirovic, M. B.; Klie, R.; Sasaki, K.; Adzic, R. R. *J. Phys. Chem. B* **2004**, *108*, 10955-10964.
(23) Brankovic, S. R.; Wang, J. X.; Adzic, R. R. *Surf. Sci.* **2001**, *474*, L173-L179.
(24) Vukmirovic, M. B.; Bliznakov, S. T.; Sasaki, K.; Wang, J. X.; Adzic, R. R. *Electrochem. Soc. Interface* **2011**, *20*, 33-40.
(25) Wang, J. X.; Inada, H.; Wu, L.; Zhu, Y.; Choi, Y.; Liu, P.; Zhou, W.-P.; Adzic, R. R. *J. Am. Chem. Soc.* **2009**, *131*, 17298-17302.
(26) *Multi-Year Research, Development and Demonstration Plan: Planned Program Activities for 2005-2015*, Department of Energy, 2009.

Chapter 3. Size-Dependent Enhancement of Electrocatalytic Performance in Relatively Defect-Free, Processed, Ultrathin Platinum Nanowires

3.1 Introduction

By contrast with commercial 0D Pt NP/C, single-crystalline, inherently anisotropic 1D structures possess (a) high aspect ratios, (b) the potential for fewer surface defect sites and (c) can be synthesized to expose long smooth segments of low energy (100) and (111) facets.[1-3] Collectively, these intrinsic structural advantages are expected to contribute to a delay in the passivation of 1D noble metal nanostructures to higher potentials, when compared with analogous NPs and promote more facile ORR kinetics.[1,4,5] From a practical perspective, the inherent anisotropy in these structures is expected to promote improved long term durability by minimizing the effects of particle dissolution and ripening.[6-9]

Not surprisingly, several early reports in 2007 – 2009 by our group and others demonstrated that both elemental Pt and Pd nanowires (NWs) and nanotubes (NTs) consistently maintain improved activity and durability as compared with analogous NP/C motifs.[10-12] For example, our group has successfully demonstrated the synthesis of unsupported Pt NTs with diameters of approximately 200 nm utilizing an ambient, surfactantless template-based technique.[12] The submicron NTs maintain a specific ORR activity (0.38 mA/cm^2) that was more than double that of commercial Pt NP/C. Similar improvements were observed with platinum NTs prepared by Yan and co-workers that displayed a four-fold enhancement in area-specific activity when compared with carbon-supported platinum NPs.[11] Since these first examples, there has been a considerable increase in the attention devoted to elemental 1D structures because of their intrinsically higher performance when compared with analogous NP catalysts.[13-20]

Although the morphology-dependent enhancement has been well documented in elemental Pt and Pd nanostructures, there have been very few reports that rationally correlate trends in the physicochemical properties of 1D nanostructures to their performance. For example, the exploration of size-dependent phenomena is of critical importance in the functional design of electrocatalysts, since the size of nanostructures is inherently linked to the surface-to-volume ratio and the corresponding precious metal loading.[21] In the context of nanoparticulate catalysts, extensive studies have demonstrated that particle diameter is not only linked to surface area and catalyst usage but is also linked to intrinsic ORR performance.[21-26] In fact, it has been widely demonstrated that the specific and mass activity of Pt NP/C decreases by more than 50% in some cases as the diameter is decreased below 2 – 3 nm.[21] The decreased performance in these catalysts is believed to immerge from a combined effect of the increased defect site density and size-dependent electronic effects, which are believed to strength the relative interaction with oxygen adsorbates in the potential window relevant for ORR. Thus, despite their high surface area-to-volume ratio, nanoparticulate catalysts do not display beneficial size-dependent properties in the context of ORR electrocatalysis.

However, the relevant literature involving the size-dependent electronic and structural properties of 1D nanostructures reveals that they are anticipated to possess a distinctive size-dependent enhancement in performance as the diameter is decreased toward 1 nm. Specifically, previous analysis of the size-dependent structure of noble metal NWs by DFT (*i.e.* Pt, Pd, Au, and Ir) has predicted that the NW structure is expected to undergo a reconfiguration and compression of the surface the atoms when the diameter is decreased below a critical value of approximately 2 nm.[27-29] Surface contractions of platinum have been shown both experimentally[30,31] and theoretically[32,33] to improve the surface ORR activity because it is

thought that such contractions weaken the binding of oxygen and increase ORR kinetics at low overpotentials.[30] Therefore, these initial results involving the size-dependent properties of 1D structures points towards a predicted enhancement as size is decreased into the so-called "ultrathin" regime (*i.e.* 2 nm > *d*). More importantly, the use of ultrathin NWs maximizes the surface area-to-volume ratio and therefore decreases the amount of catalytically inactive support material present within the interior of the wire.[2] When these parameters are combined, the potential for a highly active, ultra-small 1D catalyst with diameters below 2 nm becomes a key target in developing novel electrocatalysts

In this chapter, therefore, we report on the synthesis of high quality, crystalline Pt NWs with ultrathin diameters below 2 nm synthesized by an optimized ambient, solution based technique.[19] In addition, a novel acid-treatment protocol is developed to controllably decrease the diameter of the NWs, remove surface defect sites and purify the as-synthesized NWs of residual inorganic impurities. We couple UV-visible spectroscopy with the acid-treatment protocol to provide an *in situ* methodology for monitoring the rate and degree of Pt dissolution, which has important commercial applications in the processing of functional Pt nanostructures.[34] More importantly, we investigate for the first time the size-dependent electrocatalytic ORR performance in anisotropic 1D structures with diameters that range from the submicron range (1000 > *d* > 100 nm) to the ultrathin regime (2 nm > *d*). Our results confirm that there is nearly a four-fold enhancement in specific ORR activity as the diameter of the Pt NWs is decreased from 200 nm to 1.3 nm and a seven-fold enhancement is observed when the processed ultrathin Pt NWs are compared with commercial Pt NP/C. Therefore, not only does this report provide further evidence of a morphology-dependent enhancement in 1D nanostructures, it is the first report to the best of our knowledge demonstrating a remarkable size-dependent enhancement in

performance as the diameter of Pt NWs is systematically decreased to the ultrathin regime. In addition, an investigation of the morphology-dependent performance of Pt NWs and Pt NP/C confirm a significant enhancement in the electrocatalytic activity of the Pt NWs toward ethanol oxidation, further highlighting their versatility as multi-functional catalysts.

3.2 Synthesis of Ultrathin Pt NWs & A Novel Acid Treatment Protocol

The fabrication of small-diameter platinum NWs was accomplished by a modification of a previously published synthetic route from the Miyake[35] and co-workers, so as to yield smaller diameters and improved dispersibility in water. In a typical synthesis, a 2.5 mL aliquot of a hexachloroplatinic (IV) acid hydrate ($H_2PtCl_6 \cdot x\ H_2O$, >99.9%, Aldrich) solution (10.0 mM, aqueous) was dissolved in a solvent system comprised of 20 mL dimethylformamide (EMD, anhydrous), 12.5 mL toluene (Acros, reagent grade), and 2.5 mL triethylamine (Fisher, reagent grade). The Pt precursor was reduced by the addition of 20 mg of sodium borohydride while stirring, and the reaction was allowed to proceed for 3 h. The resulting black product was precipitated by centrifugation and washed several times with either absolute methanol or ethanol. A sample of platinum NPs was also generated by a modification of the aforementioned NW synthesis. The platinum precursor solution was reduced with 10 mg of sodium borohydride in a solvent system devoid of toluene.

A novel acid-treatment protocol was developed to selectively remove defect sites from the surface and to reduce the diameter of the as-synthesized Pt nanostructures.[34] Prior to treatment, the isolated product was precipitated from the ethanol or methanol solution utilizing centrifugation. In a typical treatment process, the washed solid black powder was dispersed into a solution of 6 M HCl by sonication and allowed to remain dispersed in the solution for a period

of time, typically 1 – 5 minutes. The degree of etching can be monitored *in situ* by UV-visible spectroscopy, which detects the emergence of H_2PtCl_6 in solution resulting from the dissolution of residual amorphous Pt salts and impurities and surface defect sites. Once the desired amount of Pt impurities were dissolved, the Pt nanostructures were rapidly isolated from the 6 M HCl treatment solution by centrifugation and washed several times with water to quench the etching process and remove residual acid and dissolved impurities. In this case, UV-visible spectra were collected at high resolution on a Thermospectronics UV1 spectrometer using quartz cells with a 10 mm path length. For all measurements a 6 M HCl solution was used for background correction. As a controlled experiment, the concentration of dissolved Pt as H_2PtCl_6 was examined in the various alternative solutions used to treat the Pt nanostructures such as ethanol and water in the place of 6 M HCl. For each test, aliquots of the solution were diluted in 6 M HCl to maintain the fully protonated form of hexachloroplatinic acid within solution.[36]

3.3 Results & Discussion

3.3.1. Structural Characterization of Pt NWs

In our studies, the crystallinity and purity of as-prepared ultrathin platinum NWs were studied by means of X-ray powder diffraction. Crystallographic analysis (Figure 3.1) of the solid confirmed that all of the peaks could be readily indexed to the (111), (200), (220) and (311) reflections of the face-centered cubic platinum (Fm3m, JCPDS #04-0802). No detectable impurity peaks were observed in the XRD pattern. The significant broadening of the peaks was an indication that small crystallite sizes had been achieved and is consistent with the production of nanosized Pt structures.

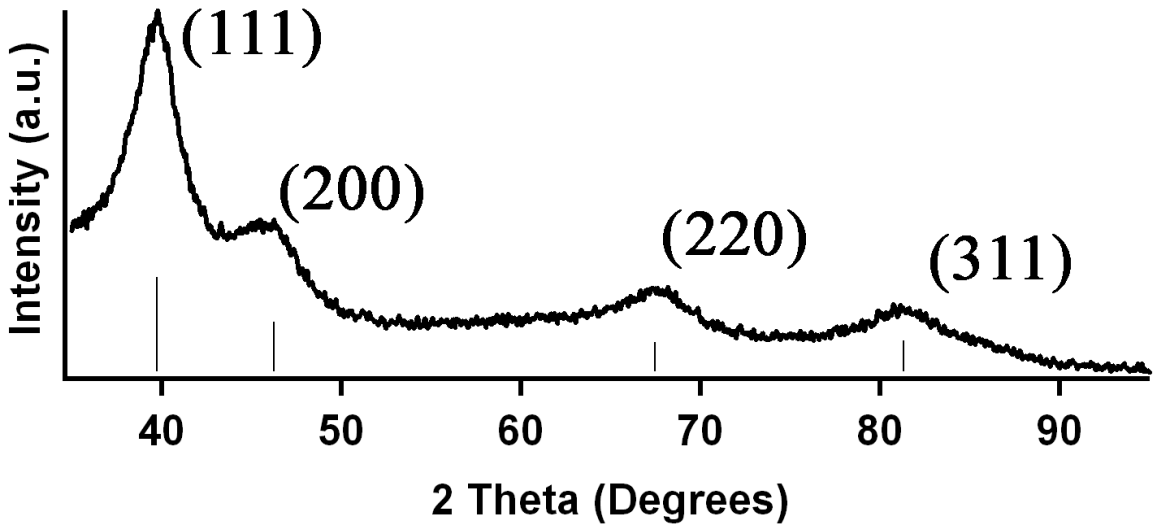

Figure 3.1 Representative experimental X-ray powder diffraction pattern of as-prepared ultrathin Pt NWs with the corresponding JCPDS standard shown immediately below. (Reprinted with permission from Ref. 19. Copyright 2010 American Chemical Society)

The morphology of the NWs and NPs was characterized by transmission electron microscopy (TEM). Overview TEM images of the acid-treated Pt NPs (Figure 3.2A) prepared by the reduction of the precursor without the presence of toluene in the solvent system revealed NPs with an average diameter of 2.8 ± 0.7 nm. The addition of toluene to the reaction resulted in a majority of NWs (85 – 90%) (Figure 3.2B) forming a net-like structure with some NPs distributed throughout the net. The average diameter of the wires was determined from the TEM images to be 1.8 ± 0.3 nm with an average length of 100 ± 25 nm. After acid-treatment, the wire diameters measurably decreased to 1.3 ± 0.4 nm (Figure 3.2C) with an associated decrease in the perceptible degree of aggregation. The overview TEM image in Figure 3.2C shows the presence of well-defined individual NWs, which have been exfoliated by the acid-wash.

Inspection of the individual, acid-treated NWs by high-resolution TEM (HRTEM) shown in Figure 3.2D reveals that they are polycrystalline, *i.e.* consist of multiple crystalline segments with an average length of 6 ± 2 nm that extend along the axis of the NW. The majority of the single crystalline segments making up the NWs have lattice spacings of 0.23 nm and 0.19 nm, consistent with the (111) and (200) lattice planes, respectively. The selected area electron diffraction (SAED) pattern shown in Figure 3.2E highlights not only continuous rings that can be indexed to platinum's (111), (200), (220), (311) and (331) planes, respectively, but also discrete diffraction spots indicating that the high degree of substructure observed is representative of the whole ensemble of NWs that contributed to the diffraction pattern. The composition of individual NWs investigated by EDAX (Figure 3.2F) performed in STEM mode suggests only the presence of Pt, as expected, with Cu peaks emanating from the TEM grid.

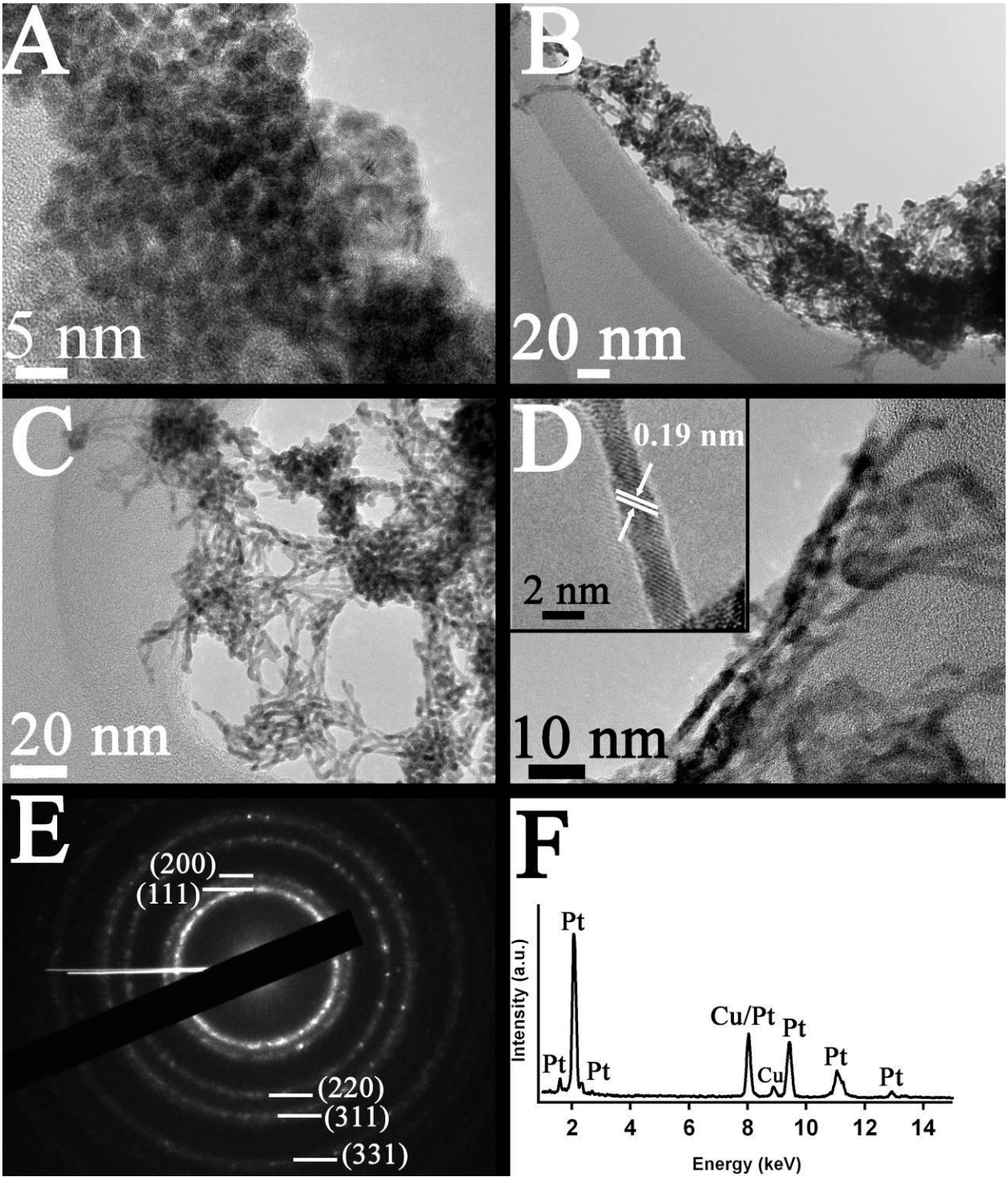

Figure 3.2 Electron microscopy of acid-treated Pt NWs and Pt NPs. Low resolution TEM images of acid-washed Pt NPs (A) and ultrathin Pt NWs both before (B) and after (C) treating with acid. An HRTEM image (D) of a single acid-washed NW is shown as an inset with an image containing a representative collection of these NWs. Associated SAED (E) and EDAX (F) patterns of these 1D nanostructures. (Reprinted with permission from Ref. 19. Copyright 2010 American Chemical Society)

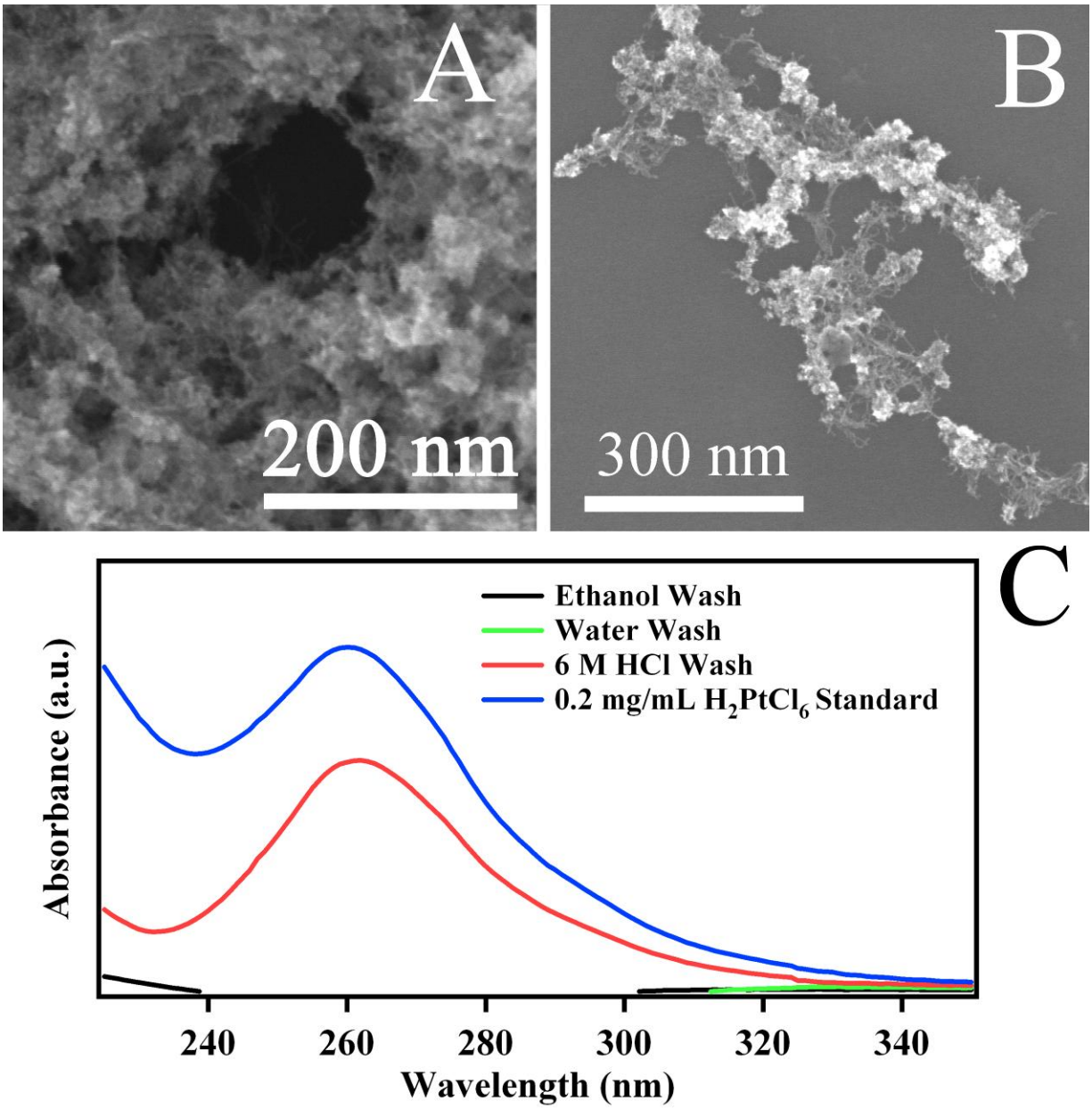

Figure 3.3 Purification of Pt NWs utilizing an acid-wash protocol. Representative SEM images of the NWs washed with water (A) and 6 M HCl (B). UV-Visible spectra (C) obtained from solutions used to purify the Pt NWs with a 0.2 mg/mL solution of H_2PtCl_6 serving as a reference for the presence of dissolved Pt species in 6 M HCl. (Adapted with permission from Ref. 19. Copyright 2010 American Chemical Society.)

3.3.2. Purification of Pt NWs by a Novel Acid Treatment

The novel use of an acid wash was critical in achieving suitably exfoliated NWs maintaining ultrathin diameters. Acid washes are ubiquitous in nanomaterial purification, especially with respect to the purification of platinum thin films after plasma etching.[37] Figure 3.3A – 3.3B shows representative scanning electron microscopy (SEM) images of NWs washed with water and with 6 M HCl. When washed in water (Figure 3.3A), the NWs are highly aggregated into a monolithic net-like structure and are encased in an amorphous residue apparent between the NW bundles. By comparison, acid-washed NWs (Figure 3.3B) displayed are exfoliated with a much lower degree of aggregation and in fact, individual NWs could be resolved. We attribute the improvement in dispersibility and NW exfoliation to the solubilization of residual amorphous platinum and platinum salts such as $PtCl_x$ and PtO_x by the HCl.[38]

Moreover, the apparent diameter of the NWs after acid-treatment (Figure 3.2C) is decreased from ~2 nm to ~1.3 nm size after acid treatment of acid-washed NWs as the length of the treatment protocol was increased from 1 – 5 min. We attribute this change in wire diameter to a symmetrical etching of the exposed surfaces by oxygen, which is catalyzed by the selective presence of the chloride anion. The catalyzed oxidative etching of noble metal nanostructures by O_2/Cl^- has been demonstrated by Xia and co-workers in the shape-dependent seed mediated growth of Pd and Pt nanostructures.[39] Specifically, mechanistic insights suggest that defect sites are the most susceptible to oxidative etching leading to the selective formation of low energy (111) and (100) facets and consequently to a variety of distinctive shapes depending upon the synthetic parameters and the capping agent employed.[40] However, we demonstrate for the first time herein that oxidative etching can be utilized on preformed noble metal nanostructures to not only (i) remove residual amorphous impurities but to (ii) selectively etch defect sites present on

the surface and (iii) decrease particle size, without influencing the morphology of the pre-formed structure. This represents a significant advance in the processing of noble metal nanostructures for use in practical applications since this treatment protocol is applicable to a broad range of nanostructures and is independent of synthetic technique, morphology or dimensions.

To further expand upon the practicality of this purification technique, we have coupled the acid-treatment protocol with UV-visible spectroscopy to provide an *in situ* quantitative technique to probe the rate and degree of etching. During the acid-treatment of ultrathin Pt NWs and Pt NPs, visual inspection of the 6 M HCl solution reveals the evolution of a light yellow color, which is consistent with the dissolution of Pt and Pt salts forming solubilized H_2PtCl_6. Examination of the acid wash solution by UV-visible spectroscopy (Figure 3.3C) reveals a prominent absorption peak at 362 nm, which is consistent with the presence of dissolved H_2PtCl_6 in HCl shown as a standard.[36] Interestingly, the use of UV-visible spectroscopy is advantageous because the concentration of H_2PtCl_6 can be determined in solution from Beer's law enabling the direct *in situ* detection of the quantity of Pt redissolved by the HCl treatment. For example, a typical acid treatment of the Pt NWs results in the solubilization of 2.5 mg of platinum representing ~50% of the product on the basis of the quantity of precursor utilized in the reaction. This important finding is consistent with a reduction in the diameter of the NWs from 2 nm to 1.3 nm. From a mechanistic perspective, the 6 M HCl solution was rationally substituted with ethanol (Figure 3.3C, black trace) and water (Figure 3.3C, green trace). UV-visible spectroscopy obtained from these solutions showed the presence of no H_2PtCl_6 confirming that the etching and solubilization process only takes place when both O_2 and Cl^- are mutually present in the 6 M HCl solution.

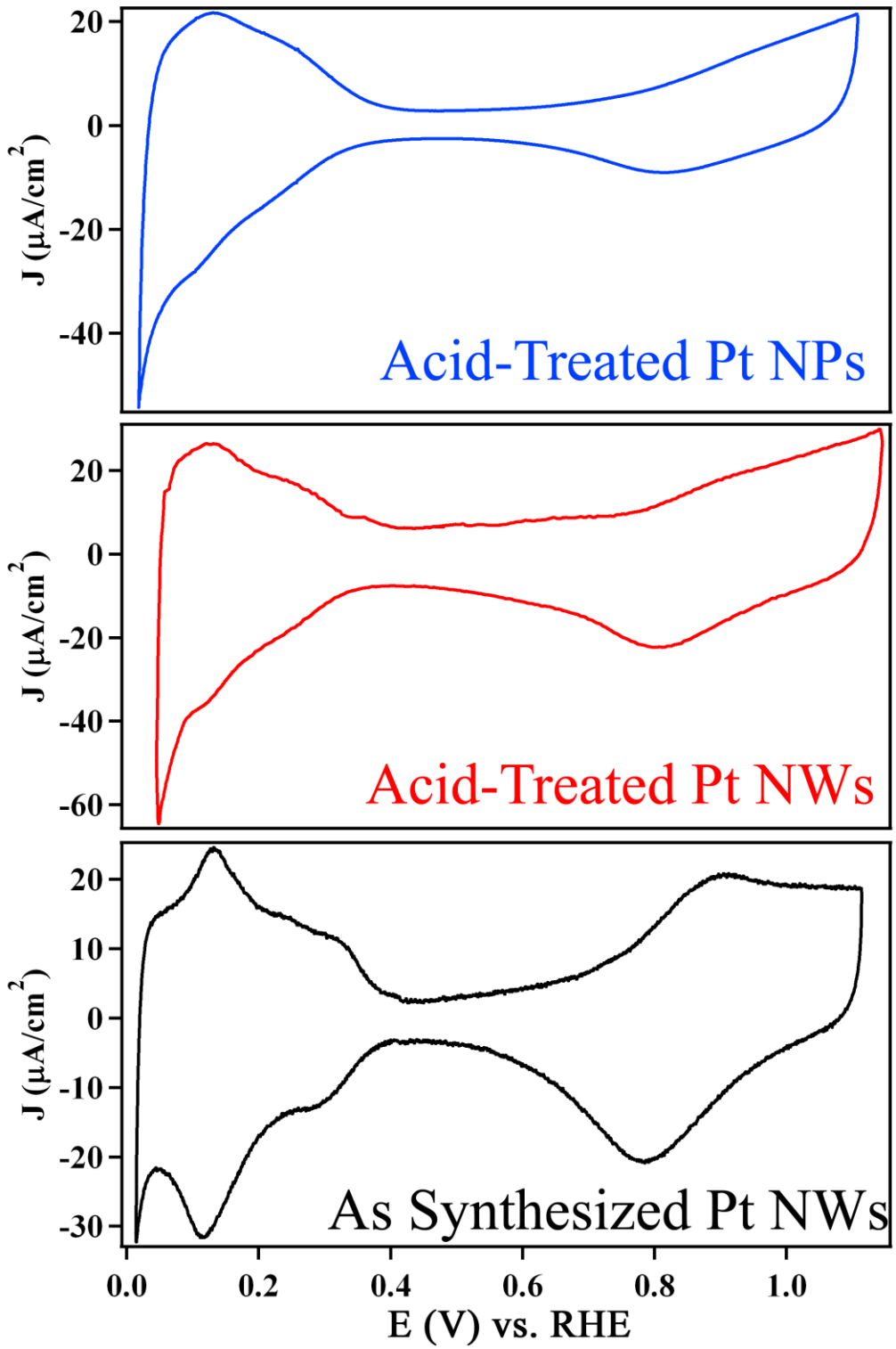

Figure 3.4 Cyclic voltammograms obtained from as-synthesized ultrathin Pt NWs (black), acid-treated ultrathin Pt NWs (red) and acid-treated Pt NPs (blue).

3.3.3. Size-Dependent Electrochemical Performance of Pt NWs toward Oxygen Reduction

The cathodic ORR kinetics of the as-synthesized NW samples were probed by thin layer rotating disk cyclic voltammetry. Initially, stationary electrode cyclic voltammograms (CVs) were obtained of RDEs loaded with the platinum NWs in deoxygenated 0.1 M $HClO_4$ solution in order to retrieve the electrochemically addressable surface areas (Figure 3.4). For comparison, the sample of acid-washed platinum NPs prepared by modification of the NW synthesis is shown. Initially, the active surface areas of the both electrodes were determined by the integrated hydrogen adsorption (H_{ads}) charge measured.[41]

The peaks associated with H_{ads} in the CV in Figure 3.4 indicate the presence of the 110 and 100 oriented steps for the as-prepared NWs. For the acid-treated Pt NWs, the number of low-coordinated sites is significantly lower as compared with that found with as-prepared NWs, as evidenced by the absence of distinct peaks in the 0 – 0.2 V region.[26] Not surprisingly, defect sites are also selectively etched from the Pt NP sample, which confirms that the acid treatment is effective on Pt nanostructures with diverse morphologies. Thus, it appears that the acid wash contributed to the removal of atoms occupying low coordination sites, in addition to removing amorphous deposits. This assertion is consistent with previous reports that have shown that high energy metallic surfaces[40] and defect sites[39] are preferentially etched by acidic solutions. Thus, we can attribute the lack of extraneous, undesirable low-coordination sites to the etching effect of the acid wash, leaving behind primarily desirable smooth, crystalline, and defect-free surfaces. In addition, it also apparent that the acid-treatment contributes to a suppression of the onset of the formation of the surface oxide region (0.6 – 1.0 V), which is indicative that a more active catalytic surface is obtained after treatment.[42]

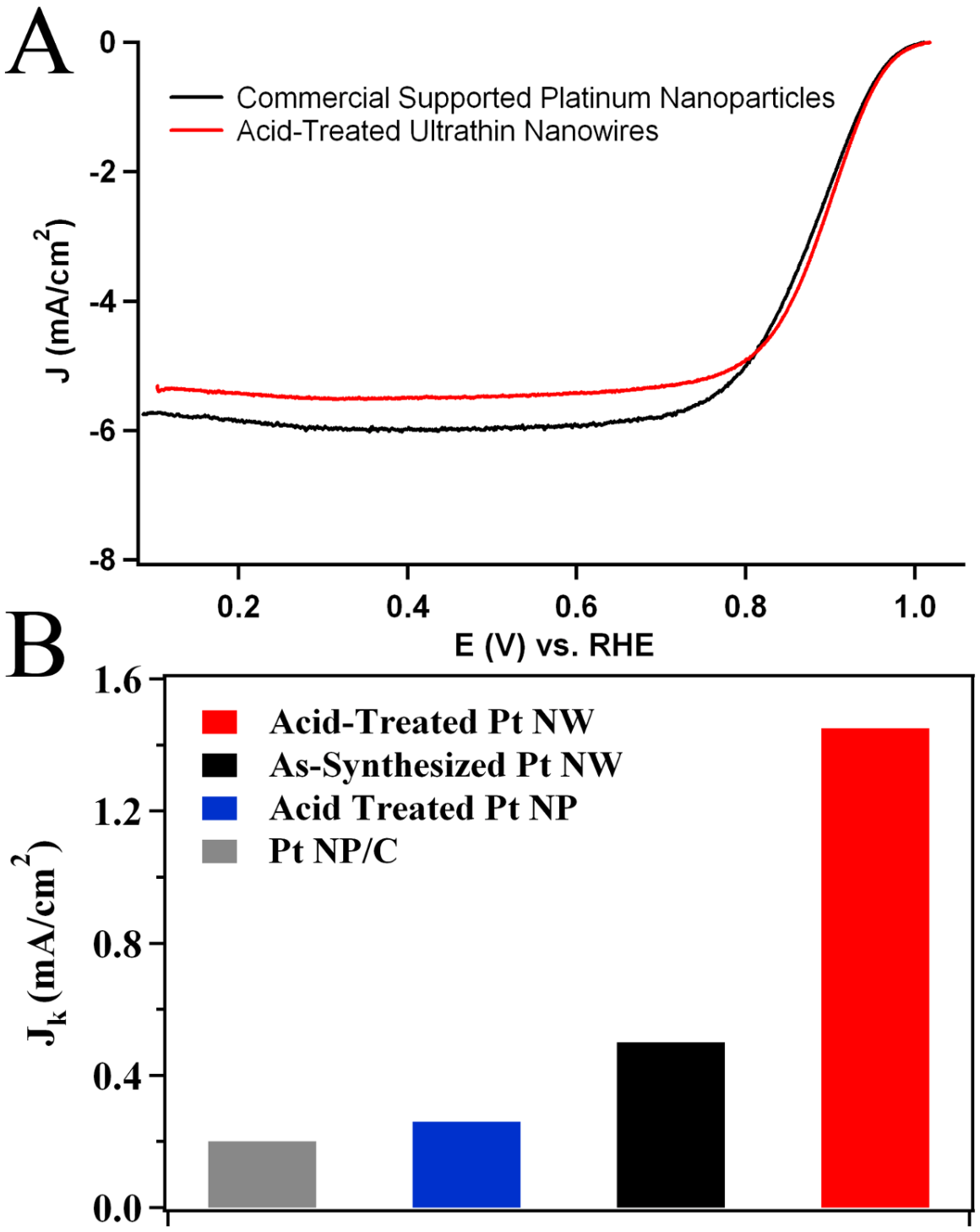

Figure 3.5 Electrocatalytic performance of ultrathin Pt NWs toward ORR. The polarization curve (A) for the acid-treated ultrathin Pt NWs as compared with commercial Pt NP/C obtained in 0.1 M $HClO_4$ at 1600 rpm. The measured specific activity (B) at 0.9 V from acid-treated Pt NWs and Pt NPs with as-synthesized Pt NWs and commercial Pt NP/C serving as a comparison to demonstrate the beneficial effects of the acid-treatment protocol on ORR performance.

The ORR activity for the NW samples was measured electrochemically by obtaining polarization curves in an oxygen saturated 0.1 M $HClO_4$ solution (Figure 3.5A). The Pt NWs show an ORR onset between 0.7 and 0.8 V, as expected, with nanostructured platinum electrocatalysts. It is important to note that the slightly lower than expected current density between 0.2 – 0.6 V associated with the primarily diffusion controlled region of the polarization curve can be attributed to the insufficient dispersion of the unsupported Pt NW catalysts on the electrode. Efforts are underway to improve the distribution of the catalyst by supporting the ultrathin Pt NWs on carbon. Regardless, the measured kinetic currents were normalized to the real surfaces areas so as to probe the intrinsic activity of each Pt nanostructure sample. Based on this protocol, the acid-washed ultrathin NWs displayed an outstanding specific activity (J_K) for an unsupported nanostructured material of 1.45 mA/cm^2.

In the context of the acid wash protocol, Figure 3.5B clearly demonstrates that the acid-treatment protocol significantly and measurably increases the performance of the Pt NWs when compared with the as-synthesized Pt NWs by nearly three-fold. This observation is consistent with the TEM and CV results, which mutually demonstrate that the acid-wash protocol (i) exfoliates the Pt NWs, (ii) removes amorphous residues thereby exposing active sites and more importantly, (iii) selectively removes defect sites. In this context, we also observed that the unsupported acid-treated Pt NPs displayed comparable but slightly enhanced activity as compared with their commercial Pt NP/C analogues, further highlighting the benefits of the acid treatment. However, the activity displayed by the acid-treated Pt NPs is lower when compared with the acid-treated Pt NW counterparts. This provides strong evidence that the superior performance observed in the NW system is strictly derived from the ultrathin, 1D motif of the NW morphology and is in agreement with prior reports.[8,9]

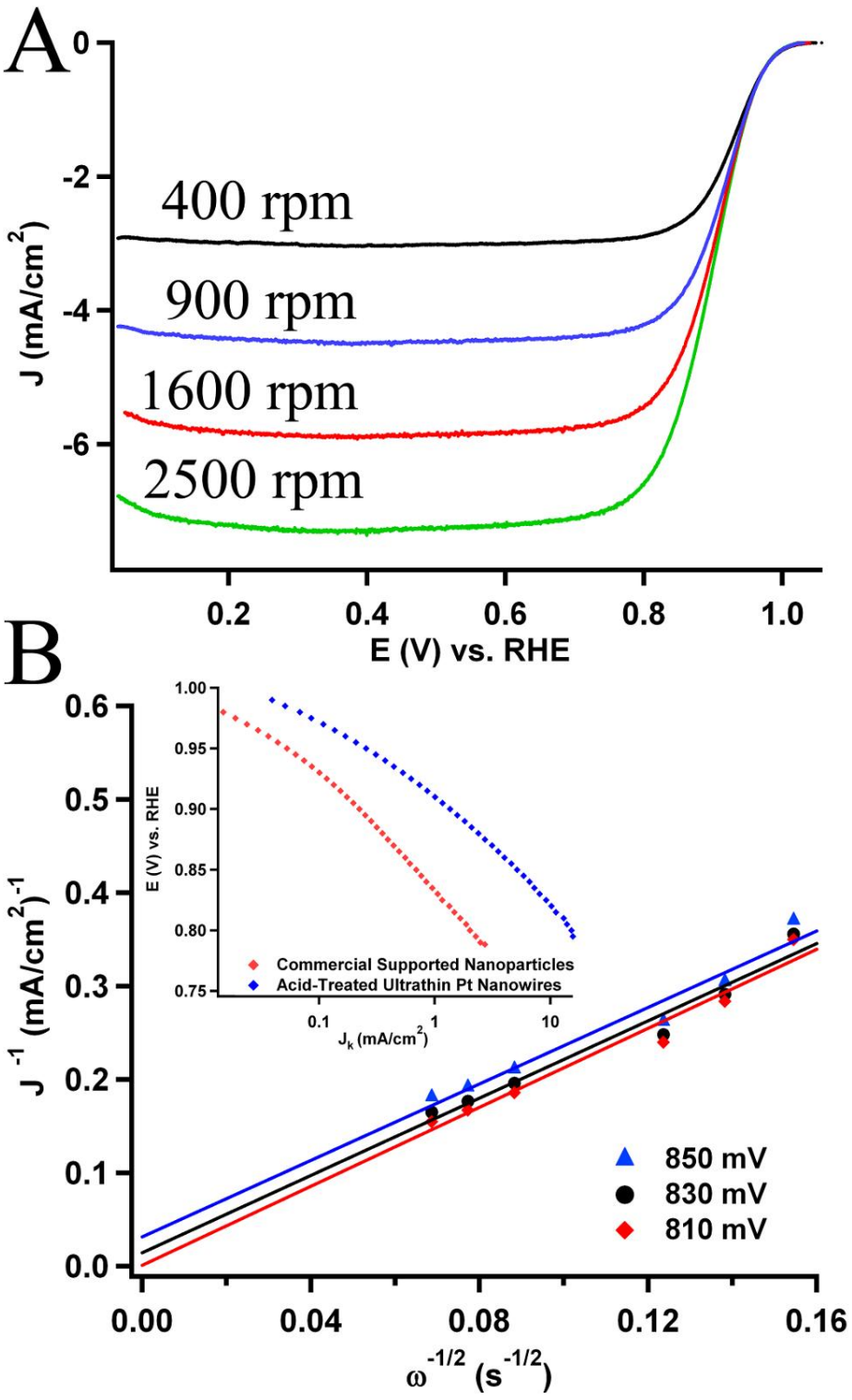

Figure 3.6 Detailed investigation of the ORR process on acid treated Pt NWs. Polarization curves (A) of acid-treated ultrathin Pt NWs at various rates of rotation. Koutecky-Levich plots (B) at different potentials obtained from the data in (A). A plot of the potential vs. specific activity (E vs. J_K) is also shown as an inset to B. (Reprinted with permission from Ref. 19. Copyright 2010 American Chemical Society)

To further explore the kinetics of ORR at the ultrathin Pt NW electrode, we constructed a Koutecky-Levich (K-L) plot at various potentials, which is shown in Figure 3.6B. In Equation (1), the J is the measured disk current density, J_K is the kinetic current density, B is a constant, and ω is rotation speed. Thus, the experimental values for J_K and B can be extracted from the Koutecky-Levich plot from the y-intercept and slope, respectively at a given potential. For comparison with the experimental data, the B from Equation (2) was calculated based on the published values of the diffusion coefficient of O_2 ($D_{O2} = 1.93 \cdot 10^{-5}$ cm^2 s^{-1}), the kinetic viscosity of the solution ν ($\nu = 1.009 \cdot 10^{-2}$ cm^2 s^{-1}),[43] the concentration of dissolved O_2 in solution ($C_{O2} = 1.26 \cdot 10^{-3}$ mol L^{-1}),[2] the Faraday constant (F), and the electrode's geometric area (A_g).

$$\frac{1}{J} = \left(\frac{1}{J_K} + \frac{1}{J_D} \right) = \frac{1}{J_K} + \frac{1}{B\omega^{1/2}} \qquad (1)$$

$$B = 0.62 n F A_g D_{O_2}^{2/3} \nu^{-1/6} C_{O_2} \qquad (2)$$

The experimental fit yields a value of 0.096 mA s$^{-1/2}$ for B which agrees well with the theoretical value of 0.092 mA s$^{-1/2}$ calculated for an ideal, four-electron reduction process and suggests that the ORR at the NW electrode largely follows a 4e$^-$ pathway. Furthermore, the data at each potential closely fit the K-L linear relationship and a consistent slope (*i.e.* consistent B value) is maintained over all of the potentials. Taken together these observations suggests first-order kinetics[44] with respect to molecular oxygen, which is highly desirable. In addition, the so called potential verses kinetic current density (E vs. J_K) plots (inset to Figure 3.6B) of acid-treated Pt NWs and commercial Pt NPs are also shown.[45,46] The E vs. J_K plots clearly reveal that

the acid-treated NWs maintain significantly higher kinetic currents over the entire range of operating potentials. Overall, these observations provide additional evidence that the ultrathin acid-treated NWs display greatly enhanced ORR kinetics as compared with commercial Pt NPs, further demonstrating the general morphology-dependent enhancement in ORR activity in 1D Pt nanostructures.

More importantly, we demonstrate in Figure 3.7 that there is a remarkable size-dependent enhancement in performance as the diameter of the 1D nanostructures is decreased to the ultrathin regime. Specifically, the unsupported ultrathin Pt NWs (1.3 nm) possessed an exceptional specific activity of 1.45 mA/cm^2, representing nearly a two-fold and four-fold enhancement over the 45 nm nanosized (0.82 mA/cm^2) and 200 nm submicron (0.38 mA/cm^2) NWs, respectively. Representative images of the 200 nm and 45 nm Pt nanostructures prepared from a template-based technique are shown in Figure 3.7A and Figure 3.7B, respectively highlighting the distinctive and dramatic differences in diameter.

The size-dependent enhancement raises an interesting question in terms of ORR electrocatalysis, since the experimental trend in 1D systems contrasts starkly with that observed in analogous 0D nanoparticulate systems. In the case of Pt and Pd NP/C, decreases in particle size tend to result in lower activity as a result of size-dependent variations in the electronic properties of the particle as well as an increased density of defect sites and low coordination atoms (LCAs).[25] This contributes to significantly lower specific activity as the particle size is decreased below 2 nm as a result of an increased interaction with the oxygen adsorbate.

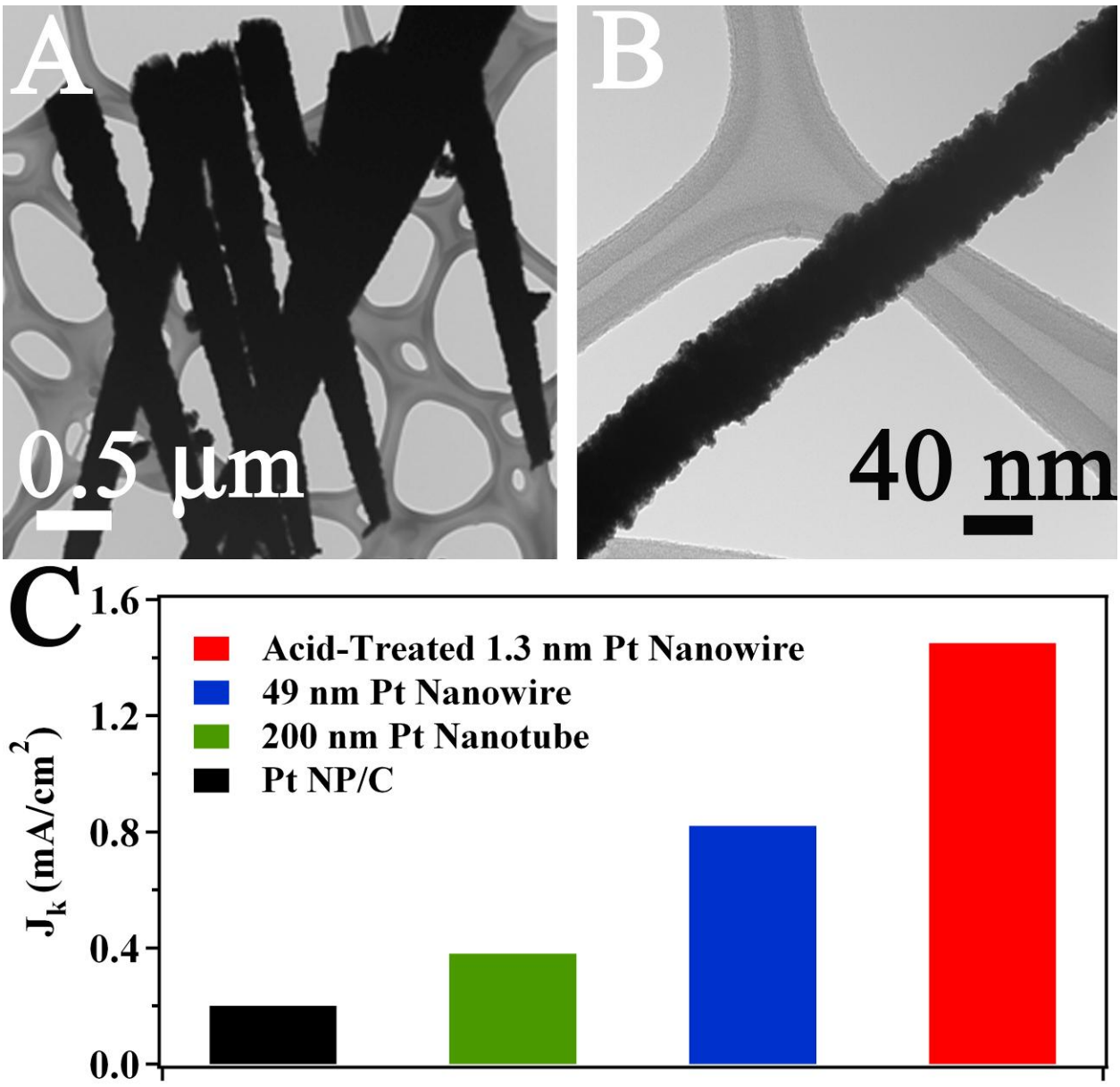

Figure 3.7 The size-dependent trend in 1D Pt nanostructures of specific ORR activity measured at 0.9 V with commercial Pt NP/C serving as a commercial reference system is illustrated in (C). Representative TEM images collected from individual isolated 200 nm Pt NTs (A) and 45 nm Pt NWs (B), mutually prepared by an ambient, template-based technique. (Adapted in part with permission from Ref. 8. Copyright 2012 American Chemical Society)

By contrast with NPs, our collective experimental results including CV and HRTEM data confirm that the ultrathin NWs maintain well-ordered (111) and (100) facets, possessing very few defect sites as compared with their nanoparticulate analogues.[19,47-49] Accomplishing this feat necessitated the use of basic amine-terminated surfactants, in this case triethylamine (TEA) to selectively promote the exposure of the (100) facet and lead to the desirable <111> growth direction apparent in Figure 3.2D. Moreover, cathodic and anodic features typically associated with (110)-type defect sites, which are clearly observed in commercial Pt NP/C, are almost indiscernible in the corresponding data associated with our acid-treated ultrathin Pt NWs.[19,49] The key point to emphasize is that our 1D motifs do not necessarily suffer from higher defect densities and LCAs, as diameter is decreased into the ultrathin size regime, and this observation may explain the general enhancement in activity, characteristic of the 1D morphology.

Nevertheless, the size-dependent performance is neither completely nor solely explained by the relatively defect-free nature of 1D catalysts. More recently, the structural and electronic properties inherent to NWs have been postulated to be a key element in the origin of their size-dependent performance. That is, in terms of size-dependent electronic and structural effects, several theoretical[27-29] and experimental[50-52] studies have asserted that noble metal NWs (*e.g.* Pt, Pd, Ir, Au etc.) undergo a characteristic contraction of the surface atoms, as the NW is decreased into the ultrathin regime, particularly when the NW diameter is below 2 nm. Contractions of the surface atoms are predicted to cause a down-shift of the *d*-band center to lower energies and thereby result in significantly weakened interactions with adsorbates, such as CO and oxygen species.[30,32,33] In fact, recent theoretical work performed by Matanović et al. has provided for excellent DFT evidence in favor of a size-dependent enhancement in ORR activity, as the diameter of 1D platinum nanostructures is decreased below 2 nm.[53] Specifically, it was shown in

this theoretical work that ultrathin NWs may undergo additional surface reconfiguration upon adsorption of oxygen leading to a downshift in the *d*-band center and this may in fact point toward the origin of the enhanced kinetics.[54]

From an experimental perspective, the predicted downshift in the Pt *d*-band in ultrathin noble metal NWs has been observed experimentally by Guo and co-workers utilizing X-ray photoelectron spectra (XPS). This was the first spectroscopic data that demonstrated that ultrathin Pt NWs maintained lower binding energies for the Pt $4f_{7/2}$ signal in the NWs as compared with commercial Pt NPs and bulk Pt.[52] Herein, the CV data obtained from our submicron and ultrathin Pt NWs reveal that the oxide reduction peak is shifted to higher potentials by ~10 mV, as the size of the NWs is decreased into the ultrathin regime. Not only is this observation in agreement with the XPS results but also it provides strong evidence of a systematic decrease and weakening in the interaction with adsorbates, as the NW diameter is decreased into the ultrathin regime.

As we will demonstrate in Section 3.3.4 and Chapter 5, we have also utilized CO stripping voltammetry to probe the relative interactions with adsorbates in ultrathin Pd & Pt NWs. As expected, the measured CO stripping peak was observed to shift negatively from 0.925 V to 0.906 V, as the size of the Pd NWs was decreased from 270 nm to 2 nm. Although the size-dependent phenomena of Pd NWs is discussed in detail in Chapters 5, the CO stripping results obtained for ultrathin Pd NWs, the oxide reduction results gathered for Pt NWs, and the XPS results collected for ultrathin Pt NWs and NPs collectively provide for a strong argument for a surface reconstruction process and a corresponding down-shift in the *d*-band center, thereby resulting in an enhanced ORR performance. Furthermore, the excellent CO stripping kinetics

observed may also render these ultrathin catalysts as potentially effective alcohol oxidation catalysts.[49,52]

3.3.4. Morphology-Dependent Enhancement toward Ethanol Oxidation in Ultrathin Pt NWs

The ultrathin Pt NWs also maintain a significant morphology-dependent enhancement toward the ethanol oxidation reaction (EOR), when compared with Pt NP/C.[49] The specific EOR activity for the Pt NWs and Pt NP/C was measured at an operating potential of 0.65 V over the course of 60 min utilizing chronoamperometry (CA) in 0.2 M ethanol supported in a 0.1 M $HClO_4$ electrolyte. The results of the test (Figure 3.8A) confirm that the Pt NWs maintain higher specific EOR activity over the course of the test. After 60 min, the Pt NWs maintain a specific activity of 0.076 mA/cm^2, which represents a two-fold enhancement over the corresponding Pt NP/C (0.036 mA/cm^2). Similar enhancements were noted when the CA experiment was performed with operating potentials of 0.55 V, 0.60 V and 0.65V. In each case, the activity was measured after 500 s of electrode operation (Figure 3.8A) and a consistent three-fold enhancement in EOR activity was noted in the Pt NWs. In addition to performing CA, the reaction kinetics of EOR was also studied by obtaining linear sweep voltammograms (LSVs) in 0.2 M ethanol/0.1 M $HClO_4$. The results confirmed that the Pt NWs maintained a considerable lower onset potential (measured at J = 0.01 mA/cm^2) for EOR of ~0.23 V, in comparison with the Pt NP/C (0.45 V). The LSVs also confirmed that the Pt NWs evince a higher current density over the entire voltammetric sweep and a near two-fold enhancement in the peak current density, further confirming the enhanced EOR performance.

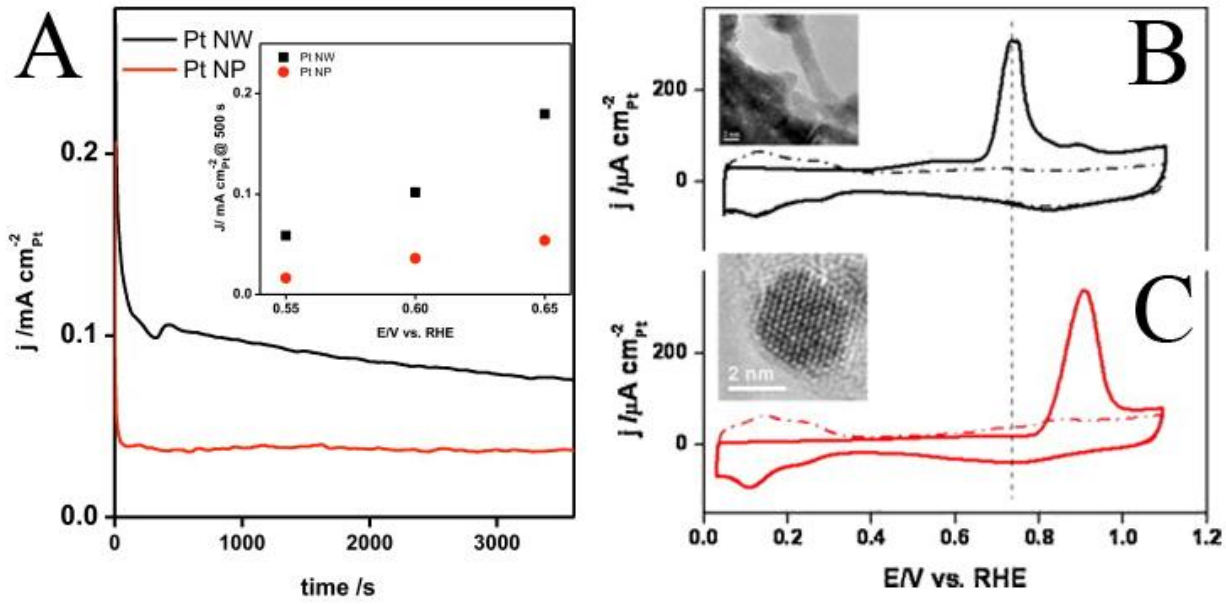

Figure 3.8 Electrocatalytic performance of ultrathin Pt NWs toward EOR. Chronoamperometry results (A) for ethanol oxidation activity of Pt NWs (black) and Pt NP/C (red) in 0.2 M ethanol/0.1 M $HClO_4$ solution at 0.65 V over a period of 3600 s reaction time. The current densities measured from Pt NWs and Pt NP/C after 500 s of reaction time with operating potentials of 0.55 V, 0.60 V and 0.65 V are shown as an inset to the chronoamperometry results. CO stripping curves obtained at a scan rate of 50 mV/s for the Pt NWs (B) and Pt NP/C (C) are also shown. The solid line denotes the first scan and the dashed line denotes the second scan. Typical HRTEM images of the Pt NWs and Pt NP/C are shown as insets to the CO stripping results.

To rationalize the morphology-dependent performance in ultrathin Pt NWs, CO stripping voltammograms were obtained to determine the relative interaction of the Pt nanostructures with this key intermediate. The formation of adsorbed CO as an intermediate in the process of ethanol oxidation has been identified as a key challenge in attaining suitably high kinetics, since the strong interaction of CO with Pt results in a poisoning effect. This typically necessitates high overpotentials beyond the thermodynamic potential for EOR, in order to suitably decrease the CO coverage and increase the relative availability of Pt active sites for ethanol adsorption. Interestingly, the CO stripping voltammograms highlight a significant shift in the CO oxidation peak potential for the Pt NWs (Figure 3.8B, 0.73 V), when compared with the Pt NP/C (Figure 3.8C, 0.90 V). The enhanced CO oxidation performance in this case likely immerges from the electronic properties associated with ultrathin Pt NWs. Specifically, the observed down-shift in the energy of the weighted center of the *d*-band is expected to significantly weaken the interaction between the Pt NW's surface sites and the CO adsorbate leading to enhanced CO oxidation kinetics. The intrinsically high tolerance to CO is an important finding and may render ultrathin Pt NWs active toward the oxidation of methanol and formic acid for example.

3.4 Conclusions

We have synthesized crystalline platinum NWs with an ultrathin diameter of 1.3 ± 0.4 nm. As-prepared NWs were treated with an acid wash protocol in order to suitably exfoliate the NWs and re-dissolve amorphous platinum deposits so as to expose the active surface areas of the wires themselves. Moreover, cyclic voltammetry revealed that the acid-washed NWs displayed fewer undesirable surface defects, which was also attributed to the acid wash itself. The acid-treated ultrathin Pt NWs displayed an outstandingly specific activity of 1.45 mA/cm^2, which was

significantly higher than that reported for both commercial Pt NP/C and analogous acid-treated Pt NP confirming a morphology-dependent enhancement in performance in 1D structures. More importantly, we have also demonstrated for the first time a remarkable size-dependent enhancement in 1D Pt nanostructures as the diameter is decreased toward the nanometer scale. On the basis of our HRTEM, CV and CO-stripping results, this size-dependent enhancement is believed to arise from the size-dependent electronic properties of 1D noble metal nanostructures. In addition, the Pt NWs were also found to maintain a measureable morphology-dependent enhancement toward EOR performance in comparison with Pt NP/C. Collectively, these results highlight ultrathin Pt NWs as a versatile catalyst system relevant to both the anodic and cathodic reactions in PEMFCs.

3.5 References

(1) Subhramannia, M.; Pillai, V. K. *J. Mater. Chem.* **2008**, *18*, 5858-5870.
(2) Cademartiri, L.; Ozin, G. A. *Adv. Mater.* **2009**, *21*, 1013-1020.
(3) Xia, Y.; Yang, P.; Sun, Y.; Wu, Y.; Mayers, B.; Gates, G.; Yin, Y.; Kim, F.; Yan, H. *Adv. Mater.* **2003**, *15*, 353-389.
(4) Adzic, R. R.; Strbac, S.; Anastasijevic, N. *Mater. Chem. Phys.* **1989**, *22*, 349-375.
(5) Wang, C.; Waje, M.; Wang, X.; Tang, J. M.; Haddon, R. C.; Yan *Nano Lett.* **2003**, *4*, 345-348.
(6) Morozan, A.; Jousselme, B.; Palacin, S. *Energy Environ. Sci.* **2011**, *4*, 1238-1254.
(7) Antolini, E.; Perez, J. *J. Mater. Sci.* **2011**, *46*, 1-23.
(8) Koenigsmann, C.; Scofield, M. E.; Liu, H.; Wong, S. S. *J. Phys. Chem. Lett.* **2012**, *3*, 3385-3398.
(9) Koenigsmann, C.; Wong, S. S. *Energy Environ. Sci.* **2011**, *4*, 1161 - 1176.
(10) Xiao, L.; Zhuang, L.; Liu, Y.; Lu, J.; Abruña, H. c. D. *J. Am. Chem. Soc.* **2008**, *131*, 602-608.
(11) Chen, Z.; Waje, M.; Li, W.; Yan, Y. *Angew. Chem. Int. Ed.* **2007**, *46*, 4060-4063.
(12) Zhou, H.; Zhou, W.-p.; Adzic, R. R.; Wong, S. S. *J. Phys. Chem. C* **2009**, *113*, 5460-5466.
(13) Liang, H.-W.; Cao, X.; Zhou, F.; Cui, C.-H.; Zhang, W.-J.; Yu, S.-H. *Adv. Mater.* **2011**, *23*, 1467-1471.
(14) Alia, S. M.; Zhang, G.; Kisailus, D.; Li, D.; Gu, S.; Jensen, K.; Yan, Y. *Adv. Funct. Mater.* **2010**, *20*, 3742-3746.
(15) Xiao, Q.; Cai, M.; Balogh, M.; Tessema, M.; Lu, Y. *Nano Res.* **2012**, *5*, 145-151.

(16) Lim, B.; Jiang, M.; Camargo, P. H. C.; Cho, E. C.; Tao, J.; Lu, X.; Zhu, Y.; Xia, Y. *Science* **2009**, *324*, 1302-1305.
(17) Sun, S.; Jaouen, F.; Dodelet, J.-P. *Adv. Mater.* **2008**, *20*, 3900-3904.
(18) Górzny, M. Ł.; Walton, A. S.; Evans, S. D. *Adv. Funct. Mater.* **2010**, *20*, 1295-1300.
(19) Koenigsmann, C.; Zhou, W.-p.; Adzic, R. R.; Sutter, E.; Wong, S. S. *Nano Lett.* **2010**, *10*, 2806-2811.
(20) Uota, M.; Hayashi, Y.; Ohyama, K.; Takemoto, H.; Iriki, R.; Kishishita, T.; Shimoda, M.; Yoshimura, T.; Kawasaki, H.; Sakai, G.; Kijima, T. *J. Nanosci. Nanotechnol.* **2010**, *10*, 5790-5795.
(21) Shao, M.; Peles, A.; Shoemaker, K. *Nano Lett.* **2011**, *11*, 3714-3719.
(22) Mavrikakis, M.; Hammer, B.; Nørskov, J. K. *Phys. Rev. Lett.* **1998**, *81*, 2819.
(23) Mayrhofer, K. J. J.; Blizanac, B. B.; Arenz, M.; Stamenkovic, V. R.; Ross, P. N.; Markovic, N. M. *J. Phys. Chem. B* **2005**, *109*, 14433-14440.
(24) Mukerjee, S.; McBreen, J. *J. Electroanal. Chem.* **1998**, *448*, 163-171.
(25) Tritsaris, G.; Greeley, J.; Rossmeisl, J.; Nørskov, J. *Catal. Lett.* **2011**, *141*, 909-913.
(26) Tsou, Y. M.; Cao, L.; Castro, E. D. *ECS Transactions* **2008**, *13*, 67-84.
(27) Fiorentini, V.; Methfessel, M.; Scheffler, M. *Phys. Rev. Lett.* **1993**, *71*, 1051-1054.
(28) van Beurden, P.; Kramer, G. J. *J. Chem. Phys.* **2004**, *121*, 2317-2325.
(29) Haftel, M. I.; Gall, K. *Phys. Rev. B: Condens. Matter* **2006**, *74*, 035420-035412.
(30) Adzic, R.; Zhang, J.; Sasaki, K.; Vukmirovic, M.; Shao, M.; Wang, J.; Nilekar, A.; Mavrikakis, M.; Valerio, J.; Uribe, F. *Top. Catal.* **2007**, *46*, 249-262.
(31) Wang, J. X.; Inada, H.; Wu, L.; Zhu, Y.; Choi, Y.; Liu, P.; Zhou, W.-P.; Adzic, R. R. *J. Am. Chem. Soc.* **2009**, *131*, 17298-17302.
(32) Rossmeisl, J.; Nørskov, J. K. *Surf. Sci.* **2008**, *602*, 2337-2338.
(33) Nørskov, J. K.; Rossmeisl, J.; Logadottir, A.; Lindqvist, L.; Kitchin, J. R.; Bligaard, T.; Jonsson, H. *J. Phys. Chem. B* **2004**, *108*, 17886-17892.
(34) Wong, S. S.; Koenigsmann, C. Nanostructures Having Enhanced Catalytic Performance and Method for Preparing the Same.U.S. Patent Application 20120088656, 2012.
(35) Shen, Z.; Yamada, M.; Miyake, M. *Chem. Commun.* **2007**, 245-247.
(36) Teranishi, T.; Kurita, R.; Miyake, M. *J. Inorg. Organomet. Polym.* **2000**, *10*, 145-156.
(37) Ranpura, H. M.; Butler, D. H.; Chang, L. H.; Tracy, C. J.; Beaudoin, S. P. *J. Electrochem. Soc.* **1999**, *146*, 3114-3118.
(38) Dean, J. A. *Lange's Handbook of Chemistry*; 14th ed.; MacGraw Hill: New York, NY, 1992.
(39) Xiong, Y.; Xia, Y. *Adv. Mater.* **2007**, *19*, 3385-3391.
(40) Xu, S.; Tang, B.; Zheng, X.; Zhou, J.; An, J.; Ning, X.; Xu, W. *Nanotechnology* **2009**, *20*, 415601.
(41) Strmcnik, D.; Tripkovic, D.; van der Vliet, D.; Stamenkovic, V.; Markovic, N. M. *Electrochem. Commun.* **2008**, *10*, 1602-1605.
(42) *Fuel Cell Catalysts*; Koper, M. T. M., Ed.; Wiley Interscience: Hoboken, NJ, 2009.
(43) Lide, D. R. *CRC Handbook of Chemistry & Physics*; 75 ed.; CRC Press: Boca Raton, FL, 1994.
(44) Anastasijevic, N. A.; Vesovic, V.; Adzic, R. R. *J. Electroanal. Chem.* **1987**, *229*, 317-325.
(45) Wang, J. X.; Markovic, N. M.; Adzic, R. R. *J. Phys. Chem. B* **2004**, *108*, 4127-4133.

(46) Stamenkovic, V.; Schmidt, T. J.; Ross, P. N.; Markovic, N. M. *J. Phys. Chem. B* **2002**, *106*, 11970-11979.
(47) Koenigsmann, C.; Santulli, A. C.; Gong, K.; Vukmirovic, M. B.; Zhou, W.-p.; Sutter, E.; Wong, S. S.; Adzic, R. R. *J. Am. Chem. Soc.* **2011**, *133*, 9783-9795.
(48) Koenigsmann, C.; Santulli, A. C.; Sutter, E.; Wong, S. S. *ACS Nano* **2011**, *5*, 7471-7487.
(49) Zhou, W.-P.; Li, M.; Koenigsmann, C.; Ma, C.; Wong, S. S.; Adzic, R. R. *Electrochim. Acta* **2011**, *56*, 9824-9830.
(50) Kondo, Y.; Takayanagi, K. *Phys. Rev. Lett.* **1997**, *79*, 3455.
(51) Kondo, Y.; Takayanagi, K. *Science* **2000**, *289*, 606-608.
(52) Wang, S.; Jiang, S. P.; Wang, X.; Guo, J. *Electrochim. Acta* **2011**, *56*, 1563-1569.
(53) Matanović, I.; Kent, P. R. C.; Garzon, F. H.; Henson, N. J. *J. Phys. Chem. C* **2012**, *116*, 16499-16510.
(54) Matanović, I.; Kent, P. R. C.; Garzon, F. H.; Henson, N. J. *J. Electrochem. Soc.* **2013**, *160*, F548-F553.

Chapter 4. Enhanced Electrocatalytic Performance in Processed, Ultrathin, Carbon Supported Pt_{ML}~Pd Core-Shell Nanowire Catalysts for the Oxygen Reduction Reaction

4.1 Introduction

Given the remarkable size-dependent enhancement in performance, ultrathin noble metal NWs have been highlighted as a crucial new structural paradigm for electrocatalysis, since these structures maximize catalytic activity, while minimizing the precious metal content at the catalysts core.[1,2] In the previous chapter, we demonstrated an enhancement in specific ORR activity of more than four-fold, as the diameter of 1D Pt nanostructures is decreased from 200 nm to less than 2 nm.[3] Although the observed enhancements in area-specific activity associated with ultrathin Pt NWs is promising, a continuing challenge with the development of electrocatalysts composed entirely of platinum has been its prohibitive cost (greater than $1,600 US/ounce)[4] as well as its relatively low abundance.[5] This practical challenge associated with Pt-based catalysts has sparked several parallel efforts to try to minimize Pt content.

For example, promising results have been achieved with catalysts consisting of metal oxides, organometallic complexes, and biologically-inspired catalysts.[6] However, the issues with durability, stability, and activity will necessitate fundamental and long-term development in order to assess their potential for commercialization. An alternative approach with rapid potential for commercialization has been the concurrent development of catalysts that substitute Pt for less expensive and more abundant metals.[2,6-8] Currently, palladium represents a key candidate, because of its similar electronic and structural properties to Pt and its relatively lower cost (~$750 US/ounce).[4,9] However, the measured activity of bulk palladium is considerably lower than bulk platinum owing to the measurably stronger interaction of Pd with oxygen adsorbates at potentials relevant for ORR, by comparison with Pt.[10] Accordingly, there has been considerable

interest in the literature in terms of developing palladium-based catalysts consisting of either elemental palladium or palladium-based alloys, including first row transition metals, so as to achieve activities comparable to or higher than Pt.[11-13]

Considering the proven and intrinsic advantages of 1D architectures, there have also been several reports, which couple the intrinsic catalytic advantages of 1D architectures with palladium to achieve improved specific and mass activity.[14-16] For example, Abruña and co-workers[14] have observed a characteristic structure-dependent enhancement in ORR activity with palladium-based nanorod catalysts prepared by electrodeposition directly onto a carbon support. Utilizing a combinatorial approach, the enhanced activity in this case was attributed to the preferential display of certain low energy crystal facets, which have been predicted by DFT to be most active towards ORR in the case of Pd. Despite the significantly enhanced activity, the activity of these as-prepared nanorods did not surpass the activity of bulk platinum, which is largely considered to be one of the most active surfaces for ORR. In another report, Yan and co-workers[15] prepared polycrystalline PtPd nanotubes, which maintained a 1.4 fold higher Pt mass activity of approximately 0.1 A/mg_{Pt} at 0.85 V as compared with commercial Pt black catalysts. Similarly, Xia and co-workers have recently observed a degree of enhancement in mass activity of isotropic Pt dendrites, grown directly onto Pd NPs.[16] Despite these tangible gains, continued improvement is necessary in order to meet the 2015 U.S. Department of Energy (DOE) target[17] for ORR performance under membrane electrode assembly (MEA) conditions, namely a Pt mass activity of 0.44 A/mg_{Pt} (at 0.9 V).

The opportunity to tailor morphology represents a key advance in designing novel Pd-based catalysts with higher activity and durability. However, it is clear in the context of these preliminary results that simply tailoring the morphology of elemental structures alone will not

provide for sufficient flexibility in terms of increasing performance to exceed the DOE target set forth for 2015. In terms of meeting this goal, it is evident that successful methodologies must be developed in order to control not only morphology but also composition, structure, and homogeneity. For example, a promising route towards improving platinum mass activity, that has achieved considerable attention recently, has been the development of Pd nanocrystals possessing a Pt monolayer shell (Pt_{ML}), a strategy pioneered by Adzic and co-workers.[10,18-20] The highly controlled core-shell structure in this case has been achieved by first electrochemically depositing a monolayer of Cu atoms through the use of Cu underpotential deposition (UPD) followed by the controlled displacement of these ad-atoms with platinum via galvanic exchange.[21]

In a recent report, the activity of the optimized Pt_{ML} supported onto commercial Pd NPs was studied systematically, and as-prepared catalysts were found to possess outstanding mass and specific ORR activities of 0.96 A/mg_{Pt} and 0.5 mA/cm^2, respectively.[22] The significant enhancements in activity have been attributed to the advantageous core-shell motif, which modifies both the structural and electronic properties of platinum for enhanced activity. Specifically, the Pd substrate is thought not only to apply a compressive strain upon the Pt_{ML} but also to impart a so-called "ligand-effect." These phenomena mutually result in a lower energy of the weighted center of the Pt *d*-band. The resulting suppression of the Pt *d*-band energy is thought to directly provide for a weakened interaction with OH_{ads} groups, thereby yielding improved ORR activity.[23,24] Although outstanding results have been achieved with 0D core-shell catalysts based upon the platform of commercial Pd NPs, to the best of our knowledge, there have been no reports prior to our own study[25] in 2011 on the structural and morphological dependence of ORR activity in catalysts bearing this core-shell motif.

In this Chapter therefore, we describe the first successful synthesis, characterization, and electrocatalytic performance of a 1D core-shell catalyst consisting of a homogeneous Pt_{ML} shell supported onto a high-quality, ultrathin 2 nm Pd NW core.[25] In essence, we combine the advantageous core-shell motif with the known electrocatalytic advantages of ultrathin one-dimensional nanostructures in order to enhance the activity and durability of the resulting catalyst. In particular, the development of ultrathin noble metal NW cores is particularly advantageous, as a result of the slight contraction of the atoms at their surfaces and the unique down-shift in their *d*-band energy.[26-32] This phenomenon has been attributed by our group and others to be the origin for the enhanced performance toward ORR in elemental Pt NWs.[3,33] In the context of core-shell motif, a contraction of the core NW surface would be highly advantageous for ORR electrocatalysis, since this would enhance the strain induced contraction of the Pt_{ML} and therefore correspondingly improve upon the inherent ORR activity.

The synthesis of this distinctive, heterostructured catalyst draws from rational bottom-up design principles,[34] wherein solution-based synthetic techniques are merged with electrochemical deposition in order to provide for a method that can be readily scaled for production. In terms of synthesis, we first discuss the synthesis and characterization of ultrathin ~2 nm Pd NWs supported onto conductive carbon supports (Pd NW/C). This objective was accomplished by a surfactant-based synthetic technique coupled with a novel methodology for supporting these as-prepared NWs on Vulcan XC-72 carbon nanoparticles. The as-synthesized, carbon-supported composites maintain excellent homogeneity and a uniform three-dimensional dispersion of the Pd NWs on the carbon surface. In addition, we have demonstrated that the extended Pd NWs consist of multiple, anisotropic, 6 – 8 nm single crystalline segments, which represent the functional catalytic sub-structure.

In going beyond mere synthesis, we also developed a simple two-step protocol to purify the surfaces of the as-synthesized Pd NW/C composites of residual organic impurities present from the surfactants utilized in the synthesis.[35] The development of practical methodologies for removing organic impurities is critical to the commercial development of anisotropic catalyst materials, since the anisotropic crystalline growth in 1D noble metal nanostructures is often achieved by organic surfactants and capping agents.[34,36] However, these residual impurities strongly adsorb to the surfaces of the nanostructures after isolation and significantly reduce performance by blocking active sites. Herein, we have developed a treatment protocol that rationally combines a pre-treatment (*e.g.* either an acid wash, ligand exchange, or ozone oxidation) with a novel, selective CO adsorption process in order to remove organic impurities. The process is advantageous, since the surface can be purified without either damaging the desirable 1D morphology or reducing the overall homogeneity of the NWs on the carbon support. The impact of these diverse treatment protocols upon the electrochemical properties of the nanostructures has been analyzed.

We then explored the structure-dependent enhancement of ORR activity of as-prepared ultrathin Pd NWs by comparison with commercial Pd NP/C. Ultimately, the desired Pt_{ML} shell ~ Pd NW (Pt_{ML}~Pd NW) core structure can be prepared by utilizing Cu UPD followed by galvanic displacement. Specifically, the size-dependent enhancement of both area and mass-specific activity has been investigated herein. We find that the ozone-treated Pt_{ML}~Pd NW shell nanostructures maintain a platinum mass activity of 1.83 A/mg_{Pt}, which is more than double that associated with optimized core-shell catalysts, based upon NP motifs.

4.2 Synthesis and Activation of Ultrathin, Carbon Supported Pd NWs

4.2.1. Synthesis of Pd NW/C Composites

Initially, unsupported ultrathin Pd NWs were prepared, utilizing a modified procedure previously reported by Teng et al.[37] Briefly, palladium nitrate (13.0 mg, Alfa Aesar 99.9%), octadecylamine (400 mg, Acros Organics 90%), and dodecyltrimethylammonium bromide (60 mg, TCI >99%) were dissolved in 7 mL of toluene under vigorous magnetic stirring. The mixture was brought under an inert atmosphere, utilizing standard Schlenk procedures, and was sonicated for 20 min. Separately, solid sodium borohydride (13 mg, Alfa Aesar 98%) was dissolved into 2 mL of deoxygenated distilled water, and the solution was added dropwise to the precursor mixture, while stirring. After one hour, the reaction mixture was diluted with 2 mL aliquots of distilled water and chloroform, resulting in the separation of the organic and aqueous phases. The black organic phase was isolated, diluted with 10 mL of absolute ethanol, and centrifuged for 10 min, thereby resulting in the precipitation of a black solid. The black solid was subsequently washed several times with ethanol and allowed to dry in air.

Adsorption of these as-prepared NWs onto conductive carbon support (Vulcan XC-72, Cabot) was achieved by first dispersing the isolated black solid containing a mixture of Pd NWs and residual surfactant into 6 mL of chloroform, until a homogeneous black mixture was formed. An equal mass of Vulcan carbon (~6 mg) was then added to this mixture and the mixture was subsequently sonicated for 30 min in a bath sonicator. As-prepared composites were then isolated by centrifugation and fixed onto the carbon substrate by immersion in hexanes for 12 h. After washing several times with hexanes and ethanol, as-prepared composites were further cleansed with either hexane or acetone in order to remove residual surfactants prior to drying overnight.

4.2.2. Activation of Pd NW/C Catalysts

The activation of the Pd NW/C was accomplished by developing a two-step protocol to remove residual organic impurities present from the synthesis. In the first step, three separate pre-treatments were employed to suitably weaken the interactions of the organic impurities with the surfaces of the noble metal nanostructure.

Pre-treatment Protocol 1: We optimized an acid-treatment protocol previously described for Pd NPs[38] in the literature for removing organic capping agents. Dried, as-prepared catalyst powder was dispersed in 5 mL of glacial acetic acid (Fisher Scientific) by bath sonication for 30 min within a fume hood. The mixture was then brought to 50°C for 1 h, the mixture was centrifuged while still hot, and the acetic acid was later decanted. The treated composites were then washed several times with ethanol, and allowed to dry overnight.

Pretreatment Protocol 2: We utilized a novel time-controlled ozone treatment. In this case, dried, as-prepared catalyst powder was dispersed into ethanol by sonication after which several drops were placed onto a silicon wafer. The wafers were placed into a ultraviolet (UV) lamp ozone generator (UVOCS Model # T10X10-0ES), and treated for 15 min. As-treated NWs were then isolated from the wafers by sonication into a 25% IPA solution, thereby ultimately yielding the final catalyst ink solution of approximately 1 mg/mL.

Pretreatment Protocol 3: A ligand exchange protocol was employed to replace the long-chain surfactants employed in the synthesis, such as octadecylamine (ODA) in this case, with butylamine. The ligand exchange is advantageous, since butylamine is significantly easier to remove from the surface by means of selective CO adsorption than their long-chain surfactant counterparts. The Pd NW/C composites are then dispersed into n-butylamine (BA, Acros Organics, +99.5%) by sonication and the resulting dispersion is stirred for a period of three days

to ensure complete exchange of the ODA with BA. The treated product is isolated by centrifugation and washed with ethanol to remove excess BA.

After pre-treatment, the residual surfactant was removed from the surface of the treated Pd catalyst by displacement of the surface ligand with carbon monoxide (CO) followed by CO stripping. Adsorption of CO was achieved by immersing the electrode in a CO-saturated 0.1 M $HClO_4$ solution under a CO atmosphere for 30 minutes. During this immersion, the residual organic impurities are selectively displaced by the dissolved CO, which strongly binds to the surface forming a CO monolayer. A pristine surface is achieved by transferring the electrode to a fresh electrolyte solution and performing CO stripping by a potential sweep, running up to 0.85 V at 20 mV/s. In this process, the CO monolayer is oxidized to CO_2, leaving behind pristine active sites with no organic impurities. The effectiveness of the combined pre-treatment and selective CO adsorption protocol was evaluated by means of electron microscopy in order to probe the quality and homogeneity of the product after treatment and electrochemistry to study the effect of the treatment itself upon purity and catalytic activity.

For the sake of comparison, we utilized a heat treatment process typically used in the literature for removing residual organic surfactants. Specifically, the Pd NW/C powder was heated to 250°C in air for 1.5 h within a muffle furnace to thermally desorb the ODA surfactant. The heat-treated powder was then dispersed in ethanol for the purposes of electron microscopy.

4.3 Results & Discussion

4.3.1. Synthesis & Characterization of Pd NW/C

The synthesis of the Pd NW core in this case was readily achieved by utilizing a surfactant-based method[37] wherein the reduction of Pd^{2+} is directed by the surfactant agent,

ocatadecylamine (ODA). The crystallinity and purity of the subsequent as-prepared NWs was verified using XRD. The crystallographic analysis Figure 4.1A revealed that all of the peaks could be readily attributed to the (111), (200), (220), and (311) reflections of face-centered cubic palladium (*Fm3m*, JCPDS #46-1043), respectively. There were no detectable crystalline impurities observed in the XRD pattern. The morphology of as-prepared Pd NWs was initially characterized by electron microscopy. An overview TEM image presented in Figure 4.1B revealed that as-prepared NWs maintained ultrathin diameters of 2.0 ± 0.5 nm with average lengths in excess of 100 nm. High magnification SEM images (inset to Figure 4.1B) confirmed the inherent quality and dimensions of as-prepared Pd NWs. However, it was apparent that there was still a substantial undesirable surfactant residue present, despite multiple washes with ethanol. Based upon the high solubility of ODA in chloroform,[39] as-prepared NWs were washed multiple times with chloroform in order to remove the residual surfactant. However, overview TEM image of the chloroform-washed product revealed that the NWs became heavily agglomerated and the desirable morphology was lost. Similarly, rapid agglomeration was observed after washing with other solvents, including dimethylformamide (DMF) and toluene.

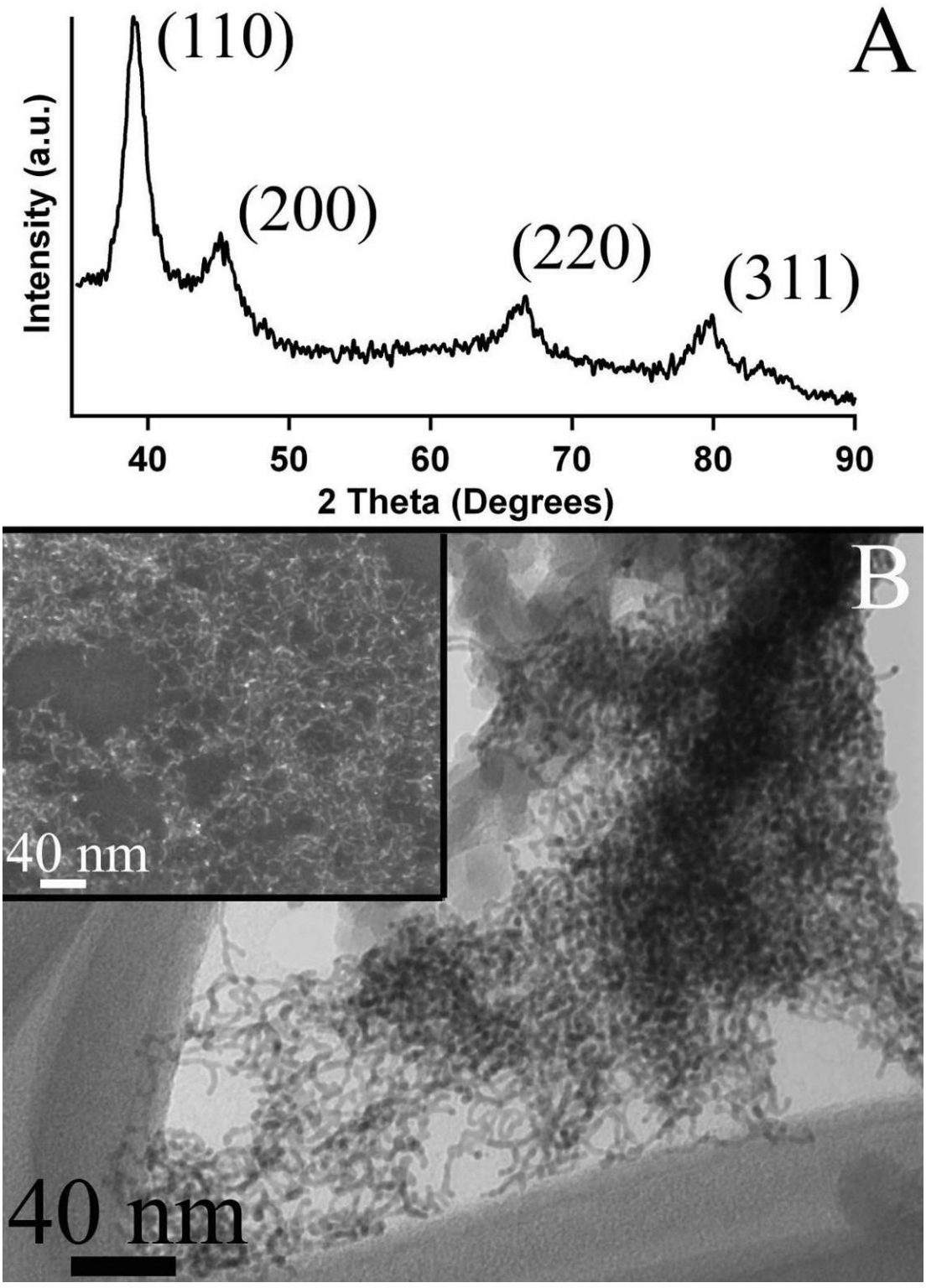

Figure 4.1 Characterization of unsupported, as-prepared ultrathin Pd NWs. A representative XRD pattern (A) of as-prepared unsupported Pd NWs. Overview TEM (B) and SEM (inset) images of as-prepared unsupported Pd NWs. (Reprinted with permission from Ref. 25. Copyright 2011 American Chemical Society)

Hence, a methodology was developed so as to reproducibly immobilize the as-prepared nanostructures onto a conductive carbon support in order to prevent rapid agglomeration upon removal of the surfactant. Conductive carbon supports are ubiquitous in nanostructured catalyst design, since they impart excellent durability to the supported nanostructures, slow Oswald ripening processes under applied potential, and increase the conductivity of the catalyst layer in working fuel cells.[40] In addition, the high degree of dispersion that can be achieved with nanostructures supported on carbon has been previously shown to enhance the mass activity of catalysts.[41] A critical element in the process of supporting nanostructures is the determination of an optimum solvent, *i.e.* chloroform, so as to maximize the dispersibility and uniformity of the catalyst onto the surface of the conductive carbon support. In fact, the as-prepared NWs remained dispersed in chloroform for up to several months, whereas in other solvents, such as water and ethanol for instance, precipitation and agglomeration occurred, essentially overnight. Adsorption onto commercial carbon was achieved by a brief period of sonication with both components mutually dispersed in chloroform followed by centrifugation. Subsequently, the precipitated composites were dispersed into hexanes overnight in order to remove excess surfactant and affix the NWs onto the carbon surface.

Interestingly, the aforementioned hexane wash was critical in achieving sufficient adsorption of the NWs to the carbon. When the hexane washing step was excluded, the NWs desorbed from the surface of the carbon when immersed in solvents such as ethanol, thereby leading to the formation of large NW agglomerates. By contrast, the Pd NW/C composites isolated after immersion in hexanes for 24 h could be re-dispersed in a broad range of solvents with sonication without either any apparent desorption or aggregation of the NWs. We believe the hexane wash essentially “fixes” the Pd NWs onto the carbon substrate by dissolving excess

ODA and contributing to a strengthened interaction between the Pd NWs and the carbon support. The ability for hexane to fix the Pd NWs on the carbon support may arise from the fact that the ODA is soluble in hexane. However, the ODA-capped Pd NWs are not readily dispersible in hexane. Similar results have been achieved in Pd NPs capped with oleylamine, which is an analogous surfactant.[42] Collectively, these results confirm that tuning the polarity of solvents used to purify carbon supported nanostructures is key to achieving homogeneous and uniform distributions of 1D nanostructures on carbon supports.

Once supported, the structure and crystallinity of the Pd NW/C composites were studied by XRD and electron microscopy. The XRD pattern shown in Figure 4.2A of the Pd NW/C revealed that the adsorption process had no effect upon the purity and crystallinity of the sample, since all of the peaks could again be readily indexed to the (111), (200), (220), and (311) reflections, respectively, of the FCC palladium phase. Overview TEM images (Figure 4.2C) of the composites revealed that the NWs largely maintained their wire-like morphology as well as their dimensionality, *e.g.* their ultrathin diameter of approximately 2 nm (2.2 ± 0.5 nm). However, a small percentage (~5 %) of NPs was apparent. The supported wires possessed measurably smaller lengths as compared with as-prepared NWs, with lengths estimated to be only up to 30 nm. Field emission SEM (FESEM, Figure 4.2B) images further confirmed the presence of Pd NWs adsorbed onto the carbon surface and also revealed that a uniform distribution of catalyst could be achieved. The presence of NPs and the observed decrease in NW length could be readily attributed to the effect of the agitation and mechanical strain associated with sonication of the NWs in the presence of the carbon support.

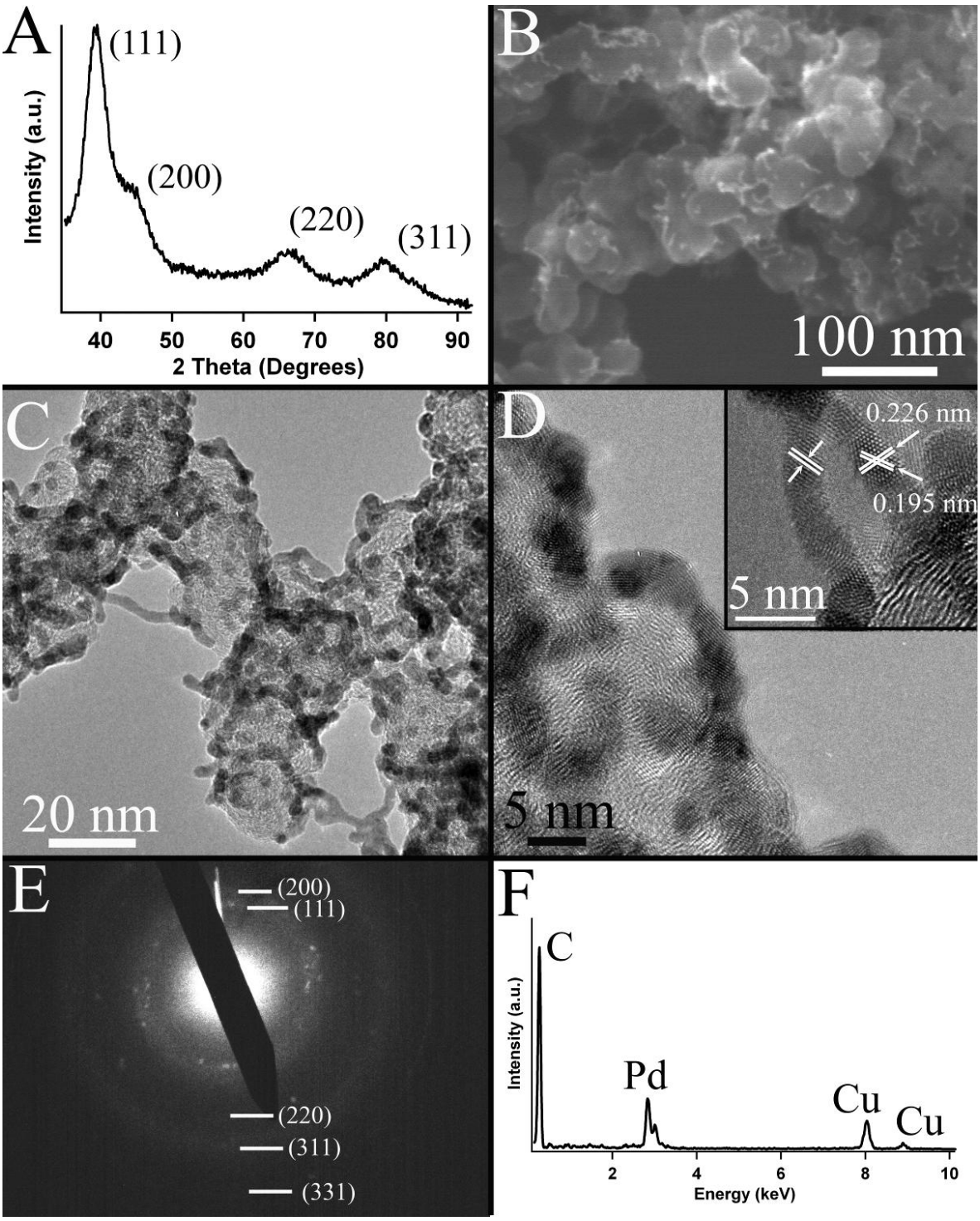

Figure 4.2 Characterization of Pd NW/C composites. Representative experimental powder XRD pattern (A) of as-prepared Pd NW/C composites. Overview FESEM (B) and TEM (C) of as-prepared Pd NW/C composites. A high resolution TEM image of individual Pd NWs is shown as an inset within an image (D) of a representative collection of these NWs. Associated SAED (E) and EDAX (F) patterns of the Pd NW/C composites. (Reprinted with permission from Ref. 25. Copyright 2011 American Chemical Society).

Based upon the HRTEM images shown in Figure 4.2D, the NWs are polycrystalline and are composed of multiple single crystalline segments with lengths of 6 ± 1 nm, that extend along the axis of the NW. The single crystalline segments making up the NWs possess lattice spacings of 0.226 nm and 0.195 nm, consistent with (111) and (200) lattice spacings, respectively. The selected area electron diffraction (SAED) pattern shown in Figure 4.2E highlights the presence of not only continuous rings that can be indexed to palladium's (111), (200), (220), (311), and (331) planes, respectively, but also discrete diffraction spots indicating that the high degree of crystalline substructure observed is representative of the whole ensemble of NWs that contributed to the observed diffraction pattern. The composition of individual NWs was investigated using EDAX (Figure 4.2F) in scanning TEM mode with an electron beam size of 0.2 nm and highlights only the elemental presence of Pd and C, with the Cu peaks emanating from the TEM grid.

4.3.2. Activation of Pd NW/C for Effective Electrocatalysis

The electrochemical performance and surface contamination of as-prepared Pd NW/C composites were initially studied by cyclic voltammetry in order to determine if organic residues were present on the surface of the NWs. Cyclic voltammograms obtained in 0.1 M $HClO_4$ solution (Figure 4.3A) revealed that the surface of the Pd NWs was entirely passivated by residual surfactant, in spite of the ethanol and hexane washes. By comparison with commercial Pd NP/C, the Pd NW/C composites showed an almost complete suppression of the H_{ads} peaks in the region of 0 – 0.35 V, and a delay in the formation of the oxide region to almost 0.9 V, thereby confirming that the active surface sites were not readily accessible to the electrolyte.

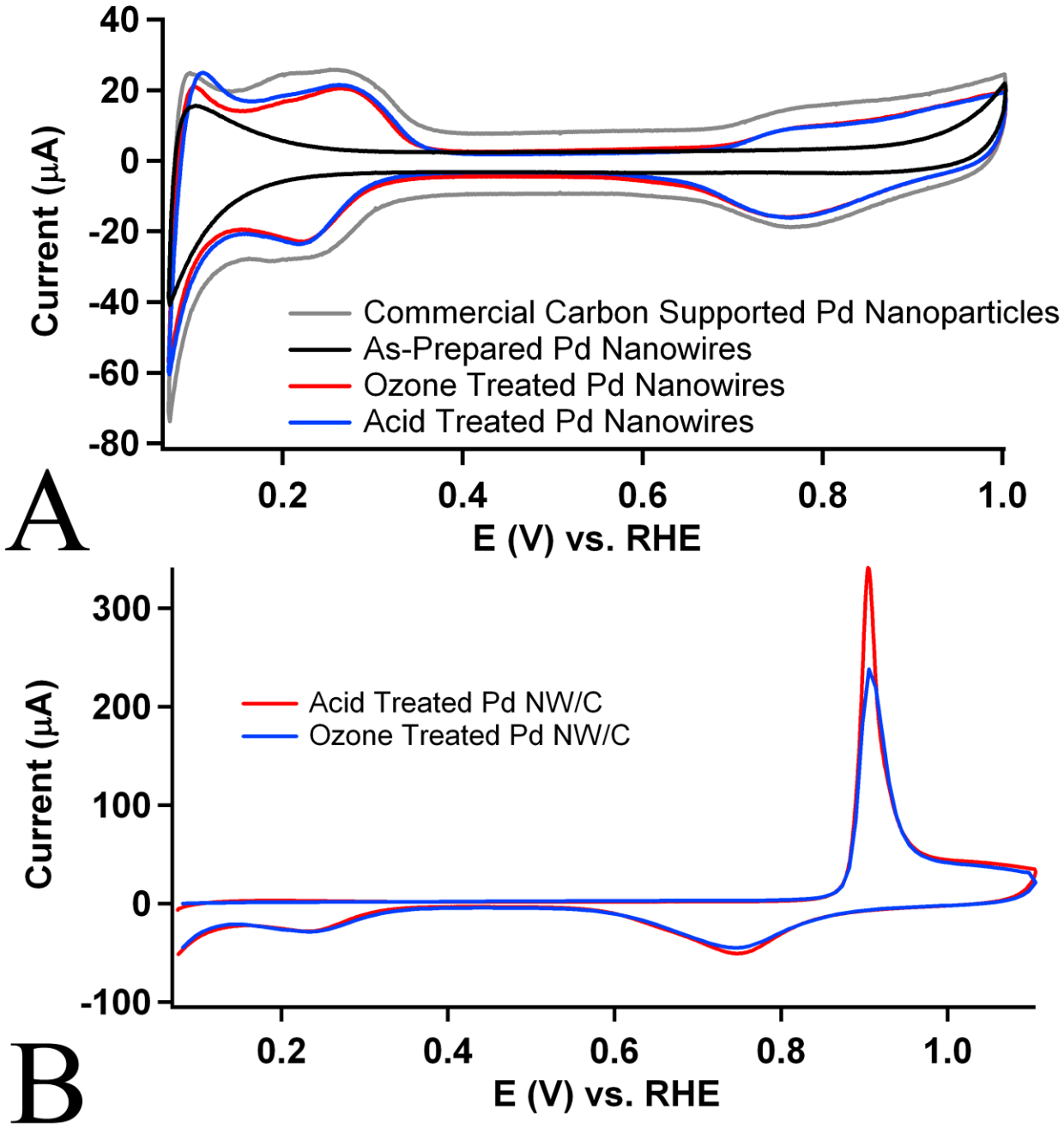

Figure 4.3 Electrochemical properties of ultrathin Pd NW/C before and after selective CO adsorption. Cyclic voltammograms (A) and CO stripping voltammograms (B) obtained from the as-prepared Pd NW/C (black), ozone-treated Pd NW/C (red), and acid-treated Pd NW/C (blue), respectively, by comparison with commercial Pd NP/C catalysts (grey). (Adapted with permission from Ref. 25. Copyright 2011 American Chemical Society)

We utilized a novel two-step method to completely desorb coordinated organic molecules, in order to suitably expose the surface of the Pd NWs.[35] In the first step, the surface of the NW is pretreated by either an acid-wash or by UV generated ozone oxidation to suitably weaken the interaction between the organic impurities and the surface of the nanostructure. In the second step, the organic residues are exchanged by immersing the pre-treated nanostructures into a solution saturated with gaseous CO. The strong interaction of the surface with CO promotes the desorption and exchange of the organic residues with a monolayer of strongly coordinated CO.[43,44] Subsequently, the pristine surfaces of the catalyst can be readily exposed by oxidation of the CO monolayer in a process commonly referred to as CO stripping.

Initially, the as-prepared Pd NW/C composites were supported onto a GCE and selective adsorption of CO was attempted in a CO saturated 0.1 M $HClO_4$ solution under reducing potentials. However, the CO stripping voltammogram showed no peak associated with CO oxidation and the subsequent cyclic voltammogram remained unchanged despite more than 2 h of immersion in the CO saturated solution. The absence of any change in the CV was a clear indication that the residual ODA on the surface sufficiently blocked the adsorption of CO. In this case, the strong adsorption of the amine functional group to the surface of Pd and the inherent hydrophobicity of the alkyl chain present in ODA prevent effective adsorption of CO from the solution. Not surprisingly, a previous study has shown that Pd NPs, when capped with an analogous amine-terminated dendrimer chain, prevented effective heterogeneous catalysis of the Suzuki reaction.[45] By contrast, the Suzuki reaction was not hindered by the presence of other surfactants, such as polyvinyl pyrrolidone (PVP) and certain block co-polymers. Therefore, it is believed that the strong interaction between the terminal amine functionality in ODA and the Pd surface in combination with the strongly hydrophobic end groups of the adsorbed surfactant (i)

blocks the active Pd surface sites and (ii) prevents effective transport of reactants onto the surface of Pd.

On the basis of this initial result, it was evident that additional pre-treatments of the organic capped Pd NW/C composites were necessary in order to activate the selective CO adsorption process. To achieve this objective, we utilized two separate treatment protocols so as to weaken the interaction of the ODA with the surface of the Pd NWs and thereby enhance the selective adsorption of CO. The *first* treatment method involves the use of an acid wash protocol previously utilized for oleylamine-capped Pd NPs[38] that has been suitably optimized in order to maintain the one-dimensional morphology of our as-prepared catalysts. In this report, the Pd NW/C composites are processed in glacial acetic acid for 1 h at elevated temperatures in order to suitably destabilize the interaction between the ODA and the Pd surface. Overview TEM and SEM images of the acid-treated Pd NW/C are shown in Figures 4.4A and 4.4B, respectively. Treated Pd NWs possess a largely one-dimensional morphology and the ultrathin diameter of 2.3 ± 0.5 nm was maintained. However, the rigorous nature of the acid treatment is apparent in both TEM and SEM images, which revealed that the acid contributes to significant aggregation of the NWs into net-like bundles. There is also a concurrent increase in the fraction of NPs present to approximately 10-15%.

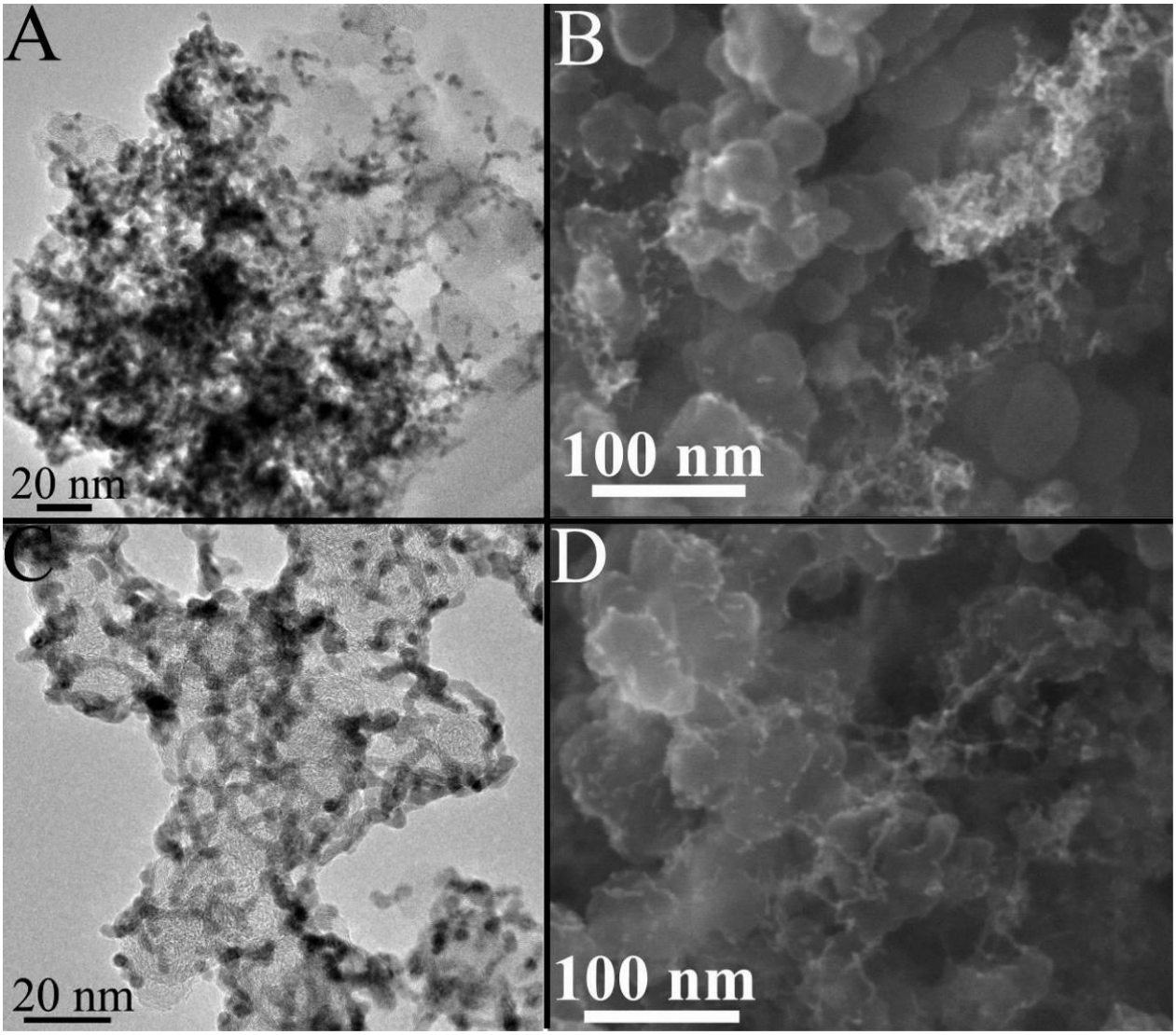

Figure 4.4 Characterization of acid and ozone-treated Pd NW/C. Representative TEM (A and C) and SEM (B and D) images of supported Pd NW/C composites after treatment in acid (A and B) and UV-generated ozone (C and D), respectively. (Reprinted with permission from Ref. 25. Copyright 2011 American Chemical Society)

Cyclic voltammetry (Figure 4.3A) of the acid-treated Pd NW/C obtained after selective CO adsorption followed by CO stripping (Figure 4.3B) displayed both characteristic H_{ads} peaks in the region of 0 to 0.2 V and the onset of oxide formation at ~0.7 V. The strong similarity between the voltammetric response of the acid-treated Pd NW/C composites and that of commercial Pd NP/C confirmed that the surfactant had been successfully removed from the surface. In previous reports, both organic and inorganic acids have been found to weaken the interaction of amine-based surfactants with Pd NPs at pH values of less than 2 by collectively contributing to the protonation of the amine functional group and an increase in the ionic strength of the solution.[38,45] In addition, it is also feasible that heating the catalyst powder in the glacial acetic acid may further facilitate surfactant removal by thermal desorption. Thus, we believe that the suppression of the ODA~Pd interaction by the acid treatment contributes to an enhancement in the selective adsorption of CO and the inevitable displacement of the surfactant.

The *second* treatment involves the time-controlled exposure of the Pd NW/C composites to UV-generated ozone. Recently, UV-ozone has been successfully utilized to remove amine terminated surfactants from both Pt[46] and Au[47] NP monolayers supported on solid substrates. However, there have been a number of mixed results with respect to the effectiveness of UV-ozone for activating capped NPs for use as electrocatalysts.[48-50] In one report, UV-ozone was successfully utilized to remove the residual organic residue present on a monolayer of unsupported FePt NPs deposited onto a gold electrode substrate for the purposes of formic acid oxidation.[51] By contrast, a recent report from Nikles and co-workers suggested that the UV-ozone treatment was not as effective in removing an amine-terminated surfactant, analogous to ODA, from Pt NPs supported onto commercial Vulcan carbon.[49,52]

Rather than utilizing the UV-ozone to entirely oxidize and remove the surfactant, we used a short 15 min UV-ozone treatment herein in order to suitably weaken the interaction between the residual ODA and the surface Pd. Representative overview TEM and SEM images of the Pd NW/C composites after UV-ozone treatment are shown in Figures 4.4C and 4.4D, respectively. By comparison with the electron microscopy data associated with untreated samples (Figure 4.2B – 4.2C), the ozone treatment does not contribute to any significant change in either the morphology or distribution of as-prepared Pd NW/C. Based upon the TEM images, the ozone-treated NWs largely retain the desirable 1D, wire-like morphology. However, there is some fragmentation of the NWs, resulting in the presence of short wire fragments as well as some NPs. Nevertheless, the SEM images of ozone-treated NWs, which show a broader perspective and larger area analyzed, confirm the presence of a majority of long NWs and NW fragments with some NPs present. There is no significant change in the reported ultrathin diameter of 2.2 ± 0.8 nm. By contrast with the acid-treated samples, the ozone-treated samples maintain a high degree of dispersion on the carbon substrate, and there is little appreciable aggregation. Overview SEM images highlight the presence of longer NWs with lengths in excess of 100 nm that are apparent on larger carbon aggregates as well as short wire-like fragments with lengths of 26 ± 11 nm.

After ozone treatment, the Pd NW/C composites were deposited onto a GCE and selective CO adsorption was performed in order to remove the residual surfactant. After CO stripping, cyclic voltammograms (Figure 4.3A) of the Pd NW/C composites showed H_{ads} and oxide formation features that were in excellent agreement with the commercial Pd NPs, thereby confirming that the surfactant was removed. More importantly, the H_{ads} profile of the ozone-treated composites is in excellent agreement with that of the acid-treated composites, which clearly demonstrates that both methods are equally effective at removing the residual surfactant.

In this pre-treatment, the formation of gaseous ozone, *i.e.* a weak oxidizing agent, is thought to oxidize the organic molecules, coating the nanocrystals.[47,51] However, the complete volatilization of long-chain amine-terminated compounds may require up to several hours of exposure and will result in an unwanted oxidation of the nanostructure itself.[46] Thus, we utilized a short treatment time of 15 min to only partially oxidize the carbon chain and more importantly, the terminal amine functional group, so as to weaken the interaction of the ODA surfactant with the surface. Thus, by suitably oxidizing the terminal amine functional group, the interaction between the ODA and the Pd surface can be sufficiently reduced in order to allow for enhanced adsorption of CO to the surface.

Recently, we have also successfully developed a *third* pre-treatment protocol wherein organic impurities on the surface are selectively exchanged simply by immersing the as-synthesized powder in BA. On the basis of our initial electrochemical results, it is evident that the long-chain length of the ODA capping agent herein prevents effective removal of the organic molecules by selective CO adsorption.[25] In this case, we performed a so-called "ligand exchange" process so as to selectively cap the surfaces of the noble metal nanostructures with BA, which is more readily exchanged by selective CO adsorption. The BA is particularly advantageous, since it is inexpensive and is a liquid at room temperature, thereby enabling the pre-treatment to take the form of a simple immersion step without the need for additional solvents or heating. Thus, the BA treatment is amenable to scale up, and is inherently less chemically rigorous, since neither strong oxidizing or acidic conditions are required. After a typical ligand exchange protocol on Pd NW/C, we have demonstrated that the selective CO adsorption (Figure 4.5) can successfully remove the residual BA and the CV data confirm that the Pd active sites are exposed.

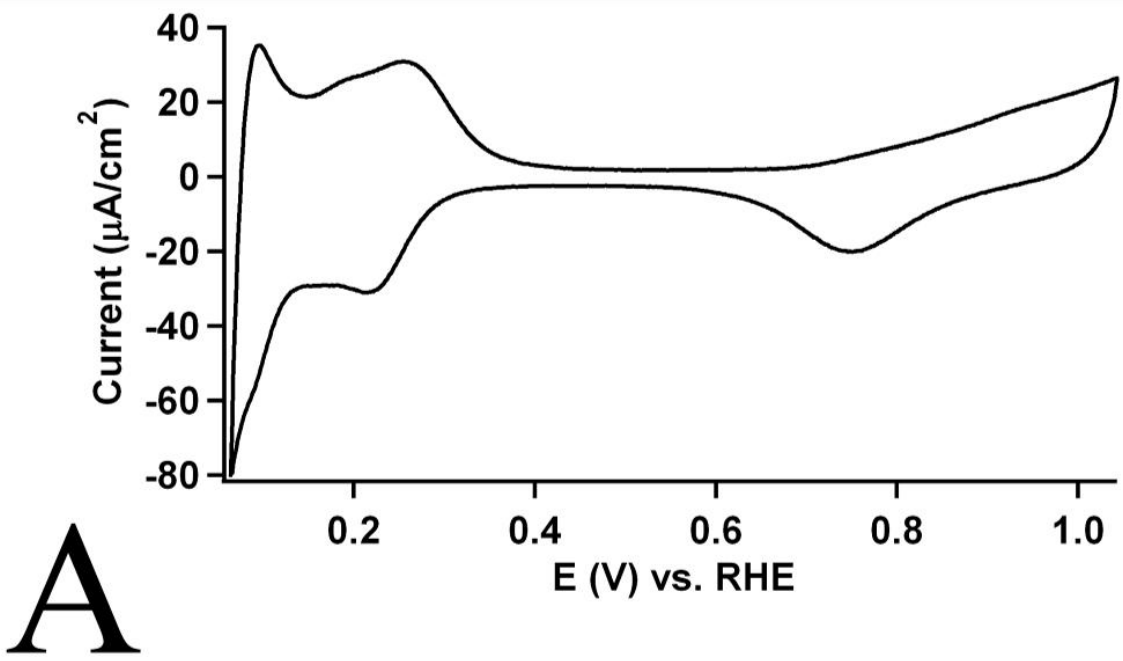

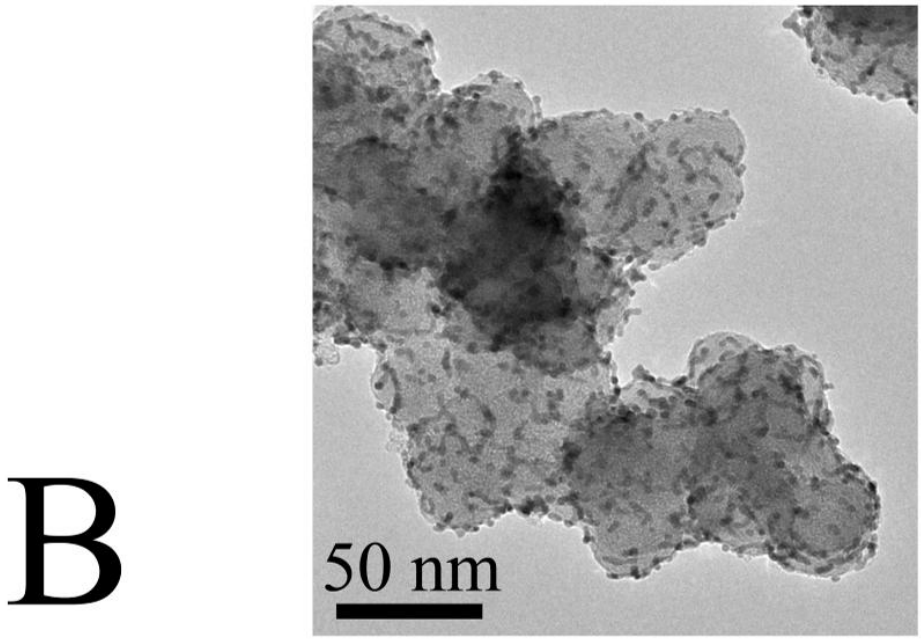

Figure 4.5 Pre-treatment of Pd NW/C by n-butylamine. A representative CV (A) obtained from Pd NW/C after ligand exchange by BA and selective CO adsorption. A TEM image (B) of the Pd NW/C isolated after ligand exchange by BA.

The diversity of pre-treatment protocols demonstrated herein is a crucial step in developing a robust methodology for removing organic capping agents. A critical aspect of these treatment protocols is that the single crystalline segments are maintained despite some fragmentation and aggregation. These single crystalline segments represent the key structural unit of the NWs, since they are expected to possess the most catalytically active surface sites for ORR. The advantages of our completely novel approach to removing organic impurities is apparent when the results are compared with two methods commonly employed in the literature for removing surfactants from noble metal NPs.[53]

For example, heat treatments have become ubiquitous in removing organic impurities and capping agents from spherical NPs by means of either thermal desorption or combustion. Although heat treatments are advantageous in the context of potentially crystallizing the sample, the exposure to high temperature often promotes particle ripening and aggregation, thereby leading to larger particle size and poor homogeneity.[34] Herein, we undertook thermogravimetric analysis (TGA) to systematically design a heat treatment protocol so as to thermally desorb the ODA from the Pd surface. Based upon TGA isotherms, the Pd NW/C powder was heated to 250°C in air or in nitrogen for 1.5 h in order to completely remove the undesired organic residue. Alternatively, it is feasible to remove organic residues electrochemically by cycling the electrode to potentials above the oxidation potential for carbon-containing species. However, the oxidation process is not limited to the organic capping agent, and hence, considerable corrosion of the carbon support and the noble metal nanostructure itself has been observed.[54] In this case, we utilized cyclic voltammetry, wherein the potential was cycled to ~1.65 V vs. RHE, so as to selectively oxidize the amine functional group of the ODA and thereby expose the active catalyst surface.

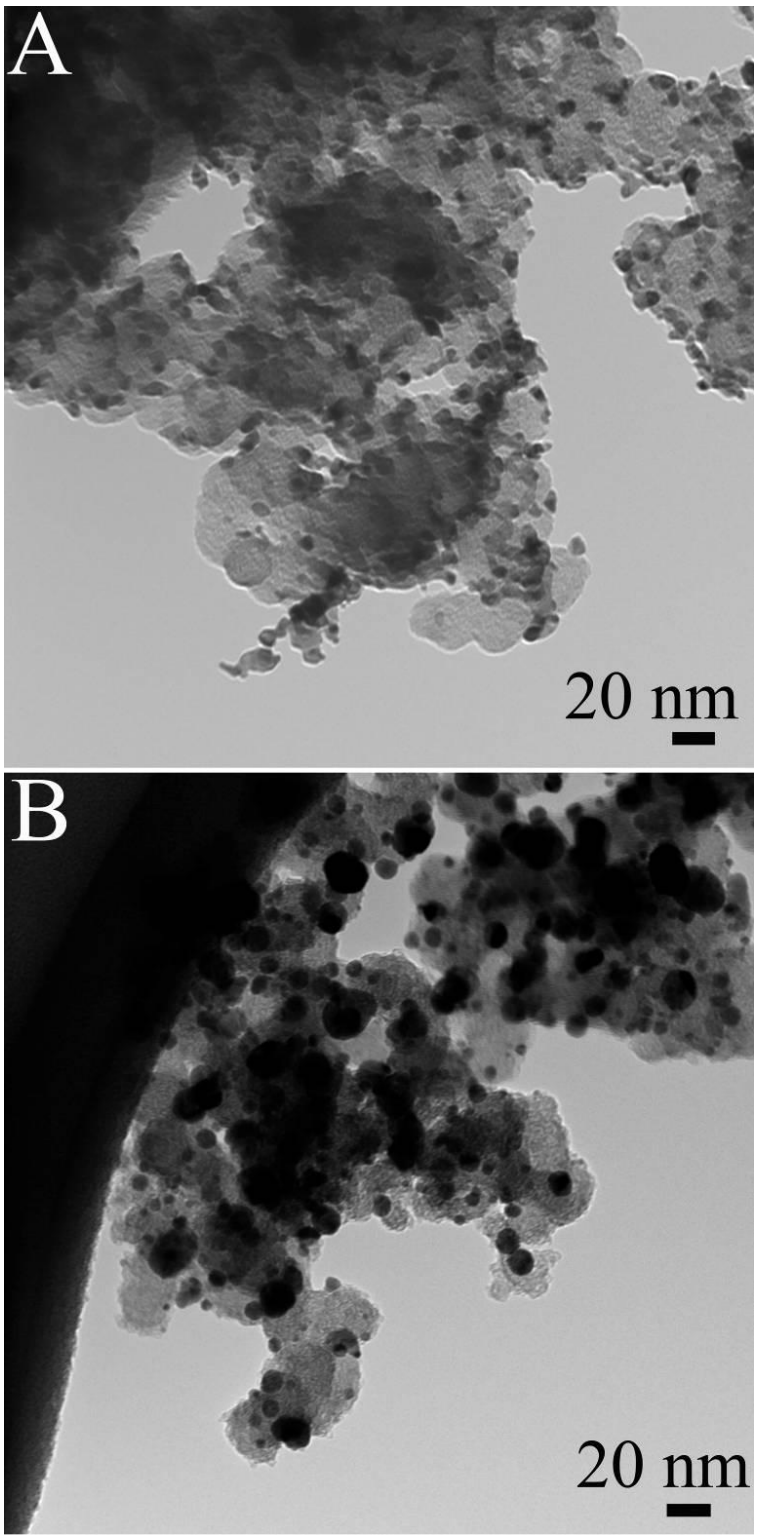

Figure 4.6 Traditional methods for removing organic impurities leads to a loss of the desirable morphology of Pd NW/C. Representative TEM images of the Pd NWs after treatment with high potential cycling (A) and high temperature annealing (B). (Adapted with permission from Ref. 25. Copyright 2011 American Chemical Society)

Not surprisingly, representative TEM images of the products isolated after these two traditional treatment protocols (Figure 4.6) showed complete conversion of the NWs to NP aggregates. Hence, effective protocols conventionally utilized for the activation of nanoparticulate catalysts cannot be blindly applied to 1D catalysts with the expectation of a conservation of morphology. More importantly, this system of methodologies highlights the versatility of selective CO adsorption, wherein undesirable organic residues can be removed without the need for harsh reaction conditions and the potential for deleterious structural reconfiguration.

4.3.3. Structure-Dependent ORR Activity in Pd NW/C Composites

Initially, the ESA of NW and commercial NP catalysts was determined by integration of the CO stripping peak shown in Figure 4.3B. We elected to utilize the CO stripping charge (cf. Chapter 2, Section 5 for additional discussion) in the case of the Pd nanostructures, because it is widely known that the H_{ads} profile is less reliable as a result of measureable hydrogen absorption.[55] Subsequently, the ORR activity for the treated Pd NW samples was measured electrochemically by obtaining polarization curves (Figure 4.7) in an oxygen-saturated 0.1 M $HClO_4$ solution. The measured kinetic currents at 0.8 V were normalized to the ESA (inset to Figure 4.7) so as to probe the intrinsic activity of the catalysts. We have elected to measure the kinetic current at 0.8 V, since the Pd-based catalysts showed almost no activity at 0.9 V. On the basis of this protocol, the ozone-treated Pd NWs displayed a specific activity of 3.62 mA/cm^2, which was approximately 1.4 fold higher as compared with that of acid-treated NWs (2.67 mA/cm^2).

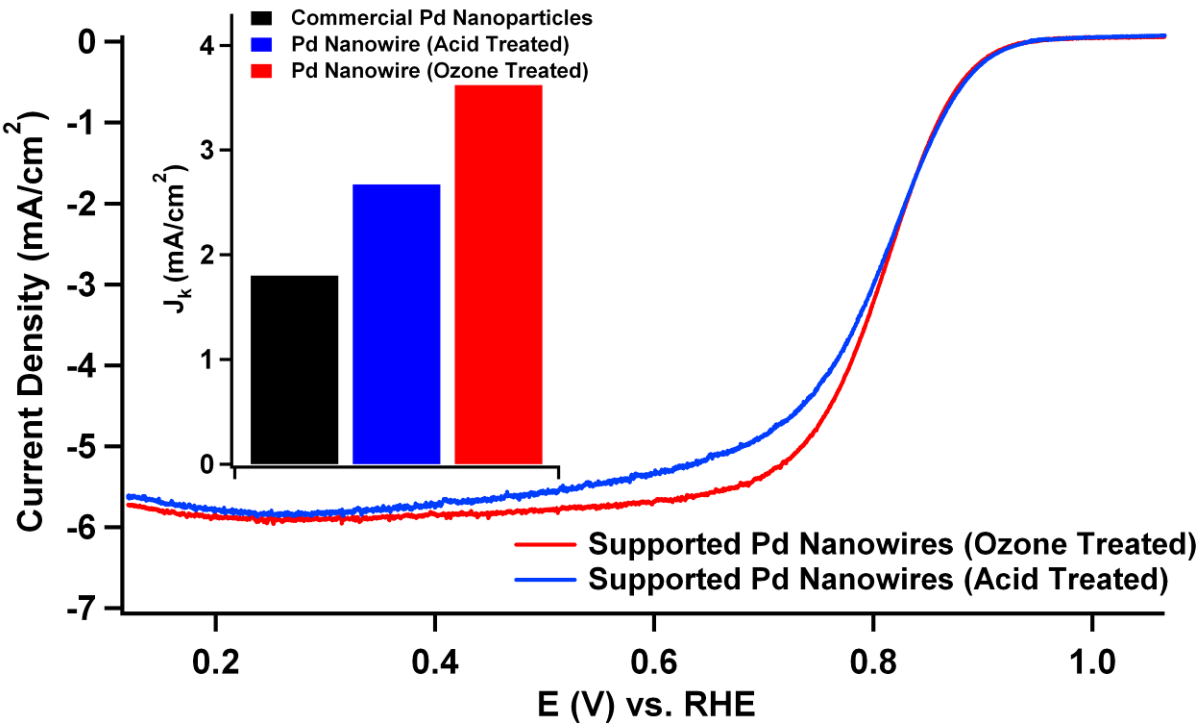

Figure 4.7 Electrocatalytic performance of the treated Pd NW/C composites toward ORR. Polarization curves for treated Pd NW/C samples obtained in 0.1 M $HClO_4$ at 1600 rpm and at 20°C. The specific ORR activities measured at 0.8 V for the treated Pd NW/C are shown as an inset by comparison with commercial Pd NP/C. (Reprinted with permission from Ref. 25. Copyright 2011 American Chemical Society)

The higher activity in the ozone-treated NWs is readily explained by the advantageous nature of the ozone treatment. From a structural perspective, the key structural unit of the Pd NW/C composites is the elongated single crystalline segment that composes the wires. Although both treatment protocols preserve these elongated single crystalline segments, the primary difference is that the ozone-treated NWs maintained (i) an improved dispersion of the wires on the carbon, (ii) less aggregation of the wires during processing, and (iii) the formation of fewer NPs as compared with the acid-treated NWs. As expected, the structure of the polarization curve in the mixed control region (0.65 – 0.85 V) indicates that the ozone-treated NWs maintain an improved dispersion on the carbon and correspondingly less aggregation.[56,57] As we have previously shown, both minimizing aggregation and exfoliating individual ultrathin NWs are key to maximizing the performance of these nanostructures, particularly in the context of ORR.[3] Interestingly, this observed difference in the kinetic current at 0.8 V highlights the importance of treatment protocols, since there is a clear correlation between structure and the resulting activity of the as-generated catalysts.

In addition to observing a treatment-dependent ORR activity, the NWs also showed a structure-dependent enhancement, when the catalytic activity of the NWs was compared with that of commercial Pd NP/C. In fact, the ozone and acid-treated Pd NW/C samples showed a greater than 2 fold and 1.5 fold higher specific activities, respectively, as compared with the activity of commercial Pd NP/C composites alone (1.8 mA/cm^2). The 1D nanostructures displayed significantly enhanced activities, which can be attributed in part to their anisotropic structure. The observed electrochemical enhancement in the Pd NW/C samples, especially when compared with the commercial Pd NP/C samples, is consistent with the results of our group (*i.e.* ultrathin Pt NWs) and others.[2,3,14,25]

Although there is some debate in the literature,[14] analysis of ORR activity on Pd single crystals[58] and well-defined Pd nanocubes[59] has shown that the Pd (100) facet is significantly more active than the Pd (111) facet. Recently for example, Abruña and co-workers have provided further evidence through a combinatorial approach that the adsorption of oxygen on the Pd (100) facet is actually considerably weaker than on the corresponding Pd (111), which is expected to facilitate increased ORR kinetics.[14] Consistent with this assertion, the Pd NW/C NWs are analogous to our platinum NWs in so far as they are selectively synthesized with ODA,[37] a basic, amine-terminated surfactant.[25] It has been previously observed that the use of basic amine-terminated surfactants results in the preferential growth along the <111> crystallographic direction as a result of selective adsorption to the (100) facets.[60] Hence, the significantly enhanced activity of our ultrathin Pd NWs is understandable, since commercial Pd NPs predominantly display the less active Pd (111) facets.[59]

In addition, the CV data observed from the treated Pd NW/C composites also highlight the potential for fewer defect sites and low coordination atoms (LCAs). Specifically, the H_{ads} profile of the Pd NW/C composites in Figure 4.3A is unique especially when compared with that of the Pd NP/C catalyst. Specifically, the CV of the Pd NP/C displays two broad peaks centered at approximately 0.27 and 0.20 V in the anodic sweep segment, respectively, whereas the Pd NW/C CV shows only a single peak centered at 0.27 V with a corresponding shoulder at 0.20 V. The presence of fewer peaks in the H_{ads} region may suggest a more uniform surface. However, it is very difficult to evaluate the H_{ads} profile in nanostructured palladium, since hydrogen adsorption is overshadowed by hydrogen absorption on well-defined Pd single crystals. Despite this challenge, we believe that the Pd NW/C nanostructures possess more uniform defect-free surfaces, thereby resulting in a suppression of the cathodic overpotential and a corresponding

increase in the ORR activity, an assertion which is based on previous results from analogous ultrathin Pt NWs and the corresponding analysis of our Pd NW/C composites. Although it is beyond the scope of this study, further exploration of the origin of this enhancement is necessary to fully understand the activity of these composites. Nonetheless, the observed structure-dependent enhancement confirms that the ultrathin Pd NWs should represent a superior substrate for Pt_{ML} deposition.

4.3.4. Structure-Dependent ORR Activity in Pt_{ML}~Pd NW Shell Composites

The deposition of a Pt_{ML} onto the surface of the treated Pd NW/C composites was achieved by Cu UPD followed by galvanic displacement of the Cu ad-atoms with Pt^{2+}. Given the extensive prior characterization of Pt_{ML} core-shell structures, we confirmed the quality of the Pt_{ML} by electrochemical means. Specifically, cyclic voltammetry of the resulting Pt_{ML} shell ~ Pd NW/C core (Pt_{ML}~Pd NW/C) (Figure 4.8A) showed (i) a H_{ads} region that was consistent with the deposition of Pt and (ii) a delay in the onset of the surface oxide feature to higher potentials, when compared with the Pd NW/C. These results are in excellent agreement with those from previous reports of Pt_{ML} deposited onto Pd single crystals[18] and more importantly, both elemental[20] and alloyed[19,22] palladium NPs. It is important to highlight that the Cu UPD charge is in excellent agreement with the H_{ads} charge obtained after Pt_{ML} deposition, thereby confirming the near monolayer deposition of Pt.

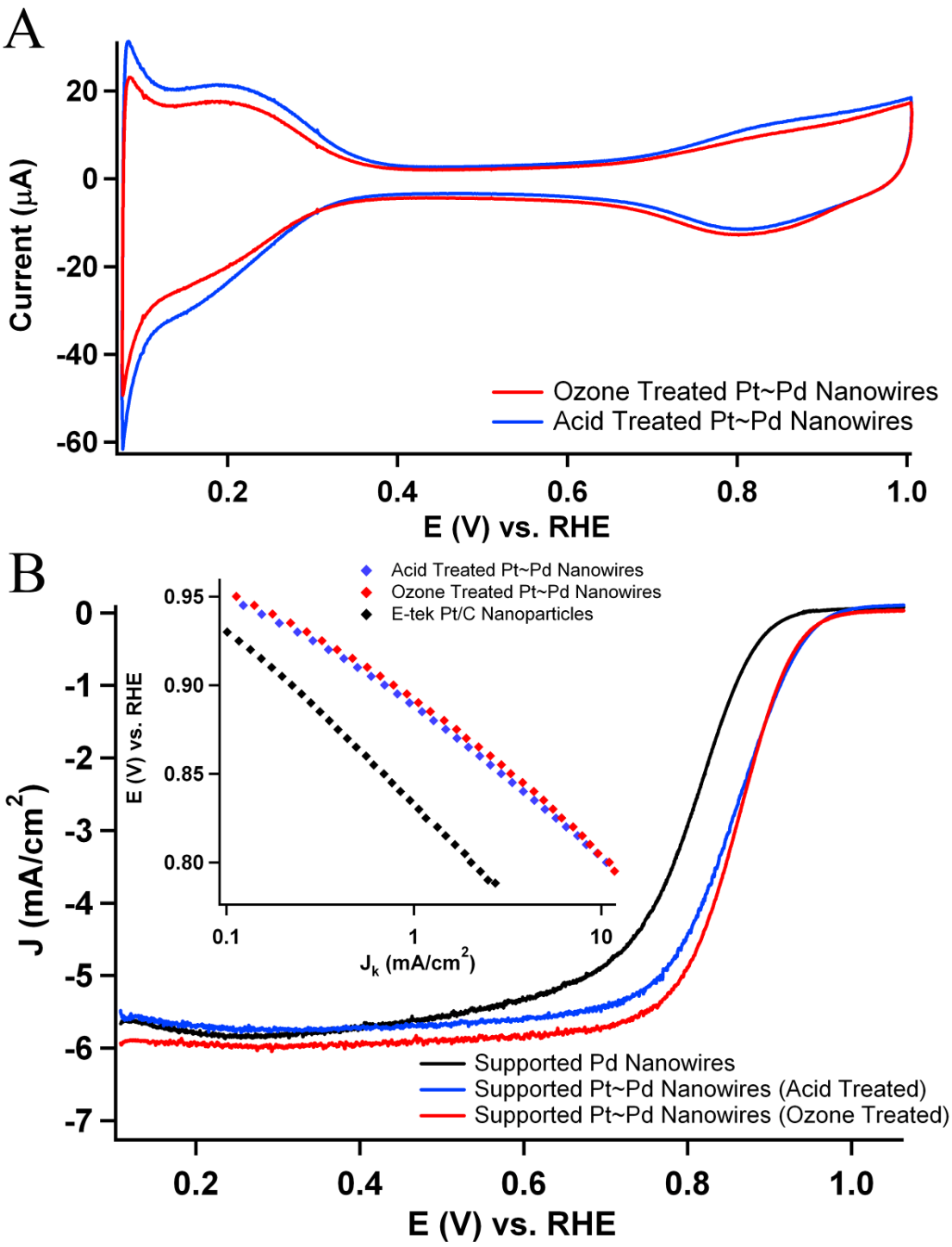

Figure 4.8 Electrocatalytic performance of the Pt_{ML}~Pd NW/C composites toward ORR. Cyclic voltammograms (A) obtained from the ozone and acid-treated Pt_{ML}~Pd NW/C core-shell NWs, after Pt_{ML} deposition. The polarization curves (B) for the treated Pt_{ML}~Pd NW/C composites are shown in comparison with the Pd NW/C. Also highlighted are *E* vs. J_K plots of the treated Pt_{ML}~Pd NW/C composites by comparison with commercial Pt NP/C as an inset. (Reprinted with permission from Ref. 25. Copyright 2011 American Chemical Society)

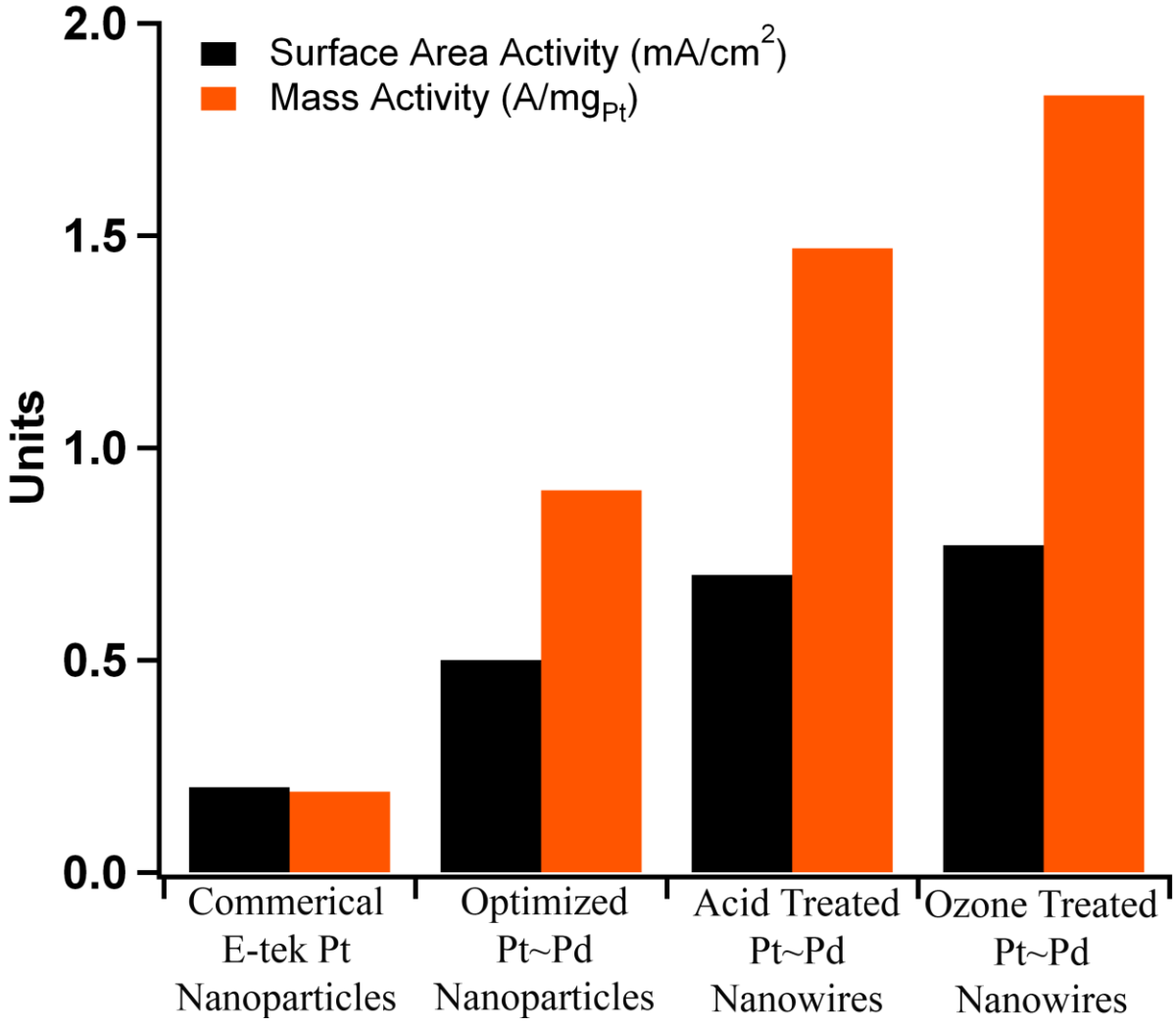

Figure 4.9 The ORR activities normalized to ESA (mA/cm^2) and to Pt mass (A/mg_{Pt}) at 0.9 V for the Pt_{ML}~Pd NW/C samples. Also shown are the activities for commercial Pt NP/C determined experimentally as well as analogous, optimized core-shell Pt_{ML}~Pd NP/C from a prior report.[22] (Reprinted with permission from Ref 25. Copyright 2011 American Chemical Society)

The ORR activity of the Pt_{ML}~Pd NW/C composites was measured electrochemically by obtaining polarization curves in oxygen-saturated 0.1 M $HClO_4$ (Figure 4.8B) solution. The Pt_{ML}~Pd NW/C composites displayed a positive shift of ~75 mV in the half wave potential and dramatically enhanced ORR activity as compared with the Pd NW/C catalyst before Cu UPD, which is shown in Figure 4.8B for clarity. This observation further confirms the successful deposition of a Pt_{ML} atop the Pd NW substrate. In order to probe the intrinsic activity of the core-shell NWs, the measured kinetic currents at 0.9 V were normalized to the measured ESA. Similarly, the platinum mass activity was deduced by normalizing the measured kinetic current to the mass of Pt deposited, which can be readily extracted from the integrated Cu UPD charge.

The area and mass-specific activities of the treated core-shell NWs are summarized in Figure 4.9 by comparison with commercial Pt NP/C and optimized Pt_{ML}~Pd core-shell NP/C[22] prepared analogously. The ozone-treated NWs maintained outstanding area specific and Pt mass specific activities of 0.77 mA/cm^2 and 1.83 A/mg_{Pt}, respectively. By comparison, the acid-treated NWs also evinced high area and mass specific activities of 0.70 mA/cm^2 and 1.47 A/mg_{Pt}, which were, however, noticeably lower in magnitude as compared with that of ozone-treated NWs. The structure of the polarization curve in the mixed control region again indicates that the ozone-treated NWs maintain an improved dispersion on the carbon as well as the presence of less aggregation. This observation readily explains the significant difference in mass specific activity, which is dependent upon the dispersion of the catalyst and the degree of aggregation. Since there is little difference in the area-specific activity, it is evident that the UV-ozone pre-treatment promotes enhanced performance by minimizing aggregation of the Pd NWs on the carbon surface.[10]

Nonetheless, both core-shell NW systems maintain dramatically enhanced activities when compared with 0D commercial Pt NP/C and optimized Pt_{ML}~Pd NP/C. Although the as-obtained activities greatly exceed the mass activity target of 0.44 A/mg_{Pt} projected for 2015 by the DOE, further testing under MEA conditions (*c.f.* Chapter 7) is required in order to fully understand the potential of these catalysts.[17] Specifically, care must be taken when comparing the values obtained herein and the reported targets, since RDE methods yield comparable but not necessarily identical activity results to those acquired under actual MEA conditions. To highlight the outstanding activity of the core-shell NWs, a plot of the kinetic current vs. the potential or so-called E vs. J_K plot (inset to Figure 4.8B) demonstrably reveals that the core-shell NWs maintain higher kinetic currents over the entire range of operating potentials as compared with commercial Pt NP/C.

Surprisingly, the NWs display a distinctive structure-dependent enhancement as compared with analogous core-shell Pt_{ML}~Pd NP/C.[22] Specifically, the ozone and acid-treated core-shell NW systems display enhancements in area-specific activity of 1.54 and 1.40 fold, respectively, as well as enhancements in Pt mass-specific activity of 2.03 and 1.60 fold, respectively. Given that palladium is also considered to be a platinum group metal (PGM), the mass activity can also be reported with respect to the total PGM loading, as determined by TGA. The PGM mass activity for the ozone-treated and acid-treated Pt_{ML}~Pd NW/C samples were determined to be 0.55 A/mg_{PGM} and 0.32 A/mg_{PGM}, respectively. Both of these represent a true enhancement especially when compared with the PGM mass activity values of 0.25 A/mg_{PGM} and 0.19 A/mg_{PGM} obtained for the analogous optimized core-shell Pt_{ML}~Pd NP/C and commercial Pt NP/C, respectively.

On the basis of our results obtained with elemental Pt NWs, the enhanced performance in this case likely emerges from the structural interaction between the Pd NW core and the Pt_{ML} shell. The contraction of the surfaces of noble metal NWs particularly consisting of Pt and Pd has been observed experimentally[31] and is predicted theoretically.[28,62] Therefore, ultrathin Pd NW/C represent an ideal core material by comparison with Pd NP/C since surface contractions of the NW should increase the strain induced upon the Pt_{ML} shell, thereby leading to a further weakening of the interaction with oxygen adsorbates and improved ORR kinetics in this 1D system.[10,22,23] This same effect has been achieved in Pd NPs alloyed with certain third-row transition metals and recently, in more elegant transition metal core – noble metal shell NPs, wherein the surface of the Pd is contracted by the presence of transition metals with smaller atomic radii.[19,61-64] However, the incorporation of less noble transition metals can lead to an inevitable increase in corrosion processes under operating conditions, which can compromise the durability of these nanostructures for long-term use in fuel cells.[7]

Thus, we believe that the properties of ultrathin NWs can allow for the enhancement of Pt_{ML} activity by increased strain-induced effects without the need for additional third row transition metal dopants and without potentially compromising the durability of the resulting core-shell composite. It is also conceivable that the unique electronic properties of ultrathin noble metal NWs, such as the lower weighted *d*-band center measured in ultrathin Pt NWs by comparison with Pt NP/C, may play a key role in modifying the Pt_{ML}'s electronic properties for enhanced performance. Collectively, it is evident from the activity results that ultrathin Pd NWs provide for a better core material than corresponding Pd NP/C, which demonstrates that the universal morphology-dependent enhancement observed can be generalized to core-shell motifs, as well.

4.3.5. Accelerated Durability Testing of Pt_{ML}~Pd NW/C Composites

The electrochemical durability of the ozone-treated Pt_{ML}~Pd NW/C composites was studied under half-cell conditions. In this report, we have elected to apply an accelerated durability test outlined by the DOE for catalysts under MEA conditions.[17] Specifically, the potential was cycled between 0.6 and 1.0 V so as to bracket the relevant potential region wherein ORR can feasibly occur in a working fuel cell. The electrode was immersed in naturally aerated 0.1 M $HClO_4$ solution. Although half-cell conditions provide a useful method for studying the durability of catalysts, we highlight that care must be taken when comparing these results to those obtained under actual MEA conditions. Hence, identical experiments were performed on high performance (HP) Pt NP/C catalysts supported on carbon, which are the most commonly utilized catalysts associated with commercial fuel cells, for the purposes of comparison. Based upon this protocol, the measured surface area and the activity normalized to the mass of Pt deposited on the electrode by Cu UPD could be independently probed by obtaining cyclic voltammograms (Figure 4.10A & 4.10B) and polarization curves (Figure 4.10C & 4.10D), respectively, over the course of an accelerated test (30,000 cycles). The trend in surface area and Pt mass activity is summarized over the course of the test (Figure 4.10E & 4.10F) as a function of the measured value measured after cycling with respect to the initial value before the durability test.

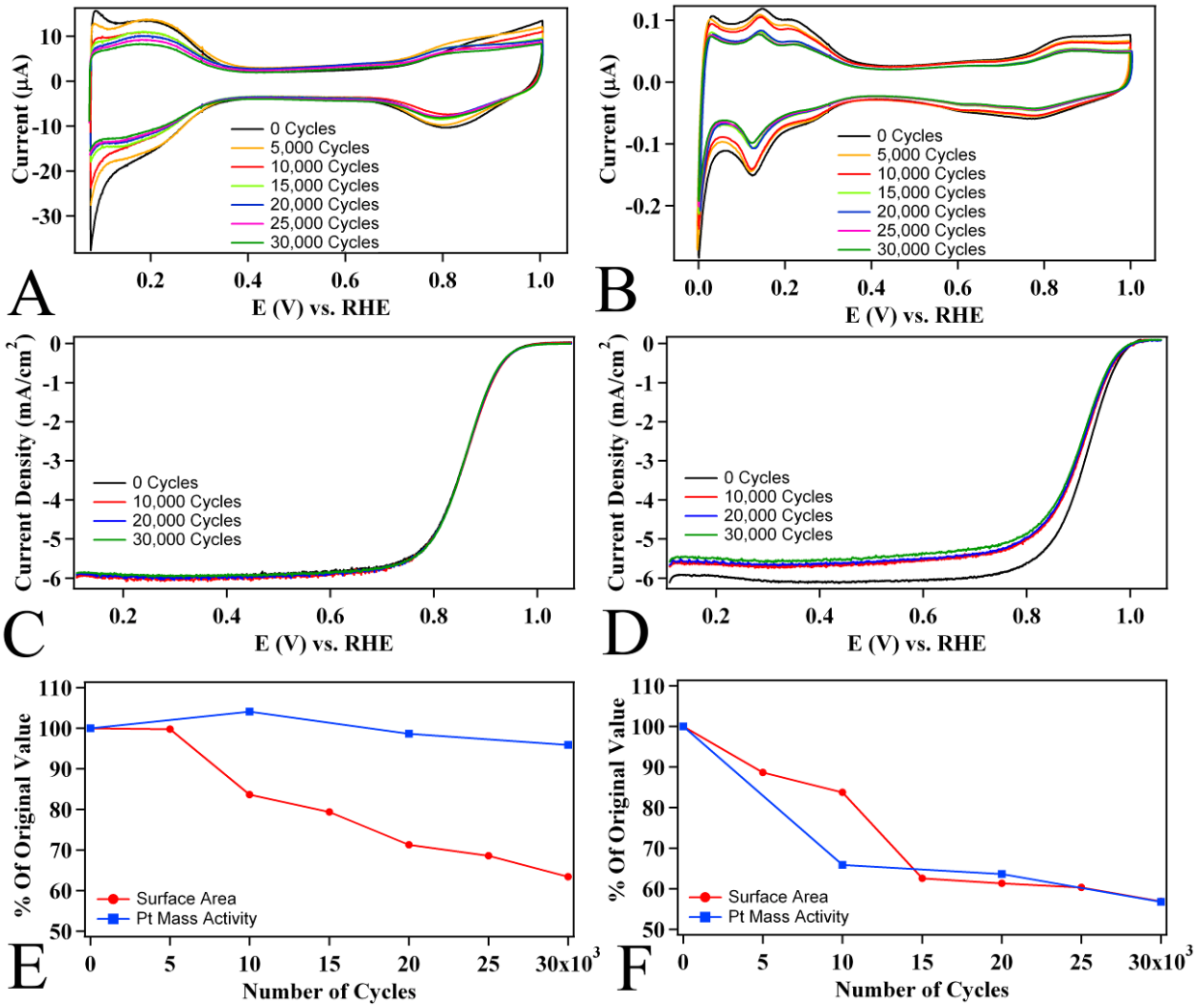

Figure 4.10 Accelerated durability test of the Pt_{ML}~Pd NW/C composites in comparison with Pt NP/C. Cyclic voltammograms (A & B) and polarization curves (C & D) obtained at 5,000 and 10,000 cycle intervals, respectively from Pt_{ML}~Pd NW/C (A & C) and Pt NP/C (B & D) over the course of a 30,000 cycle durability test. The Pt mass activity and surface area are shown over the course of the test relative to the value obtained prior to durability testing (*i.e.* percent of original value) for the Pt_{ML}~Pd NW/C (E) and HP Pt NP/C (F), respectively. (Adapted with permission from Ref 25. Copyright 2011 American Chemical Society)

In terms of the surface area, the ozone-treated Pt_{ML}~Pd NW/C composites and the Pt NP/C maintained ~60% of their initial measured ESA. As expected, the ESA of the Pt NP/C catalysts rapidly decreases to ~60% over the first 15,000 cycles, inevitably reaching a steady state. The rapid decline in ESA observed with NP catalysts can be attributed to the agglomeration, dissolution, and ripening of the NPs under operating potentials.[54] However, the core-shell NWs displayed a more linear decline in the ESA, and by 15,000 cycles, our NWs still retained more than 80% of their original ESA. The steady decline in ESA in Pt_{ML}~Pd NW core-shell catalysts has been attributed to the preferential dissolution of Pd from the catalyst core and represents supporting proof that the NW morphology does not undergo either significant aggregation or ripening.[65] To demonstrate this point, TEM images of ozone-treated Pt_{ML}~Pd NW samples were obtained after 30,000 cycles.[25] As expected, the long NWs were shown to have been converted largely into wire fragments with lengths that are commensurate with the single crystalline segments present in the initial long NWs. Based upon the fragmentation pattern of the NWs, the loss of ESA can be attributed largely to the preferential dissolution of the NWs at the interconnects between the single crystalline segments and to the concomitant formation of some NPs.

In addition to monitoring the ESA, the Pt mass activity of the ozone-treated Pt_{ML}~Pd NW/C composites and Pt NP/C was also studied over the course of a catalyst lifetime. Interestingly, there is no substantial change either in the half wave potential (*i.e.* 3 mV loss after 30,000 cycles) or in the diffusion controlled current of the polarization curve even after 30,000 cycles, which suggests that there is no overall loss in activity from the electrode. Therefore, there is essentially no loss in the Pt mass activity (Figure 4.10E) over the course of the test, which is an exciting and promising result. By contrast, the Pt mass activity of the commercial HP Pt NP/C

(Figure 4.10F) declines by almost 40% over the course of the test, consistent with the significant decline in the half wave potential of 15 mV and an associated decrease in the diffusion controlled current. Hence, as-prepared core-shell NW catalysts maintain far superior durability in terms of both resistance to surface area loss and more importantly, activity loss when compared with commercial Pt NP/C catalysts. In essence, we have demonstrated that the Pt_{ML}~Pd NP/C have the potential to be far more cost-effective over their lifetime as compared with analogous Pt NP/C

4.4 Conclusions

In this report, we have synthesized crystalline Pd NWs with a diameter of 2.0 ± 0.5 nm and reliably supported them onto carbon with a highly uniform catalyst distribution. As-prepared NWs were treated with UV-generated ozone, glacial acetic acid, or butylamine, followed by selective CO adsorption in order to remove the residual, undesirable organic residue. Based upon electron microscopy and electrochemical measurements, it was determined from the ozone treatment results that the Pd NW/C system possesses higher activity and durability as compared with acid- treated NWs, an observation attributable to the retention of morphology and dispersion upon ozone treatment. After activation, the structure-dependent activity of the Pd NW/C composites was studied by comparison with commercial Pd NP/C; it was found that the ozone-treated NWs maintained an enhanced area-specific activity that was more than double that of the commercial NPs. Subsequently, the desired Pt_{ML} shell ~ Pd NW/C core motif was achieved by Cu UPD followed by galvanic displacement of the Cu ad-atoms with Pt^{2+} and the resulting deposition process was confirmed by both cyclic voltammetry and ORR activity data.

The surface area and mass activity of the acid and ozone-treated NWs were explored with respect to commercial Pt NP/C and optimized core-shell Pt_{ML}~Pd NP/C. Ozone-treated NWs were found to maintain outstanding specific, Pt mass, and PGM mass activities of 0.77 mA/cm^2, 1.83 A/mg_{Pt} and 0.55 A/mg_{PGM}, respectively, which were significantly enhanced as compared with commercial Pt NP/C, Pt_{ML}~Pd NP/C, and acid-treated Pd NW/C. Ozone-treated NWs also maintained excellent electrochemical durability under accelerated half-cell testing, and it was found that there was no decline in the activity with respect to the initial Pt mass over the course of a simulated catalyst lifetime. Collectively, these results point towards ultrathin Pd NWs as excellent support materials for Pt_{ML}, particularly when the activity results are considered in relation to the proposed 2015 activity target outlays set by the U.S. DOE.

4.5 References

(1) Koenigsmann, C.; Scofield, M. E.; Liu, H.; Wong, S. S. *J. Phys. Chem. Lett.* **2012**, *3*, 3385-3398.
(2) Koenigsmann, C.; Wong, S. S. *Energy Environ. Sci.* **2011**, *4*, 1161 - 1176.
(3) Koenigsmann, C.; Zhou, W.-p.; Adzic, R. R.; Sutter, E.; Wong, S. S. *Nano Lett.* **2010**, *10*, 2806-2811.
(4) *Monthly Average Commercial Price of Platinum*, Johnson & Matthey, February 2013.
(5) *Platinum Availability and Economics for PEMFC Commercialization*, Tiax LLC & United States Department of Energy, 2003.
(6) Morozan, A.; Jousselme, B.; Palacin, S. *Energy Environ. Sci.* **2011**, *4*, 1238-1254.
(7) Antolini, E. *Energy Environ. Sci.* **2009**, *2*, 915-931.
(8) Antolini, E.; Perez, J. *J. Mater. Sci.* **2011**, *46*, 1-23.
(9) *Monthly Average Commercial Price of Palladium*, Johnson & Matthey, February 2013.
(10) Adzic, R.; Zhang, J.; Sasaki, K.; Vukmirovic, M.; Shao, M.; Wang, J.; Nilekar, A.; Mavrikakis, M.; Valerio, J.; Uribe, F. *Top. Catal.* **2007**, *46*, 249-262.
(11) Wang, X.; Kariuki, N.; Vaughey, J. T.; Goodpaster, J.; Kumar, R.; Myers, D. J. *J. Electrochem. Soc.* **2008**, *155*, B602-B609.
(12) Xu, C.; Zhang, Y.; Wang, L.; Xu, L.; Bian, X.; Ma, H.; Ding, Y. *Chem. Mater.* **2009**, *21*, 3110-3116.
(13) Li, B.; Greeley, J.; Prakash, J. *ECS Transactions* **2009**, *19*, 109-116.
(14) Xiao, L.; Zhuang, L.; Liu, Y.; Lu, J.; Abruña, H. c. D. *J. Am. Chem. Soc.* **2008**, *131*, 602-608.
(15) Chen, Z.; Waje, M.; Li, W.; Yan, Y. *Angew. Chem. Int. Ed.* **2007**, *46*, 4060-4063.

(16) Lim, B.; Jiang, M.; Camargo, P. H. C.; Cho, E. C.; Tao, J.; Lu, X.; Zhu, Y.; Xia, Y. *Science* **2009**, *324*, 1302-1305.
(17) *Multi-Year Research, Development and Demonstration Plan: Planned Program Activities for 2005-2015*, Department of Energy, 2009.
(18) Zhang, J.; Vukmirovic, M. B.; Xu, Y.; Mavrikakis, M.; Adzic, R. R. *Angew. Chem. Int. Ed.* **2005**, *44*, 2132-2135.
(19) Zhang, J.; Lima, F. H. B.; Shao, M. H.; Sasaki, K.; Wang, J. X.; Hanson, J.; Adzic, R. R. *J. Phys. Chem. B* **2005**, *109*, 22701-22704.
(20) Zhang, J.; Mo, Y.; Vukmirovic, M. B.; Klie, R.; Sasaki, K.; Adzic, R. R. *J. Phys. Chem. B* **2004**, *108*, 10955-10964.
(21) Brankovic, S. R.; Wang, J. X.; Adzic, R. R. *Surf. Sci.* **2001**, *474*, L173-L179.
(22) Wang, J. X.; Inada, H.; Wu, L.; Zhu, Y.; Choi, Y.; Liu, P.; Zhou, W.-P.; Adzic, R. R. *J. Am. Chem. Soc.* **2009**, *131*, 17298-17302.
(23) Rossmeisl, J.; Nørskov, J. K. *Surf. Sci.* **2008**, *602*, 2337-2338.
(24) Greeley, J.; Nørskov, J. K. *J. Phys. Chem. C* **2009**, *113*, 4932-4939.
(25) Koenigsmann, C.; Santulli, A. C.; Gong, K.; Vukmirovic, M. B.; Zhou, W.-p.; Sutter, E.; Wong, S. S.; Adzic, R. R. *J. Am. Chem. Soc.* **2011**, *133*, 9783-9795.
(26) Fiorentini, V.; Methfessel, M.; Scheffler, M. *Phys. Rev. Lett.* **1993**, *71*, 1051-1054.
(27) Gibbs, D.; Ocko, B. M.; Zehner, D. M.; Mochrie, S. G. J. *Phys. Rev. B: Condens. Matter* **1988**, *38*, 7303.
(28) Haftel, M. I.; Gall, K. *Phys. Rev. B: Condens. Matter* **2006**, *74*, 035420-035412.
(29) Hansen, H. A.; Rossmeisl, J.; Nørskov, J. K. *PCCP* **2008**, *10*, 3722-3730.
(30) Kondo, Y.; Takayanagi, K. *Phys. Rev. Lett.* **1997**, *79*, 3455.
(31) Kondo, Y.; Takayanagi, K. *Science* **2000**, *289*, 606-608.
(32) van Beurden, P.; Kramer, G. J. *J. Chem. Phys.* **2004**, *121*, 2317-2325.
(33) Koenigsmann, C.; Santulli, A. C.; Sutter, E.; Wong, S. S. *ACS Nano* **2011**, *5*, 7471-7487.
(34) Tiano, A. L.; Koenigsmann, C.; Santulli, A. C.; Wong, S. S. *Chem. Commun.* **2010**, *46*, 8093-8130.
(35) Adzic, R. R.; Gong, K.; Cai, Y.; Wong, S. S.; Koenigsmann, C. Method for Removing Strongly Adsorbed Surfactants and Capping Agents from Metal to Facilitate their Catalytic Applications.U.S. Patent Application 20130178357, 2013.
(36) Xia, Y.; Yang, P.; Sun, Y.; Wu, Y.; Mayers, B.; Gates, G.; Yin, Y.; Kim, F.; Yan, H. *Adv. Mater.* **2003**, *15*, 353-389.
(37) Teng, X.; Han, W.; Ku, W.; Hucker, M. *Angew. Chem. Int. Ed.* **2008**, *47*, 2055-2058.
(38) Mazumder, V.; Sun, S. *J. Am. Chem. Soc.* **2009**, *131*, 4588-4589.
(39) Dean, J. A. *Lange's Handbook of Chemistry*; 14th ed.; MacGraw Hill: New York, NY, 1992.
(40) Yu, X.; Ye, S. *J. Power Sources* **2007**, *172*, 133-144.
(41) Dicks, A. L. *J. Power Sources* **2006**, *156*, 128-141.
(42) Wang, C.; Daimon, H.; Onodera, T.; Koda, T.; Sun, S. *Angew. Chem. Int. Ed.* **2008**, *47*, 3588-3591.
(43) Gonzalez, S.; Illas, F. *Surf. Sci.* **2005**, *598*, 144-155.
(44) Kato, H. S.; Okuyama, H.; Yoshinobu, J.; Kawai, M. *Surf. Sci.* **2002**, *513*, 239-248.
(45) Li, Y.; El-Sayed, M. A. *J. Phys. Chem. B* **2001**, *105*, 8938-8943.
(46) Aliaga, C.; Park, J. Y.; Yamada, Y.; Lee, H. S.; Tsung, C.-K.; Yang, P.; Somorjai, G. A. *J. Phys. Chem. C* **2009**, *113*, 6150-6155.

(47) Pang, S.; Kurosawa, Y.; Kondo, T.; Kawai, T. *Chem. Lett.* **2005**, *34*, 544-545.
(48) Tanuma, T.; Terazono, S. *J. Power Sources* **2008**, *181*, 287-291.
(49) Prabhuram, J.; Wang, X.; Hui, C. L.; Hsing, I. M. *J. Phys. Chem. B* **2003**, *107*, 11057-11064.
(50) Park, J.; Aliaga, C.; Renzas, J.; Lee, H.; Somorjai, G. *Catal. Lett.* **2009**, *129*, 1-6.
(51) Chen, W.; Kim, J.; Sun, S.; Chen, S. *PCCP* **2006**, *8*, 2779-2786.
(52) Liu, Z.; Shamsuzzoha, M.; Ada, E. T.; Reichert, W. M.; Nikles, D. E. *J. Power Sources* **2007**, *164*, 472-480.
(53) Mazumder, V.; Lee, Y.; Sun, S. *Adv. Funct. Mater.* **2010**, *20*, 1224-1231.
(54) Shao, Y.; Yin, G.; Gao, Y. *J. Power Sources* **2007**, *171*, 558-566.
(55) Kobayashi, H.; Yamauchi, M.; Kitagawa, H.; Kubota, Y.; Kato, K.; Takata, M. *J. Am. Chem. Soc.* **2008**, *130*, 1828-1829.
(56) *Fuel Cell Catalysts*; Koper, M. T. M., Ed.; Wiley Interscience: Hoboken, NJ, 2009.
(57) Martín, A. J.; Chaparro, A. M.; Folgado, M. A.; Rubio, J.; Daza, L. *Electrochim. Acta* **2009**, *54*, 2209-2217.
(58) Kondo, S.; Nakamura, M.; Maki, N.; Hoshi, N. *J. Phys. Chem. C* **2009**, *113*, 12625-12628.
(59) Shao, M.; Yu, T.; Odell, J. H.; Jin, M.; Xia, Y. *Chem. Commun.* **2011**, *47*, 6566-6568.
(60) Teng, X.; Yang, H. *Nano Lett.* **2005**, *5*, 885-891.
(61) Zhang, J.; Vukmirovic, M. B.; Sasaki, K.; Nilekar, A. U.; Mavrikakis, M.; Adzic, R. R. *J. Am. Chem. Soc.* **2005**, *127*, 12480-12481.
(62) Gong, K.; Chen, W.-F.; Sasaki, K.; Su, D.; Vukmirovic, M. B.; Zhou, W.; Izzo, E. L.; Perez-Acosta, C.; Hirunsit, P.; Balbuena, P. B.; Adzic, R. R. *J. Electroanal. Chem.* **2010**, *649*, 232-237.
(63) Ghosh, T.; Vukmirovic, M. B.; DiSalvo, F. J.; Adzic, R. R. *J. Am. Chem. Soc.* **2010**, *132*, 906-907.
(64) Knupp, S.; Vukmirovic, M.; Haldar, P.; Herron, J.; Mavrikakis, M.; Adzic, R. *Electrocatalysis* **2010**, *1*, 213-223.
(65) Sasaki, K.; Naohara, H.; Cai, Y.; Choi, Y. M.; Liu, P.; Vukmirovic, M. B.; Wang, J. X.; Adzic, R. R. *Angew. Chem. Int. Ed.* **2010**, *49*, 8602-8607.

Chapter 5. Ambient Surfactantless Synthesis, Growth Mechanism and Size-Dependent Electrocatalytic Behavior of High-Quality, Single Crystalline Palladium Nanowires

5.1 Introduction

The ability to tailor size at the nanoscale represents a key and fundamental challenge in the progression towards the production of nanostructured materials with practical applications in PEMFC devices.[1-4] For example, in Chapters 3 and 4, we have demonstrated that ultrathin NWs consisting of Pt and Pd maintain outstanding electrocatalytic performance in relation to analogous Pt NP/C.[5,6] In fact, we also noted in Chapter 4 that ultrathin Pd NWs can serve as high performance core materials for the deposition of a uniform Pt_{ML}, which evinced an outstanding Pt-mass normalized ORR activity of 1.83 A/mg_{Pt}.[5] In all of these cases, the enhanced performance has been achieved by systematically examining the size-dependent trends in ORR performance in 1D nanostructures.[2] Therefore, it is evident that robust synthesis techniques are required in order to successfully probe the size-dependent phenomena in 1D noble metal nanostructures.

However, a continuing challenge in the exploration of size-dependent trends with 1D nanostructures, particularly those composed of Pd, has been the development of environmentally friendly methods for the generation of crystalline, high quality nanostructures with high aspect ratios and predictable dimensions.[7] For example, several ambient solution-based techniques have been employed for the preparation of ultrathin Pd NWs with diameters ranging from 2 nm to 6 nm, utilizing organic surfactants as shape-directing agents, and sodium borohydride as a strong reducing agent.[8-11] We demonstrated in Chapter 4 that high-quality ultrathin Pd NWs can be generated with homogeneous diameters of ~2 nm and can be reliably supported onto carbon with an excellent three-dimensional distribution of the Pd NWs on the carbon surface.[5] Similarly,

templating of bimetallic PtRh and PtPd NWs can also be accomplished by utilizing either Rh or Pd nanocubes as precursor seeds for the subsequent generation of Pt-forming NW networks.[12,13] Metallic NWs composed of Te[14] and Ag[15], for example, have been used as sacrificial templates for the production of Pd NWs through galvanic displacement reactions, under ambient conditions. In addition, the colloidal growth of noble metal NWs has also been achieved at elevated temperatures, so as to broaden the range of reducing agents, that can be employed, to include alcohols and amines, for instance.[16] For example, Xia and co-workers have developed effective solvothermal-based methods for the preparation of anisotropic structures of Pd, such as rods, plates, cubes, and twinned particles, wherein the control of the reaction kinetics in the presence of certain additives results in predictable morphologies.[17] The generation of high-quality NWs and nanorods of Pd with diameters of 9.0 nm has been achieved hydrothermally by employing PVP as both a surfactant and an *in situ* reducing agent.[18]

Although all of these methods can generate high-quality 1D Pd nanostructures, a key limitation of these synthetic protocols is that the organic surfactant molecules that serve as capping agents are typically strongly adsorbed onto the surfaces of the resulting nanostructures.[2] This experimental reality can be particularly challenging when these as-prepared materials are employed as ORR electrocatalysts, because exposure of the bare surface is critical for high activity.[5,19] To overcome this challenge, we have developed a highly effective methodology to remove residual organic impurities from the surfaces of as-synthesized noble metal nanostructures, utilizing selective CO adsorption.[5,6,20] However, the removal of organic impurities from electrocatalysts by post-processing techniques represents a significant technological challenge in the context of effectively scaling up colloidal reactions to produce gram-scale quantities. More importantly, colloidal techniques are significantly limited in their

ability to tailor the dimensions of the resulting 1D nanostructures, including both their diameter and aspect ratio. This intrinsic disadvantage of colloidal-based techniques arises from the fact that particle dimensions are controlled by a complex set of variables, including reaction temperature, relative adsorption strength of the shape directing agent, concentration, and reduction rate, to name only a few. Therefore, in many cases, colloidal techniques are limited in the production of 1D nanostructures with a finite diameter[8,21] or in some cases, with the ability to tailor the diameter over a small range of a few nanometers,[22] for instance. A thorough discussion of the challenges associated with controlling the dimensions of 1D nanostructures, utilizing colloidal techniques, can be found in a recent review by our group.[7]

In light of these real and practical limitations, a conceivably simple approach to the challenge of size-dependent synthesis has been to employ a template or "mold" so as to confine the nucleation and growth of the nanostructure and to produce 1D structures with predictable dimensions.[7,23] Specifically, the size and morphology of the resulting nanostructures can be controlled by the physical geometry and dimensions of the originating template pore channels themselves.[7,23-28] In this context, a broad range of template materials has been employed in the production of metallic NWs, including porous filter membranes,[25,29] the channels of mesoporous silica,[30] liquid crystals,[31,32] surfactant micelles,[33,34] and even the central cavities of viruses.[35] Although a broad range of templates exist, the use of porous filter membranes, such as track-etched polycarbonate (PC) and anodized aluminum oxide (AAO) membranes, has become ubiquitous in the production of noble metal nanostructures, owing to their many advantages.[25] For example, commercially available PC and AAO membranes maintain a high density of oriented anisotropic pores with homogeneous nanoscale diameters. More importantly, membranes can be purchased with homogeneous pore sizes that span a broad range of diameters

from as small as 10 nm to larger than 10 μm. Thus, the dimensions of the resulting 1D structures can be directly and predictably controlled by tailoring the pore sizes of either the PC or AAO template employed in the synthesis.

In the case of nanostructured noble metals, the reduction and nucleation of the metal is often achieved through electrochemical deposition, commonly referred to as "electrodeposition" of precursors within the spatial confines of the pores of either a PC or AAO template.[7,25] The electrodeposition process involves (i) an oriented diffusion of charged growth species (*i.e.* precursor cations) through an electrolyte solution when an electrical field is applied, followed by (ii) reduction of the precursor ions at the growth surface, which acts as both the deposition surface and the cathodic electrochemical interface. Since the AAO and PC templates themselves maintain poor conductivity, the templates are suitably modified with a thin metallic backing film typically consisting of either Au or Ag, by means of physical vapor deposition (PVD). In this architecture, application of an electric field between the anode and the cathode results in the reduction of precursor cations at the surface of the metallic thin film and the nucleation and growth of the NW is subsequently defined by the rigid 1D pore space of the template. Subsequently, the growing metallic NW itself serves as the cathode and reduction occurs at the interface between the NW and the electrolyte, until the template pores are entirely filled. Utilizing this technique, arrays of Pd NWs with highly uniform diameters of 80 nm have been prepared by electrodeposition within the confines of an AAO template, possessing pore sizes of ~ 80 nm, for example.[36]

Despite its popularity in the literature, electrodeposition protocols have several drawbacks inherent to their reliance upon applied external electrical fields to achieve appropriate reduction. First, the electrodeposition process necessarily requires caustic reaction media in order

to solubilize the metal precursor ions, facilitate the reduction process, and sufficiently increase the conductivity between the anode and cathode. In addition, it requires additional electrochemical (*i.e.* potentiostat) and PVD equipment in order to electrochemically deposit NWs within the pores of insulating filter membranes. Therefore, the need for expensive and potentially complex instrumentation renders template-mediated electrodeposition as less amenable to scale up and more costly than simple solution-based techniques.[25] With the growing concern over the potentially harmful environmental impacts of synthesizing nanostructures, a key consideration in the broader development of nanostructured electrocatalysts is that synthetic protocols should be reasonably efficient, ambient, and inexpensive, as well as minimize the use of harmful precursors and processes.[37]

In pursuing these generalized strategies, we have employed the U-tube double diffusion device (Figure 5.1) as an ambient, surfactantless method for the reliable preparation of high-quality, diameter-controlled Pd NWs.[38-40] Our U-tube device consists of two half-cells mutually separated by a commercial membranous template, which serves as the scaffold for the subsequent growth of NWs. Past successful examples in our group have included metal tungstates, binary oxides, phosphates, sulfides, fluorides, and elemental metals.[29,41-47] Recently, the U-tube device has been highlighted for its versatility as both an effective and green method for the production of high-quality 1D metallic nanostructures under ambient conditions.[37] For example, we have employed this technique to produce the 200 nm Pt NTs and 45 nm Pt NWs highlighted in Chapter 3. Herein, for the first time, we have employed the U-tube double diffusion device to prepare high-quality, *single crystalline*, submicron (270 nm) and nanosized (45 nm) Pd NWs.[38,48] The U-tube methodology is advantageous, since high-quality Pd NWs are grown under ambient conditions without requiring either electrochemical equipment or PVD,

which are typically necessary for electrodeposition. In addition, we can substitute the caustic electrolytes (0.1 – 1 M H_2SO_4) with a dilute reducing agent solution, consisting of 5 mM sodium borohydride. Based upon careful analysis of partially formed NWs, we have gained important insight into the growth mechanism of the Pd NWs within the confines of PC templates. As a proof of concept, we have demonstrated that it is feasible to produce segmented NWs wherein control over the chemical composition has been achieved along the long axis of the NW itself.[40] In fact, we have been able to predictably synthesize segmented Pd/Au and Pd/Pt NWs with direct and predictable control over segment length, by systematically controlling the reaction time.

In the current report, we also exploit the ability to readily and predictably control the diameter of single crystalline Pd NWs to explore size-dependent electrocatalytic relationships in both elemental Pd NWs and Pt_{ML}~Pd NWs possessing diameters that range from submicron to ultrathin < 5 nm dimensions with the goal of further generalizing the size-dependent performance trend already observed in 1D Pt nanostructures. To this end, we have systematically explored the size-dependent electrochemical performance of both submicron and nanosized Pd NWs by comparison with ultrathin Pd NW/C composites obtained, utilizing a surfactant-based technique that has been previously reported.[5] Ultimately, the desired Pt_{ML}~Pd NW catalysts have been prepared by Pt_{ML} deposition and the size-dependent ORR activity has been studied in these well-defined, diameter-controlled core-shell electrocatalysts. In both cases, we have observed consistently reproducible enhancements of 2-fold in terms of electrocatalytic activity as the diameter is decreased from the submicron to ultrathin levels. Interestingly, this observation further demonstrates that the general size-dependent trend observed in elemental Pt NWs can be broadened to include elemental Pd NWs and more importantly, core-shell type Pt_{ML}~Pd NWs, which is an important finding in the progression toward practical 1D electrocatalysts.

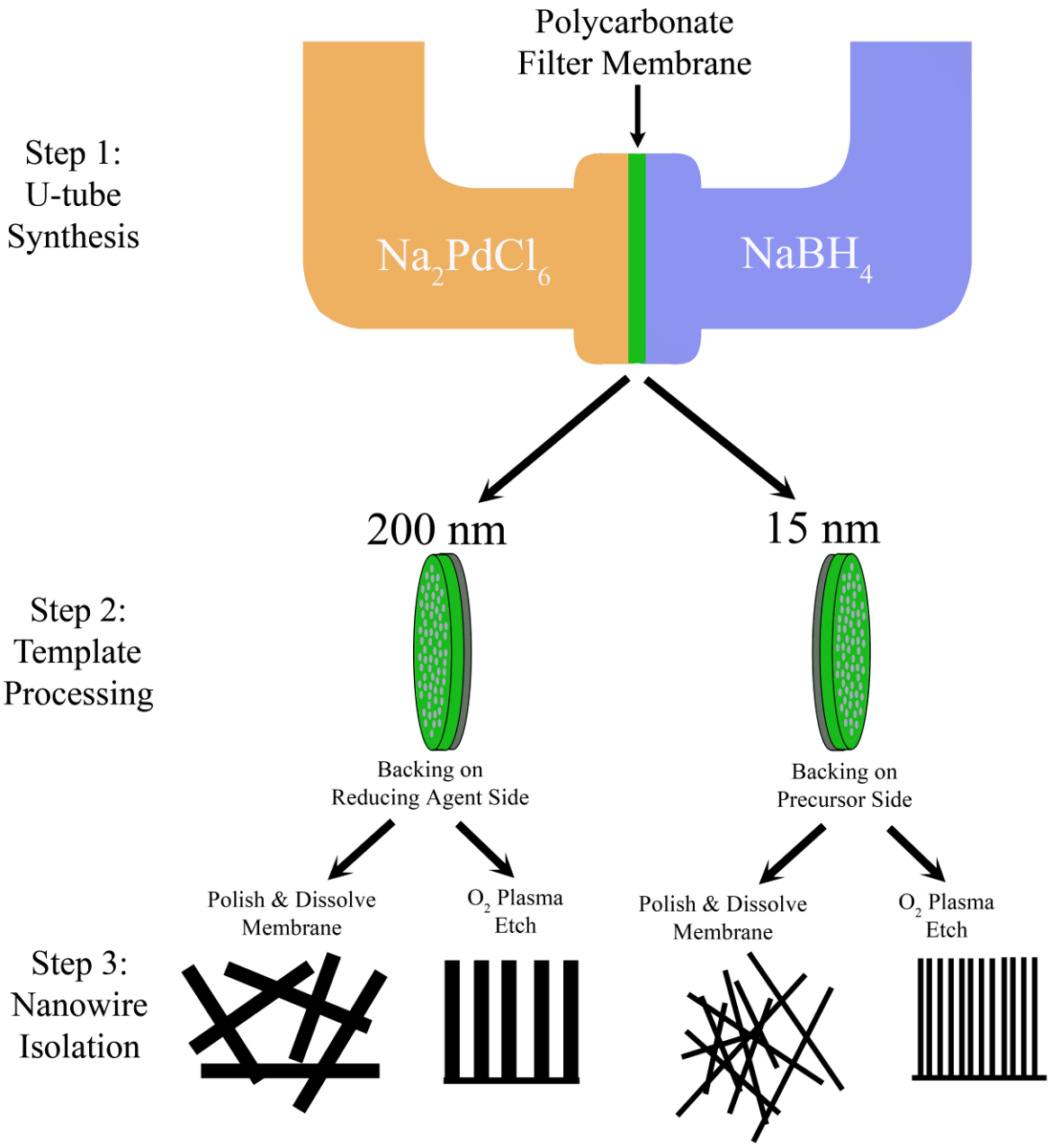

Figure 5.1 The production of Pd NWs with predictable diameters from the U-tube double diffusion device. In Step 1, the U-tube device (top) is assembled with the PC template separating the precursor and reducing agent half-cells. After NW formation, the as-prepared templates filled with NWs are removed from the U-tube device. The thin films of excess metallic material on the surface of the template is shown (middle) for the 200 nm (film on surface exposed to reducing agent half-cell) and 15 nm (film on surface exposed to the precursor half-cell). In Step 2, the NW filled template is washed to remove the residual precursor and reducing agent. Finally, isolated individual NWs or free-standing NW arrays are obtained in Step 3 either by dissolving the membrane or by oxidative etching of the membrane, respectively. (Adapted with permission from Ref. 38. Copyright 2011 American Chemical Society)

5.2 Synthesis of Pd NWs, Segmented Pd/Au and Pd/Pt NWs and a Novel Method for Investigating the Growth of Pd NWs under Double-Diffusion Conditions

5.2.1. Size-Dependent Synthesis of Pd NWs Utilizing the U-tube Double Diffusion Device

The synthesis and isolation of submicron (270 nm) and nanosized (45 nm) palladium NWs (Pd NWs) was accomplished by utilizing a U-tube double diffusion device, and the process is shown schematically in Figure 5.1. Specifically, sodium hexachloropalladate hydrate (87.5 mg $Na_2PdCl_6 \cdot x\ H_2O$, Alfa Aesar 99.9%) was dissolved in 5 mL of absolute ethanol in order to create a saturated precursor solution. Separately, a 5 mM sodium borohydride ($NaBH_4$, Alfa Aesar 98%) solution was prepared by dissolving the solid powder into 5 mL of ethanol with a brief period of sonication in order to create a reducing agent solution. Immediately prior to performing the reaction, commercially available PC membranes (Whatman, Nucleopore track etched) with pore sizes of either 200 nm or 15 nm were sonicated in ethanol to pre-saturate the pores with the ethanol solvent.

In Step 1, an ethanol-saturated membranous template was clamped between the two half-cells of the U-tube device, and the half-cells were separately filled with precursor and reducing agent solutions, respectively. After 16 min of reaction time, the reaction completion was signaled by the visible formation of metallic material on the exterior surfaces of the template; the filled template membrane was then removed from the U-tube and gently rinsed with ethanol, in Step 2. In Step 3, the as-prepared Pd NWs are isolated from the PC template to give either individual isolated NWs or vertically oriented, free standing NW arrays:

Individual Isolated NWs: Residual metal present on the external surfaces of the template was physically removed by polishing the template on a commercially available, soft Arkansas Wet-Stone (Tools for Working Wood Company, Brooklyn, NY) with mineral oil serving as a

lubricant. The PC template itself was dissolved away by immersing the membrane in dichloromethane (DCM) for a minimum of 15 min and the NWs suspended in the DCM/PC solution were isolated by centrifugation. The wires were then washed of residual organic impurities by dispersing the grey powder into fresh aliquots of DCM and isolating by centrifugation for a minimum of five washing cycles. Subsequently, purified isolated NWs could be obtained by washing the grey-black powder in ethanol.

Vertically Oriented Arrays: Free-standing arrays of the NWs could be obtained by affixing the template onto a Si wafer with double-sided Cu tape and exposing the wafer to an oxygen plasma for a total of 20 min in a reactive ion etcher (March Plasma).

5.2.2. Synthesis of Segmented Pd/Pt and Pd/Au NWs with Control over the Relative Lengths of the Axial Segments

The individual segments of the Pd/Pt or Pd/Au NWs were synthesized in a two-step process involving (i) the deposition of an initial metallic Pd NW segment followed by (ii) the subsequent deposition of a second Pt or Au segment.[40] Specifically, a Pd NW segment was first grown utilizing the procedure, as described in Section 5.2.1. The length of the Pd NW segment was controlled by the reaction time, which was varied between 10 – 60 min, yielding corresponding NWs with lengths ranging from 1 – 6 μm, respectively. Once the desired Pd NW segment length was achieved, a second metallic segment was grown from the existing Pd NW segment, utilizing a second electroless deposition process. To accomplish this, the Pd precursor and reducing agent solutions were removed from the respective half cells, thereby effectively quenching the growth of the Pd NW segment. Subsequently, aliquots of ethanol were added into the half-cells, so as to remove residual traces of precursors and reducing agent from the template

pores for a duration of 5 minutes. After removal of the ethanol wash, the precursor half-cell was loaded with either a 50 mM tetrachloroauric acid ($HAuCl_4 \cdot xH_2O$, 99.999%, Alfa Aesar) solution in the case of Pd/Au NWs or a 100 mM hexachloroplatinic acid (H_2PtCl_6, 99.9%, Alfa Aesar) solution in the case of Pd/Pt NWs. The reducing agent half-cell was simultaneously filled to capacity with a 200 mM $NaBH_4$ reducing agent solution. The completion of the reaction was signaled by the formation of a thin layer of metallic material on the outer surface of the template, adjacent to and exposed to the precursor half-cell. The isolation of the as-synthesized segmented NWs was achieved, utilizing the same techniques for elemental NWs described in Section 5.2.1.

5.2.3. A Novel Method for Addressing the Structure of 1D Nanostructures Directly within the Template Pores of Polycarbonate Filter Membranes

We employ microtome cross-sectioning to directly probe the structure, crystallinity, and chemical composition of as-synthesized Pd NWs directly within the 1D pore spaces of the PC filter membrane, which served as a template for their growth. Microtome cross-sectioning is a sample preparation technique traditionally normally employed for examining biological samples with TEM. In a typical preparation, the desired tissue sample is embedded in a polymeric resin and is cut into sections with thicknesses ranging from 50 – 250 nm for investigation by TEM. Herein, we have employed the 1D pore channels of PC filter membranes as nanostructured reaction chambers for the growth of high-quality palladium-based NWs.[38,39,49] To investigate the growth mechanism of the NWs within the template pores, we have embedded portions of the template containing as-synthesized Pd NWs in Epon resin and utilized a Reichert-Jung UltracutE Ultramicrotome to prepare 80 nm sections of the template for subsequent examination by TEM and HRTEM.

The cross-sections were supported onto a Formvar coated, copper slot grid and examined by an FEI Titan 80-300 TEM instrument, equipped with a Cs-corrector, operated at 300 kV.[38] This instrument is particularly advantageous for probing the structure of the NWs in the polymeric matrix of the membrane template, because the voltage, current, and size of the beam can be tailored to avoid damage to the polymer. The crystallinity of the as-synthesized Pd NWs was examined by studying SAED and HRTEM images along the axis of the NW. Similarly, the composition of the NW can be studied by obtaining EDAX measurements at points along the long axis of the nanowire, and this study has had relevant applicability to understanding the formation of bimetallic NWs (*c.f.* Chapter 6) within these porous templates. Collectively, the ability to address the crystallinity and chemical composition as well as to image the NWs directly within the confines of the pore spaces has enabled us to develop a detailed growth mechanism as a function of template pore size. This has proven useful in the development of segmented Pd/Pt and Pd/Au NWs, which exploits the unique growth mechanism with 200 nm template in order to achieve control of composition along the axis of individual NWs.

5.3 Results & Discussion

5.3.1. Synthesis and Characterization of Pd NWs

The synthesis of submicron and nanosized Pd NWs with highly monodisperse dimensions has been readily achieved by utilizing an ambient, surfactantless template-based method.[38,48] The crystallinity and purity of the as-prepared NWs were characterized by powder XRD data, shown in Figure 5.2A and 5.3A for the Pd NWs prepared from 15 nm (referred to as nanosized NWs) and 200 nm (referred to as submicron NWs) PC templates, respectively. Crystallographic analysis confirms that all of the peaks for the nanosized and submicron NWs

could be readily assigned to the (111), (200), (220), and (311) reflections of face-centered cubic Pd (*Fm3m*, JCPDS #46-1043), respectively. The measured *d*-spacing is determined to be 2.243 Å for both the submicron and nanosized wires and is in excellent agreement with the standard value of 2.245 Å. In addition, there were no detectable crystalline impurities in the XRD pattern for either the submicron or the nanosized Pd NW samples.

The morphology of as-prepared NW samples was initially characterized by SEM. Overview SEM images (Figure 5.2B and 5.3B) reveal that the NWs maintain diameters of 45 ± 9 nm and 270 ± 45 nm with high aspect ratios of 73 ± 22 and 13 ± 4, for samples derived from the 15 and 200 nm template pores, respectively. The apparent size discrepancy between the commercially reported pore diameter and the experimentally measured diameter is expected and has been previously reported by our group, as well as by other groups.[29,50] This divergence has been widely attributed to an expansion and inhomogeneity of the pore diameter within the interior of the membrane in combination with swelling of the pores during the growth of the NWs. In addition to obtaining individual isolated NWs, free-standing NW arrays, shown in Figures 5.2C and 5.3C, have also been readily obtained by affixing the filled templates onto a Si substrate and exposing the array to an oxygen plasma etch in order to suitably remove the PC template. The highly uniform nature of the resulting arrays and the ability to affix them onto a wide variety of substrates have rendered these systems as excellent candidates for diverse applications in gas sensing[51,52] and alcohol electroxidation.[53] The methods for obtaining both isolated NWs and free standing NW arrays are shown schematically in Figure 5.1.

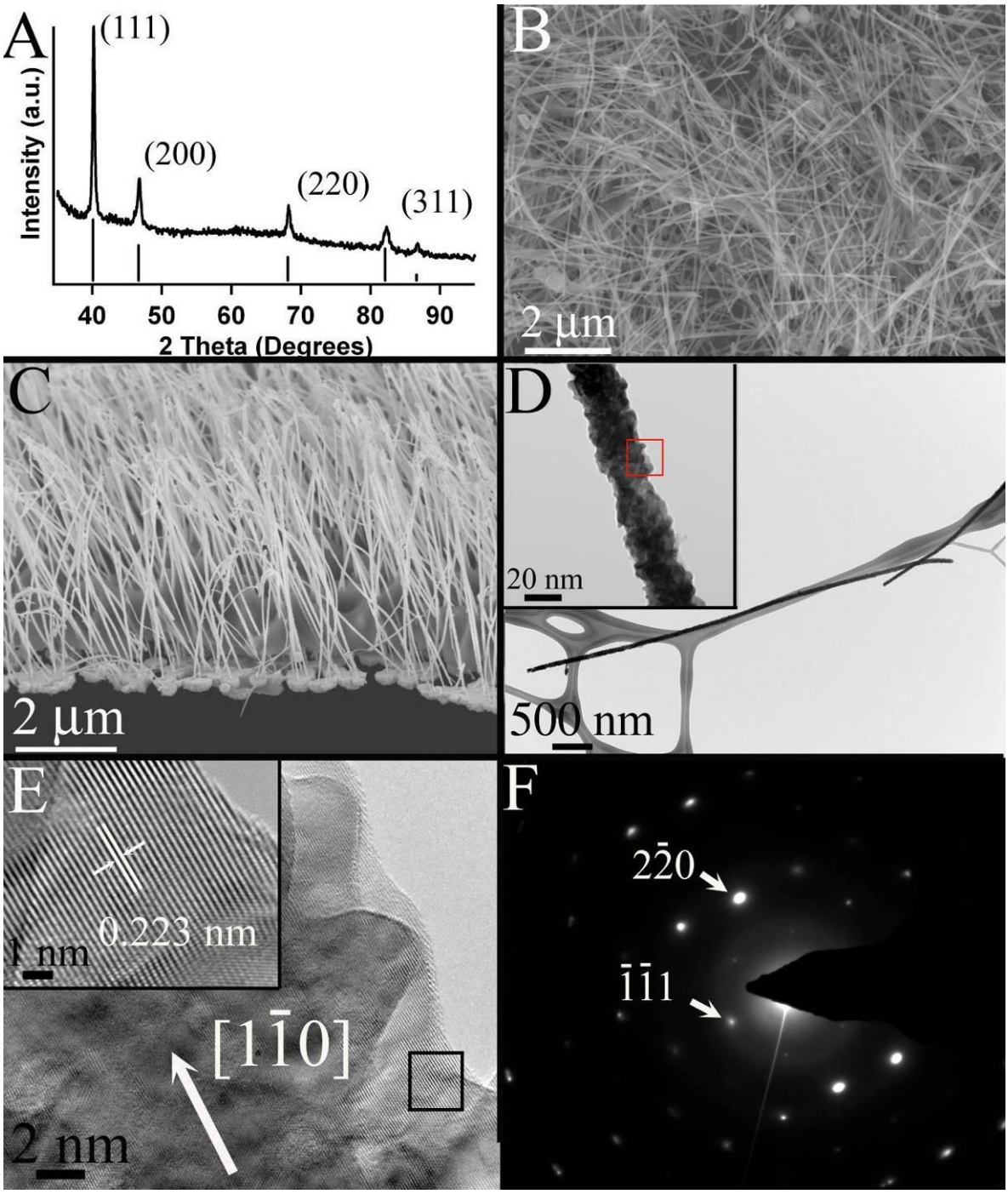

Figure 5.2 Characterization of 45 nm Pd NWs. Representative XRD patterns (A), SEM images of the individual, isolated NWs (B) and free-standing NW arrays (C). An overview TEM image of an individual NW (D) is shown with a TEM image highlighting a section of the NW is shown as an inset, and the red box denotes the area where the high resolution TEM image (E) was obtained. A selected area denoted by the black box highlighting the well-defined lattice planes is shown as an inset to panel E. The SAED pattern (F) corresponding to the high resolution TEM image is also highlighted. (Reprinted with permission from Ref. 38. Copyright 2011 American Chemical Society)

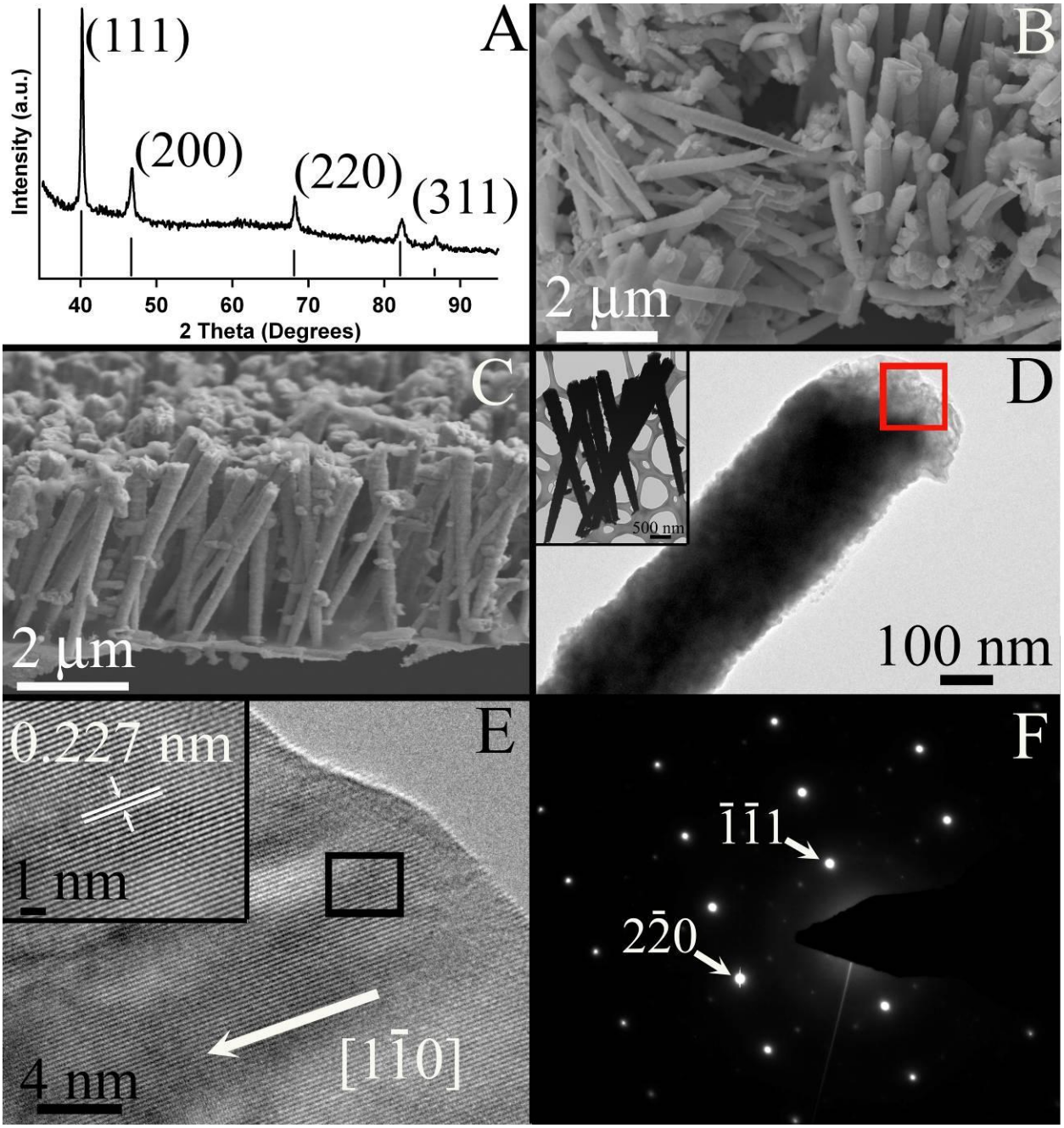

Figure 5.3 Characterization of 270 nm Pd NWs. Representative XRD patterns (A), SEM images of the individual, isolated NWs (B) and free-standing NW arrays (C). An overview TEM image of an individual NW (D) is shown with a TEM image highlighting a section of the NW is shown as an inset, and the red box denotes the area where the high resolution TEM image (E) was obtained. A selected area denoted by the black box highlighting the well-defined lattice planes is shown as an inset to panel E. The SAED pattern (F) corresponding to the high resolution TEM image is also highlighted. (Reprinted with permission from Ref. 38. Copyright 2011 American Chemical Society)

Representative TEM images shown in Figure 5.2D and 5.3D not only confirm the quality and high aspect ratio of the NWs but also reveal that the NWs maintain uneven, roughened surfaces, likely originating from the textured, imperfect structure of the originating pore walls of the PC template itself.[47] The high-resolution TEM images (HRTEM) (Figures 5.2E and 5.3E) show that the NWs are single-crystalline, with the exception of a short polycrystalline segment at the end of the NW. The presence of this short polycrystalline segment can likely be attributed to the formation process of these NWs, which is discussed in greater detail in Section 5.3.2. The high-resolution TEM images in Figures 5.2E and 5.3E indicate the presence of well resolved lattice planes that are straight and equidistant with a lattice spacing of 2.25 ± 0.03 Å, in perfect agreement with the bulk Pd (111) lattice spacing.

To assess the crystal structure over the entire length of the NW, we have employed electron diffraction in TEM. The diffraction patterns (DPs) taken along the length of the NWs demonstrate that these NWs are highly textured and essentially single crystalline over the greater part of their length. Figures 5.2F and 5.3F show diffraction patterns obtained with the electron beam incident along the $[\bar{1}12]$ axis of Pd. Diffraction data in combination with HRTEM images suggest that the long axis of the NWs formed in both the 200 nm and 15 nm pores is oriented along the $[\bar{1}10]$ crystallographic direction. This unique growth direction of the Pd NWs has been observed previously when metallic NWs have been electrodeposited within highly anisotropic nanostructured pores. However, it is unclear in the existing literature as to which primary experimental influence ultimately determines the observed growth direction.[54] Given the lack of dependence on the pore size, we believe that the growth direction of these NWs arises from the relatively slow reduction kinetics observed in this synthetic scheme. This hypothesis is discussed in more detail in Section 5.3.2.

Although there are many advantages of the U-tube methodology, the use of nanostructured templates may inherently prevent high product yields or even the acquisition of ultralow diameters, as the smallest commercially available PC template consists of ~15 nm diameter pores. In light of these limitations, in parallel, we have prepared ultrathin Pd NWs utilizing a scalable wet-chemical technique wherein the reduction of a Pd precursor and growth is directed by a surfactant.[5,8] The as-prepared NWs in this case can be reliably supported onto high surface area carbon, which prevents aggregation of the NWs during treatment and imparts significantly improved durability. Extensive characterization the purity, crystallinity and quality of these NWs can be found in Chapter 4, both before and after support on Vulcan XC-7R.

5.3.2. Insights into the Growth Mechanism of Noble Metal NWs under Double Diffusion Conditions

In addition to preparing optimized nanostructures for use as size-dependent core-shell electrocatalysts, we have also gained insight into the formation process of metallic NWs within the spatial boundaries and constraints associated with PC templates, under double diffusion conditions. Previously, our group has achieved the reliable synthesis of metallic Au, Ag, and Pt NWs within the structural confines of 200 nm PC templates by utilizing relatively high concentrations of 0.1 M and 0.5 M for the metal precursor and the sodium borohydride, respectively.[29] The Pt NWs prepared with the analogous H_2PtCl_6 precursor in this previous report were found to be polycrystalline and the growth was determined to have followed a heterogeneous nucleation mechanism. Similarly, another group has prepared Ag NWs by utilizing a double diffusion device, wherein a so-called “self-propulsion mechanism” was proposed to explain their growth.[55]

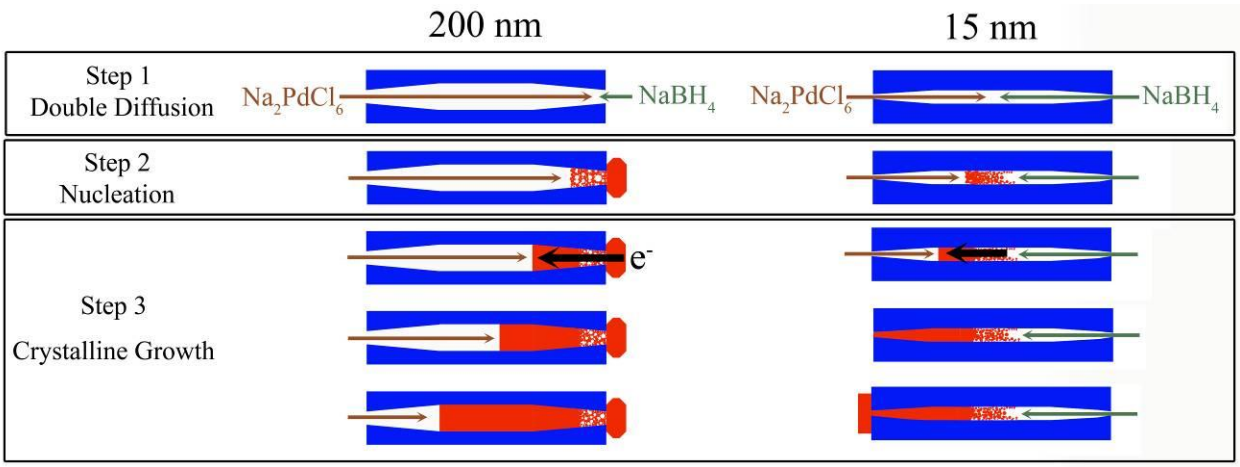

Figure 5.4 A schematic representation of the proposed NW formation process under double diffusion conditions in the 200 nm (left) and 15 nm (right) diameter template pores. The left side of the graphic represents the precursor half-cell and the right side of the graphic denotes the reducing agent half-cell. In the double diffusion step (Step 1), we highlight the difference in the point of nucleation that is observed in the case of the 200 nm and 15 nm template pores. In both cases, the growth is initiated by rapid nucleation of metallic Pd (Step 2) as the diffusion fronts of the precursor and reducing agent intersect within the template pores. Once the formation of the polycrystalline segments blocks the diffusion of the reducing agent into the pore, the growth of the primary single crystalline segments proceeds by an electroless deposition process (Step 3) where electrons are transported through the growing wire (black arrow). Observed metallic backing layers present on the external surfaces of the 200 nm and 15 nm templates are found on the reducing agent and precursor half-cell sides, respectively, and are highlighted in red. (Reprinted with permission from Ref. 38. Copyright 2011 American Chemical Society)

By contrast, the synthesis of Pd NWs in this report was accomplished with significantly lower concentrations of 37 mM Na_2PdCl_6 and 5 mM $NaBH_4$ as a result of the inherently low solubility of the Pd precursor in ethanol. Interestingly, we find that the synthesis of Pd NWs is distinctive from that of other template-based syntheses conducted under similar double-diffusion conditions. In this section, we explored the growth mechanism in the 200 nm and 15 nm template pores utilizing complementary techniques that provide insight into the structure and location of the NW within the template pore, as the reaction progresses. To achieve this objective, we have developed a new characterization technique that couples microtome cross-sectioning with HRTEM to directly address the crystallinity, chemical composition, and morphology of the Pd NWs within the template pores themselves.

Growth of Pd NWs within 200 nm Pores: Based upon the analysis of our data, we believe that the growth of the NWs within the PC templates follows a two-step process, which is shown schematically in Figure 5.4. In the first step, the precursor and reducing agent diffuse into the pore space and inevitably, the diffusion fronts intersect, resulting in the reduction of the Pd precursor and nucleation of the Pd metal. In the case of the 200 nm template pores, the nucleation of the Pd metal is initiated near the interface of the template pore and reducing agent half-cell. This initial rapid reduction followed by a nucleation process yields both a short polycrystalline NW segment within the template pore and a thin layer of metallic material on the outer surfaces of template within the reducing agent half-cell. In fact, the formation of the metallic layer on the surface of the template facing towards and thereby exposed to the reducing agent half-cell can be observed visually within the first minute of the reaction.

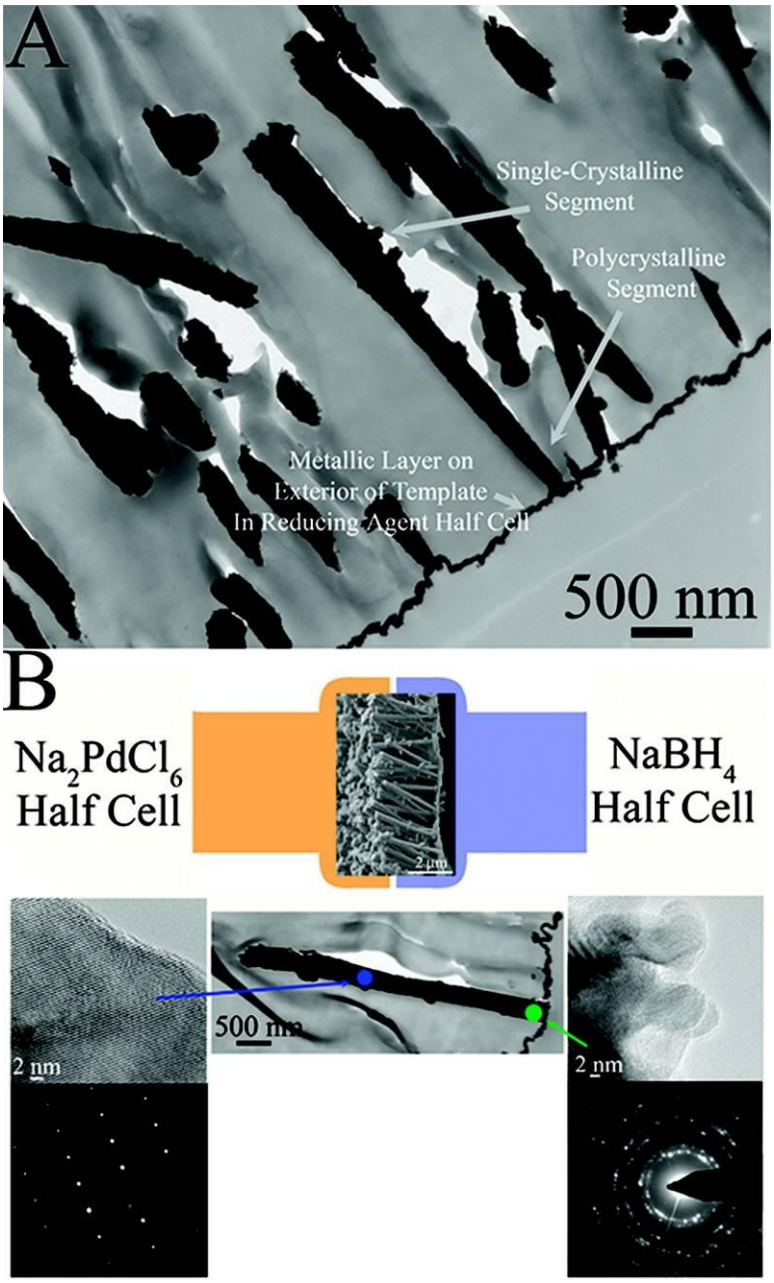

Figure 5.5 Representative cross-section of as-prepared templates containing ~270 nm NWs (A) after 16 minutes of reaction time. The presence of wire-like fragments results from the non-uniformity and irregular distribution of the template pores, which results in portions of wires being excised during the microtoming process. Cross-sectional SEM images of free-standing NWs prepared in the 200 nm (B) diameter pores of PC templates shown within a schematic of the U-tube double-diffusion apparatus. The metallic layer present on the surface of the 200 nm templates is exposed to the reducing agent half-cell, in this case. Immediately below are individual NWs within the template pore with corresponding HRTEM and SAED patterns obtained from a representative isolated NW in selected locations where either nucleation or crystalline growth predominate. (Reprinted with permission from Ref. 38, Copyright 2011 American Chemical Society)

As complementary evidence, TEM analysis of a representative cross-section of the template shown in Figure 5.5A confirms the presence of a thin metallic layer localized on the external surface of template that is exposed to the reducing agent half-cell with NWs that are directly affixed onto the metallic layer. Higher magnification images reveal that the first 500 nm of the NW affixed to the metallic layer is composed of highly interconnected crystalline grains.

To explore the crystallinity of the NW near the interface of the template pore, HRTEM images and SAED patterns (Figure 5.5B) were obtained on a representative isolated Pd NW at positions near the pore interface where it is thought that nucleation first occurs. The corresponding HRTEM images reveal that the polycrystalline segment is composed of multiple crystalline domains that give rise to the distinct diffraction rings in the SAED pattern. Based upon the low-resolution and high-resolution TEM images, the polycrystalline component represents the first 200 – 500 nm of the NW, which is directly affixed onto the metallic material, coating the exterior of the template. The observation of the initial polycrystalline segment is consistent with prior results since we have previously demonstrated that the direct reduction of metallic precursors, including H_2PtCl_6 for example, results in polycrystalline nanostructures.[29] The polycrystallinity arises from the rapid reaction kinetics when $NaBH_4$ directly interacts with and reduces the metal precursor, a process which favors the formation of many discrete nuclei as opposed to simple crystalline growth.[29] Hence, we propose that the polycrystalline segment arises in the first growth step from the rapid nucleation of Pd metal, when there is direct chemical interaction between the diffusing Pd precursor and the $NaBH_4$ solution.

Surprisingly, careful analysis of the cross-sectional images reveals that the polycrystalline segment transforms into a uniform homogeneous segment towards the interior of the template pore. HRTEM images and SAED patterns (Figure 5.5B) obtained on a

representative NW toward the interior of the pore confirm that this segment of the wire is essentially single crystalline with highly resolved lattice planes that run uniformly across the entire structure. This gives rise to the well-defined diffraction spots present on the corresponding SAED. Hence, the short polycrystalline segment segues into a second single crystalline segment that comprises the remaining 3 – 4 μm portion of the NW. However, the extended single-crystalline segment that is observed extending towards the precursor half-cell is not necessarily consistent with the idea of the direct reduction of $PdCl_6^{2-}$ by $NaBH_4$. By contrast, these findings imply that a different growth process likely predominates in creating this single crystalline segment.

Hence, we believe that the single-crystalline growth observed in the template pore arises from a second, *in situ* "electroless deposition" process wherein the rate of reduction is significantly slowed. We believe this allows for crystalline growth to predominate as opposed to a series of rapid nucleation steps. Invariably, the formation of the aforementioned polycrystalline material and the metallic layer prevents the direct diffusion of precursor and borohydride ions into the template pores, thereby preventing the direct reduction of Pd. Subsequently, we believe that both the thin metallic layer and polycrystalline segment serve as a conductive layer through which electrons are transported from the reducing agent half-cell towards the interior portion of the pore, thereby reducing the Pd precursor. This process in turn results in the lengthening of a distinct single crystalline segment towards the precursor half-cell.

As a matter of note, we believe that electrochemical neutrality is maintained during the electroless deposition process by the corresponding diffusion of positive Na^+ ions from the reducing agent half-cell into the precursor half-cell. Previously, it has been proposed by Sharabani *et al.* in their study of the electroless deposition of Ag NWs under double diffusion

conditions that the diffusion of Na^+ ions occurs through the physical spaces and cavities present between the growing NW and the surrounding pore walls.[55] Moreover, it has been demonstrated that the pore spaces of the PC templates are non-uniform and that pore branches exist throughout the template. These dispersed spaces may represent possible channels and physical pathways for the diffusion of counter ions.[50] Although all of these scenarios exist as plausible routes for Na^+ ion diffusion, it is critical to highlight that the determination of the precise mode of counter ion diffusion is beyond the scope of our analysis, and will be addressed in the future.

Recently, single-crystalline Pd NWs have been grown within nanostructured templates using a potentiostatic electrodeposition process involving careful control over the pore size and the reduction overpotential.[54] It was found in that experiment that reducing the pore size from 65 nm to 35 nm as well as utilizing a low reduction overpotential (0.3 V vs. Ag/AgCl) favored the growth of single crystalline NWs as opposed to polycrystalline NWs. The smaller pore sizes in combination with a slower reaction rate were thought to limit the diffusion in the system, thereby lowering the reaction rate and promoting single crystalline growth. Based upon these prior results as well as the HRTEM and SAED data, we believe that the growth of the single-crystalline NW segment herein arises from an ambient, electroless deposition process that is primarily diffusion-limited. This assertion is consistent with the proposed mechanism due to the inherent coupling between the reaction rate and the diffusion rate of both the precursors into the pores and the Na^+ ions into the precursor half-cell. Essentially, the limitation of the reaction kinetics to the rate of diffusion may suitably slow the reduction rate and promote the growth of the observed single crystalline segment.

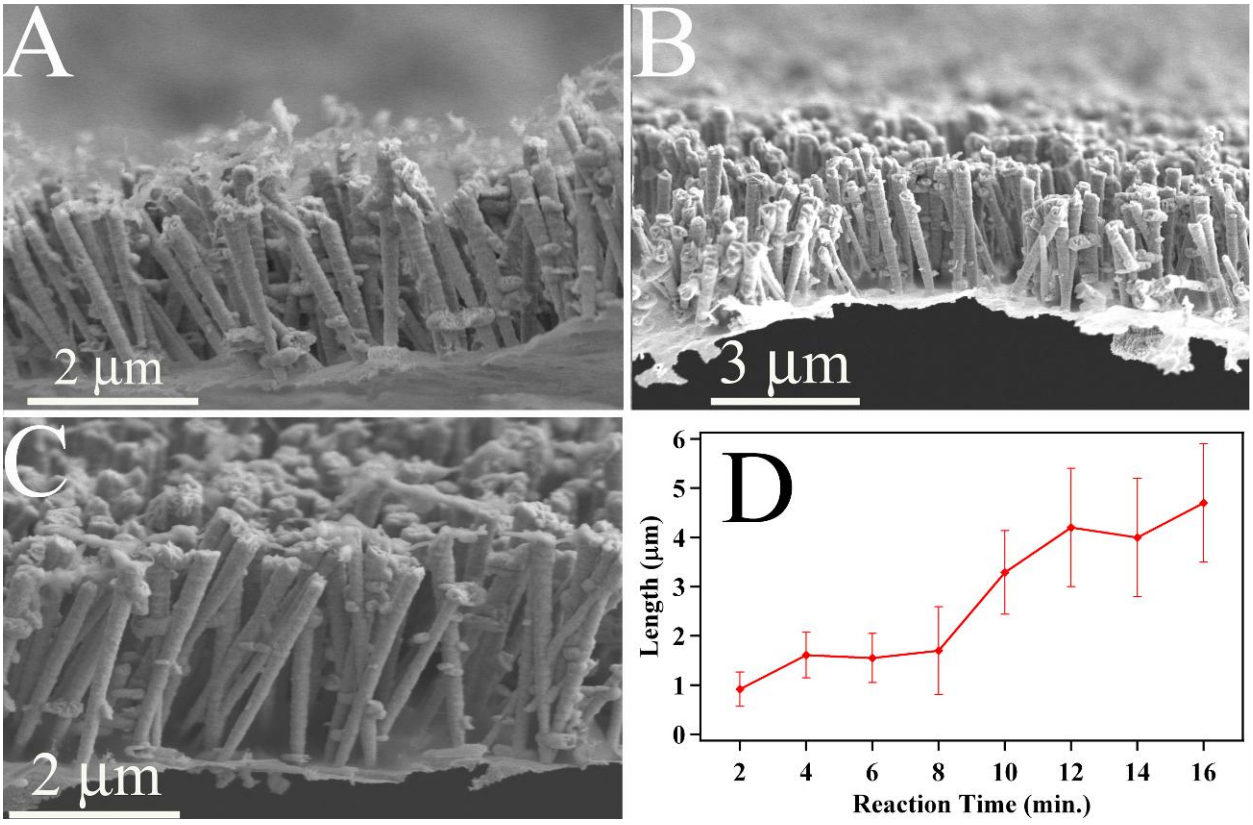

Figure 5.6 Cross-section SEM images of free-standing NW arrays prepared in 200 nm templates isolated after reaction times of 4 mins (A), 8 mins (B) and 12 mins (C). A graph depicting the measured length (D) obtained from individual, isolated NWs as a function of reaction time in 200 nm pore-sized templates is also shown. (Adapted with permission from Ref. 38. Copyright 2011 American Chemical Society)

Based upon the proposed growth mechanism, the proposed electroless deposition process should result in longer single crystalline segments and longer overall NWs with increasing reaction in an analogous fashion to potentiostatic electrodeposition. To test this hypothesis, we isolated free-standing NW arrays after various reaction times ranging from 4 – 16 min and measured the lengths of these NWs as a function of the reaction time (Figure 5.6A – 5.6C). The lengths of the NWs were found to increase consistent with our hypothesis from approximately 2 μm to over 3 μm as the reaction time is increased from 4 – 16 min. To gain a more quantitative insight, these as-prepared 1D nanostructures were isolated as individual NWs (Figure 5.6D) from reactions conducted in 2 min increments and the length was found to increase from 0.92 ± 0.35 μm to 4.0 ± 1.8 μm, as the reaction time was correspondingly increased from 2 min to 12 min, thereby representing almost the entire thickness of the template (~6 μm). Hence, it is clear that the growth of the NWs continues even after the initial polycrystalline segment effectively prevents direct interaction and contact between reducing agent and precursor molecules. These observations are collectively suggestive of a second, continuous electroless deposition step within the template pore itself.

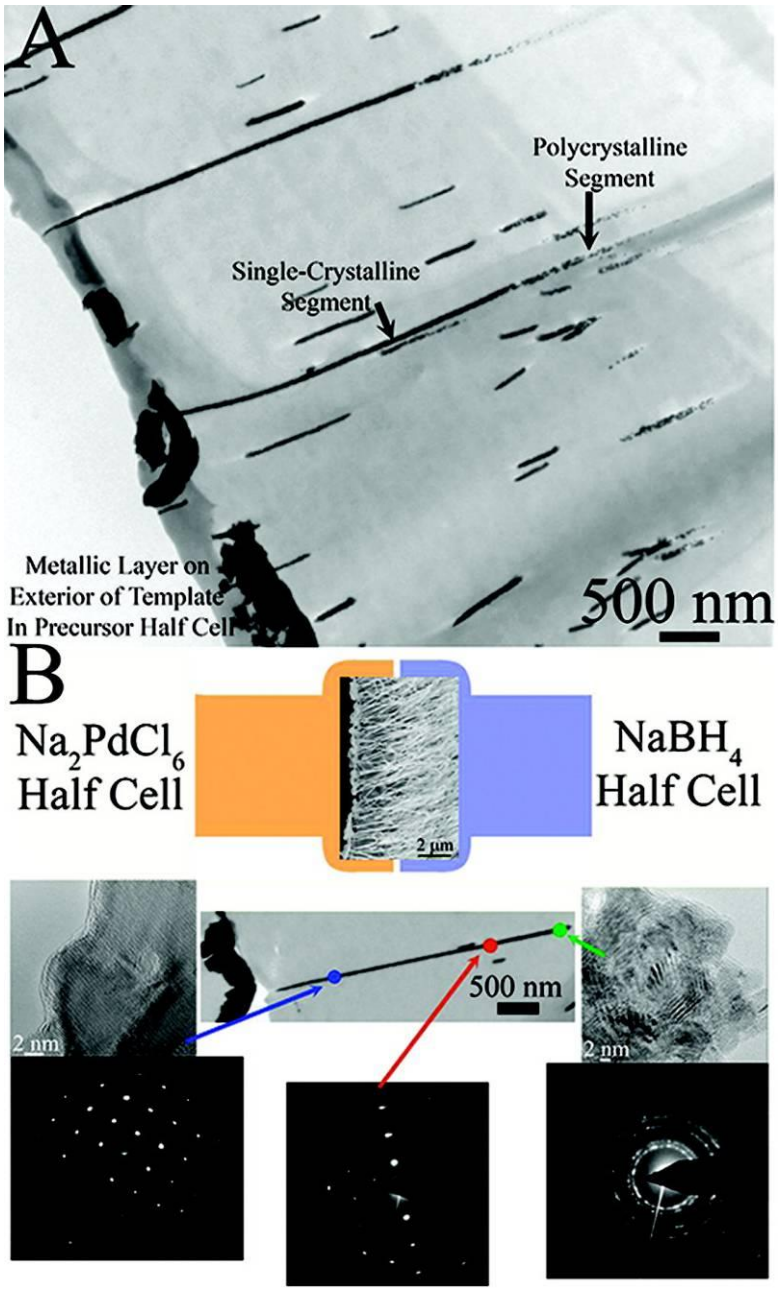

Figure 5.7 Representative cross-section of as-prepared templates containing ~45 nm NWs (A) after 16 min of reaction time. The presence of wire-like fragments arises from the non-uniformity and irregular distribution of the template pores, which results in portions of wires being excised during the microtoming process. Cross-sectional SEM images of free-standing NWs prepared in the 15 nm (B) diameter pores of PC templates shown within a schematic of the U-tube double-diffusion apparatus. The metallic layer present on the surface of the 15 nm templates is exposed to the precursor half-cell, in this case. Immediately below are individual NWs within the template pore with corresponding HRTEM and SAED patterns obtained from a representative isolated NW in selected locations where either the nucleation or crystalline growth process predominates. (Reprinted with permission from Ref. 38. Copyright 2011 American Chemical Society)

Growth of Pd NWs within 15 nm Pores: The growth of the NWs in the 15 nm template pores follows a similar two-step process that is observed within the 200 nm template. However, a key distinction in the formation of the NWs in the 15 nm pores is that the initial nucleation of the Pd likely occurs within the interior of the pore (near the center of the pore channel), as opposed to at the interface of the pore with the reducing agent half-cell. TEM images of cross-sections of the template (Figure 5.7A) in addition to HRTEM analysis (Figure 5.7B) of a representative isolated NW confirm the presence of a polycrystalline segment located towards the center of the template pore. The shift in the location of the nucleation process likely arises from the smaller pore size, which is expected to significantly limit the diffusion of the precursor into the pore space.[56,57] Based upon the cylindrical pore geometry, the point of contact between advancing diffusion fronts of the precursor and reducing agent is thereby expected to shift towards the interior of the pore and give rise to a primary nucleation process occurring closer towards the precursor half-cell. To explore this issue in more detail, we performed a series of reactions, wherein the precursor and reducing agent concentrations were altered systematically to explore the influence of diffusion rate upon the corresponding length of the wire.[38] In effect, the results of this analysis confirm that the shift in the point of nucleation in the case of the 15 nm PC template to the center of the pore arises from a slower diffusion rate of the precursor.

In an analogous fashion to the 200 nm NWs, HRTEM analysis of the NWs at points closer towards the precursor half-cell confirms that the polycrystalline segment transitions into an extended single-crystalline segment. We believe that the single-crystalline segment arises from a second electroless deposition step, which consistent with growth of the NWs in 200 nm pores. However, an interesting distinction in this case is that the crystalline growth of the NW proceeds beyond the pore, forming a metallic layer that coats the surface of the template in the

precursor half-cell. The aforementioned metallic layer on the surface of the template exposed to the precursor half-cell is apparent in Figure 5.7A. The morphology of this film is apparent in Figure 5.2C, and it is evident that the film is composed of interconnected Pd material that extends beyond the template pores. In fact, visual observation of the template during the course of the reaction reveals that the template darkens from a transparent coloration to a black coloration over the first 2 - 4 min of the reaction and then, a metallic layer becomes apparent on the surface of the template in the precursor half-cell after 4 – 6 min of reaction.

As further support for the proposed growth mechanism, we have isolated free-standing NW arrays after various reaction times (4 – 16 min) to confirm that the NW growth direction proceeds from the point of nucleation towards the precursor half-cell. On the basis of the growth mechanism in this case, we demonstrate that the length of the wire is defined by the relative precursor and reducing agent concentrations, since nucleation occurs within the interior of the template pore. Accordingly, SEM images of arrays obtained after 4 min, 8 min, and 12 min of reaction time, respectively, reveals that the length of the NWs does not change significantly from 4 min (2.9 ± 0.6 μm) to 16 min (2.8 ± 0.6 μm).

In this case, the growth of the NWs from the point of nucleation to the pore opening appears to have been completed within the first 4 min of the reaction, which is consistent with the empirical observation of the formation of the metallic material within a 4 to 6 min interval on the surface of the template in the precursor half-cell. Interestingly, the filling of the pore proceeds at a much faster rate in the 15 nm pores as compared with the 200 nm pores, which is can be explained by the fact that less Pd is obviously required to fill in the smaller pores. Hence, all of these observations complement the analysis of the template cross-section and confirm that the growth is likely initiated within the interior of the pore space and then proceeds towards the

precursor half-cell, inevitably producing a metallic layer on the surface of the template exposed to the precursor half-cell.

5.3.3. Proof of Concept: Successful Synthesis of Segmented "A/B" Type Pd/Pt and Pd/Au NWs under Ambient Electroless Conditions in 200 nm PC Templates

Recently, segmented nanostructures have been highlighted as an exciting structural architectural motif for achieving multifunctional nanomaterials.[24,25,58] Typically, segmented NWs consist of two or more discrete 1D sub-units oriented along the long axis of crystalline NWs and can therefore combine the distinctive characteristics of each sub-unit into a single nanostructure. Quantitative manipulation of the relative lengths of the various segments composing the overall nanostructure can hence afford a powerful method for tailoring the properties of these nanomaterials.[24] Thus, coupling the flexibility of this structural architecture with the highly favorable optical, electronic, and catalytic properties of noble metals has rendered this class of segmented materials as excellent candidates for a broad range of applications including but not limited to sensors,[58,59] bio-analysis,[60,61] nanomotors,[25,62-70] colloidal transport,[71,72] catalysis,[73-75] and nano-electronics.[76] In the previous section, we demonstrated that essentially the same growth mechanism associated with electrochemical deposition can be achieved without requiring electrochemical equipment, PVD equipment or caustic reaction media. Inspired by this highly advantageous and optimized growth mechanism, we have developed for the first time herein a simple two-step protocol to produce segmented NWs under ambient electroless conditions in 200 nm template pores.[40]

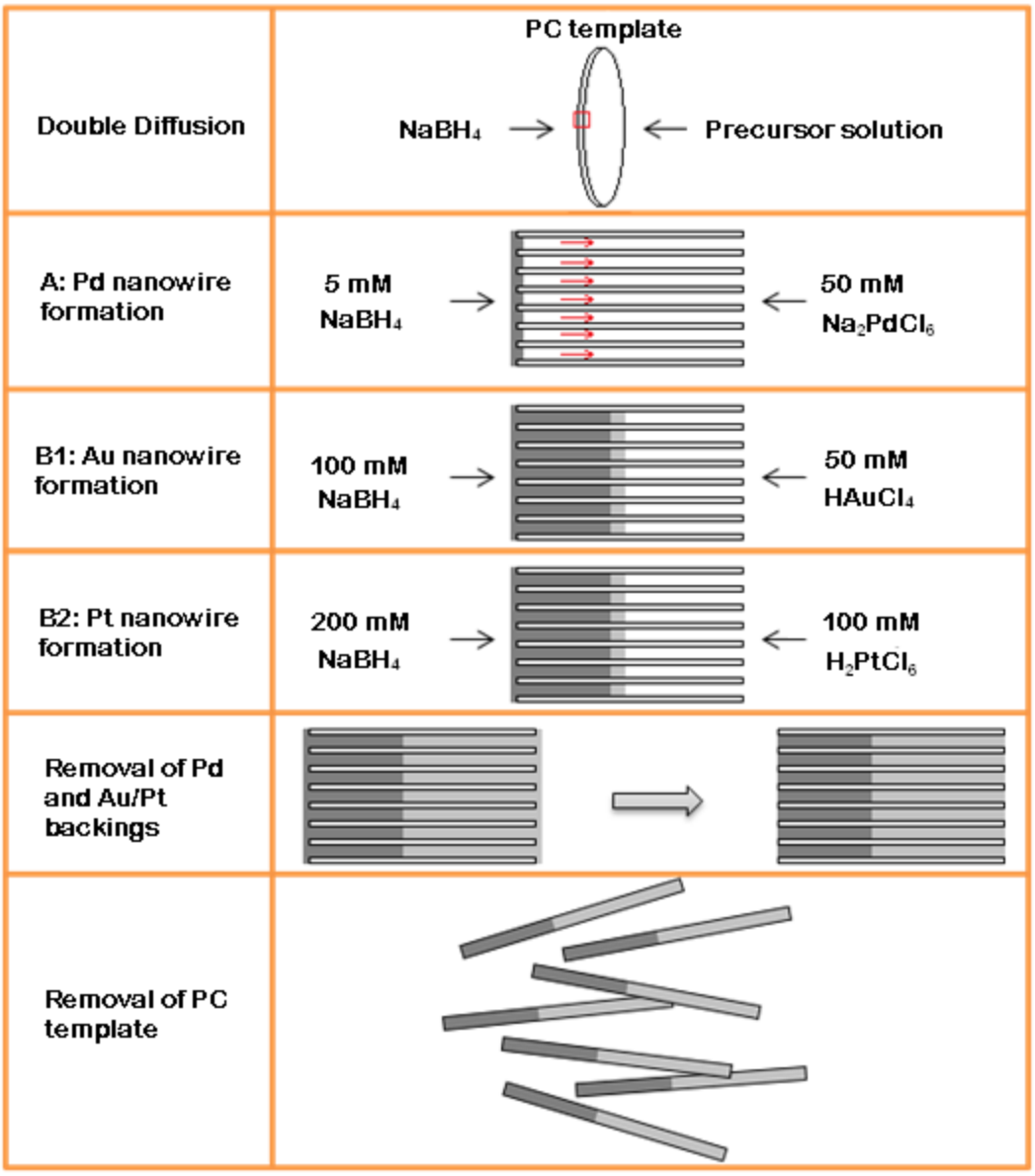

Figure 5.8 A schematic representation of the growth of segmented Pd/M (M = Pt or Au) NWs under double diffusion conditions within a representative array of 200 nm PC template pores. (Reprinted with permission from Ref. 40. Copyright © 2012 WILEY-VCH Verlag GmbH & Co. KGaA, Weinheim)

A detailed synthetic scheme of this two-step protocol in a series of representative template pore cross-sections is shown in Figure 5.8. In the first step, a high-quality single-crystalline Pd NW 'base' segment is grown into the template pore. The initiation of the reaction is signaled by visual corroboration of the formation of metallic material on the surface of the template directly exposed to the reducing agent half-cell. Subsequently, the single crystalline Pd NW segment elongates toward the precursor half-cell, as the reaction is allowed to continue. Once the desired length of the Pd NW is achieved, the electroless deposition process is suitably quenched by removing the palladium precursor and reducing agent solutions from the pores. The second segment consisting of either Au or Pt is then grown directly from the existing Pd NW segment by a second electroless deposition process, utilizing the appropriate precursor solution (*e.g.* either $HAuCl_4$ or H_2PtCl_6 depending on the desired result). The growth of this secondary segment is initiated at the surface of the existing metallic Pd NW, which serves as a conduit for the relatively efficient transport of electrons from the reducing agent half-cell to the interior of the pore space. The secondary segment, *i.e.* either Au or Pt, then elongates during this electroless deposition step, until crystalline growth extends beyond the template pore length, thereby resulting in the formation of metallic material on the template surface exposed to the precursor half-cell. Thus, the formation of a black or gold colored film in the case of the Pd/Pt and Pd/Au NWs, respectively on the surface of the template exposed to the precursor half-cell is an important visual cue provides key confirmation that the reaction has completed.

The relative lengths of the NW segments can be reliably and easily tuned by manipulating the reaction time for the growth of the Pd NW segment in the first electroless deposition step. Specifically, longer reaction times allow for increased crystalline growth and correspondingly longer Pd NW lengths within the template pore. Examination of the Pd segment

length in Pd/Au NWs by scanning electron microscopy (SEM) confirms that the length of the Pd segment grown in the first step systematically increases from 0.9 ± 0.1 μm to 6.7 ± 0.7 μm, as the reaction time is increased from 0 to 48 min. Not only is this trend in excellent agreement with that observed from the analogous Pd/Pt NWs but also these results are collectively consistent with prior data[38] obtained from elemental Pd NWs (*c.f.* Section 5.3.2 & Figure 5.6D). Since the pore channels of the commercially available PC templates that we use in our experiments maintain a nominal length of 6 – 8 μm, the ability to reproducibly and systematically tune the Pd NW length allows for direct control over the respective lengths of the individual segments, since the secondary segment consisting of either Pt or Au will necessarily occupy the remaining length of the template pore left unreacted by the Pd.

In essence, longer initial reaction times led to increased Pd NW lengths, leaving a proportionally smaller fraction of the full pore channel in which either the Au or Pt segment could grow. SEM images (Figure 5.9) obtained from as-prepared Pd/M ('M' = Pt or Au) NWs confirm that the trend in the relative length of the Pd and M segment is highly dependent upon the reaction time employed in the first electroless reduction step. The relative length of the Pd segment increased from 22.1% to 74.6% of the total NW length, as the initial reaction time was correspondingly raised from 10 to 45 min, for example. Thus, these results collectively substantiate our premise that high-quality, crystalline bimetallic NWs can be prepared with a broad range of segment lengths under completely ambient conditions without the need for either electrodeposition or PVD. Thus, the ability to achieve direct spatial control over chemical composition in noble metal NWs under ambient, solution-based conditions represents a critical and large advance towards the production of multifunctional nanostructures with a host of tunable and complementary functionalities.

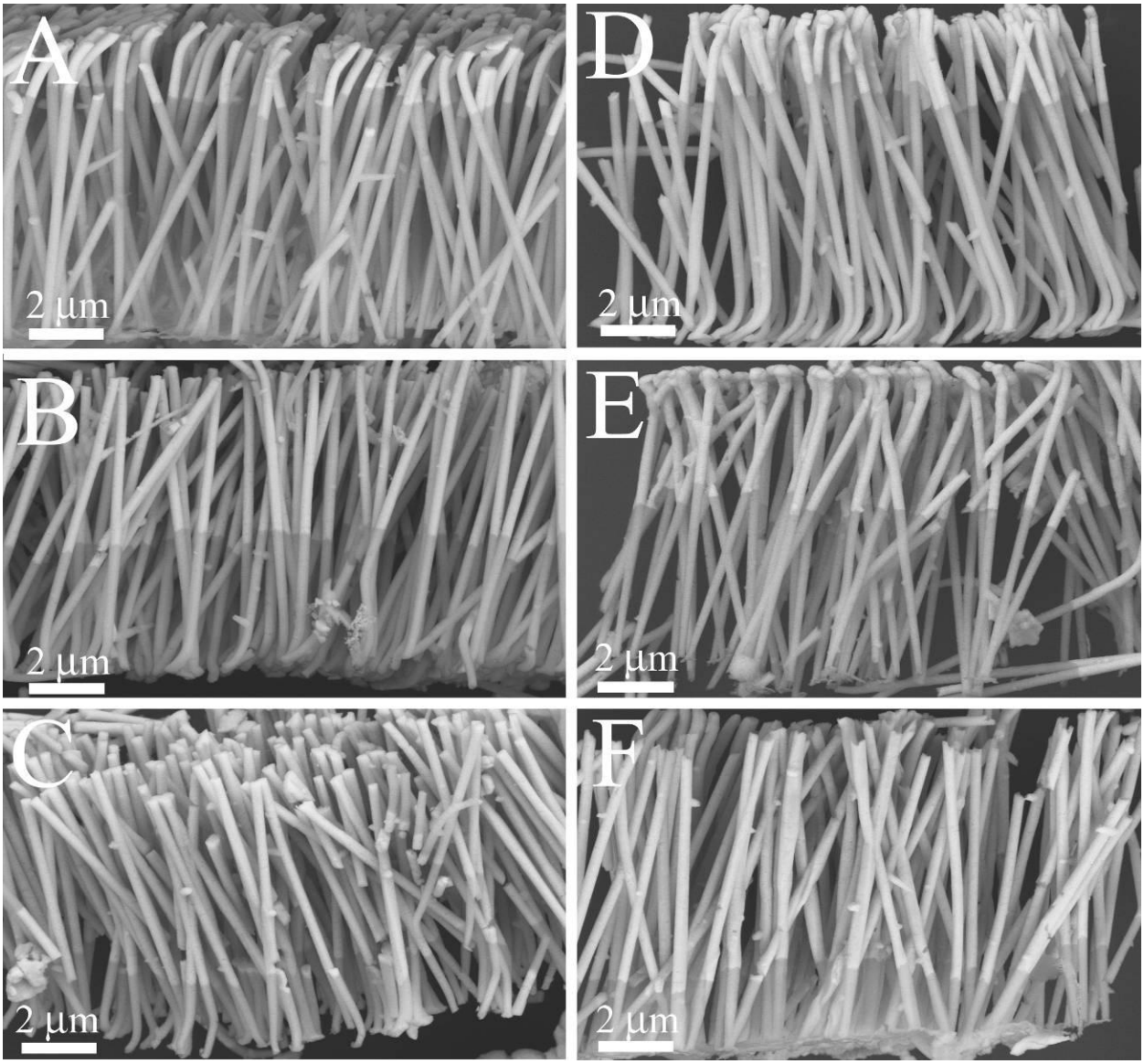

Figure 5.9 Characterization of segment length in A/B nanowires. SEM images of Pd/Pt (A – C) and Pd/Au (D – F) NWs with palladium representing 75 (A, D), 50 (B, E) and 25% (C, F) of the relative NW length. (Reprinted with permission from Ref. 40. Copyright © 2012 WILEY-VCH Verlag GmbH & Co. KGaA, Weinheim)

The quality and purity of the as-synthesized A/B nanostructures was probed by means of electron microscopy. First, SEM was employed to examine the morphology of as-prepared Pd/Pt and Pd/Au NWs as a function of the different segment lengths. Specifically, SEM images (Figure 5.9) obtained from collections of Pd/Pt and Pd/Au NWs with relative lengths of 1/3, 1/1, and 3/1 confirm that the as-prepared NWs maintain homogeneous anisotropic 1D structures. The NWs collectively possess diameters of 260 ± 30 nm, confirming that the NW dimensions are highly uniform over a broad range of segment lengths. In addition, the stark and sharp contrast between the Pd segment (low contrast) and either the Pt or Au segments (high contrast) in the SEM images highlights not only the segmented nature of the NWs but also confirms that our synthetic approach can lead to a well-defined, differentiable transition between the sub-units without a significant degree of alloying, noticeable at the interface. It is also apparent from the images that the relative segment lengths have been predictably controlled by systematically manipulating the reaction time.

A critical parameter in evaluating the quality of our NWs has been to investigate the compositional interface between the Pd and either the Pt or Au sub-units in individual NWs. In particular, we have taken specific steps in our reaction scheme so as to ensure the generation of segmented NWs with a sharp, well-defined interface between the two distinctive sub-units and to maximize the corresponding elemental purity of the respective sub-units. First, we employed a washing step between the growth of the Pd NW segment and the subsequent Pt or Au segment in order to remove residual Pd precursor from the template. Second, we purposefully and dramatically increased the concentration of reducing agent during the growth of the Pt and Au segments in order to suppress the galvanic displacement of the Pd NW by the Pt and Au precursors, and to thereby prevent alloy formation at the interface.

To examine the quality of the interface and purity of the elemental sub-units, we employed energy dispersive X-ray spectroscopy (EDAX) in scanning TEM mode. A representative EDAX map (Figure 5.10A) obtained at the interface of the Pd and Pt sub-units in a 1/1 Pd/Pt NW reveals a dramatic and precipitous boundary between Pd and Pt. The individual Pt-*L* edge (Figure 5.10B) and Pd-*L* edge (Figure 5.10C) confirm that there is a minimal degree of alloying present beyond the interfacial region. A high angle annular dark field image (HAADF) image shown as an inset to Figure 5.10A also reveals a sharp, abrupt, well-defined compositional interface between the Pd and Pt segments, thereby further reinforcing the notion of the intrinsically high quality of our as-prepared NWs. To complement the EDAX maps and HAADF images, an EDAX line scan centered about the interface (Figure 5.10D) was obtained to provide more detailed spatial information into the transitional region between the Pd and Pt sub-units. It is apparent from the line scan that the interface region of the NW with Pd and Pt coexisting at appreciable levels spans a length of 75 – 100 nm, representing only ~2% of the entire NW's length. More importantly, nearly undetectable Pt and Pd signals exist beyond the interfacial region associated with the Pd and Pt sub-units, implying that the degree of alloying is minimal. Similar data have been obtained in the characterization of the Pd/Au interface present on a representative 1/1 Pd/Au NW, a finding which further highlights the versatility of our synthesis.[40]

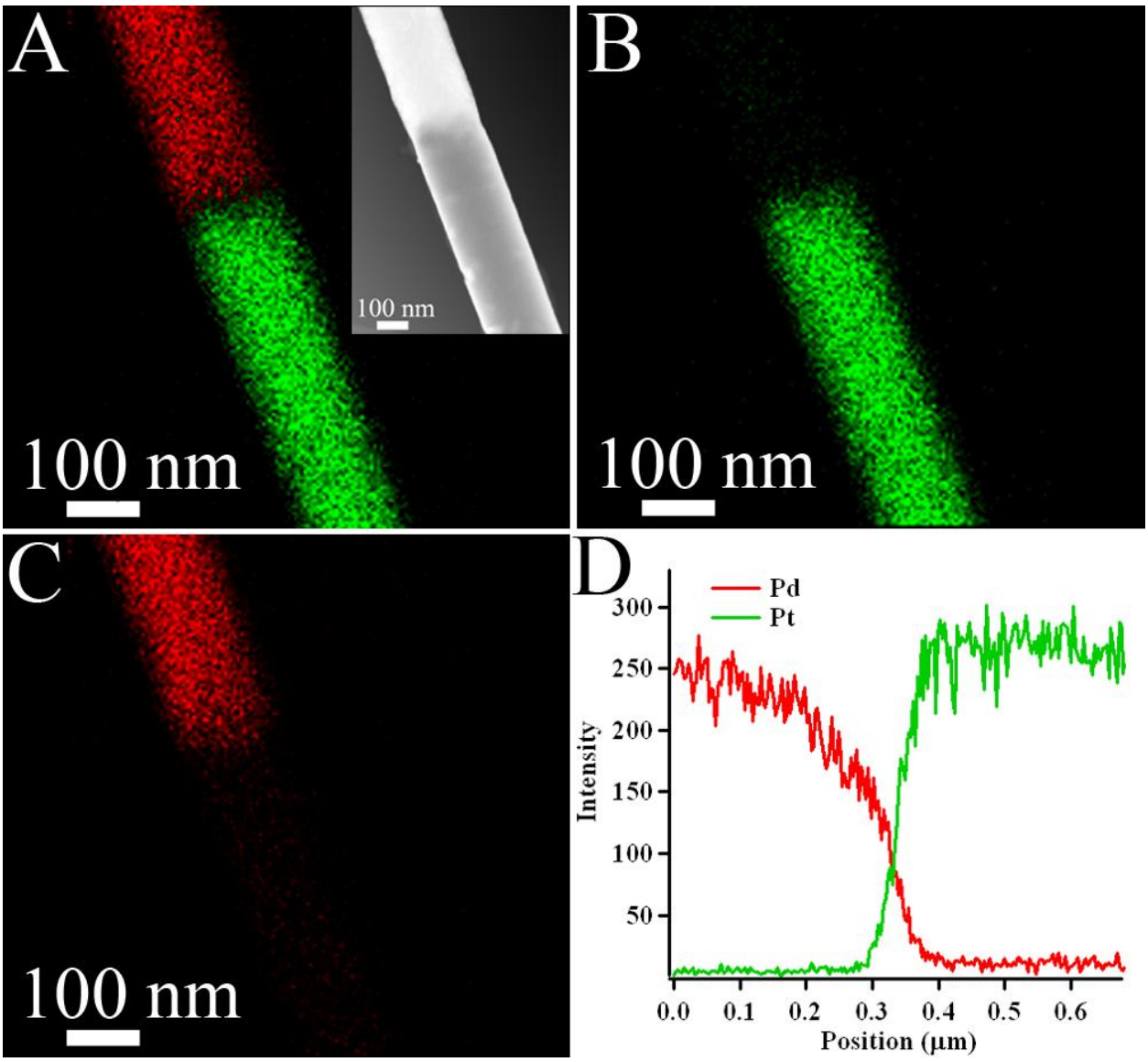

Figure 5.10 Characterization of the interfacial region in a representative segmented Pd/Pt NW. EDAX map of the combined Pd-*L* edge (red) and Pt-*L* edge (green) signals (A) and HAADF (inset) are shown, corresponding to the interfacial region between the Pd and Pt segments of a representative Pd/Pt segmented NW. EDAX maps separately highlighting the Pt signal (B) and Pd (C) are also shown. The intensity of the Pd (red line) and Pt (green line) EDAX signals is plotted (D) as a function of spatial position across the interfacial region. (Reprinted with permission from Ref. 40. Copyright © 2012 WILEY-VCH Verlag GmbH & Co. KGaA, Weinheim)

In the context of preparing segmented NWs as multifunctional nanostructures, we have investigated the performance of our as-prepared NWs as both electrocatalysts and as nanomotors.[40] In terms of electrocatalytic performance, cyclic voltammetry and CO stripping experiments indicate that the Pd/Pt and Pd/Au NWs maintain catalytically active Pd, Au, and Pt surface sites, reflective of the high purity of the elemental sub-units. In addition, we also examined the electrocatalytic oxygen reduction performance of the segmented NW systems and noted that the NWs possess ORR activities that are commensurate with their elemental analogues. Specifically, we observed that the Pd/Au NWs and Pd/Pt NWs maintain area-normalized ORR activities of 0.27 mA/cm^2 and 0.49 mA/cm^2, consistent with the mutual presence of elemental Pd and either Au or Pt, respectively. These results collectively suggest that the individual elemental sub-units preserve their distinctive inherent electrocatalytic properties, even when combined into a single segmented nanostructure. Therefore, these structures have the capacity to potentially serve as multifunctional catalysts, wherein different constituent components of a single NW might feasibly catalyze dissimilar types of reaction, such as ORR and MOR, for example.

To complement our examination of the catalytic properties, we also examined the potential of our as-prepared NWs as so-called nanomotors by characterizing the spontaneous locomotion of the Pd/Au and Pd/Pt NWs in a hydrogen peroxide (H_2O_2) solution, utilizing confocal microscopy.[40] These results established that the Pd/Au and Pd/Pt NWs maintain velocities of 3.15 μm/s and 4.15 μm/s in 9 M H_2O_2, respectively, which are three and four-fold higher than the corresponding velocities measured in distilled H_2O (*i.e.*, 1.36 μm/s and 1.07 μm/s, respectively). The measured velocity of the NWs can be reliably tuned by manipulating the concentration of H_2O_2 present in solution. Hence, these results collectively suggest that our

template-based approach (i) generates high-quality, high-purity, crystalline, segmented NWs with reliable control over the relative segment length and (ii) serves as a reasonably efficient, simple, scalable, and environmentally benign protocol for producing operationally effective multifunctional nanostructures on a sustainable basis.

5.3.4. Size-Dependent ORR Activity of Pd NWs

In addition to developing segmented NWs, the synthesis protocol was also employed to study the size-dependent electrocatalytic performance toward ORR in Pd NWs with diameters ranging from 270 nm to 2 nm. Initially, the electrochemical performance of the NWs was explored by cyclic voltammetry and CO stripping measurements. Specifically, cyclic voltammograms (CVs) obtained in a 0.1 M $HClO_4$ solution (Figure 5.11A) evinced the hydrogen adsorption/desorption (H_{ads}) peaks in the region of 0 – 0.2 V and the onset of surface oxide formation at approximately 0.7 V, which are consistent with that of nanostructured Pd catalysts and commercial Pd NP/C. The ESA of the various NW catalysts was determined in this case by integration of the CO stripping peak (Figure 5.11B). The CO stripping charge is used (*cf.* Chapter 2, Section 5) to estimate surface area, because in the case of Pd, the absorption of hydrogen into the lattice of Pd can contribute significantly to the measured H_{ads} charge, thereby making it unreliable for the accurate determination of surface area.

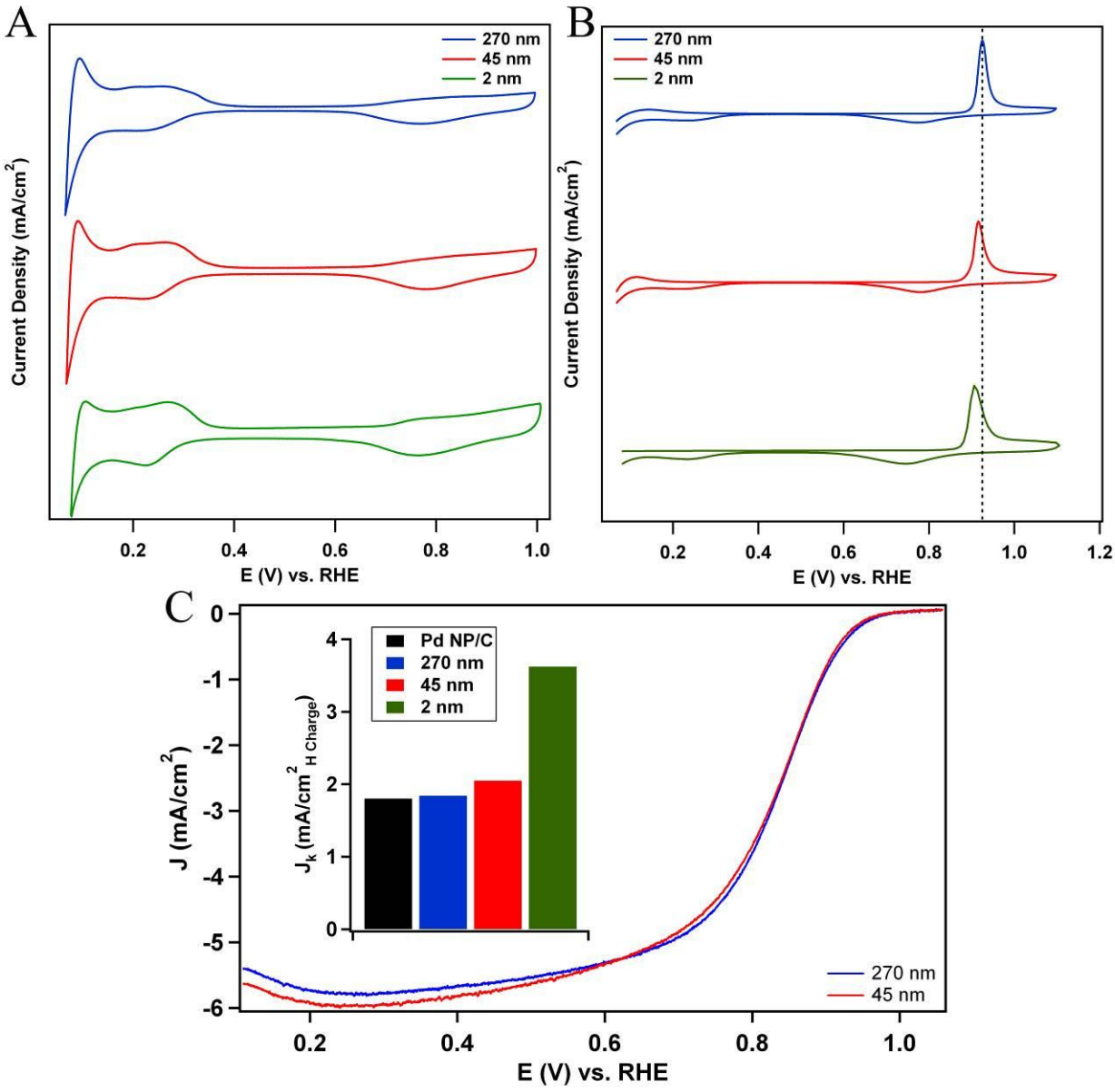

Figure 5.11 Size-dependent electrochemical properties and catalytic ORR performance in high-quality Pd NWs. Cyclic voltammograms (A) and CO stripping voltammograms (B) of the submicron and nanosized Pd NWs by comparison with the ultrathin Pd NW/C. Polarization curves (C) obtained from the submicron and nanosized Pd NWs immobilized on a Vulcan XC-72R modified GCE. The specific activities of the submicron and nanosized Pd NWs at 0.8 V are shown as an inset by comparison with the ultrathin Pd NW/C catalysts and commercial Pd NP/C catalysts. (Reprinted with permission from Ref. 38. Copyright 2011 American Chemical Society)

To explore the ORR activity of the submicron and nanosized Pd NWs, polarization curves shown in Figure 5.11C for the submicron and nanosized wires were obtained in oxygen-saturated 0.1 M $HClO_4$ solutions. The kinetic currents were extracted at 0.8 V and normalized to the ESA in order to probe the specific activity (shown in the inset of Figure 5.11C) of the catalysts. In this case, we have elected to utilize the kinetic currents at 0.8 V, since the catalysts show insignificant activity above 0.85 V. On the basis of this protocol, we have found that the measured specific activity doubles from 1.84 mA/cm^2 to 3.62 mA/cm^2, as the catalyst size is decreased from 270 nm to 2 nm. In this case, it is apparent that the submicron and nanosized Pd NWs maintain essentially the same performance as commercial Pd NP/C (*i.e.* 1.80 mA/cm^2), which is an important finding in demonstrating the significantly enhanced performance in ultrathin Pd NWs.

Although the structure-dependent enhancement in ORR activity has been previously explored in ultrathin Pd NWs and commercial Pd NP/C (*c.f.* Chapter 4, Section 3), the distinctive size-dependent enhancement specifically observed in this report is of critical interest, since activity tends to be enhanced with decreasing NW diameter. This trend starkly contrasts with analogous behavior observed in 0D NP catalysts, wherein decreases in size tend to result in lower activity as a result of an increased defect density as well as changes to the electronic structure of the catalysts.[77] In Chapter 3, we report a similar size-dependent enhancement in analogous Pt NW catalysts, wherein the specific activity increased from 0.38 mA/cm^2 to 1.45 mA/cm^2 in progressing from 200 nm Pt NTs to ultrathin ~1 nm Pt NWs.[6] Hence, the size-dependent performance enhancement appears to be quite generalized in the case of elemental, noble metal 1D ORR catalysts.

On the basis of prior theoretical[78-80] and experimental[81,82] results, the remarkable enhancement in activity of noble metal NWs as the diameter of the NW is decreased into the ultrathin regime (*e.g.* $d < 5$ nm) can be attributed to an advantageous structural reconfiguration, and a corresponding shift in the weighted center of the *d*-band.[2,3] On the basis of our discussion in Chapter 3, X-ray photoelectron spectra (XPS) data collected on ultrathin 2 nm Pt NW provided the first tangible spectroscopic evidence for a down-shift in the *d*-band owing to the anisotropic, ultrathin NW structure.[83] In support of this spectroscopic data, we have obtained CO stripping voltammograms (Figure 5.11B) for the various Pd NW catalysts tested. In effect, the down-shift of the *d*-band center due to surface-contracting strain is expected to weaken the CO binding strength and to improve its surface diffusion rate, which may lead to an improvement in CO monolayer oxidation kinetics.[84,85] In accordance with this supposition, the CO stripping peak did shift negatively from 0.925 V to 0.906 V, as the size of the NWs was decreased from 270 nm to 2 nm, which suggests that there is improved CO oxidation kinetics as the size of the NWs decreases. Hence, we believe that the trend in the CO stripping peak potential coupled with the recent XPS analysis of ultrathin Pt NWs provides for strong and complimentary evidence for a surface reconstruction process and a corresponding down-shift in the *d*-band energy, as the size of the NWs is decreased.

We should emphasize that variations in the crystalline facets likely do not play a significant role in the size-dependent electrocatalytic enhancement of the as-prepared NWs observed in this report. It has been previously shown with Pd single crystals that the (111), (100) and (110) facets maintain characteristic CO stripping and Cu UPD profiles owing to the unique surface structure of each facet.[86,87] Thus, CO stripping and Cu UPD represent useful tools for determining the surface structure of Pd NWs selectively and preferentially possessing different

low energy facets.[86] Herein, the structure of the Cu UPD and CO stripping profiles of our as-prepared NWs of various diameters remain largely identical as a function of size, with the obvious exception of the shift in peak potential, suggesting that these NWs possess similar surface facets. Hence, the shift in the CO stripping peak potential in combination with the recent XPS data point towards surface contraction as the main origin of the observed electrocatalytic enhancement in NW activity herein.

5.3.4. Size-Dependent ORR Activity of Core-Shell Pt_{ML}~Pd NWs

Although the size-dependent ORR activity of elemental catalysts has been previously studied in the case of Pt, there have been no reports, to the best of our knowledge, exploring the size-dependent activity in 1D nanostructured core-shell catalysts. However, determination of the size and structure-dependent properties of these highly active, hierarchical structures represents a critical step towards optimizing their performance for applications in working fuel cells. In this case, we utilized the well-defined Pd NWs from the previous section as substrates for Pt_{ML} deposition in order to develop size-controlled 1D Pt_M shell ~ Pd NW core (Pt_{ML}~Pd NW) catalysts for the purpose of studying the size-dependent electrocatalytic activity in these structures.

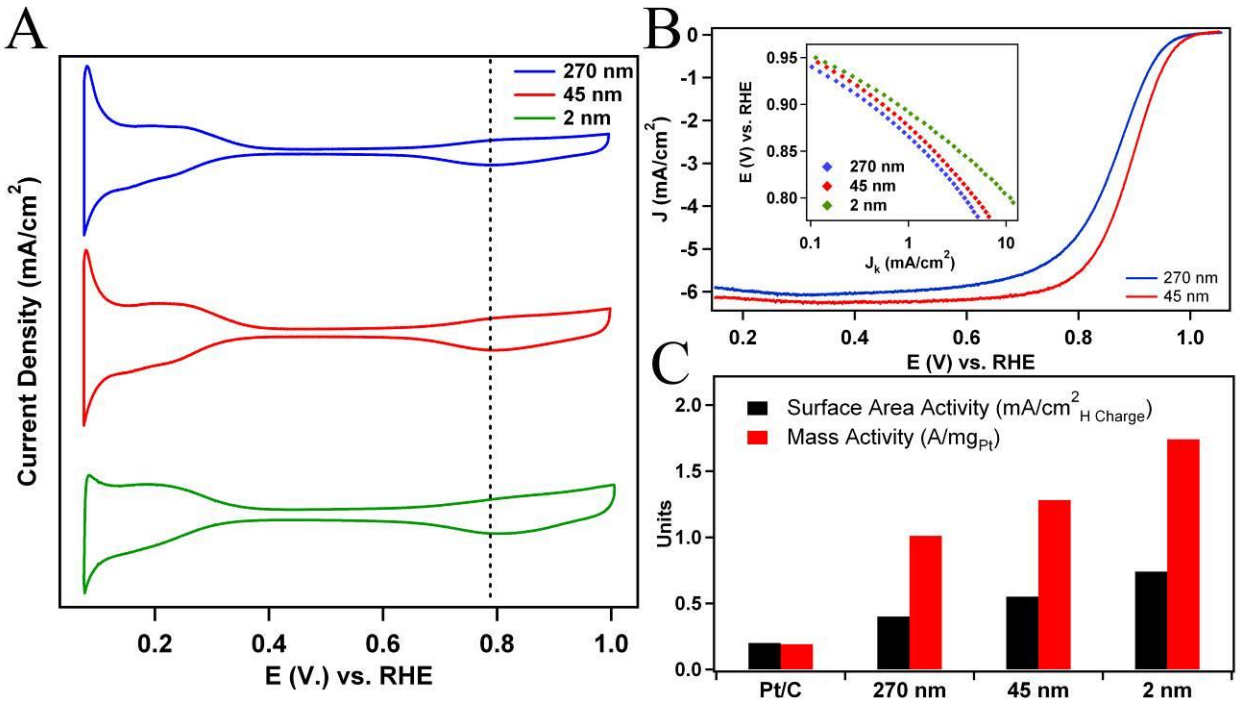

Figure 5.12 Size-dependent electrocatalytic properties in Pt_{ML}~Pd NWs. Cyclic voltammograms (A) obtained after Pt_{ML} deposition of the submicron and nanosized Pt_{ML}~Pd NWs by comparison with ultrathin Pt_{ML}~Pd NW/C composites. Polarization curves (B) of the submicron and nanosized Pt_{ML}~Pd NWs obtained on the NWs immobilized on a Vulcan XC-72 modified GCE. A potential vs. specific activity plot (J_K) is shown as an inset, corresponding to ultrathin Pt_{ML} ~ Pd NW/C, noted as a comparison. The specific activity (mA/cm^2) and the mass activity (A/mg_{Pt}) at 0.9 V for the Pt_{ML}~Pd NW samples are shown (C) by comparison with the ultrathin Pt_{ML} ~ Pd NW/C composites and commercial Pt NP/C. (Reprinted with permission from Ref. 38. Copyright 2011 American Chemical Society)

In this Chapter, the deposition of a Pt_{ML} onto the surface of the various Pd NWs was achieved by Cu UPD followed by galvanic displacement, in an analogous fashion to Chapter 4. Cyclic voltammograms obtained after the Pt_{ML} deposition process (Figure 5.12A) confirmed that a nearly complete Pt_{ML} was deposited onto the surface. More importantly, we also observed that the potential of the surface oxide reduction peak shifts from 0.788 V to 0.803 V, as the diameter of the NWs is decreased from 270 nm to 2 nm. A shift in the surface oxide feature to higher potentials is consistent with a weakening of the interaction between the metal surface and the oxygen adsorbate. Based upon the density functional theory (DFT) results of Nørskov and co-workers,[88,89] the observed weakening of the interaction with the oxygen adsorbate is consistent with a down-shift in the Pd *d*-band towards lower energies, a scenario which is likely expected to improve oxygen reduction kinetics and is consistent with the CO stripping results.

As expected, the core-shell NWs maintain significantly enhanced activity as compared with the Pd NWs (Figure 5.12B) before Pt_{ML} deposition, which further confirms the near monolayer deposition of Pt. In this case, the specific activity of the Pt_{ML}~Pd NW was determined by normalizing the measured kinetic currents obtained at 0.9 V to the measured ESA of the core-shell NWs, which can be directly deduced from the integration of the H_{ads} peaks of the composite structure. Similarly, the Pt mass activity can be readily obtained by normalizing the measured kinetic current at 0.9 V to the mass of Pt deposited, which can itself be determined from the Cu UPD profiles. We have summarized the average specific activity and platinum mass activity of the submicron, nanosized, and ultrathin Pt_{ML}~Pd NWs obtained from three separately prepared electrodes in Figure 5.12C, with commercial Pt NPs/C serving as a comparison. The measured area-specific and mass-specific activities were found to increase from 0.40 mA/cm^2 and 1.01 A/mg_{Pt} to 0.74 mA/cm^2 and 1.74 A/mg_{Pt}, respectively, as the measured NW diameter was

decreased from 270 nm to 2 nm. A potential vs. kinetic current plot presented as an inset to Figure 5.12B reveals that the size-dependent enhancement in activity is observed over the entire range of plausible operating potentials for a fuel cell cathode.

In a recent report by Adzic and co-workers, the ORR activity was studied as a function of particle size in 0D Pt_{ML}~Pd NP/C core-shell catalysts, and it was found that the measured activity decreases as the particle size is decreased below 10 nm, a finding consistent with those of elemental metal NPs.[90] However, the activity data in the case of 1D core-shell nanostructures are again in direct contrast with the trend observed for 0D catalysts. Specifically, the size-dependent phenomenon observed for 1D catalysts is extremely advantageous, since greatly enhanced activities can be achieved by decreasing the diameter of the catalyst. Hence, coupling the increased activity of ultrathin NW catalysts with their high surface area-to-volume ratio maximizes the precious metal loading and decreases the amount of inactive precious metal present in the core of the nanostructure. In fact, the ultrathin 2 nm Pt_{ML}~Pd NW composites have been shown to maintain a high total PGM mass activity of 0.55 A/mg_{PGM}.

In addition, we have demonstrated that the size-dependent electrocatalytic enhancement observed in elemental Pt and Pd can be generalized further to that of core-shell 1D nanostructures. As with Pd NWs, we believe that the performance enhancement in the case of the Pt_{ML}~Pd NWs arises from a diameter-dependent contraction of the Pd NW surface. Moreover, the enhancement in the ORR activity of the Pt_{ML} supported on both Pd NP and single crystal surfaces is believed to arise from a strain-induced compression of the Pt_{ML} in combination with a so-called electronic "ligand effect".[91] Based upon the results presented in Section 5.3.3, the use of 1D catalysts, possessing a diameter-dependent surface contraction as substrates for Pt_{ML} deposition, is expected to increase the strain-induced effect upon the Pt_{ML} and yield a

corresponding increase in the ORR activity. This effect is also apparent in the CV results presented in Figure 5.12A, wherein the potential of the surface oxide reduction peak shifts to higher potentials as the size is decreased. That is, an increase in the strain-induced contraction of the Pt_{ML} is expected to result in a shift of the Pt *d*-band to lower energies, and thereby weaken the interaction with surface adsorbates, such as oxygen.

5.3.5. Durability Testing of Submicron and Nanosized Pt_{ML}~Pd NWs

The electrochemical durability of the submicron and nanosized Pt_{ML}~Pd NWs was explored under half-cell conditions designed to simulate a catalyst lifetime.[38] The primary motive for studying the stability of these model catalysts is to verify that they maintain their structural integrity and function during electrochemical testing. In this Chapter, we utilize the same an electrochemical protocol described in Chapter 4 for testing ultrathin Pt_{ML}~Pd NW/C catalysts.[92] In this section, results are shown for the submicron (Figure 5.13A) and the nanosized (Figure 5.13B) Pt_{ML}~Pd NW samples, respectively, as a function of the percentage of ESA and specific activity over the course of these 20,000 cycles of operation.

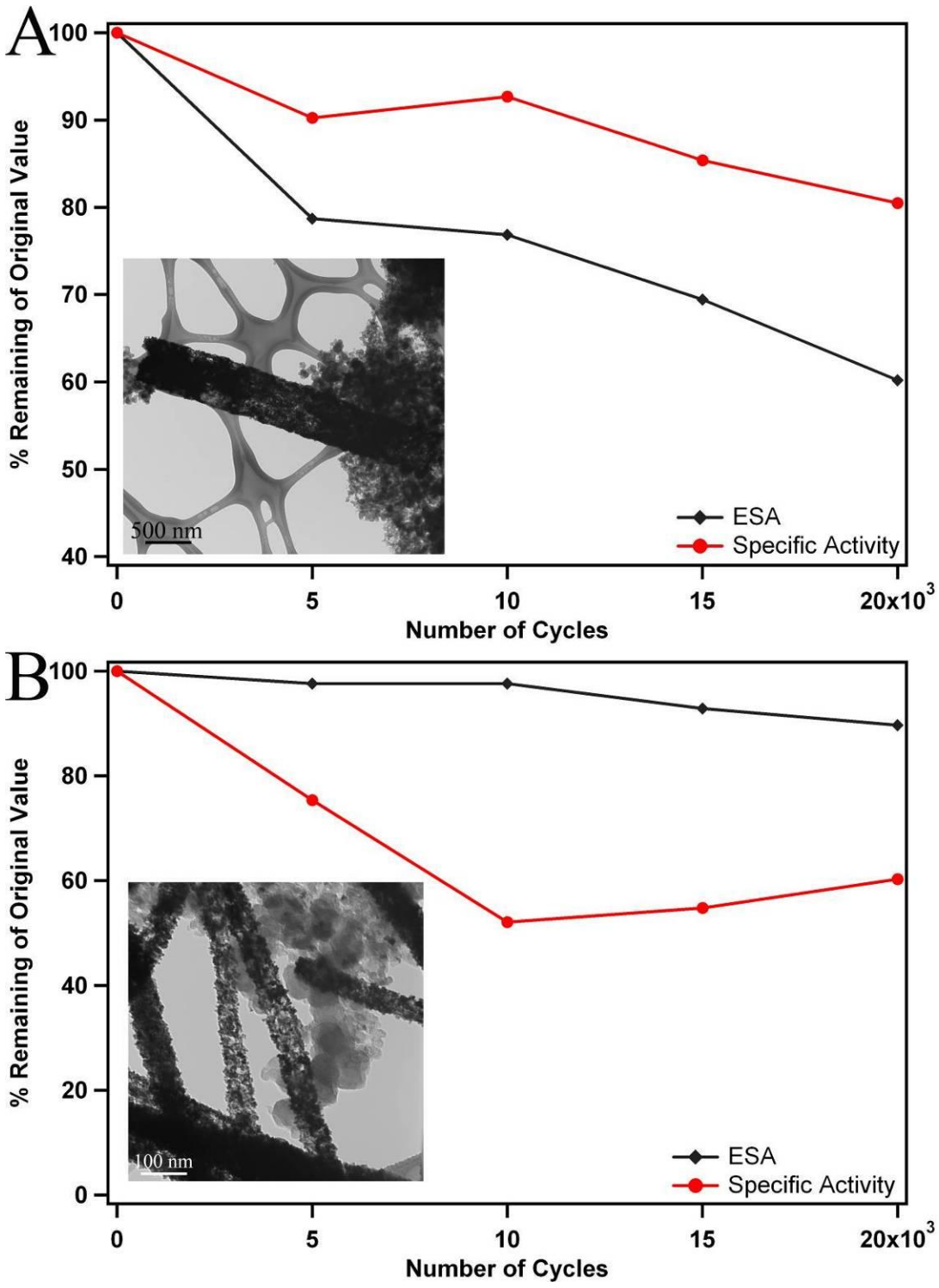

Figure 5.13 Durability results for the Pt_{ML}~Pd NW samples with submicron (A) and nanosized (B) diameters, shown as the percentage of remaining ESA (black) and specific activity (red) over the course of 20,000 cycles. Also shown as insets are representative TEM images of the nanostructures collected after 20,000 cycles of processing. (Reprinted with permission from Ref. 38. Copyright 2011 American Chemical Society)

The durability testing results show a decline in both the ESA and specific activity of the nanostructures over the course of the simulated lifetime. In the case of the surface area, the submicron and nanosized Pt_{ML}~Pd NWs retained 60.2% and 89.7% of their ESA, respectively, after 20,000 cycles. The observed trends in ESA decline can be attributed to a restructuring of the catalysts during the durability test. Based upon representative TEM images of the structures collected after 20,000 cycles, the submicron and nanosized structures largely maintain their 1D morphology. However, it is apparent that the nanosized wires evolve a textured and roughened, high surface area, porous structure, wherein the overall wire is composed of interconnected crystallites with microporous voids. The evolution of porosity in the submicron nanostructures is also apparent but analysis of many examples of these wires reveals that the effect is less substantial. Presumably, the formation of porous structures results from the preferential dissolution of the less noble Pd from the core of the nanostructures, which has been demonstrated to be the primary mechanism for ESA loss in analogous Pt_{ML}~Pd NPs.[93] At the conclusion of the test, the nanosized wires retain a higher percentage of their measured ESA by comparison with the submicron wires. It is evident from the TEM images that the corrosion of the nanosized wires promotes a greater degree of porosity, by comparison with the larger more robust submicron wires, which is consistent with the trend in ESA. However, additional insights are necessary to understand the difference in the corrosion process of these NWs.

In the case of the specific activity, the submicron and nanosized Pt_{ML}~Pd NWs retained ~80.5% and 60.3% of their specific activity, respectively, after 20,000 cycles. The proportionally higher loss of specific activity associated with nanosized wires is not surprising, given the significant morphological restructuring of the catalyst, during the cycling process. Specifically, the evolution of a porous particulate structure in combination with the formation of NPs is

expected to increase the number of defect sites significantly, thereby decreasing the catalyst's activity towards the ORR process.

5.4 Conclusions

In this report, we have prepared submicron (270 nm) and nanosized (45 nm) Pd NWs, utilizing a template-based approach that is not only sustainable but also allows for the preparation of high-quality nanostructures with predictable dimensions. The NWs in this case are largely single-crystalline and have been found to grow uniformly along the $[110]$ crystallographic direction. We observe that the growth of the NWs proceeds by two steps, wherein initially a polycrystalline segment is formed by rapid reduction and nucleation. Subsequently, we believe that the growth of the single crystalline segment continues through a secondary electroless deposition step, wherein electrons are transported through the growing wire itself. As a proof of concept, we have employed our U-tube technique to produce segmented Pd/Au and Pd/Pt NWs by performing two sequential electroless depositions. The as-prepared segmented NWs possess highly uniform elementally pure segments with well-defined interfaces between the segments and control over the relative length is readily achieved by varying the reaction time in the first deposition step.

The ORR activity of optimized submicron and nanosized Pd NWs was determined electrochemically and compared with the activity of ultrathin 2 nm Pd NW/C samples, which revealed a size-dependent electrocatalytic enhancement of nearly two-fold, as the wire diameter was decreased. After the deposition of a Pt_{ML} onto the Pd NW substrates, the core-shell Pt_{ML}~Pd NWs displayed a similar size-dependent enhancement of nearly two-fold in both specific activity and platinum mass activity. Thus, this current report demonstrates that the diameter-dependent

enhancement in ORR activity can be generalized from not only Pt but also, for the first time, to Pd and Pt_{ML}~Pd core-shell NW structures. We believe that the observed size-dependent trend results from a diameter-dependent contraction of the Pd NW surface, as the diameter is decreased, an observation which is expected to increase the inherent ORR activity.

The observed size-dependent trend reported herein is of great interest, since it starkly contrasts with the trend observed in analogous 0D NP catalysts. The activity in 1D structures can be optimized by decreasing the diameter, which has the added benefit of maximizing the precious metal loading of these catalysts. More importantly, we expect that this size-dependent property can be further generalized to include alloyed, segmented, and hierarchical metallic NWs, which will allow for further optimization of activity.

5.5 References

(1) *Fuel Cell Catalysts*; Koper, M. T. M., Ed.; Wiley Interscience: Hoboken, NJ, 2009.
(2) Koenigsmann, C.; Scofield, M. E.; Liu, H.; Wong, S. S. *J. Phys. Chem. Lett.* **2012**, *3*, 3385-3398.
(3) Koenigsmann, C.; Wong, S. S. *Energy Environ. Sci.* **2011**, *4*, 1161 - 1176.
(4) Antolini, E.; Perez, J. *J. Mater. Sci.* **2011**, *46*, 1-23.
(5) Koenigsmann, C.; Santulli, A. C.; Gong, K.; Vukmirovic, M. B.; Zhou, W.-p.; Sutter, E.; Wong, S. S.; Adzic, R. R. *J. Am. Chem. Soc.* **2011**, *133*, 9783-9795.
(6) Koenigsmann, C.; Zhou, W.-p.; Adzic, R. R.; Sutter, E.; Wong, S. S. *Nano Lett.* **2010**, *10*, 2806-2811.
(7) Tiano, A. L.; Koenigsmann, C.; Santulli, A. C.; Wong, S. S. *Chem. Commun.* **2010**, *46*, 8093-8130.
(8) Teng, X.; Han, W.; Ku, W.; Hucker, M. *Angew. Chem. Int. Ed.* **2008**, *47*, 2055-2058.
(9) Song, Y.; Garcia, R. M.; Dorin, R. M.; Wang, H.; Qiu, Y.; Coker, E. N.; Steen, W. A.; Miller, J. E.; Shelnutt, J. A. *Nano Lett.* **2007**, *7*, 3650-3655.
(10) Ksar, F. a.; Surendran, G.; Ramos, L.; Keita, B.; Nadjo, L.; Prouzet, E.; Beaunier, P.; Hagège, A. s.; Audonnet, F.; Remita, H. *Chem. Mater.* **2009**, *21*, 1612-1617.
(11) Caihong, F.; Zhang, R.; Yin, P.; Li, L.; Guo, L.; Shen, Z. *Nanotechnology* **2008**, *19*, 305601.
(12) Yuan, Q.; Zhou, Z.; Zhuang, J.; Wang, X. *Chem. Mater.* **2010**, *22*, 2395-2402.
(13) Yuan, Q.; Zhuang, J.; Wang, X. *Chem. Commun.* **2009**, 6613-6615.
(14) Liang, H.-W.; Liu, S.; Gong, J.-Y.; Wang, S.-B.; Wang, L.; Yu, S.-H. *Adv. Mater.* **2009**, *21*, 1850-1854.

(15) Chen, Z.; Waje, M.; Li, W.; Yan, Y. *Angew. Chem. Int. Ed.* **2007**, *46*, 4060-4063.
(16) Wang, C.; Daimon, H.; Onodera, T.; Koda, T.; Sun, S. *Angew. Chem. Int. Ed.* **2008**, *47*, 3588-3591.
(17) Xiong, Y.; Xia, Y. *Adv. Mater.* **2007**, *19*, 3385-3391.
(18) Huang, X.; Zheng, N. *J. Am. Chem. Soc.* **2009**, *131*, 4602-4603.
(19) Lu, Y.; Wang, Y.; Chen, W. *J. Power Sources* **2011**, *196*, 3033-3038.
(20) Koenigsmann, C.; Sutter, E.; Adzic, R. R.; Wong, S. S. *J. Phys. Chem. C* **2012**, *116*, 15297-15306.
(21) Teng, X.; Feygenson, M.; Wang, Q.; He, J.; Du, W.; Frenkel, A. I.; Han, W.; Aronson, M. *Nano Lett.* **2009**, *9*, 3177-3184.
(22) Sun, Y.; Zhang, L.; Zhou, H.; Zhu, Y.; Sutter, E.; Ji, Y.; Rafailovich, M. H.; Sokolov, J. C. *Chem. Mater.* **2007**, *19*, 2065-2070.
(23) Xia, Y.; Yang, P.; Sun, Y.; Wu, Y.; Mayers, B.; Gates, G.; Yin, Y.; Kim, F.; Yan, H. *Adv. Mater.* **2003**, *15*, 353-389.
(24) Hurst, S. J.; Payne, E. K.; Qin, L.; Mirkin, C. A. *Angew. Chem. Int. Ed.* **2006**, *45*, 2672-2692.
(25) Kline, T. R.; Tian, M.; Wang, J.; Sen, A.; Chan, M. W. H.; Mallouk, T. E. *Inorg. Chem.* **2006**, *45*, 7555-7565.
(26) Liang, H.-W.; Liu, S.; Yu, S.-H. *Adv. Mater.* **2010**, *22*, 3925-3937.
(27) Perry, J. L.; Martin, C. R.; Stewart, J. D. *Chem-Eur. J.* **2011**, *17*, 6296-6302.
(28) Chen, A.; Holt-Hindle, P. *Chem. Rev.* **2010**, *110*, 3767-3804.
(29) Zhou, H.; Zhou, W.-p.; Adzic, R. R.; Wong, S. S. *J. Phys. Chem. C* **2009**, *113*, 5460-5466.
(30) Wang, Z.-j.; Xie, Y.; Liu, C.-j. *J. Phys. Chem. C* **2008**, *112*, 19818-19824.
(31) Azulai, D.; Belenkova, T.; Gilon, H.; Barkay, Z.; Markovich, G. *Nano Lett.* **2009**, *9*, 4246-4249.
(32) Kijima, T.; Yoshimura, T.; Uota, M.; Ikeda, T.; Fujikawa, D.; Mouri, S.; Uoyama, S. *Angew. Chem. Int. Ed.* **2004**, *43*, 228-232.
(33) Xu, Z.; Shen, C.; Sun, S.; Gao, H. J. *J. Phys. Chem. C* **2009**, *113*, 15196-15200.
(34) Zhang, J.; Liu, H.; Wang, Z.; Ming, N. *Adv. Funct. Mater.* **2007**, *17*, 3295-3303.
(35) Tsukamoto, R.; Muraoka, M.; Seki, M.; Tabata, H.; Yamashita, I. *Chem. Mater.* **2007**, *19*, 2389-2391.
(36) Wang, H.; Xu, C.; Cheng, F.; Jiang, S. *Electrochem. Commun.* **2007**, *9*, 1212-1216.
(37) Patete, J. M.; Peng, X.; Koenigsmann, C.; Xu, Y.; Karn, B.; Wong, S. S. *Green Chem.* **2011**, *13*, 482-519.
(38) Koenigsmann, C.; Santulli, A. C.; Sutter, E.; Wong, S. S. *ACS Nano* **2011**, *5*, 7471-7487.
(39) Koenigsmann, C.; Sutter, E.; Chiesa, T. A.; Adzic, R. R.; Wong, S. S. *Nano Lett.* **2012**, *12*, 2013-2020.
(40) Koenigsmann, C.; Tan, Z.; Peng, H.; Sutter, E.; Jacobskind, J.; Wong, S. S. *Isr. J. Chem.* **2012**, *52*, 1090-1103.
(41) Zhang, F.; Yiu, Y.; Aronson, M. C.; Wong, S. S. *J. Phys. Chem. C* **2008**, *112*, 14816-14824.
(42) Zhang, F.; Wong, S. S. *ACS Nano* **2009**, *4*, 99-112.
(43) Zhang, F.; Wong, S. S. *Chem. Mater.* **2009**, *21*, 4541-4554.
(44) Zhang, F.; Sfeir, M. Y.; Misewich, J. A.; Wong, S. S. *Chem. Mater.* **2008**, *20*, 5500-5512.
(45) Zhang, F.; Mao, Y.; Park, T.-J.; Wong, S. S. *Adv. Funct. Mater.* **2008**, *18*, 103-112.

(46) Mao, Y.; Zhang, F.; Wong, S. *Adv. Mater.* **2006**, *18*, 1895-1899.
(47) Mao, Y.; Wong, S. S. *J. Am. Chem. Soc.* **2004**, *126*, 15245-15252.
(48) Wong, S. S.; Koenigsmann, C. Surfactantless Metallic Nanostructures and Methods for Synthesizing Same.U.S. Patent Application 20130084210, 2013.
(49) Koenigsmann, C.; Semple, D. B.; Sutter, E.; Tobierre, S. E.; Wong, S. S. *ACS Appl. Mater. Interfaces* **2013**, *5*, 5518-5530.
(50) Schönenberger, C.; van der Zande, B. M. I.; Fokkink, L. G. J.; Henny, M.; Schmid, C.; Krüger, M.; Bachtold, A.; Huber, R.; Birk, H.; Staufer, U. *J. Phys. Chem. B* **1997**, *101*, 5497-5505.
(51) Favier, F.; Walter, E. C.; Zach, M. P.; Benter, T.; Penner, R. M. *Science* **2001**, *293*, 2227-2231.
(52) Yun, M.; Myung, N. V.; Vasquez, R. P.; Lee, C.; Menke, E.; Penner, R. M. *Nano Lett.* **2004**, *4*, 419-422.
(53) Cheng, F.; Wang, H.; Sun, Z.; Ning, M.; Cai, Z.; Zhang, M. *Electrochem. Commun.* **2008**, *10*, 798-801.
(54) Kartopu, G.; Habouti, S.; Es-Souni, M. *Mater. Chem. Phys.* **2008**, *107*, 226-230.
(55) Sharabani, R.; Reuveni, S.; Noy, G.; Shapira, E.; Sadeh, S.; Selzer, Y. *Nano Lett.* **2008**, *8*, 1169-1173.
(56) Cui, S. T. *J. Chem. Phys.* **2005**, *123*, 054706-054704.
(57) Crank, J. *The Mathematics of Diffusion*; Oxford University Press: Oxford, UK, 1975.
(58) Keating, C. D.; Natan, M. J. *Adv. Mater.* **2003**, *15*, 451-454.
(59) Stoermer, R. L.; Cederquist, K. B.; McFarland, S. K.; Sha, M. Y.; Penn, S. G.; Keating, C. D. *J. Am. Chem. Soc.* **2006**, *128*, 16892-16903.
(60) Brunker, S. E.; Cederquist, K. B.; Keating, C. D. *Nanomedicine* **2007**, *2*, 695.
(61) Reich, D. H.; Tanase, M.; Hultgren, A.; Bauer, L. A.; Chen, C. S.; Meyer, G. J. *J. Appl. Phys.* **2003**, *93*, 7275.
(62) Kline, T. R.; Paxton, W. F.; Mallouk, T. E.; Sen, A. *Angew. Chem. Int. Ed.* **2005**, *44*, 744-746.
(63) Ibele, M. E.; Wang, Y.; Kline, T. R.; Mallouk, T. E.; Sen, A. *J. Am. Chem. Soc.* **2007**, *129*, 7762-7763.
(64) Paxton, W. F.; Sundararajan, S.; Mallouk, T. E.; Sen, A. *Angew. Chem. Int. Ed.* **2006**, *45*, 5420-5429.
(65) Dhar, P.; Fischer, T. M.; Wang, Y.; Mallouk, T. E.; Paxton, W. F.; Sen, A. *Nano Lett.* **2006**, *6*, 66-72.
(66) Hong, Y.; Blackman, N. M. K.; Kopp, N. D.; Sen, A.; Velegol, D. *Phys. Rev. Lett.* **2007**, *99*, 178103.
(67) Hong, Y.; Velegol, D.; Chaturvedi, N.; Sen, A. *PCCP* **2010**, *12*, 1423-1435.
(68) Ibele, M.; Mallouk, T. E.; Sen, A. *Angew. Chem. Int. Ed.* **2009**, *48*, 3308-3312.
(69) Paxton, W. F.; Sen, A.; Mallouk, T. E. *Chem. Eur. J.* **2005**, *11*, 6462-6470.
(70) Wang, Y.; Hernandez, R. M.; Bartlett, D. J., Jr.; Bingham, J. M.; Kline, T. R.; Sen, A.; Mallouk, T. E. *Langmuir* **2006**, *22*, 10451-10456.
(71) Sundararajan, S.; Lammert, P. E.; Zudans, A. W.; Crespi, V. H.; Sen, A. *Nano Lett.* **2008**, *8*, 1271-1276.
(72) Wang, J. *ChemPhysChem* **2009**, *10*, 1748-1755.
(73) Liu, F.; Lee, J.; Zhou, W. *Small* **2006**, *2*, 121-128.
(74) Liu, F.; Lee, J. Y.; Zhou, W. *J. Electrochem. Soc.* **2006**, *153*, A2133-A2138.

(75) Liu, F.; Lee, J. Y.; Zhou, W. J. *Adv. Funct. Mater.* **2005**, *15*, 1459-1464.
(76) Shaijumon, M. M.; Ou, F. S.; Ci, L.; Ajayan, P. M. *Chem. Commun.* **2008**, 2373-2375.
(77) Shao, M.; Peles, A.; Shoemaker, K. *Nano Lett.* **2011**, *11*, 3714-3719.
(78) Fiorentini, V.; Methfessel, M.; Scheffler, M. *Phys. Rev. Lett.* **1993**, *71*, 1051-1054.
(79) van Beurden, P.; Kramer, G. J. *J. Chem. Phys.* **2004**, *121*, 2317-2325.
(80) Haftel, M. I.; Gall, K. *Phys. Rev. B: Condens. Matter* **2006**, *74*, 035420-035412.
(81) Kondo, Y.; Takayanagi, K. *Phys. Rev. Lett.* **1997**, *79*, 3455.
(82) Kondo, Y.; Takayanagi, K. *Science* **2000**, *289*, 606-608.
(83) Wang, S.; Jiang, S. P.; Wang, X.; Guo, J. *Electrochim. Acta* **2011**, *56*, 1563-1569.
(84) Maillard, F.; Savinova, E. R.; Stimming, U. *J. Electroanal. Chem.* **2007**, *599*, 221-232.
(85) Maillard, F.; Eikerling, M.; Cherstiouk, O. V.; Schreier, S.; Savinova, E.; Stimming, U. *Faraday Discuss.* **2004**, *125*, 357-377.
(86) Xiao, L.; Zhuang, L.; Liu, Y.; Lu, J.; Abruña, H. c. D. *J. Am. Chem. Soc.* **2008**, *131*, 602-608.
(87) Hara, M.; Linke, U.; Wandlowski, T. *Electrochim. Acta* **2007**, *52*, 5733-5748.
(88) Nørskov, J. K.; Rossmeisl, J.; Logadottir, A.; Lindqvist, L.; Kitchin, J. R.; Bligaard, T.; Jonsson, H. *J. Phys. Chem. B* **2004**, *108*, 17886-17892.
(89) Greeley, J.; Nørskov, J. K. *J. Phys. Chem. C* **2009**, *113*, 4932-4939.
(90) Wang, J. X.; Inada, H.; Wu, L.; Zhu, Y.; Choi, Y.; Liu, P.; Zhou, W.-P.; Adzic, R. R. *J. Am. Chem. Soc.* **2009**, *131*, 17298-17302.
(91) Zhang, J.; Vukmirovic, M. B.; Xu, Y.; Mavrikakis, M.; Adzic, R. R. *Angew. Chem. Int. Ed.* **2005**, *44*, 2132-2135.
(92) *Multi-Year Research, Development and Demonstration Plan: Planned Program Activities for 2005-2015*, Department of Energy, 2009.
(93) Sasaki, K.; Naohara, H.; Cai, Y.; Choi, Y. M.; Liu, P.; Vukmirovic, M. B.; Wang, J. X.; Adzic, R. R. *Angew. Chem. Int. Ed.* **2010**, *49*, 8602-8607.

Chapter 6. Highly Enhanced Electrocatalytic Oxygen Reduction and Methanol Oxidation Performance in Bimetallic Palladium-Based Nanowires Prepared Under Ambient, Surfactantless, Conditions

6.1 Introduction

Throughout Chapters 3 – 5, the primary focus has been on developing a robust understanding of structure-property correlations in novel 1D noble metal nanostructures. Specifically, we have elucidated important morphology- and size-dependent behavior in noble metal NWs, which has elevated consideration of ultrathin Pt and Pd NWs as a promising new structural paradigm in the role of PEMFC catalysts.[1-3] However, a key objective in further advancing the performance of elemental platinum group metals as ORR electrocatalysts has been to control their chemical composition, so as to manipulate their corresponding electronic and structural properties for enhanced activity.[4,5] In this context, it is conceivable that electrocatalytic performance will depend heavily upon the spatial distribution of elements (Figure 6.1) present within the discrete nanostructures themselves, in addition to the nature of the chemical composition, itself.

For example, the Pt_{ML}~Pd NW structures presented in Chapters 4 & 5 combine two elements into core-shell type configurations, wherein enhanced Pt-mass normalized ORR performance is achieved by isolating the entire Pt content at the catalytic interface.[1,2] Alternatively, we have also developed a reliable synthetic approach for the production of segmented, bimetallic NWs, wherein individual bimetallic NWs consist of two, pure, elemental noble metal segments with direct and predictable control over composition (*i.e.* relative segment length).[6] The ability to tailor composition in segmented nanostructures is an important step in generating multifunctional nanostructures, wherein each individual segment is capable of performing a distinctive function within a single discrete nanostructure.

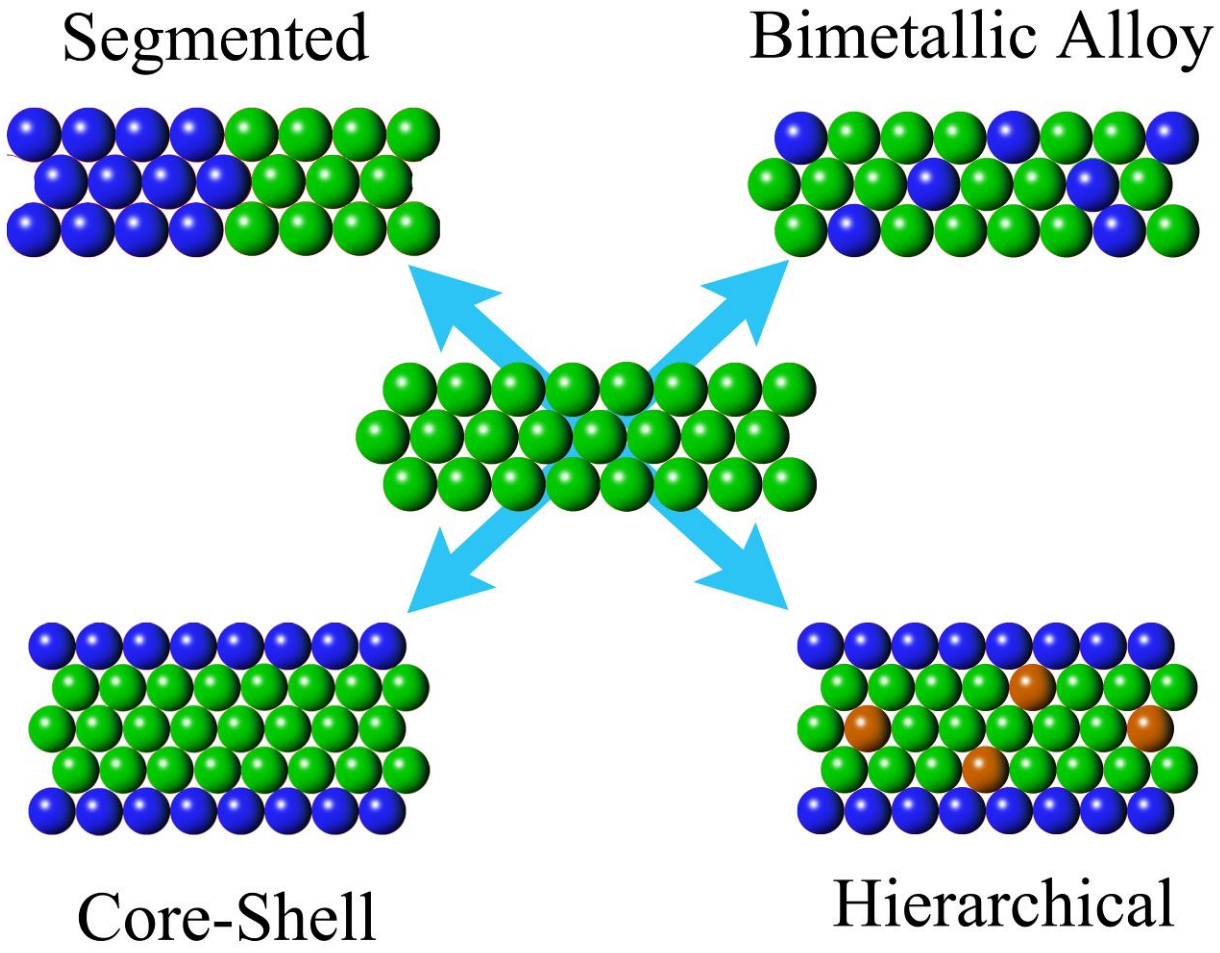

Figure 6.1 A schematic representation of different 1D structures, wherein composition is controlled spatially. Elemental NWs (center) can be combined with a second element in a homogeneous fashion to give a bimetallic alloy (top right) or in an inhomogeneous fashion to yield either segmented (top left) or core-shell structures (bottom left). Coupling two or more of these design principles can lead to interesting hierarchical structures (bottom right), for example.

In chapters 6 & 7, we consider the role of composition in bimetallic alloy-type systems, wherein the elemental composition is uniform throughout the entire catalyst.[7,8] Recently, there have been several examples in the literature, where 1D electrocatalysts are synthesized with bimetallic and ternary alloy-type compositions. Salient examples, which have evinced detectable enhancements in performance, include but are not limited to PdPt,[9-11] PdCu,[12] PdAu,[9,13] PtFe,[14-16] PtAu(Ni),[17,18] PtPdBi[19] and PtCo.[16] For example, Li and co-workers have prepared $Pt_{1-x}Fe_x$ NWs with ultrathin diameters of ~3 nm, which possess noticeable enhancements in mass activity as compared with commercial Pt NP/C, even after a mild durability test.[15] However, a lingering challenge that remains in the further development of these multi-metallic 1D catalysts has been to systematically examine the role of chemical composition in the context of complementing and strengthening the already distinctive properties of 1D architectures. This issue is important, because despite their improved specific activity, many of these bimetallic 1D systems continue to maintain mass activities that fall within the range, typically measured for commercial 0D Pt NP/C ($0.1 – 0.2$ A/mg_{Pt}).

To address this deficiency, we have optimized our template-based U-tube double diffusion technique described in Chapter 5 to enable the production of bimetallic $Pd_{1-x}Pt_x$ and $Pd_{1-x}Au_x$ NWs, wherein the chemical composition is directly and predictably controlled over the entire plausible composition regime (*e.g.* $x = 0 – 1$).[9,20] In the terms of examining composition-dependent electrocatalytic trends, this technique is particularly valuable since high quality NWs can be prepared with minimal variations in the dimensions, purity, crystallinity, homogeneity, or texture. Thus, the composition of the as-prepared NW is highlighted as the key parameter in determining electrocatalytic performance. Given the advantages of this synthetic technique, we examine the role of composition in the context of three technical challenges, which have

hindered the development of electrocatalysts for practical direct alcohol fuel cells (DAFCs), outlined in Chapter 1.[5,21,22]

First, we consider the role of composition in $Pd_{1-x}Pt_x$ and $Pd_{1-x}Au_x$ NWs toward the oxygen reduction reaction. Bimetallic Pd-based alloys have garnered particular interest in the recent literature owing to their potential for high electrocatalytic activity toward ORR. In particular, the incorporation of Au into Pd-Au alloys has been widely demonstrated to modify the structural and electronic properties of Pd contributing to greatly enhanced ORR activity, in some cases beyond that of commercial Pt NP/C.[23-28] Therefore, the $Pd_{1-x}Au_x$ alloys may represent a feasible "Pt-free" alternative to traditional Pt NP/C. On the basis of these preliminary results, we examine the composition-dependent ORR performance in high-quality $Pd_{1-x}Pt_x$ and $Pd_{1-x}Au_x$ NWs so as to examine the complex interplay between structure, composition and catalytic activity.

Second, the problem of methanol crossover from the anode to the cathode in DMFCs is significant, and can result in considerable loss of ORR performance, due to parasitic oxidation and catalyst poisoning effects.[29,30] Thus, we have systematically examined the influence of methanol (MeOH) on the ORR behavior of $Pd_{1-x}Pt_x$ and $Pd_{1-x}Au_x$ NWs as a function of chemical composition. The incorporation of palladium is advantageous, since it evinces a relatively high activity toward ORR amongst the noble metals but is largely inert to the oxidation of MeOH at potentials relevant for ORR.[31-35] More importantly, the distinctive properties of 1D noble metal nanostructures, including their size-dependent CO oxidation performance (*c.f.* Chapter 5), may render them intrinsically more tolerant to the presence of the ubiquitous small organic molecule (SOM) impurities, which are normally prevalent in actual fuel cell systems.

Third, the catalytic oxidation of SOMs, such as methanol and ethanol on noble metals, maintains slow kinetics, and often requires high overpotentials, due to the poisoning effects of carbon monoxide.[36,37] This issue has necessitated the need for high precious metal loadings within the anode of DMFCs, for example, thereby limiting their practical commercialization. In this context, considerable work has been expended towards creating 1D nanostructured materials with high activity towards SOM oxidation.[5] Specifically, consistent and reproducible enhancements have been achieved in a broad range of 1D elemental, bimetallic, and even ternary nanostructures with respect to the oxidation of methanol, ethanol, and formic acid, respectively.[27,28,38-43] However, despite the breadth of systems investigated, only a few reports have systematically investigated the correlation between chemical composition and the corresponding electrocatalytic performance.[27,28,42] Herein, we have synthesized a systematic series of alloyed $Pd_{1-x}Pt_x$ NWs with chemical compositions ranging from $1 > x > 0$, and the corresponding peak MOR current density has been found to measurably increase as the Pd content is systematically increased towards 50%. On the basis of CO stripping voltammetry and formic acid oxidation performance in these NWs, the enhanced activity in the bimetallic NWs can be ascribed to the addition of Pd, which may facilitate the direct oxidation of methanol through a non-CO pathway.

Collectively, the ability to generate high-quality bimetallic Pd-based NWs with excellent uniformity has enabled us to rationally examine the catalytic performance of $Pd_{1-x}Pt_x$ and $Pd_{1-x}Au_x$ NWs in the context of three "grand challenges" associated with DMFC development. In all cases, it is evident that significant enhancements in electrocatalytic performance can be garnered by simultaneously optimizing chemical composition and structure to achieve practical

1D electrocatalyst systems, which may have broad applications in both the anode and cathode of functional DMFCs.

6.2 Controlling Composition in Nanoscale Wires: An Ambient Synthesis of High-Quality $Pd_{1-x}Pt_x$ and $Pd_{1-x}Au_x$ NWs

6.2.1. Synthesis of $Pd_{1-x}Au_x$ and $Pd_{1-x}Pt_x$ NWs

The synthesis of the $Pd_{1-x}Au_x$ and $Pd_{1-x}Pt_x$ NWs was accomplished by utilizing a U-tube double diffusion device with a mixed precursor feed solution, which is shown schematically in Figure 6.2.[9] Initially, precursor stock solutions of sodium hexachloropalladate (87.5 mg $Na_2PdCl_6 \cdot xH_2O$, 99.9%), hexachloroplatinic acid hydrate (102.5 mg $H_2PtCl_6 \cdot xH_2O$, 99.9%), and tetrachloroauric acid hydrate (64.0 mg $HAuCl_4 \cdot xH_2O$, 99.999%) were prepared by dissolving the powders obtained from Alfa Aesar into 5 mL of absolute ethanol. The concentrations of these solutions have been optimized to achieve a high correlation between the precursor solution composition and the composition of the NWs. To achieve the desired NW composition ($Pd_{1-x}M_x$), a mixed precursor solution of identical chemical composition was produced by combining aliquots of the palladium stock solution and the metal stock solution, in the appropriate stoichiometric volume fraction so as to generate the total 5 mL volume. For example, a combined 5 mL precursor solution containing 3.75 mL of palladium stock solution and 1.25 mL of the gold stock solution was employed in the synthesis of the Pd_3Au NWs. Separately, a 5 mM sodium borohydride solution ($NaBH_4$, Alfa Aesar 98%) serving as the reducing agent solution was prepared by dissolving the solid powder into 5 mL absolute ethanol with the assistance of a brief period of sonication.

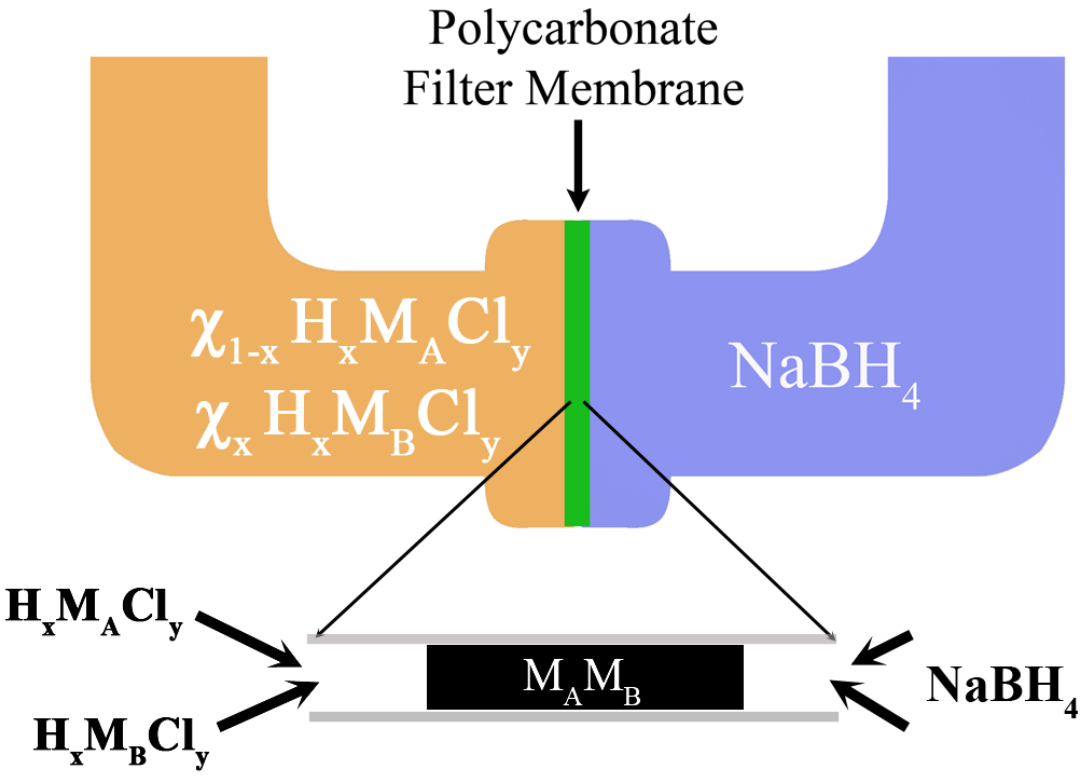

Figure 6.2 A schematic representation of the U-tube device employed in the synthesis of bimetallic NWs (top) with the left half-cell loaded with the mixed precursor solution and the right half-cell loaded with the reducing agent solution. The precursor solution is composed of a stoichiometric mixture of two metallic precursors in the ratio that is desired for as-prepared NWs. Separating the half-cells is a PC membrane, wherein the pores serve as spatially confining anisotropic reaction chambers for the subsequent formation of bimetallic NWs. Also shown is a schematic of an individual template pore (bottom) during the course of the reaction. (Adapted with permission from Ref. 9. Copyright 2012 American Chemical Society).

Immediately prior to performing the reaction, commercially available polycarbonate (PC) membranes (Whatman, Nucleopore track etched) with nominal pore sizes of 15 nm were sonicated in ethanol to pre-saturate the pores with solvent. In a typical reaction, the PC membrane is clamped between the two half cells of the U-tube device, and the half cells are separately loaded with the mixed precursor solution and the reducing agent solution, respectively. During the reaction, the precursor and reducing agent diffuse into the template pore space, which serves as a 1D reaction chamber, spatially confining the nucleation and growth of the NW. The nucleation is initiated at the point where the diffusion fronts interact, resulting in the formation of a short polycrystalline segment. Subsequently, the NW is believed to elongate through the pore by an electroless deposition process, resulting in the formation of a metal NW with excess material on the surface of the membrane.[2] After 30 minutes of reaction time, the filled template is removed from the device and briefly rinsed with ethanol to remove residual traces of precursor and reducing agent. The filled templates can then be processed to generate either individual isolated NWs or oriented free-standing arrays, utilizing the methods described in Chapter 5, Section 2.

The reaction yield is highly dependent upon the pore diameter and pore density of the membrane that is employed, and estimates of yield are typically between 0.05 and 0.1 $mg/cm^2_{template}$ for this method. Higher yields can be achieved by employing templates with higher pore densities such as anodic alumina. However, the use of PC templates provides NWs with optimum uniformity and quality**.**

6.2.2. Examining The Role of Surface Structure and Chemical Composition: Surface Modification of Elemental Pd NWs with Au Atoms

To explore the origin of enhancement in the Pd_9Au NWs, two additional samples were prepared wherein gold atoms were deposited at the surface to generate Pd-Au pair sites on elemental Pd NWs. First, we employed the Cu UPD method described in Chapter 2, Section 6 to deposit gold clusters onto the surface of Pd NWs, generating an Au_{UPD}~Pd NW.[44] Specifically, a 1/10 Cu submonolayer was deposited by sweeping the potential until 1/10 of the total Cu UPD charge was obtained. While being held at the proscribed potential, the Cu-modified electrode was transferred under an Ar atmosphere to a solution of 0.1 mM $HAuCl_4$ dissolved in 5 mM H_2SO_4 and immersed for 15 s. Thereafter, the electrode is rapidly placed in ultrapure water to quench the reaction and minimize the displacement of surface Pd atoms. The coverage of gold deposited by this method was determined to be 17% by the decrease in ESA after the deposition step. The higher than expected coverage (*e.g.* >10% coverage) suggests that the gold precursor reacted with both the Cu ad-atoms and surface Pd sites, despite the rapid quenching.

In a separate process, the surface of Pd NWs was modified by a controlled galvanic displacement of the surface Pd atoms with Au to create a mixture of Au clusters and porous Pd-Au at the surface (Au_{GD}~Pd NWs). Specifically, the Pd NWs supported on a GC-RDE were immersed in a solution of 0.l mM $HAuCl_4$ dissolved in 5 mM H_2SO_4 under a Ar–filled atmosphere for 15 s followed by immediate immersion in ultrapure water to quench the displacement process. The degree of coverage was monitored by the change in ESA after each exposure to the gold precursor solution and after two exposures, the total coverage was found to be 12%.

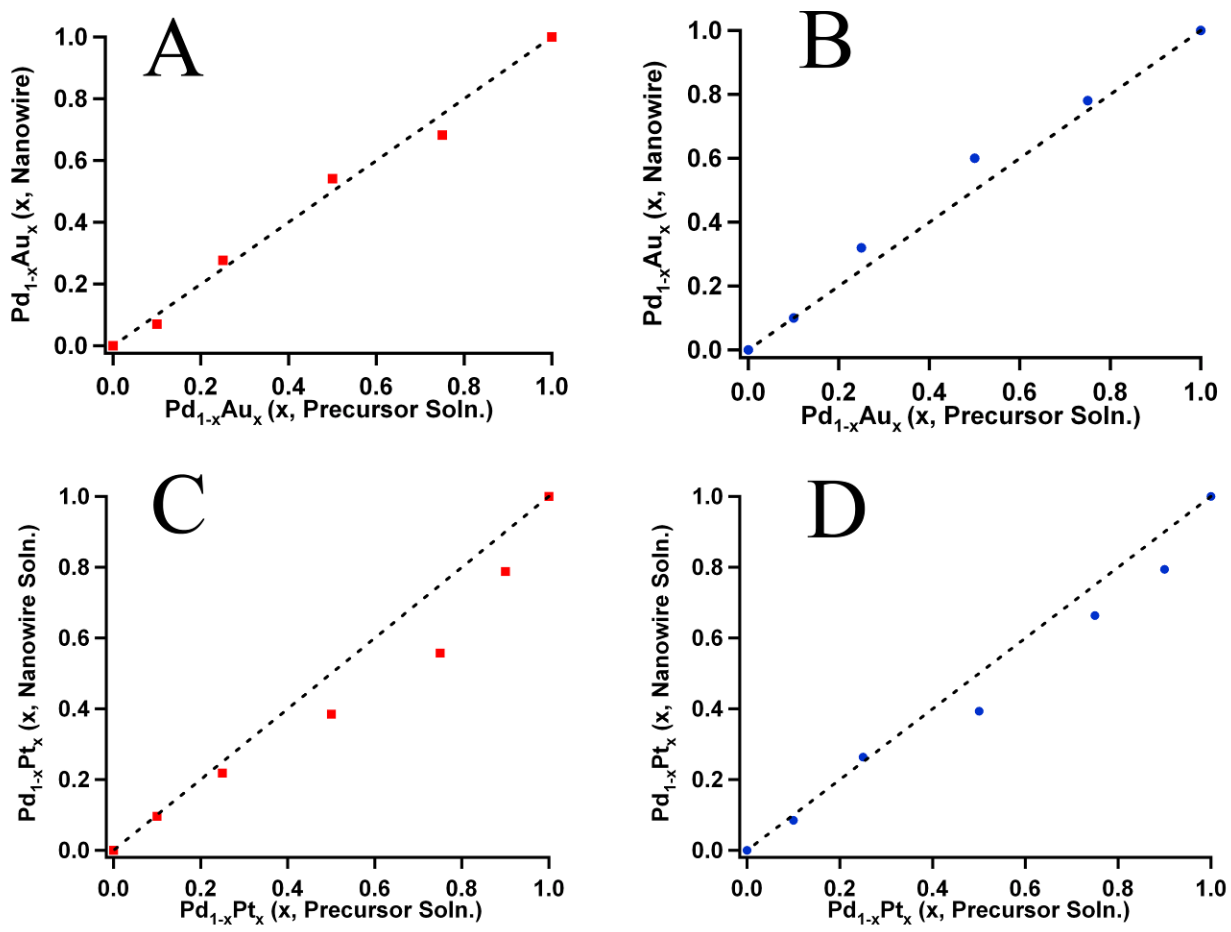

Figure 6.3 Graphs depicting the trend in NW composition as a function of the chemical composition of the precursor solution employed during the synthesis for the $Pd_{1-x}Au_x$ (A & B) and $Pd_{1-x}Pt_x$ (C & D) NW series, as determined from XRD (A & C) and EDAX (B & D) measurements. The dashed lines represent the ideal 1:1 correlation between the chemical composition of the precursor solution and the resulting NWs over the entire composition regime. (Adapted with permission from Ref. 9. Copyright 2012 American Chemical Society)

6.3 Results & Discussion

6.3.1. Synthesis & Structural Characterization of Bimetallic $Pd_{1-x}Au_x$ & $Pd_{1-x}Pt_x$ NWs

Initially, the composition of the NWs was examined by X-ray powder diffraction (XRD) and energy dispersive X-ray spectroscopy (EDAX), so as to confirm that the as-prepared NWs maintained compositions that were consistent with the contents of the precursor solution employed in the synthesis. XRD obtained on the $Pd_{1-x}Au_x$ and $Pd_{1-x}Pt_x$ NWs confirms that the NWs are homogeneous alloys with the desired face-centered cubic crystal structure. Vegard's law was employed (*c.f.* Chapter 2, Section 2) to estimate the chemical composition of the NWs on the basis of the calculated lattice parameters (Figure 6.3A & 6.3C). In addition, composition measurements were also obtained on NW collections by scanning electron microscopy and energy dispersive X-ray analysis (SEM-EDAX), and the results are shown in Figure 6.3B and Figure 6.3D. The resulting composition of the isolated $Pd_{1-x}Au_x$ nanostructures (Figure 6.3A & 6.3B) correlates with that of the corresponding precursor solution employed during each synthesis, which is in excellent agreement with prior results.[45,46] In the case of $Pd_{1-x}Pt_x$ (Figures 6.3C & 6.3D), the incorporation of Pd is favored slightly in as-prepared NWs, which may potentially arise from faster diffusion of the Pd precursor into the pore space.[47,48]

The corresponding SEM images obtained on the various $Pd_{1-x}Au_x$ and $Pd_{1-x}Pt_x$ NWs highlight the uniformity and homogeneity of the samples. It is also apparent that there is no significant difference in diameter, aspect ratio, or surface texture as a function of NW composition. Overall, as-prepared $Pd_{1-x}Au_x$ and $Pd_{1-x}Pt_x$ NWs maintain collective diameters of 50 ± 9 and 49 ± 8 nm, respectively, with lengths of up to 6 μm, consistent with the dimensions of the PC template pores. XRD and SEM characterization of the $Pd_{1-x}Au_x$ NWs is shown in Figure 6.4 as a representative example.

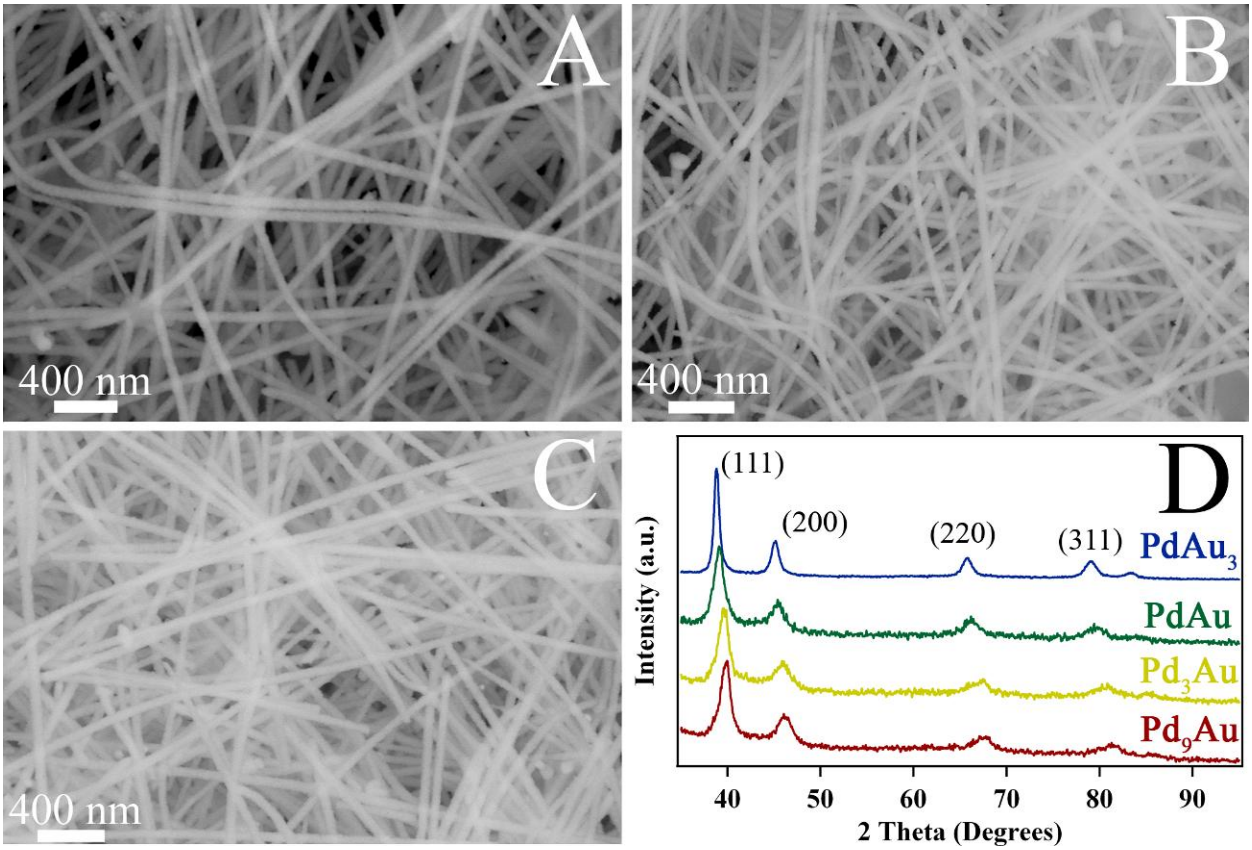

Figure 6.4 SEM and XRD characterization of Pd_9Au NWs. Representative SEM images of $Pd_{1-x}Au_x$ NWs with compositions of $x = 0.75$ (A), $x = 0.5$ (B) and $x = 0.25$ (C). XRD patterns obtained from the various $Pd_{1-x}Au_x$ NW samples with x values, ranging from 0.1 – 0.75. (Adapted with permission from Ref. 9. Copyright 2012 American Chemical Society)

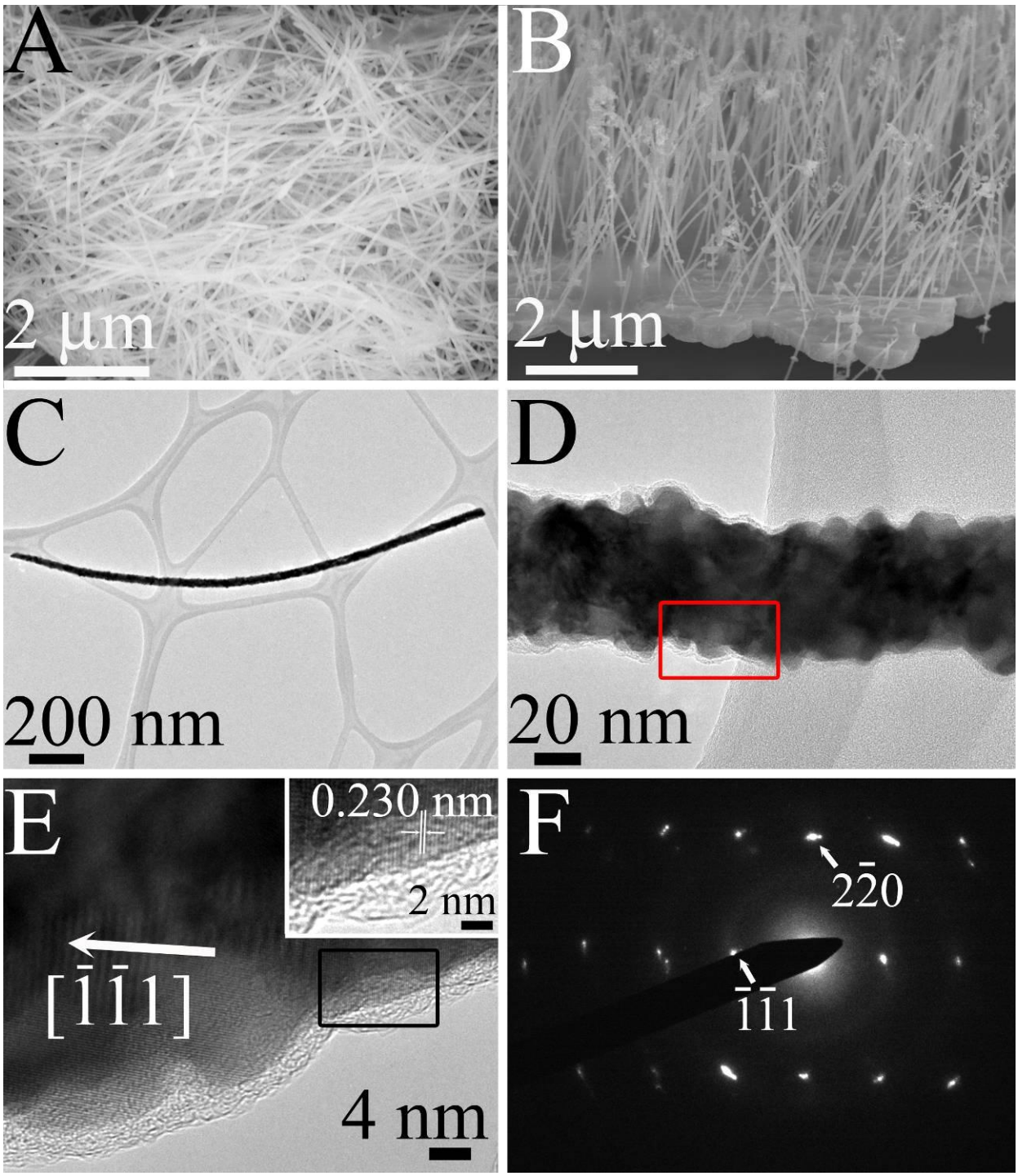

Figure 6.5 Electron microscopy characterization of 45 nm Pd_9Au NWs. Representative SEM images of the isolated Pd_9Au NWs (A) and of a free-standing NW array (B). TEM image of a single Pd_9Au NW (C) with a high-magnification image (D) highlighting the central region of the wire. The red box denotes where a high-resolution image (E) was obtained. Inset to panel E shows a selected area denoted by the black box, highlighting well resolved 111 lattice planes. Selected area electron diffraction pattern (F) corresponding to the images in (D) and (E) is shown. (Reprinted with permission from Ref. 9. Copyright 2012 American Chemical Society)

With the Pd_9Au NWs serving as a representative example, as-prepared NWs can be isolated as either individual NWs (Figure 6.5A) or as oriented free-standing NW arrays (Figure 6.5B), rendering these NWs as excellent candidates for sensing and electronics. Representative transmission electron microscopy (TEM) images (Figures 6.5C and 6.5D) of a single Pd_9Au NW show that the NWs are dense and uniform with a distinctive texture and orientation. The surfaces are uniformly faceted, and it is apparent that the facet sizes are inherently limited by the roughened uneven texture of the template's pore wall.[2] Selected area electron diffraction (SAED) patterns obtained revealed that after processing, the Pd_9Au NWs are highly textured and largely single crystalline, with short polycrystalline segments restricted to the ends of the NW. This is consistent with the two-step growth mechanism presented in Chapter 5 and further demonstrates the importance of studying the growth process under double diffusion conditions.[2]

Although not necessary to achieve a product suitable for electrocatalysis, the crystallinity of the NWs could be further improved by a brief heat treatment[‡] performed directly within the HRTEM instrument.[9] The HRTEM image (Figure 6.5E) obtained along the central single crystalline segment indicates the presence of well-resolved equidistant lattice planes with a spacing of 0.230 nm. The diffraction data (Figure 6.5F) in combination with the HRTEM images suggest that the long axis of the NWs is oriented along the [111] crystallographic direction. Similar results are observed in the case of the $Pd_{1-x}Pt_x$ NWs and structural characterization of the Pd_3Pt_7 NWs is described in detail in a previous report.[9] However, the diffraction data and associated HRTEM image reveal that these NWs are not actually single crystalline but rather are composed essentially of an aggregated ensemble of oriented crystallites.

[‡] The *in situ* heat treatment was performed with Pd_9Au NWs supported directly on a lacey carbon TEM grid. The temperature was increased incrementally up to 400°C and the crystallinity was probed by HRTEM and SAED at various points along individual NWs at each temperature. The results of this study including HRTEM images and SAED patterns are summarized in detail in Ref. 9.

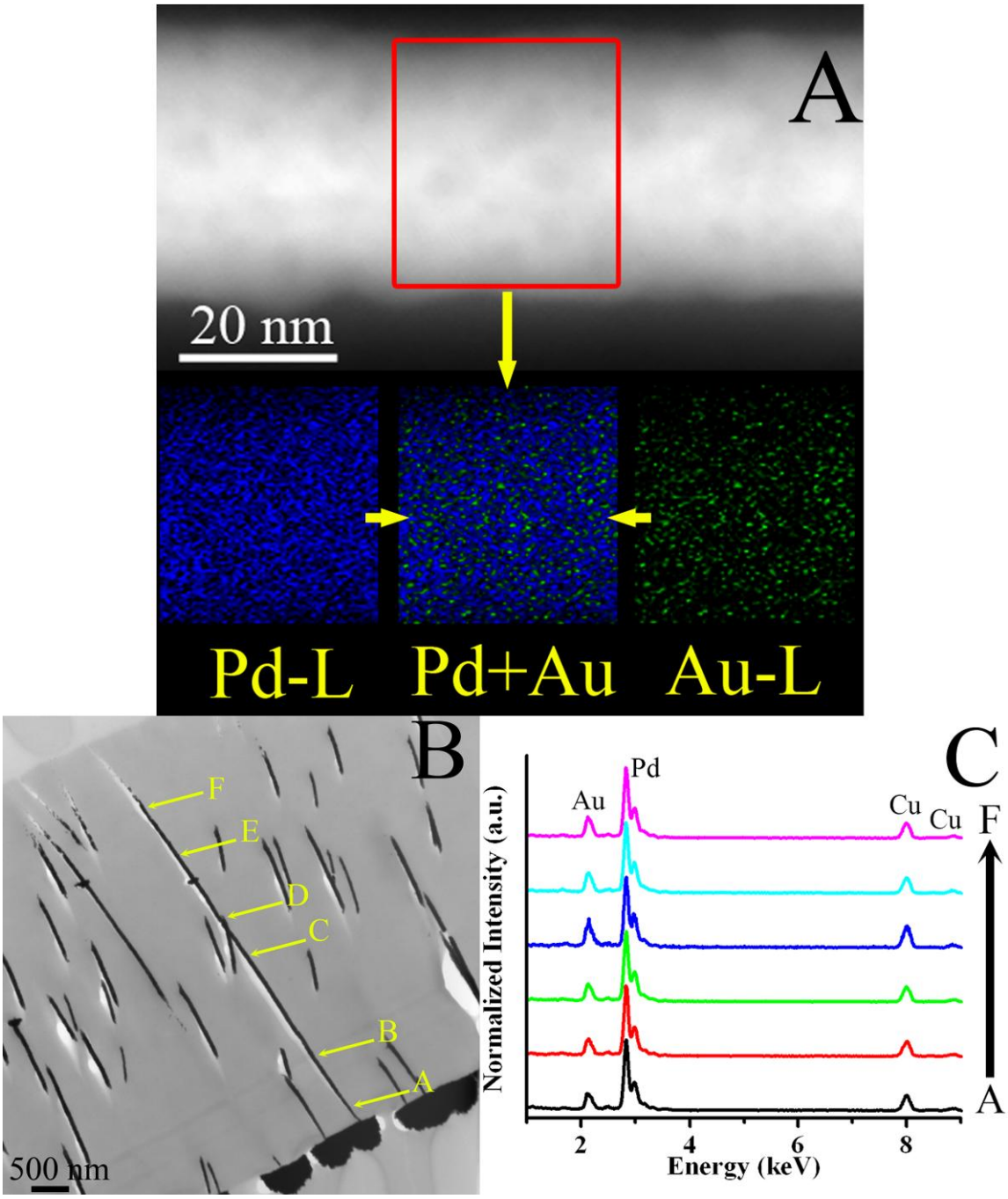

Figure 6.6 Characterization of chemical composition in Pd_9Au NWs. A representative HAADF image of the Pd_9Au NWs (A). Immediately below the HAADF image are the EDAX maps obtained from the area denoted by the red box. The Pd and Au maps derived from the respective *L*-edge signals are shown on the left and right, respectively, with the combined map shown in the center. A TEM image (B) of a representative cross-section of an as-prepared template membrane containing Pd_9Au NWs. EDAX spectra (C) obtained on an individual isolated NW at various points (A - F) along the wire are shown, corresponding approximately to those areas spatially highlighted in the TEM image. (Reprinted with permission from Ref. 9. Copyright 2012 American Chemical Society)

In addition to characterizing the crystallinity as a function of position along the NW, we also employed EDAX in scanning TEM mode to gain insight with respect to the uniformity of the NW's composition. Figure 6.6A shows a high-angle annular dark field (HAADF) image of a portion of the Pd_9Au NW. The contrast (sensitive to '*Z*') is largely homogeneous, suggesting that the NWs maintain relatively uniform and consistent composition throughout their entirety. The few areas of lighter contrast result from the uneven texture of the NW surface as well as porosity within the NW itself. Representative EDAX maps of the Pd_9Au NW also shown in Figure 6.6A reveal that the distributions of the elements are uniform throughout the NW and that no segregation of the metals into discrete phases is apparent. These results are consistent with the XRD and HRTEM results. EDAX spectra shown in Figure 6.6C were obtained at various points along the length of an individual, isolated Pd_9Au NW, corresponding to the locations shown in Figure 6.6B. The average Pd content was determined to be 90 ± 1% at all points A – F along the wire itself, confirming the notion that the distribution of Pd and Au is uniform along the length of the entire NW.

By contrast, an analogous examination of the Pd_3Pt_7 NWs summarized in a previous report[9] reveals that the NWs may become slightly enriched with Pt as it elongates in the template pore. Although several experimental factors may contribute to this enrichment process, a plausible and likely explanation is that the Pt precursor may diffuse into the template pore faster due to stronger interactions between the Pt precursor and the template walls themselves.[49] In one representative example, the Pt content was found to increase in a discrete NW from 66% at the location where growth initiated to 72% at the location where the NW growth completed. Despite the variation in composition, the average Pt content was 70 ± 3% along the entire NW, which is relatively homogenous in the context of achievable results with other synthetic methods.[50]

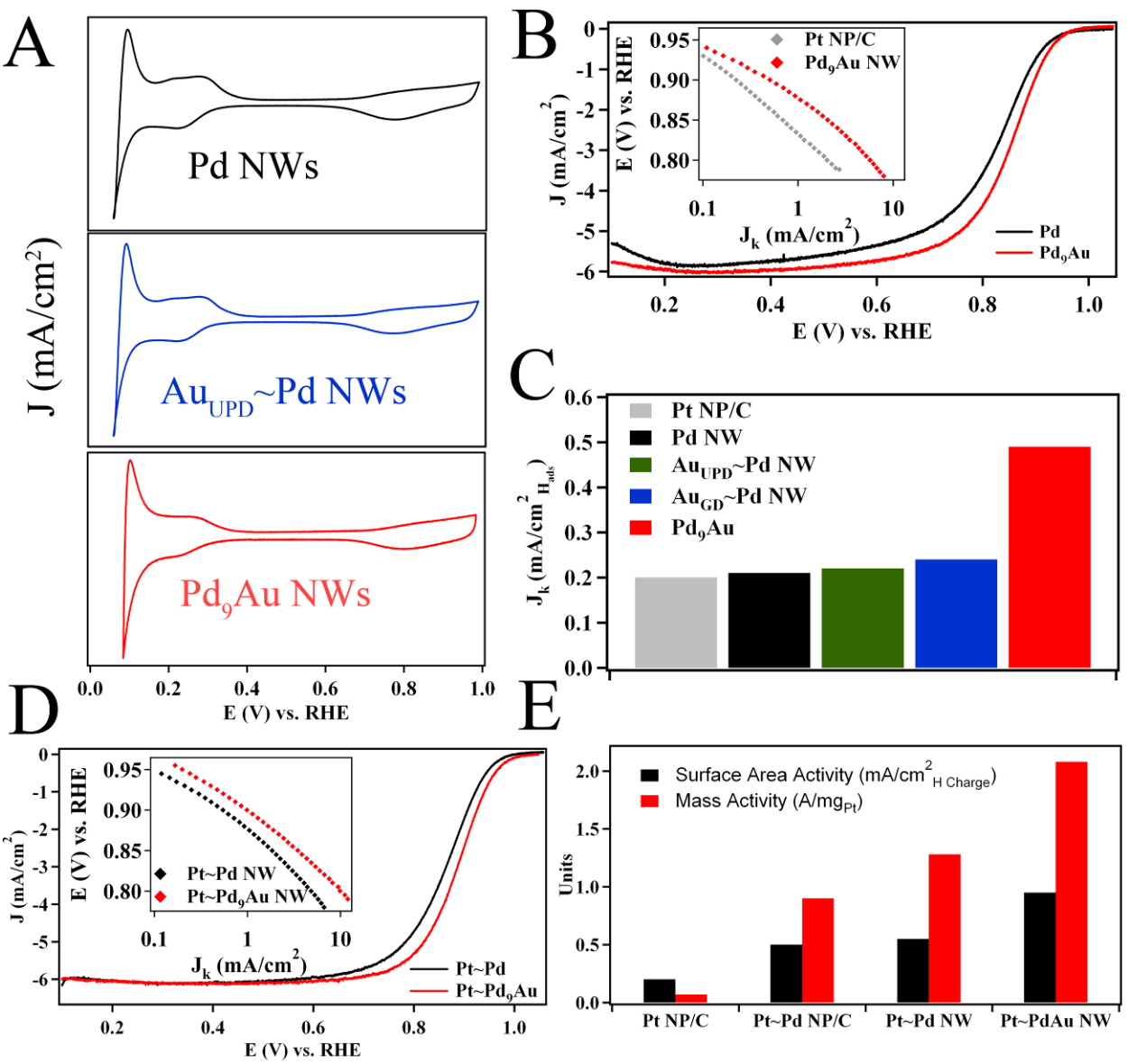

Figure 6.7 Composition-dependent electrocatalytic performance of Pd_9Au and Pt_{ML}~Pd_9Au NWs towards ORR. Cyclic voltammograms (A) obtained from as-prepared Pd NWs, Au_{UPD}~Pd NWs, and as-prepared Pd_9Au NWs, respectively. Polarization curves obtained from as-prepared Pd and Pd_9Au NWs before (B) and after (D) Pt_{ML} deposition. Potential vs. specific activity (J_k) plots of Pd_9Au NWs and Pt_{ML}~Pd_9Au NWs are shown as insets to (B) and (D) with Pt NP/C and Pt_{ML}~Pd NWs serving as a comparison, respectively. Experimentally calculated kinetic currents normalized to catalyst surface area and platinum mass obtained at 0.9 V are shown before (C) and after (E) Pt_{ML} deposition. (Reprinted with permission from Ref. 9. Copyright 2012 American Chemical Society)

6.3.2. Electrocatalytic Performance of $Pd_{1-x}Au_x$ NWs toward Oxygen Reduction

In previous reports by Adzic and co-workers, the electrocatalytic ORR performance of Pt monolayers (Pt_{ML}) deposited on $Pd_{1-x}Au_x$ NP/C was explored as a function of the NP composition and it was determined that an optimal performance could be achieved with a composition of Pd_9Au.[26,51] Hence, by analogy, in this work, we employed high quality, anisotropic Pd_9Au NWs to explore the role of morphology in the performance of bimetallic Pd-Au nanostructures towards ORR. The cyclic voltammograms collected from Pd_9Au and Pd NWs (Figure 6.7A) displayed the characteristic surface oxide formation (0.6 – 1.0 V) and H_{ads} (0.1 – 0.4 V) regions. The oxide reduction peak of the Pd_9Au NWs (0.7963 V) is significantly shifted by ~20 mV to higher potentials as compared with the Pd NWs (0.7729 V). This result suggests that the Pd_9Au NWs should maintain improved ORR performance as a result of the weaker interaction with the adsorbed oxygen species.[52,53] Additionally, it is apparent that the smooth shape and improved reversibility of the H_{ads} process associated with the H_{ads} region of the Pd_9Au NWs resemble that of the highly active Pt electrocatalysts, by comparison with elemental Pd NWs.[54]

On the basis of the polarization curves obtained in oxygen saturated 0.1 M $HClO_4$ (Figure 6.7B), the Pd_9Au NWs maintain significantly enhanced activity as compared with the Pd NWs alone. The measured kinetic currents at 0.9 V were normalized to the ESA (Figure 6.7C) to gain insight into the intrinsic activity of the Pd surface sites. The Pd_9Au NWs display an outstanding specific activity (J_K) of 0.49 ± 0.04 mA/cm^2, which is more than double that of the Pd NWs alone (0.21 ± 0.02 mA/cm^2). The activity of the Pd_9Au NWs also represents a two-fold improvement over the corresponding value measured for Pt NPs (0.21 mA/cm^2). In fact, it is also apparent from the potential versus kinetic current (E vs. J_K) plot shown as an inset to Figure 6.7B

that the activity of the Pd active sites associated with Pd_9Au NWs exceeds that of commercial Pt NP/C over the entire range of plausible operating potentials. This is a surprising and encouraging result, since we achieved activities greater than that of commercial Pt NPs alone with essentially no discernible Pt loading. The enhanced performance of our Pd_9Au NWs is in excellent agreement with a previous report demonstrating enhanced activity of PdAu bimetallic nanotubes towards ethanol electroxidation.[27]

In the existing literature regarding mixed Pd/Au electrocatalysts, the origin of enhanced ORR and alcohol electro-oxidation performance has been attributed to the presence of bimetallic Pd-Au pair sites at the surface in some cases and in others, to the properties of the PdAu alloy phase.[24,26,27,51,55] To explore the origin of enhancement in our alloyed NWs, we utilized (i) Cu UPD followed by galvanic displacement (Au_{UPD}~Pd NWs) and (ii) simple galvanic displacement (Au_{GD}~Pd NWs) reactions to deposit Au atoms at the surfaces of elemental Pd NWs.[44] These methods were selected, because they provide for two types of Pd-Au pair sites at the NW surface (*e.g.* gold clusters in the case of Cu UPD[44] and a mixture of gold clusters and porous PdAu in the case of galvanic displacement). Since the Pd NWs and Pd_9Au NWs maintain similar dimensions, crystallinity, and surface texture, the role of the Au additive is highlighted. Analysis of these samples by CV (Figure 6.7A) reveals that the gold modified Pd NWs with Pd-Au pair sites at the surface maintain H_{ads} and oxide formation features that are similar to that of the Pd NWs. It is therefore not surprising that there are only reasonably negligible enhancements in the specific ORR activity of the Pd active sites in these samples (Figure 6.7C).

These results suggest that the origin of enhancement in the Pd_9Au NWs is due to their homogeneous alloyed structure, as opposed to merely the presence of bimetallic sites localized on the NW surface. We believe that the combination of the advantageous 1D structural motif

with the beneficial structural and electronic properties of PdAu alloys[24,26,56] accounts for the enhanced performance in the case of ORR. Specifically, it is believed that the addition of Au into the face-centered cubic Pd framework (i) results in a slight expansion of the Pd lattice (3.89 Å) thereby rendering the lattice parameter of Pd_9Au (3.91 Å) closer to that of Pt (3.92 Å), and (ii) increases the relative number of electrons in the Pd *d*-band.[25,56] These mutually advantageous effects are expected to render the Pd_9Au more active, since the structural and electronic properties are closer to those of more active Pt nanostructures.

6.3.3. Towards a Pt-free Methanol Tolerant Electrocatalyst: Stability of ORR Performance in Highly-Active Pd_9Au NWs in the Presence of Methanol

On the basis of the previous section, the Pd_9Au NW system is advantageous, since the addition of 10% gold forming a bimetallic alloy results in a specific activity of 0.45 mA/cm^2 that is nearly two-fold higher than that of commercial Pt NP/C and of elemental Pd NW analogues. In the context of methanol-tolerant ORR behavior, the ability to achieve high ORR activities without requiring any Pt content whatsoever represents a unique opportunity to develop a highly active catalyst, that is also particularly stable in the presence of methanol.[20] In practical DMFC designs, the rate of methanol crossover is dependent upon a variety of operating conditions, such as the concentration of the methanol in the anode, the fuel feed pressure, the relative humidity, and the chemistry of the PEM.[29] Thus, it is difficult to characterize the concentration of methanol within the cathode half-cell during operation in practical DMFC devices. Herein, we simulated the methanol cross-over effect by obtaining ORR polarization curves in 0.1 M $HClO_4$ electrolyte with methanol purposefully added as a representative SOM impurity to the electrolyte in concentrations of 1 – 4 mM. This concentration regime is advantageous, since it is potentially

higher than the actual methanol concentration within a practical DMFC, thereby representing a possible, realistic worst-case scenario, while at the same time, also enabling the accurate determination of specific ORR activity.

As a simple screening test, the effects of methanol on the electrocatalytic properties of Pd_9Au NWs was studied by obtaining a cyclic voltammogram in 100 mM methanol supported in 0.1 M $HClO_4$. The measured CV confirmed that there was minimal anodic deflection in the area of the CV above 0.5 V, suggesting that the Pd_9Au NWs maintained minimal MOR activity. The peak associated with methanol oxidation in anodic sweep of the CV of the Pd_9Au NWs was determined to be 0.08 mA/cm^2, which was several orders of magnitude lower than that of analogous Pt NWs (1.16 mA/cm^2). Also, the addition of methanol had minimal effects on the integrated H_{ads} charge suggesting a weak interaction between the active sites and methanol. These encouraging result suggests that the Pt-free, Pd_9Au NWs maintained a high degree of electrochemical stability even in the presence of up to 100 mM methanol.

To quantitatively probe the ORR stability in the presence of methanol, polarization curves were obtained from the Pd_9Au NWs in 0 – 4 mM methanol. Interestingly, the presence of methanol yields minimal effect on the measured polarization curves shown in Figure 6.8A, which starkly contrasts with the results obtained with the bimetallic $Pd_{1-x}Pt_x$ NWs and elemental Pt NWs (*c.f.* Section 6.3.6). Given the high methanol tolerance of the Pd_9Au NWs, the stability of ORR performance in methanol (Figure 6.8B) has been compared with that of commercial Pt NP/C, Pt NWs, and Pd NWs, respectively. Of special interest, the Pd_9Au NWs retained 88% of their initial activity in the presence of 4 mM methanol, a result demonstrating considerable enhancement with respect to both conventional Pt NP/C (79%) and elemental Pt NWs (43%).

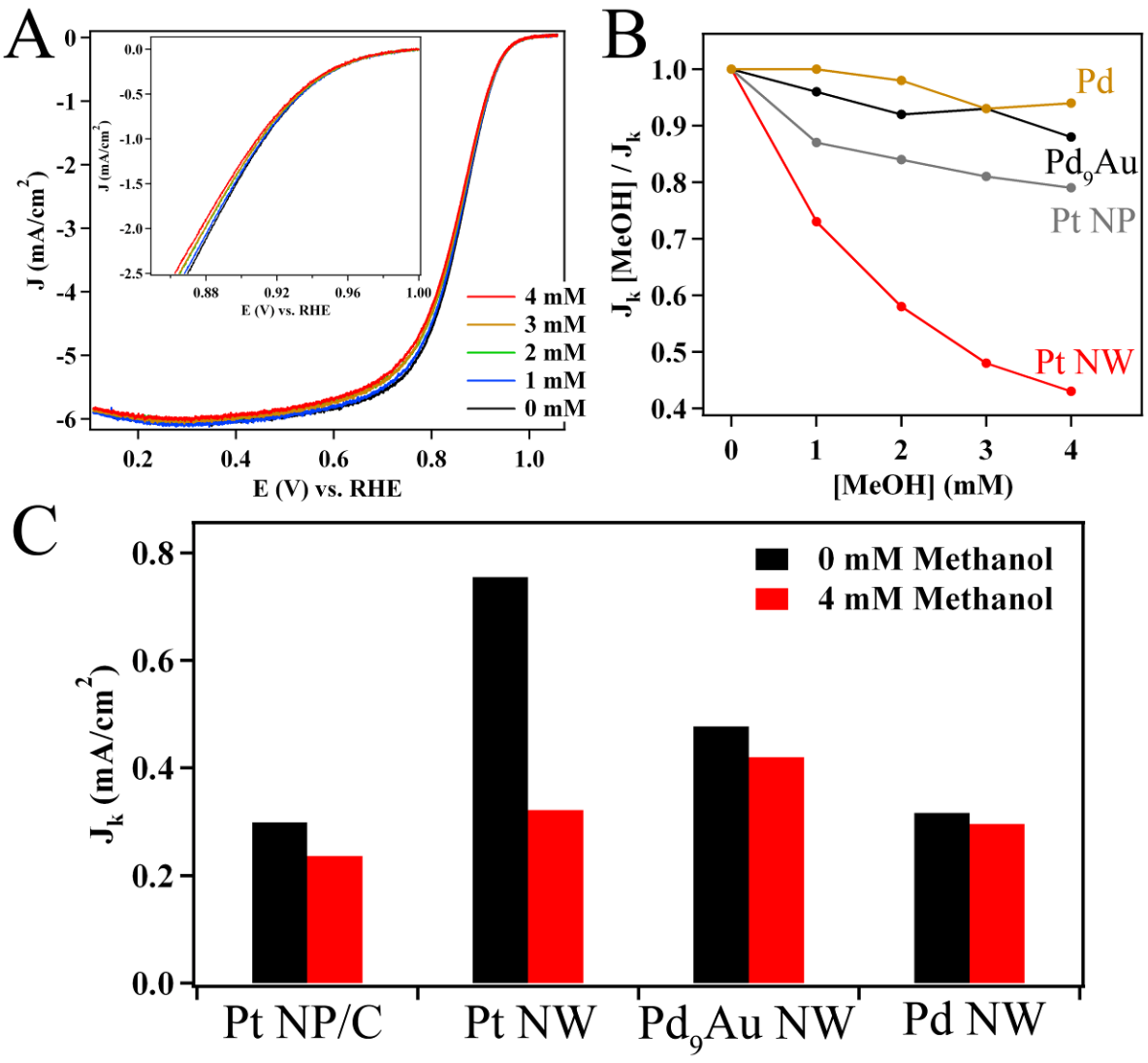

Figure 6.8 The stability of ORR performance in highly-active, Pt-free, Pd_9Au NWs. Polarization curves obtained from Pd_9Au NWs are shown with the methanol concentration, ranging from 0 – 4 mM. A plot of the ratio of the specific activity measured in the presence of methanol (J_K [MeOH]) with respect to the specific activity measured in pure electrolyte (J_K) as a function of methanol concentration (B) for the Pd_9Au NWs, Pt NWs, Pd NWs, and commercial Pt NP/C, respectively. A bar graph is shown in (C), depicting the measured specific activity of the various catalysts in pure 0.1 M $HClO_4$ as well as in 4 mM methanol supported in 0.1 M $HClO_4$. (Reprinted with permission from Ref. 20. Copyright 2013 American Chemical Society)

From a practical perspective, the measured specific activity of the Pd_9Au NWs, Pt NWs, commercial Pt NP/C, and Pd NWs is shown before and after the addition of 4 mM methanol in Figure 6.8C. In pure 0.1 M $HClO_4$, the Pt NWs maintained a demonstrably higher specific activity (0.76 mA/cm^2) as compared with Pd_9Au NWs (0.48 mA/cm^2), Pd NWs (0.32 mA/cm^2), and commercial Pt NP/C (0.30 mA/cm^2). In the presence of 4 mM methanol, the high methanol tolerance of the Pd_9Au NWs was highlighted and these NWs yielded a specific activity of 0.42 mA/cm^2, a value which is considerably enhanced beyond that of the elemental Pt NWs (0.32 mA/cm^2). Collectively, these results have demonstrated the intrinsic advantages of as-synthesized Pd_9Au and Pd NWs, since they are both highly active and also tolerant to methanol as ORR electrocatalysts.

At methanol concentrations below 4 mM, we find that Pd and Pd_9Au NWs maintain essentially similar trends in ORR stability and mutually outperform Pt analog (Figure 6.8B). However, an interesting trend immerges in Pd and Pd_9Au NWs when the performance is studied in methanol concentrations of up to 100 mM. Polarization curves obtained from Pd_9Au and Pd NWs in 25 – 100 mM methanol in 0.1 M $HClO_4$ reveal that the measured half-wave potential decreased by approximately 35 mV and 15 mV, respectively. In the context of the specific activity, the Pd NWs retained 87% of their initial activity, which was a noteworthy improvement over that of Pd_9Au NWs (57%). The lower methanol tolerance of the Pd_9Au NWs, by comparison with the elemental Pd NWs may be attributed to the effects of the gold dopant in the homogeneous $Pd_{1-x}Au_x$ alloy. According to the relevant literature regarding $Pd_{1-x}Au_x$ alloys, the addition of 10% Au into the face-centered cubic Pd framework leads to the Pd_9Au alloy maintaining electrocatalytic performance that is analogous to Pt due to the expanded lattice and the increased density of electrons in the *d*-band.[25,56] However, on the basis of Nørskov and

Hammer theory,[52,57,58] the increased number of electrons in the *d*-band is also expected to strengthen the *d*-band to π^* overlap of the $Pd_{1-x}Au_x$ NWs with adsorbed CO, by comparison with an elemental analog. This increase in the surface adsorption strength of the CO is expected to render the Pd_9Au NW more susceptible to CO-poisoning, by comparison with elemental Pd NWs when operating as an ORR catalyst in the presence of methanol. Collectively, we believe that this supports the trend in the activity loss in the Pd_9Au and Pd NWs above 25 mM.

6.3.4. Highly Enhanced Electrocatalytic Performance in Pt_{ML}~$Pd_{1-x}Au_x$ NWs Core-Shell Heterostructures toward ORR

In addition, we also employed our Pd_9Au NWs as a substrate for the deposition of a Pt_{ML} shell (Pt_{ML}~Pd_9Au NWs), prepared by Cu UPD/galvanic displacement. It is apparent from the CVs (shown in a previous report)[9] that a Pt_{ML} shell has been deposited and that the Pt_{ML}~Pd_9Au NWs maintain a favorable shift in the oxide reduction peak (0.8093 V) when compared with the Pt_{ML}~Pd NWs (0.7975 V). The corresponding polarization curves (Figure 6.7D) as well as *E* vs. J_K curves (inset to Figure 6.7D) confirm the high ORR activity of the Pt_{ML}~Pd_9Au NWs especially when compared with the Pt_{ML}~Pd NWs. As tangible evidence, specific and platinum mass activities at 0.9 V of the Pt_{ML}~Pd_9Au NWs were determined to be 0.95 ± 0.03 mA/cm^2 and 2.08 ± 0.05 A/mg$_{Pt}$, respectively. Figure 6.7E compares the measured specific and mass activity of the Pt_{ML}~Pd_9Au NWs with the corresponding activities obtained from Pt_{ML}~Pd NWs, Pt_{ML}~Pd NP/C, and commercial Pt NP/C, respectively. It is apparent that a two-fold enhancement is achieved over the activity of Pt_{ML}~Pd NWs, thereby highlighting the role of chemical composition in the measured activity. The specific activity of the Pt_{ML}~Pd_9Au NWs is also higher in comparison with the activity measured under membrane electrode assembly (MEA)

conditions from analogous Pt_{ML}~Pd_9Au NP/C (*i.e.* 0.5 mA/cm^2),[51] thereby highlighting the improvement in activity as a result of use of the 1D NW motif. In addition, we find that the Pt_{ML}~Pd_9Au NWs maintained a platinum group metal (PGM) activity of 0.16 A/mg_{PGM}, which is essentially equivalent to the value typically obtained from commercial Pt NP/C with the same total loading. Regardless, this result is encouraging since Pt, which is less abundant than Pd and Au, represents only 7.2% of the total mass of the Pt_{ML}~Pd_9Au NW sample.

The enhanced activity was accompanied by greatly improved stability and after 30,000 cycles of a durability test, the half wave potential of the polarization curve shown in Figure 6.9A decreased by only 6 mV. Accordingly, the Pt mass activity (inset to 6.9A) declines by only 18% in the case of the Pt_{ML}~Pd_9Au NWs over the course of 30,000 cycles. To highlight the stability of the Pt_{ML}~Pd_9Au NWs, TEM images obtained after 30,000 cycles (Figure 6.9C) reveal that there is essentially no perceptible change in the structural integrity and texture of the Pt_{ML}~Pd_9Au NWs. On the other hand, the elemental Pd NWs undergo a loss of over 45% over the course of the 20,000 cycles of durability testing presented in Chapter 5. The analogous Pt_{ML}~Pd NWs (Figure 6.9B) showed an apparent evolution of a porous structure as a result of significant corrosion and dissolution of the Pd core after only 20,000 cycles, which is consistent with the considerable declines in Pt mass normalized performance. Hence, the addition of 10% Au forming a stabilizing uniform alloy results in significant and clearly measurable enhancements in both ORR performance and durability.

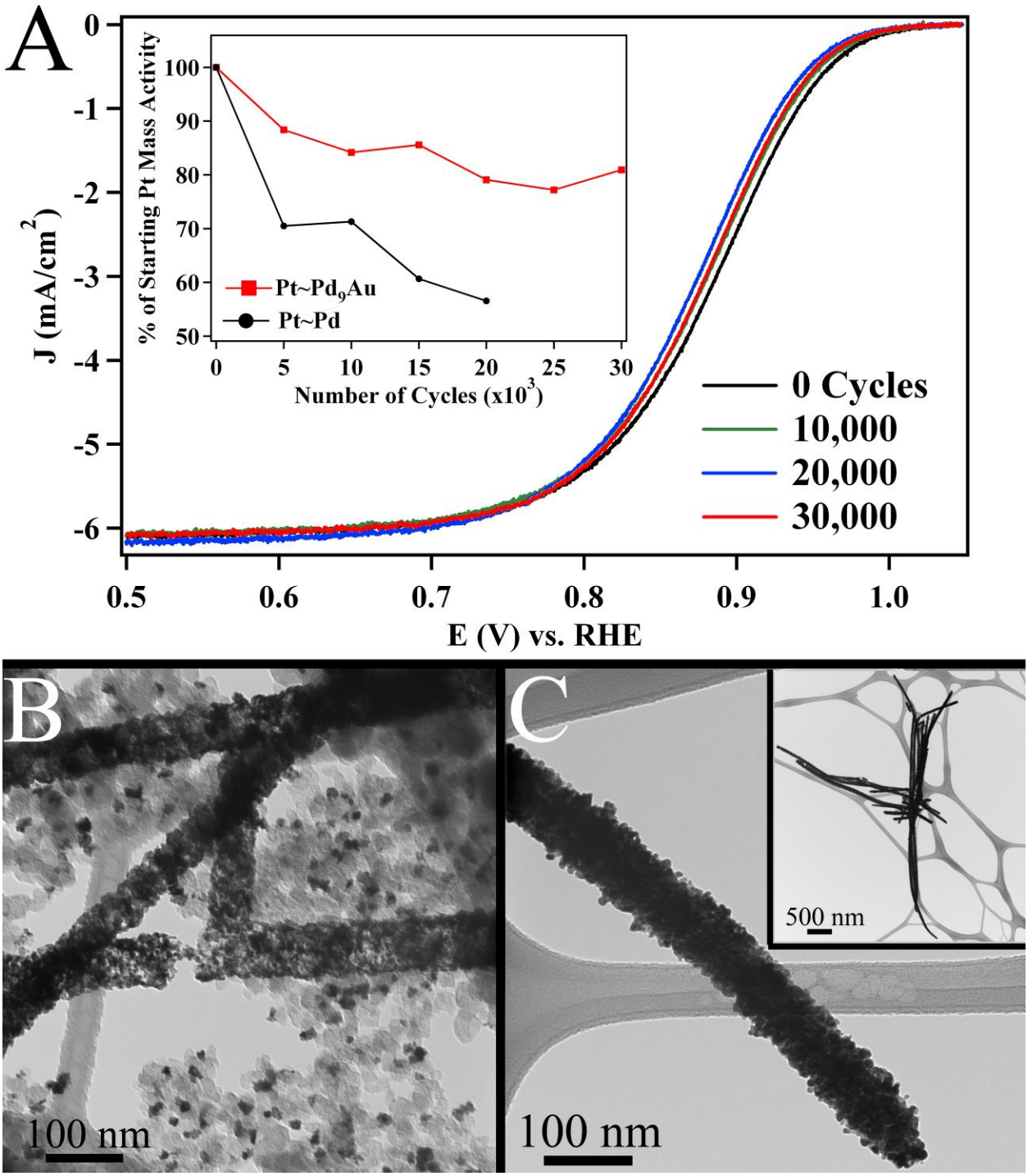

Figure 6.9 Accelerated ORR durability test of Pt_{ML}~Pd_9Au NWs. Polarization curves (A) obtained from the Pt_{ML}~Pd_9Au NWs over the course of the durability test. The results of the durability test (inset) are summarized as the percentage of the remaining Pt mass activity over the course of the 30,000 cycles. Representative TEM images of the Pt_{ML}~Pd NWs (after 20,000 cycles) and Pt_{ML}~Pd_9Au NWs (after 30,000 cycles) are also shown in (B) & (C), respectively. (Reprinted with permission from Ref. 9. Copyright 2012 American Chemical Society)

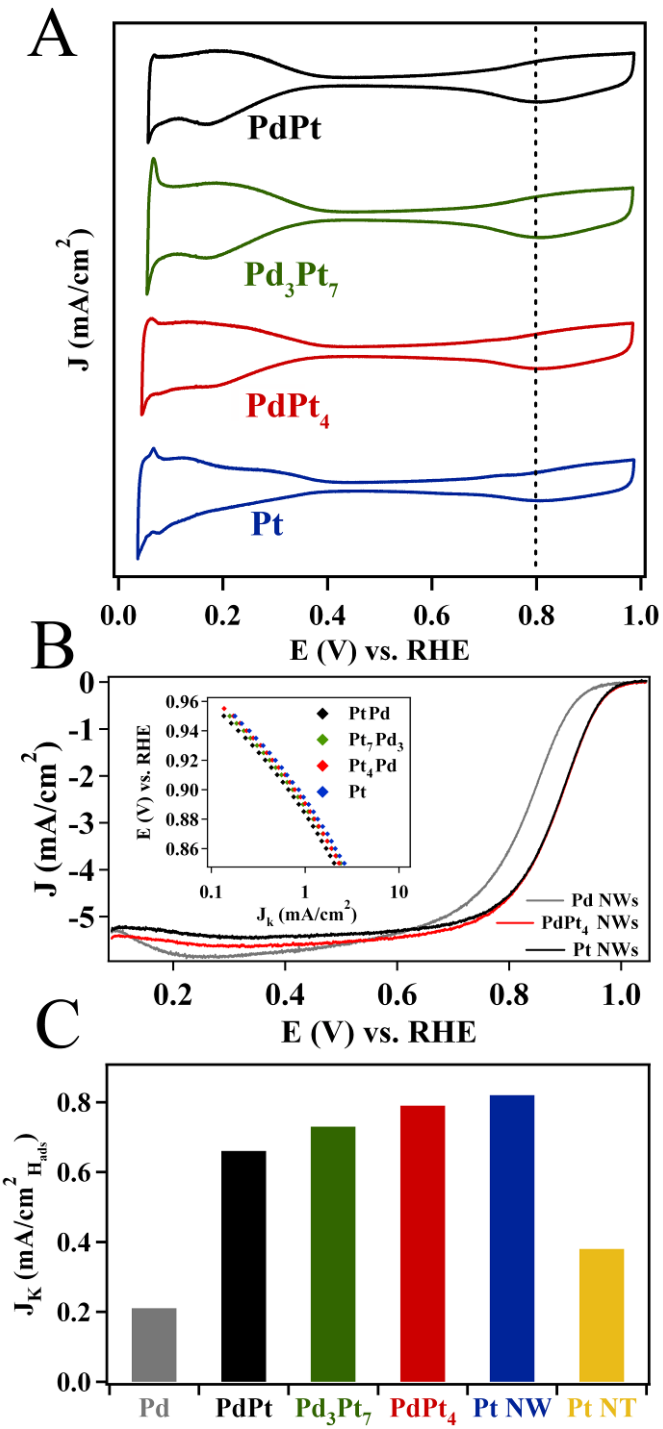

Figure 6.10 Composition-dependent ORR performance in $Pd_{1-x}Pt_x$ NWs. Cyclic voltammograms (A) obtained from as-prepared $Pd_{1-x}Pt_x$ NWs. Polarization curves (B) obtained from as-prepared Pd, $PdPt_4$, and Pt NWs. The *E* vs. J_k plot of various $Pd_{1-x}Pt_x$ NWs is shown as an inset with Pt NP/C serving as a comparison. The specific ORR activities (C) at 0.9 V of the series of $Pd_{1-x}Pt_x$ NWs are shown by comparison with both as-prepared, phase-pure Pt and Pd NWs synthesized in an analogous manner as well as with previously reported Pt NTs. (Reprinted with permission from Ref. 9. Copyright 2012 American Chemical Society)

6.3.5. Correlating Composition with Performance: Composition-Dependent Electrocatalytic ORR Behavior in $Pd_{1-x}Pt_x$ NWs

We also explored the cathodic ORR performance as a function of composition in the as-prepared $Pd_{1-x}Pt_x$ NWs and the results are summarized in Figure 6.10.[9] The CVs (Figure 6.10A) highlight a transition in the structure of the H_{ads} and oxide region to that of the elemental Pt NWs, as the proportion of Pt is increased in the as-prepared alloy NW samples. In fact, the specific activity measured at 0.9 V (Figure 6.10C) of the NWs increases from 0.64 ± 0.01 mA/cm^2 to 0.79 ± 0.01 mA/cm^2, as the Pt content correspondingly rises from 50 to 80%. This trend is further highlighted by the *E* vs. J_K curves shown as an inset to Figure 6.10B. Based on prior studies,[1,2,10,42] it is not entirely surprising that the activity of these bimetallic catalysts greatly surpasses the corresponding activity of both commercial Pt NPs (0.21 mA/cm^2) and elemental Pd NWs (0.20 mA/cm^2). However, an unexpected finding is that the activity of our PdPt NWs (0.64 mA/cm^2) also exceeds that of elemental Pt nanotubes with an outer diameter of 200 nm previously prepared and studied by our team under identical conditions,[49] while only maintaining 50% of the Pt content.

In addition, we find that the activity of the $PdPt_4$ NWs (0.79 mA/cm^2) is essentially equivalent to the activity measured for analogous Pt NWs with approximately the same diameter (0.82 ± 0.04 mA/cm^2). This fact is highlighted by the polarization curves (Figure 6.10B), which indicate that the Pd_4Pt NWs maintain almost identical performance to that of the Pt NWs when the same quantity of metal is present on the electrode. By contrast, previous reports regarding alloyed PdPt NPs have demonstrated that the activity of $Pd_{1-x}Pt_x$ ($x = 0.7 – 0.9$) alloys exceeds that of pure Pt NPs as a result of a structural contraction induced by the incorporation of Pd atoms.[59] In the case of NWs, however, the enhanced activity of these systems has been generally

attributed to a size-induced contraction of the NW surface, thereby resulting in an advantageous change in the electronic properties of the NW.[1-3,5,60,61] Hence, the observed activity trend for $Pd_{1-x}Pt_x$ NWs in this report is more complicated, and suggests that the size-induced contraction phenomenon may be dependent upon and influenced by not only their diameter but also their inherent chemical composition. Although it is beyond the scope of this report, additional investigation of the electronic and structural properties of these 1D bimetallic catalysts will be required to more precisely evaluate the origin of the activity trend.

6.3.6. Stability of ORR Performance in $Pd_{1-x}Pt_x$ NWs in the Presence of Methanol

We also examined the stability of ORR performance in the presence of methanol so as to gain fundamental insights into the potential application of Pd-based NWs as effective methanol-tolerant cathode electrocatalysts.[20] The polarization curves obtained in 0, 1, 2, 3, and 4 mM methanol are shown in Figure 6.11A – 6.11D for the Pt, $PdPt_4$, Pd_3Pt_7, and PdPt NWs, respectively. In all cases, the addition of methanol into the electrolyte medium results in a measurable positive deflection of the current in the polarization curves between 0.6 – 0.9 V, especially when compared with the polarization curves obtained in pure 0.1 M $HClO_4$. This deflection in the polarization curve increases with increasing methanol concentration, and is consistent with the overlapping oxygen reduction and methanol oxidation processes, occurring in this potential window. Careful inspection of the onset region for each set of polarization curves (insets to Figure 6.11A – 6.11D) also highlights a measurable decline in the current density in the region of the curve that follows the onset of ORR kinetics.

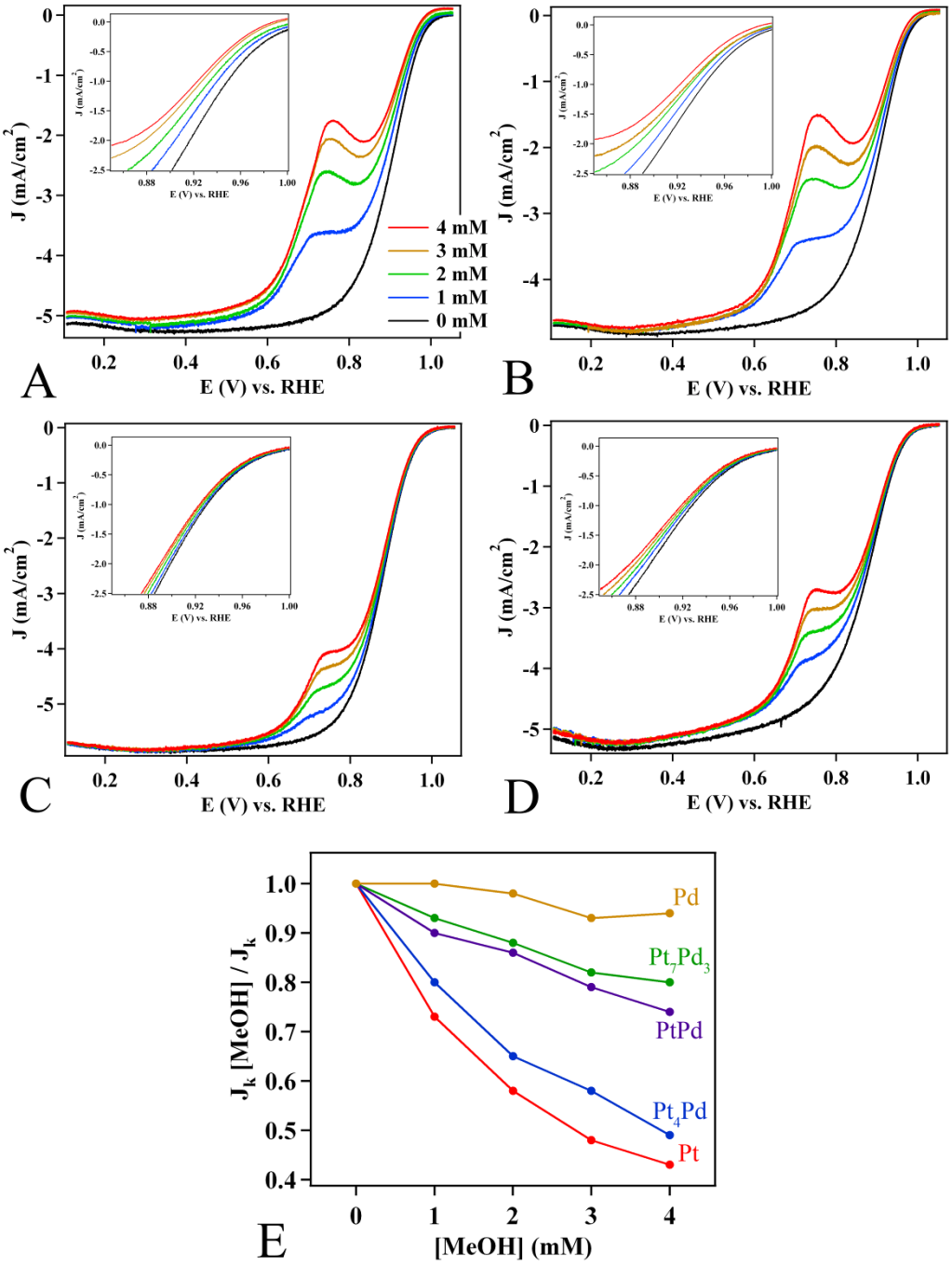

Figure 6.11 Stability of ORR activity toward the presence of methanol in $Pd_{1-x}Pt_x$ NWs. The polarization curves obtained from Pt (A), $PdPt_4$ (B), Pd_3Pt_7 (C), and PdPt (D) NWs are shown with methanol concentrations ranging from 0 – 4 mM. The onset regions of the polarization curves for each $Pd_{1-x}Pt_x$ NW are also shown as the corresponding insets. A plot (E) of the ratio of the specific activity, measured in the presence of methanol (J_K [MeOH]), with respect to the specific activity, measured in pure electrolyte (J_K), as a function of methanol concentration for the $Pd_{1-x}Pt_x$ NWs. (Adapted with permission from Ref 20. Copyright 2013 American Chemical Society)

The ratio of the calculated specific ORR activity in the presence of methanol (*e.g.* J_K [MeOH]) was normalized to the specific ORR activity measured in pure electrolyte (J_K), so as to provide for a quantitative insight into the relative decline in specific activity as a function of methanol concentration. The resulting methanol tolerance curves are shown in Figure 6.11E for the $Pd_{1-x}Pt_x$ NWs. The elemental Pd NWs maintained the highest stability in the presence of methanol with a loss of only ~6% of the activity in 4 mM methanol. This result is consistent with the observation that the Pd NWs maintained essentially no activity toward methanol oxidation (*c.f.* Section 6.3.8) by comparison with the Pt NWs. In terms of the $Pd_{1-x}Pt_x$ NWs, the increased Pt content in the alloy NWs led to a lower overall methanol tolerance as compared with the elemental Pd NWs. The elemental Pt NWs maintained the lowest stability and retained only 43% of their initial activity in the presence of 4 mM methanol.

Interestingly, the performance of the $Pd_{1-x}Pt_x$ NWs did not trend linearly with respect to increasing Pt content, and in fact, a volcano-type dependence was observed with the Pd_3Pt_7 NWs found to maintain the best ORR stability in the presence of methanol. Specifically, the Pd_3Pt_7 NWs preserved 80% of their initial activity, which was noticeably and measurably enhanced with respect to PdPt (74%) and especially $PdPt_4$ (49%). Recently, analogous studies of nanoparticulate $Pd_{1-x}Pt_x$ catalysts have demonstrated a strong inverse correlation between MOR activity and the stability of ORR performance in the presence of methanol.[31-35] This observed trend in NP analogues is not surprising, since highly active MOR catalysts are expected to be more sensitive to the presence of methanol, when operating as ORR catalysts. However, we have demonstrated herein and in Section 6.3.8 that simultaneously and carefully tailoring both morphology and chemical composition in $Pd_{1-x}Pt_x$ NWs can lead to an optimal chemical

composition (*e.g.* Pd_3Pt_7), which is not only stable as an ORR catalyst in the presence of methanol but also highly active towards MOR.

6.3.7. Morphology-Dependent Enhancement of MOR Activity in Anisotropic Pt NWs

In order to demonstrate the inherent advantages of our as-prepared NWs, we systematically examined the morphology-dependent electrocatalytic performance towards MOR in elemental Pt NWs. The development of effective, efficient, and active MOR electrocatalysts has been a crucial technological challenge in the practical development of DMFC devices. In light of this, we examine in the following section the morphology-dependent performance in elemental 1D Pt NWs, by comparison with commercial Pt NP/C. The potential to simultaneously optimize both structure and chemical composition may represent a key step in moving toward practical MOR catalysts.

In this section, the MOR performance was examined in high-quality 1D Pt NWs and in the corresponding commercial, state-of-the-art, 0D Pt NP/C by obtaining LSVs in the presence of 0.1 M methanol. The measured MOR currents were normalized to the ESA of the respective catalysts so as to provide for area-normalized LSVs, shown in Figure 6.12C. The Pt NWs displayed a nearly three-fold higher MOR peak current density, as compared with the Pt NP/C. In addition, a careful inspection of the MOR onset region, shown as an inset to Figure 6.12C, reveals that the Pt NWs and Pt NP/C maintain comparable onset potentials of ~675 mV. However, the Pt NWs possess higher overall MOR kinetics after onset, by comparison with the Pt NP/C. Collectively, all of these results demonstrate a significant and measurable morphology-dependent enhancement behavior in MOR performance, which likely can be attributed to the anisotropic 1D Pt NWs themselves.

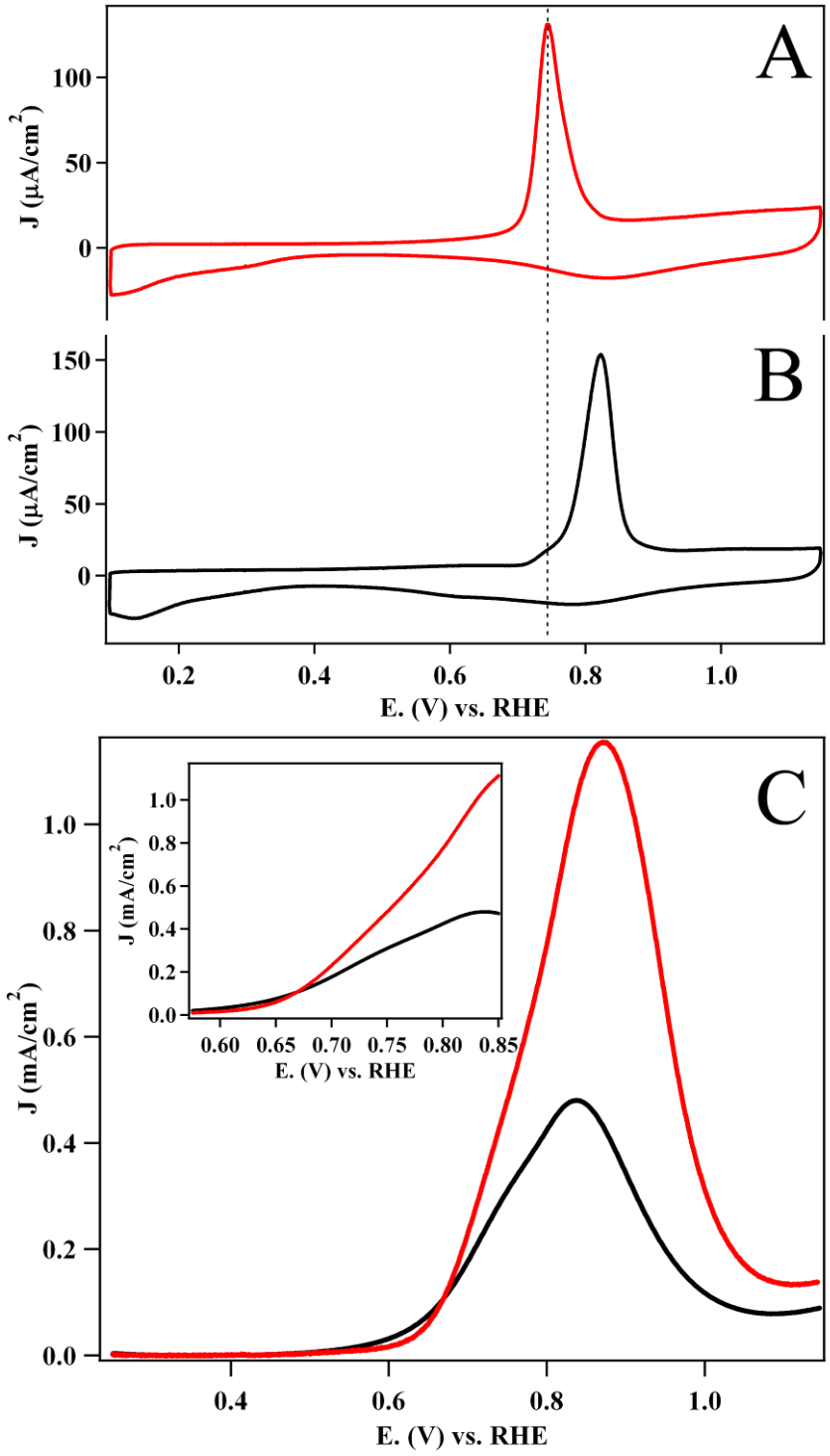

Figure 6.12 The morphology-dependent MOR performance of Pt NWs is characterized by LSVs obtained in 0.1 M methanol (C) with the onset region of the LSV, highlighted in the inset. Representative CO stripping voltammograms obtained from Pt NWs (A) and commercial Pt NP/C (B). The dashed line highlights the potential of the CO stripping peak in the Pt NWs. (Adapted with permission from Ref. 20. Copyright 2013 American Chemical Society)

The mechanism of MOR on Pt, although it is highly complex, is believed to occur in two primary steps, with CO representing a key intermediate.[62] First, adsorbed methanol on the surface of Pt is thought to undergo a rapid dehydrogenation process, thereby generating the adsorbed CO intermediate. The subsequent oxidation of CO proceeds relatively slowly at potentials close to the thermodynamic potential, due to a lack of adsorbed oxygen species, such as Pt-OH_{ads}, which are believed to facilitate the oxidation process.[58] In essence, the high coverage of CO at low potentials results in a poisoning effect and blocks effective MOR catalysis at the Pt active sites. The issue of CO poisoning on Pt nanostructures has been addressed by introducing small quantities of more oxophilic metal species, such as Ru and Sn, which would facilitate a bifunctional mechanism.[36]

In this case, however, we have demonstrated that it is feasible to increase the MOR kinetics by simply tailoring the morphology of the Pt catalyst itself. Specifically, CO stripping voltammograms obtained from the Pt NWs and Pt NP/C highlight a significant shift in the CO stripping peak potential of nearly 80 mV to lower potentials in the Pt NWs (Figure 6.12A), as compared with analogous Pt NP/C (Figure 6.12B). The improvement in CO stripping kinetics in the one-dimensional nanostructures suggests that the 1D morphology of Pt NWs facilitates CO oxidation at lower potentials. This phenomenon has been observed previously in ultrathin Pt NWs, and is believed to arise from the electronic properties associated with the 1D morphology.[60,61] Specifically, Guo and co-workers[61] have demonstrated that the significantly improved CO kinetics may arise from a shift in the weighted center of the *d*-band as a result of the observed 1D anisotropic structure, which may lead to weaker interactions between the Pt surface sites and the CO adsorbate.

Collectively, all of these results further highlight the intrinsic advantages of 1D nanostructures in terms of their desirable structural and electronic properties. More importantly, this is the first report of enhanced MOR performance in a 1D Pt nanostructure, prepared under completely ambient conditions, without the need for additional reagents such as either surfactants or other shape-directing agents. In addition, this morphology-dependent enhancement observed in 1D nanostructures, prepared by our template-directed method, further demonstrates the importance of exploring the role of chemical composition in this structural paradigm, since the electrocatalytic performance of these modified NWs can be tailored so as to achieve increased, enhanced performance beyond that of their elemental analogues.

6.3.8. Composition-Dependent Performance in $Pd_{1-x}Pt_x$ NWs with Homogeneous Alloy-Type Structures towards the Methanol Oxidation Reaction and the Formic Acid Oxidation Reaction

Given the inherent electrocatalytic advantages associated with our 1D Pt NWs toward MOR, we have undertaken a systematic investigation of the composition-dependent performance in $Pd_{1-x}Pt_x$ NWs. Recently, several reports have focused on the homogeneous $Pd_{1-x}Pt_x$ alloy as a promising bimetallic system with direct and practical application, as both highly active MOR electrocatalysts and as methanol-tolerant ORR electrocatalysts.[63] LSVs were obtained in 0.1 M methanol, supported in 0.1 M $HClO_4$ from Pt, $PdPt_4$, Pd_3Pt_7, and PdPt NWs, and these curves are shown in Figure 6.13A. The Pt and $PdPt_4$ NWs maintained an onset potential that is ~25 mV lower than that of the corresponding Pd_3Pt_7 and PdPt NWs. The lower onset potential in the Pt-rich NWs is likely a result of the larger number of Pt sites at the catalytic interface, which are expected to initiate methanol adsorption and oxidation at lower potentials as compared with Pd active sites alone.[5,28] Although the Pt and $PdPt_4$ NWs gave rise to comparable performance near

the onset potential of ~0.63 V, a careful inspection of the onset region of the LSV (inset to Figure 6.13A) showed that the activity of the $PdPt_4$ NWs exceeded that of the Pt NWs beyond ~0.72 V. To quantitatively explore their behavior in the onset region, the specific MOR activity of the various $Pd_{1-x}Pt_x$ NWs at 0.73 V was plotted with respect to NW composition in Figure 6.13B. On this basis, a volcano-type dependence in the specific MOR activity was noted in the onset region as a function of chemical composition with $PdPt_4$, yielding an optimum activity of 0.42 mA/cm^2.

Interestingly, the Pd-rich PdPt NWs and Pd_3Pt_7 NWs displayed enhanced behavior in the peak region of the LSV and maintained peak potentials of 833 mV and 836 mV, respectively. These values are considerably lower than the corresponding peak potentials for the $PdPt_4$ NWs and the Pt NWs, which were measured at 850 mV and 871 mV, respectively. In addition, the PdPt and Pd_3Pt_7 NWs possessed specific activities at the peak of LSV (Figure 6.13C) of 1.24 and 1.25 mA/cm^2, which maintain a small but measurable enhancement with respect to those of the corresponding $PdPt_4$ (1.19 mA/cm^2) and Pt NWs (1.15 mA/cm^2), respectively. Collectively, the performance metrics of the composition-controlled $Pd_{1-x}Pt_x$ NW samples are all significantly enhanced beyond the activity measured for commercial Pt NP/C, thereby further highlighting the intrinsic advantages of the 1D structural motif. We also note that the elemental Pd NWs evinced minimal MOR activity, which demonstrates that the enhanced performance emerges only with the bimetallic NW compositions. Thus, the observed composition-dependent behavior demonstrates that the addition of Pd content in $Pd_{1-x}Pt_x$ NWs within a finite composition regime can significantly and measurably improve the catalytic performance in both the onset region and the peak region of the LSV.

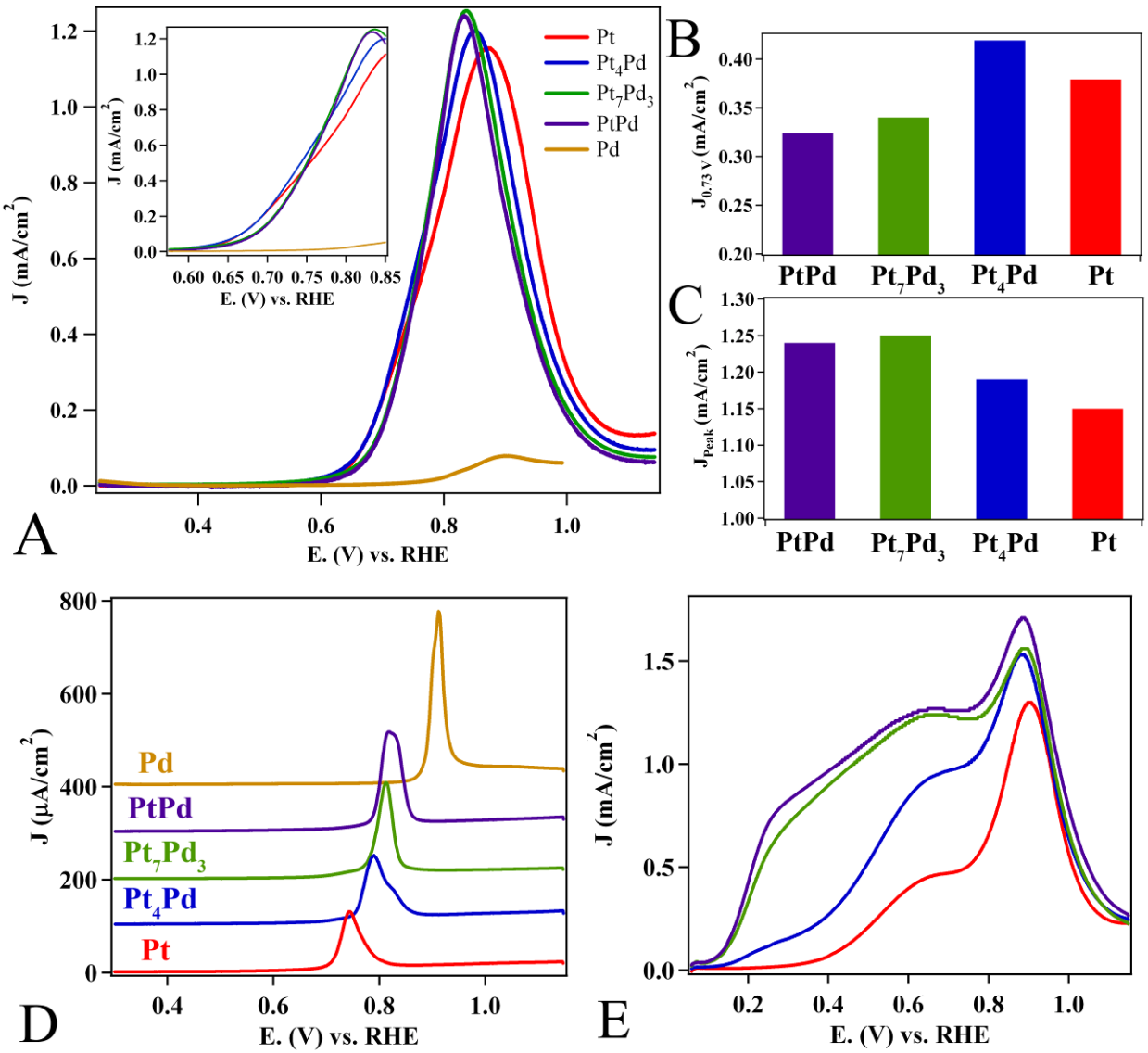

Figure 6.13 Composition-dependent electrocatalytic performance in $Pd_{1-x}Pt_x$ NWs toward MOR. Representative LSVs obtained from various $Pd_{1-x}Pt_x$ NWs, including elemental Pt and Pd NWs, in 0.1 M methanol (A) with the onset region of the LSVs highlight in the inset. The MOR kinetic current densities measured in the onset region at 0.7 V (B) and at the peak of the LSV (C) as a function of NW composition. The composition-dependent electrocatalytic behavior toward CO stripping (D) and formic acid oxidation (E) associated with $Pd_{1-x}Pt_x$ NWs. (Adapted with permission from Ref. 20. Copyright 2013 American Chemical Society)

In the recent literature, the origin of the enhanced performance in nanostructured $Pt_{1-x}M_x$ ('M' = Pd or Au) alloys has been attributed to the incorporation of either Pd or Au into the bimetallic alloy. However there has been a considerable debate regarding the origin of enhancement.[27,64-71] Specifically, it has been suggested by some in the community that the promoting effect of the Pd is a result of a surface-mediated bifunctional effect in an analogous manner to what has been found with $Pt_{1-x}Ru_x$ alloys. In the case of a bifunctional effect, the oxophilic Pd sites are expected to increase the coverage of adsorbed oxygen species at low potentials, thereby contributing to increased CO tolerance.[67]

To examine this reasonable possibility, we have systematically probed the relative interaction of the NW surface with adsorbed oxygen and CO species as a function of NW composition, utilizing both CV and CO stripping experiments. In Section 6.3.5, the oxide reduction peak of the $Pd_{1-x}Pt_x$ NWs (Figure 6.10A) is found to shift from ~820 toward ~800 mV, as the Pd content is increased from 0% to 50%. Although a shift in the onset of that oxide feature has been noted with increased Pd content, the onset of oxide formation in the PdPt NWs remains above 0.6 V.[9] The high onset of surface oxidation in these bimetallic NWs, despite the incorporation of Pd, provides for strong evidence that oxygen adsorbed to the Pd active sites does not contribute significantly to CO oxidation at potentials relevant to the onset of the MOR process, namely 0.5 – 0.6 V.

Using $Pt_{1-x}Ru_x$ alloys as a ubiquitous example of a catalyst that follows a bifunctional process, the addition of Ru to the $Pt_{1-x}Ru_x$ alloy promotes better CO oxidation kinetics and there is an observed shift in the CO stripping peak to lower potentials as Ru content is increased to ~30%. In this case however, the CO stripping voltammograms obtained from our $Pd_{1-x}Pt_x$ NWs (Figure 6.13D) highlight a contrasting trend, wherein the stripping peak potential increased from

744 mV in Pt NWs to 819 mV as the Pd content is increased to 50% in the $Pd_{1-x}Pt_x$ NWs. In fact, a plot of the CO stripping peak potential with respect to NW composition clearly shows that the CO stripping peak potential increases with increasing Pd content. Thus, the collective CV and CO stripping results yield strong evidence that the origin of enhancement does not arise from a bifunctional effect, since the addition of the Pd metal does not necessarily appear to contribute to either increased coverage of adsorbed oxygen species or to lower CO stripping peak potentials.

By contrast with the proposed bifunctional mechanism, other experimental[69,72] and first-principles[70,71] results have suggested that the enhancement in bimetallic surface alloys can be attributed to a change in the mechanism of MOR. Specifically, it is believed that in elemental Pt, the formation of the CO intermediate occurs readily via a so-called "indirect pathway", because of the presence of an abundance of Pt-Pt pair sites that catalyze the formation of CO. However, both bimetallic PdPt and PtAu alloys are believed to favor a direct oxidation or "CO-free pathway," since there are fewer Pt atoms and fewer Pt-Pt pair sites present at the catalytic interface.[69] Moreover, an examination of the electronic properties associated with the bimetallic alloys of PtAu and PdPt by means of first-principles calculations has shown that the incorporation of Pd and Au in these structures can promote the selective formation of a formate (HCOO) intermediate, as opposed to CO.[70,71]

To purposely investigate this possibility, we have probed the formic acid oxidation performance so as to analyze the composition-dependent reactivity toward this intermediate. The study of formic acid oxidation is advantageous, since it represents a key intermediate in the MOR pathway and more importantly, the oxidation of formic acid can serve as a useful probe for determining if either an indirect or direct CO-free oxidation pathway is favored.[72] Examination of the formic acid oxidation LSV (Figure 6.13E) for the elemental Pt NWs has led to an onset at

~300 mV with a characteristic peak at ~900 mV, and is consistent with prior reports for elemental Pt.[72,73] The peak at ~900 mV is believed to be associated with the indirect oxidation of formic acid, thereby leading to a CO intermediate.[72] Interestingly, as the Pd content is increased in the $Pd_{1-x}Pt_x$ NWs to 50%, the onset for formic acid oxidation is shifted to ~100 mV, and this process is accompanied by a rise in the oxidation current in the 0.1 – 0.6 V range. On the basis of prior reports,[72,74] the increased formic acid oxidation at potentials below 0.6 V is consistent with the oxidation of formic acid via a direct CO-free pathway. Thus, it is apparent that the enhancement in the bimetallic $Pd_{1-x}Pt_x$ NWs may come about as a result of a modification of the traditionally expected oxidation pathway, due to the presence of fewer Pt-Pt pair sites at the catalytic interface, particularly when the Pd composition has been increased to 50%. Notwithstanding, the significant and clearly measurable improvements in both the methanol and formic acid oxidation performance have conclusively demonstrated the importance of tailoring chemical composition to provide for enhanced electrocatalytic activity in 1D nanostructures.

6.4 Conclusions

Recently, work associated with developing electrocatalysts for DAFCs have focused on resolving three technical challenges: (i) increasing the activity and durability of ORR catalysts in the cathode, (ii) developing cathode catalysts with high ORR activity in the presence of measurable concentrations of SOMs, and (iii) improving the electrocatalytic performance of anode catalysts towards the oxidation of SOMs. In this report, we have explored and attempted to address these three important concerns in the context of a new class of 1D palladium-based NWs, wherein the physicochemical properties of the NWs, such as morphology and chemical composition, have been optimized for enhanced performance.

In the context of addressing the first and second challenges, we have rigorously examined the composition-dependent ORR performance in $Pd_{1-x}Au_x$ and $Pd_{1-x}Pt_x$ NWs in relation to elemental Pt and Pd NWs and with respect to a variety of state-of-the-art NP catalysts. Our results demonstrate that Pd_9Au NWs maintain an outstanding ORR performance, which is two-fold higher than that of commercial Pt NP/C and more importantly, the composition promotes greatly enhanced stability toward ORR in the presence of methanol. Utilizing this bimetallic NW system, we have developed a hierarchical Pt_{ML}~Pd_9Au core-shell system, which maintains outstanding enhancements in activity and durability in relation to elemental Pt_{ML}~Pd NW analogs. In terms of the final challenge, we have examined the morphology and composition-dependent performance of $Pd_{1-x}Pt_x$ NWs towards MOR. Elemental Pt NWs were found to possess a significant morphology-dependent enhancement of nearly three-fold in terms of peak MOR specific activity over commercial Pt NP/C. Drawing upon the intrinsic advantages associated with 1D NWs, we also examined the kinetics of methanol oxidation as a function of NW composition in high-quality $Pd_{1-x}Pt_x$ NWs, possessing homogeneous alloy-type structures.

Collectively, our results highlight three important findings regarding the development of 1D electrocatalysts. First, tailoring chemical-composition at the nanoscale presents a critical methodology for tuning the physicochemical properties of 1D nanostructures for enhanced performance toward a variety of reactions relevant to DMFC. Second, the observed activity trends in terms of both ORR and MOR are complex and must be rationalized in the context of the structural and electronic properties associated with 1D electrocatalysts. Third, the ability to optimize and couple several structural motifs into one discrete structure, in essence forming complex hierarchical structures, represents a key bottom-up pathway for designing and tailoring electrocatalysts for outstanding performance. Essentially, the optimization of structure and

composition can enable dramatic and remarkable improvements in performance, which can result in tangible improvements in terms of reducing both precious metal content and cost.

6.5 References

(1) Koenigsmann, C.; Santulli, A. C.; Gong, K.; Vukmirovic, M. B.; Zhou, W.-p.; Sutter, E.; Wong, S. S.; Adzic, R. R. *J. Am. Chem. Soc.* **2011**, *133*, 9783-9795.
(2) Koenigsmann, C.; Santulli, A. C.; Sutter, E.; Wong, S. S. *ACS Nano* **2011**, *5*, 7471-7487.
(3) Koenigsmann, C.; Zhou, W.-p.; Adzic, R. R.; Sutter, E.; Wong, S. S. *Nano Lett.* **2010**, *10*, 2806-2811.
(4) Koenigsmann, C.; Scofield, M. E.; Liu, H.; Wong, S. S. *J. Phys. Chem. Lett.* **2012**, *3*, 3385-3398.
(5) Koenigsmann, C.; Wong, S. S. *Energy Environ. Sci.* **2011**, *4*, 1161 - 1176.
(6) Koenigsmann, C.; Tan, Z.; Peng, H.; Sutter, E.; Jacobskind, J.; Wong, S. S. *Isr. J. Chem.* **2012**, *52*, 1090-1103.
(7) Rabis, A.; Rodriguez, P.; Schmidt, T. J. *ACS Catal.* **2012**, *2*, 864-890.
(8) Watanabe, M.; Tryk, D. A.; Wakisaka, M.; Yano, H.; Uchida, H. *Electrochim. Acta* **2012**, *84*, 187-201.
(9) Koenigsmann, C.; Sutter, E.; Chiesa, T. A.; Adzic, R. R.; Wong, S. S. *Nano Lett.* **2012**, *12*, 2013-2020.
(10) Chen, Z.; Waje, M.; Li, W.; Yan, Y. *Angew. Chem. Int. Ed.* **2007**, *46*, 4060-4063.
(11) Lim, B.; Jiang, M.; Camargo, P. H. C.; Cho, E. C.; Tao, J.; Lu, X.; Zhu, Y.; Xia, Y. *Science* **2009**, *324*, 1302-1305.
(12) Xu, C.; Zhang, Y.; Wang, L.; Xu, L.; Bian, X.; Ma, H.; Ding, Y. *Chem. Mater.* **2009**, *21*, 3110-3116.
(13) Koenigsmann, C.; Sutter, E.; Adzic, R. R.; Wong, S. S. *J. Phys. Chem. C* **2012**, *116*, 15297-15306.
(14) Shui, J.-l.; Chen, C.; Li, J. C. M. *Adv. Funct. Mater.* **2011**, *21*, 3357-3362.
(15) Zhiyong, Z.; Li, M.; Wu, Z.; Li, W. *Nanotechnology* **2011**, *22*, 015602.
(16) Guo, S.; Li, D.; Zhu, H.; Zhang, S.; Markovic, N. M.; Stamenkovic, V. R.; Sun, S. *Angew. Chem. Int. Ed.* **2013**, *52*, 3465-3468.
(17) Liu, C.-W.; Wei, Y.-C.; Liu, C.-C.; Wang, K.-W. *J. Mater. Chem.* **2012**, *22*, 4641-4644.
(18) Tan, Y.; Fan, J.; Chen, G.; Zheng, N.; Xie, Q. *Chem. Commun.* **2011**, *47*, 11624-11626.
(19) Liao, H.; Hou, Y. *Chem. Mater.* **2013**, *25*, 457-465.
(20) Koenigsmann, C.; Wong, S. S. *ACS Catal.* **2013**, ASAP.
(21) Aricò, A. S.; Srinivasan, S.; Antonucci, V. *Fuel Cells* **2001**, *1*, 133-161.
(22) Chuan-Jian, Z.; Jin, L.; Bin, F.; Bridgid, N. W.; Peter, N. N.; Rameshwori, L.; Jun, Y. *Nanotechnology* **2010**, *21*, 062001.
(23) Teng, X.; Feygenson, M.; Wang, Q.; He, J.; Du, W.; Frenkel, A. I.; Han, W.; Aronson, M. *Nano Lett.* **2009**, *9*, 3177-3184.
(24) Sarapuu, A.; Kasikov, A.; Wong, N.; Lucas, C. A.; Sedghi, G.; Nichols, R. J.; Tammeveski, K. *Electrochim. Acta* **2010**, *55*, 6768-6774.
(25) Damjanovic, A.; Brusić, V. *Electrochim. Acta* **1967**, *12*, 1171-1184.

(26) Xing, Y.; Cai, Y.; Vukmirovic, M. B.; Zhou, W.-P.; Karan, H.; Wang, J. X.; Adzic, R. R. *J. Phys. Chem. Lett.* **2010**, *1*, 3238-3242.
(27) Cui, C.-H.; Yu, J.-W.; Li, H.-H.; Gao, M.-R.; Liang, H.-W.; Yu, S.-H. *ACS Nano* **2011**, *5*, 4211-4218.
(28) Zhu, C.; Guo, S.; Dong, S. *Adv. Mater.* **2012**, *24*, 2326-2331.
(29) Heinzel, A.; Barragán, V. M. *J. Power Sources* **1999**, *84*, 70-74.
(30) Antolini, E.; Lopes, T.; Gonzalez, E. R. *J. Alloys Compd.* **2008**, *461*, 253-262.
(31) He, W.; Liu, J.; Qiao, Y.; Zou, Z.; Zhang, X.; Akins, D. L.; Yang, H. *J. Power Sources* **2010**, *195*, 1046-1050.
(32) Lee, C.-L.; Chiou, H.-P. *Appl. Catal., B* **2012**, *117–118*, 204-211.
(33) Lee, C.-L.; Chiou, H.-P.; Wu, S.-C.; Wu, C.-C. *Electrochim. Acta* **2010**, *56*, 687-692.
(34) Wang, W. M.; Li, Z. L.; Zou, Z.; Yang, H.; Feng, S. *ECS Transactions* **2008**, *16*, 613-619.
(35) Yang, J.; Zhou, W.; Cheng, C. H.; Lee, J. Y.; Liu, Z. *ACS Appl. Mater. Interfaces* **2009**, *2*, 119-126.
(36) Wee, J.-H.; Lee, K.-Y. *J. Power Sources* **2006**, *157*, 128-135.
(37) Liu, H.; Song, C.; Zhang, L.; Zhang, J.; Wang, H.; Wilkinson, D. P. *J. Power Sources* **2006**, *155*, 95-110.
(38) Rauber, M.; Alber, I.; Müller, S.; Neumann, R.; Picht, O.; Roth, C.; Schökel, A.; Toimil-Molares, M. E.; Ensinger, W. *Nano Lett.* **2011**, *11*, 2304-2310.
(39) Wang, S.; Wang, X.; Jiang, S. P. *Nanotechnology* **2008**, *19*, 455602.
(40) Maksimuk, S.; Yang, S.; Peng, Z.; Yang, H. *J. Am. Chem. Soc.* **2007**, *129*, 8684-8685.
(41) Yuan, Q.; Zhou, Z.; Zhuang, J.; Wang, X. *Chem. Mater.* **2010**, *22*, 2395-2402.
(42) Guo, S.; Zhang, S.; Sun, X.; Sun, S. *J. Am. Chem. Soc.* **2011**, *133*, 15354-15357.
(43) Niu, Z.; Wang, D.; Yu, R.; Peng, Q.; Li, Y. *Chemical Science* **2012**, *3*, 1925-1929.
(44) Zhang, J.; Sasaki, K.; Sutter, E.; Adzic, R. R. *Science* **2007**, *315*, 220-222.
(45) Zhang, F.; Sfeir, M. Y.; Misewich, J. A.; Wong, S. S. *Chem. Mater.* **2008**, *20*, 5500-5512.
(46) Zhang, F.; Wong, S. S. *ACS Nano* **2009**, *4*, 99-112.
(47) Cui, S. T. *J. Chem. Phys.* **2005**, *123*, 054706-054704.
(48) Crank, J. *The Mathematics of Diffusion*; Oxford University Press: Oxford, UK, 1975.
(49) Zhou, H.; Zhou, W.-p.; Adzic, R. R.; Wong, S. S. *J. Phys. Chem. C* **2009**, *113*, 5460-5466.
(50) Tiano, A. L.; Santulli, A. C.; Koenigsmann, C.; Feygenson, M.; Aronson, M. C.; Harrington, R.; Parise, J. B.; Wong, S. S. *Chem. Mater.* **2011**, *23*, 3277-3288.
(51) Sasaki, K.; Naohara, H.; Cai, Y.; Choi, Y. M.; Liu, P.; Vukmirovic, M. B.; Wang, J. X.; Adzic, R. R. *Angew. Chem. Int. Ed.* **2010**, *49*, 8602-8607.
(52) Nørskov, J. K.; Rossmeisl, J.; Logadottir, A.; Lindqvist, L.; Kitchin, J. R.; Bligaard, T.; Jonsson, H. *J. Phys. Chem. B* **2004**, *108*, 17886-17892.
(53) Nørskov, J. K.; Bligaard, T.; Rossmeisl, J.; Christensen, C. H. *Nat. Chem.* **2009**, *1*, 37-46.
(54) Zhang, J.; Mo, Y.; Vukmirovic, M. B.; Klie, R.; Sasaki, K.; Adzic, R. R. *J. Phys. Chem. B* **2004**, *108*, 10955-10964.
(55) Cheng, F.; Dai, X.; Wang, H.; Jiang, S. P.; Zhang, M.; Xu, C. *Electrochim. Acta* **2010**, *55*, 2295-2298.
(56) Damjanovic, A.; Brusic, V.; Bockris, J. O. M. *J. Phys. Chem.* **1967**, *71*, 2741-2742.
(57) Greeley, J.; Norskov, J. K. *J. Phys. Chem. C* **2009**, *113*, 4932-4939.

(58) Feibelman, P. J.; Hammer, B.; Nørskov, J. K.; Wagner, F.; Scheffler, M.; Stumpf, R.; Watwe, R.; Dumesic, J. *J. Phys. Chem. B* **2000**, *105*, 4018-4025.
(59) Li, H.; Sun, G.; Li, N.; Sun, S.; Su, D.; Xin, Q. *J. Phys. Chem. C* **2007**, *111*, 5605-5617.
(60) Zhou, W.-P.; Li, M.; Koenigsmann, C.; Ma, C.; Wong, S. S.; Adzic, R. R. *Electrochim. Acta* **2011**, *56*, 9824-9830.
(61) Wang, S.; Jiang, S. P.; Wang, X.; Guo, J. *Electrochim. Acta* **2011**, *56*, 1563-1569.
(62) Hamnett, A. In *Interfacial Electrochemistry: Theory, Experiment and Applications*; Wieckowski, A., Ed.; Marcel Dekker: New York, NY, 1999, p 843-879.
(63) Antolini, E. *Energy Environ. Sci.* **2009**, *2*, 915-931.
(64) Mott, D.; Luo, J.; Njoki, P. N.; Lin, Y.; Wang, L.; Zhong, C.-J. *Catal. Today* **2007**, *122*, 378-385.
(65) Luo, J.; Njoki, P. N.; Lin, Y.; Mott, D.; Wang; Zhong, C.-J. *Langmuir* **2006**, *22*, 2892-2898.
(66) Yang, L.; Yang, W.; Cai, Q. *J. Phys. Chem. C* **2007**, *111*, 16613-16617.
(67) Liu, Y.; Chi, M.; Mazumder, V.; More, K. L.; Soled, S.; Henao, J. D.; Sun, S. *Chem. Mater.* **2011**, *23*, 4199-4203.
(68) Choi, J.-H.; Park, K.-W.; Park, I.-S.; Kim, K.; Lee, J.-S.; Sung, Y.-E. *J. Electrochem. Soc.* **2006**, *153*, A1812-A1817.
(69) Yin, M.; Huang, Y.; Liang, L.; Liao, J.; Liu, C.; Xing, W. *Chem. Commun.* **2011**, *47*, 8172-8174.
(70) Zhong, W.; Liu, Y.; Zhang, D. *J. Phys. Chem. C* **2012**, *116*, 2994-3000.
(71) Yuan, D.; Gong, X.; Wu, R. *J. Chem. Phys.* **2008**, *128*, 064706-064705.
(72) Cui, C.-H.; Li, H.-H.; Cong, H.-P.; Yu, S.-H.; Tao, F. *Chem. Commun.* **2012**, *48*, 12062-12064.
(73) Zhang, S.; Shao, Y.; Liao, H.-g.; Liu, J.; Aksay, I. A.; Yin, G.; Lin, Y. *Chem. Mater.* **2011**, *23*, 1079-1081.
(74) Vidal-Iglesias, F. J.; Solla-Gullón, J.; Herrero, E.; Aldaz, A.; Feliu, J. M. *Angew. Chem. Int. Ed.* **2010**, *49*, 6998-7001.

Chapter 7. Size- and Composition-Dependent Enhancement of Electrocatalytic Oxygen Reduction Performance in Ultrathin Palladium – Gold ($Pd_{1-x}Au_x$) Nanowires

7.1 Introduction

As a culmination of our efforts throughout Chapters 3 – 6, we have drawn upon our portfolio of structure-property correlations in 1D electrocatalysts and developed a fully optimized ORR electrocatalyst, in terms of morphology, size, composition, and structure. On the basis of our results in Chapter 6,[1,2] the focus of our efforts in this chapter are centered upon the $Pd_{1-x}Au_x$ alloy NW system, which evinced noteworthy enhancements in performance over commercial Pt analogues. Nevertheless, despite the significant improvements in activity, stability and durability over commercial analogues, the Pt_{ML}~Pd_9Au NWs prepared by our group's template-based approach maintained a PGM normalized ORR activity of 0.16 A/mg, which is not significantly enhanced as compared with the 0.1 – 0.2 A/mg, representing activities typically achieved with commercial Pt NP/C.[3,4] Although Pt only comprises a total of 7.2% of the entire PGM content, it is evident that the PGM activity must be increased by several-fold in order to exceed the recommended 2015 U.S. DOE target[5] of 0.44 A/mg, and approach a viable catalyst system.

Drawing upon the noteworthy size-dependent enhancement in performance, associated with ultrathin noble metal NWs,[6-9] our goal in this report is to successfully synthesize a high-quality carbon-supported $Pd_{1-x}Au_x$ NWs with ultrathin 2 nm diameters to greatly improve upon the PGM activity.[8] The synthesis of the target alloy-type NW system is achieved by an ambient solution-based technique that is reasonably energy efficient, sufficiently scalable, and noticeably straightforward. Going beyond mere synthesis, our synthetic method is capable of precisely tuning the chemical composition of the as-prepared NWs (*e.g.* Pd_9Au, Pd_8Au_2, and Pd_7Au_3 NWs)

by simply tuning the contents of the precursor solution. Thus, we demonstrate for the first time herein a systematic and simultaneous optimization of NW diameter and composition with the overarching goal of maximizing mass activity beyond that of the DOE target.

In terms of composition, the as-prepared Pt_{ML}~$Pd_{1-x}Au_x$ NWs/C maintain a "volcano-type" dependence with respect to chemical composition, and in fact, the Pt_{ML}~Pd_9Au NW/C composites represent the peak activity with outstanding specific and Pt-mass activities of 0.98 mA/cm^2 and 2.54 A/mg_{Pt}, respectively. With the composition of ultrathin Pt_{ML}~$Pd_{1-x}Au_x$ NWs optimized, we have examined the size-dependent performance of the ultrathin 2 nm Pt_{ML}~Pd_9Au NW/C composite, as compared with analogous 45 nm Pt_{ML}~Pd_9Au NWs. The ultrathin 2 nm Pt_{ML}~Pd_9Au NWs maintained a PGM activity of 0.64 A/mg, which is more than four-fold higher than that associated with the larger 45 nm wires and also commercial Pt NP/C. Given the excellent results we have obtained at small scales, we have also successfully scaled up our synthesis in order to efficiently produce electrocatalysts in a quantity sufficient to prepare functional membrane electrode assemblies (MEAs). Preliminary MEA testing has demonstrated that this optimized catalyst system is capable of evincing high performance under practical fuel cell conditions. This exciting result provides for excellent validation that trends in performance observed under well-defined RDE conditions are relevant to those observed under realistic MEA conditions, in the case of 1D electrocatalyst architectures.

7.2 Composition-Controlled Synthesis of Ultrathin $Pd_{1-x}Au_x$ NWs Supported on Vulcan XC-72R Carbon

The synthesis of ultrathin $Pd_{1-x}Au_x$ NWs was accomplished by suitably adapting a method previously utilized in Chapter 4 for the preparation of elemental Pd NW/C

composites.[6,10,11] Initially, unsupported $Pd_{1-x}Au_x$ NWs were prepared by dissolving a total of 0.056 mmol of palladium nitrate (Alfa Aesar, 99.9%) and tetrachloroauric acid hydrate ($HAuCl_4 \cdot xH_2O$, Alfa Aesar, 99.999%) into 7 mL of toluene. To achieve the desired NW composition, a stoichiometric ratio of the metal precursors needed to achieve the intended NW composition was added to the toluene, so as to provide for a total of 0.056 mmol of metal precursor. For example, the Pd_7Au_3 NWs were prepared from a mixture of 0.0392 mmol $Pd(NO_3)_2$ and 0.0168 mmol $HAuCl_4 \cdot xH_2O$, representing 70% and 30%, respectively, of the combined 0.056 mmol of metal precursor added to the toluene solution. Subsequently, octadecylamine (400 mg, ODA, Acros Organics, 90%) and dodecyltrimethylammonium bromide (60 mg, DTAB, TCI, >99%) were also added to the toluene solvent, serving as a shape-directing agent and a phase transfer catalyst, respectively.

Once the precursor solution was prepared, the mixture was kept under an inert Ar atmosphere utilizing standard Schlenk conditions and homogenized by sonication for 20 min. In a separate vial, a reducing agent solution of sodium borohydride (13 mg, $NaBH_4$, Alfa Aesar, 98%) was prepared in 2 mL of deoxygenated distilled water. The reduction of the metal precursors was accomplished by injecting the reducing agent solution into the precursor solution dropwise, whilst stirring, thereby resulting in the evolution of a reddish-brown colored solution. Completion of the reaction was signaled by the formation of a black solution after ~1 h. In all cases, the isolation and support onto Vulcan XC-72R carbon powder were achieved in an identical manner to the elemental Pd NW analogs described in Chapter 4, Section 2. Scaled up versions of these reactions were performed identically. However, all reagents and solvents were scaled up proportionally. To verify the batch-to-batch homogeneity, seven replicates of a reaction scaled up by four-fold was performed and the combined products were characterized.

Thermogravimetric analysis profiles were obtained with a TGA Q500 (TA Instruments) on dried aliquots of the catalyst ink in order to estimate the total precious metal content.[6] Isotherms were obtained by raising the temperature from 25 to 900°C at a rate of 10°C/min under a flow of extra-dry air provided at a rate of 60 mL/min. The mass profiles confirmed that the carbonaceous material (*e.g.* Vulcan XC-72R and residual organic surfactants) was entirely removed once ~600°C was reached. The mass of residual Pd and Au could then be obtained between 600 and 800°C. TGA measurements established that the combined palladium and gold loading is 19.3 ± 0.9% on the basis of two separate experiments. Upon scaling the procedure up, the procedure was optimized to enable PGM loadings of up to 43.5%.

7.3 Results & Discussion

7.3.1. Synthesis & Structural Characterization of $Pd_{1-x}Au_x$ NWs

In this Chapter, we have employed an ambient, surfactant-based technique to prepare $Pd_{1-x}Au_x$ NWs with control over chemical composition.[8] Specifically, a mixed precursor solution containing both Pd^{2+} and Au^{3+} precursors is reacted with sodium borohydride serving as a reducing agent, and the nucleation and growth of NWs is directed by the presence of the surfactant ODA. The composition of the NWs can be readily and predictably controlled by manipulating the contents of the precursor solution. In fact, the stoichiometry of the NW can be directly controlled by appropriately modifying the stoichiometric ratio of the metal precursors within the precursor solution. In this case, $Pd_{1-x}Au_x$ NW samples are prepared with chemical compositions ranging between $x = 0$ to $x = 0.75$. Hence, this method is advantageous, because it allows for the efficient production of high-quality, homogeneous NWs possessing tunable

chemical composition and a monodisperse distribution of diameters over the relevant composition regime.

X-ray powder diffraction (XRD) obtained on the as-prepared $Pd_{1-x}Au_x$ NW/C composites (Figure 7.1A) reveals that the NWs are homogeneous alloys with the desired face-centered cubic (FCC) crystal structure. It is evident that the patterns are devoid of peaks that can be attributed to either the elemental palladium or gold phases (JCPDS card #46-1043 and #04-0784, respectively), further confirming that the reaction produces uniform alloys. As expected, a characteristic shift to lower 2θ in the FCC peaks is observed, as the gold content is increased from $x = 0$ to $x = 0.75$ within the NWs. This trend suggests that the lattice parameter of the alloy uniformly transitions from that of palladium toward that of gold as the gold content is systematically increased in the as-prepared NWs. This result is in excellent agreement with the XRD data obtained on the larger single crystalline 50 nm $Pd_{1-x}Au_x$ NWs.[1] However, in this case, the significant broadening of the diffraction peaks, as a result of the small crystallite size and the presence of carbon, prevents quantitative estimation of composition utilizing Vegard's law.

Regardless, the composition of the various as-prepared $Pd_{1-x}Au_x$ NW/C composites was examined by scanning electron microscopy and energy dispersive X-ray analysis (SEM-EDAX). For each sample, a thin film of the $Pd_{1-x}Au_x$ NW/C composites was deposited onto a Si wafer and EDAX spectra were taken at a minimum of four representative locations. The measured trend (Figure 7.2B) reveals that there is a high degree of correlation between the composition of the as-prepared NWs and the initial precursor solution.

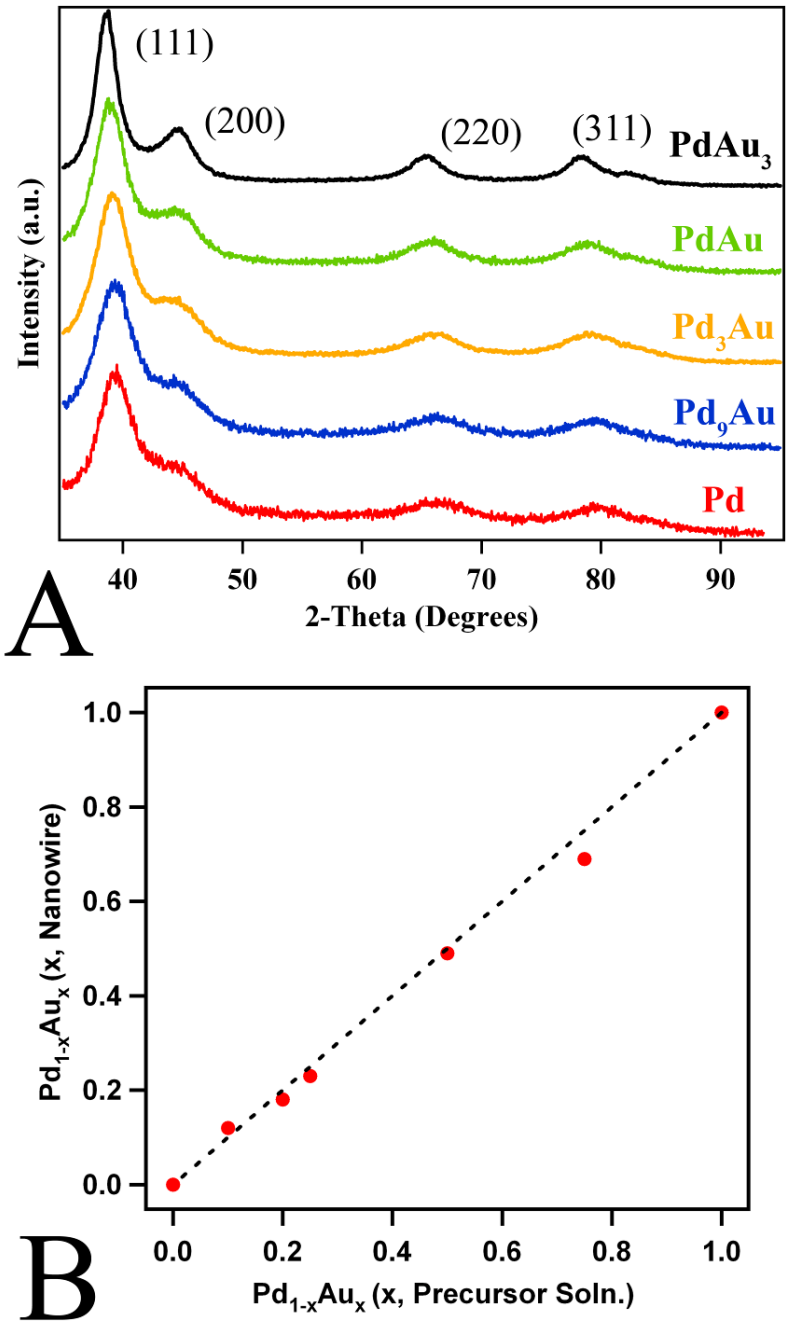

Figure 7.1 Correlating the chemical-composition of as-prepared, ultrathin $Pd_{1-x}Au_x$ NW/C to that of the precursor solution. Representative XRD patterns (A) of isolated, ultrathin $Pd_{1-x}Au_x$ NWs with *x* values ranging from 0 – 0.75. A graph (B) depicting the correlation between the chemical composition of precursor solution employed in the synthesis (bottom axis) and the composition of the corresponding NWs measured by SEM-EDAX (left axis). The dashed line is a representation of the ideal 1:1 relationship between NW composition and the contents of the precursor solution and serves to highlight the high degree of correlation in this synthesis. (Adapted with permission from Ref. 8. Copyright 2012 American Chemical Society)

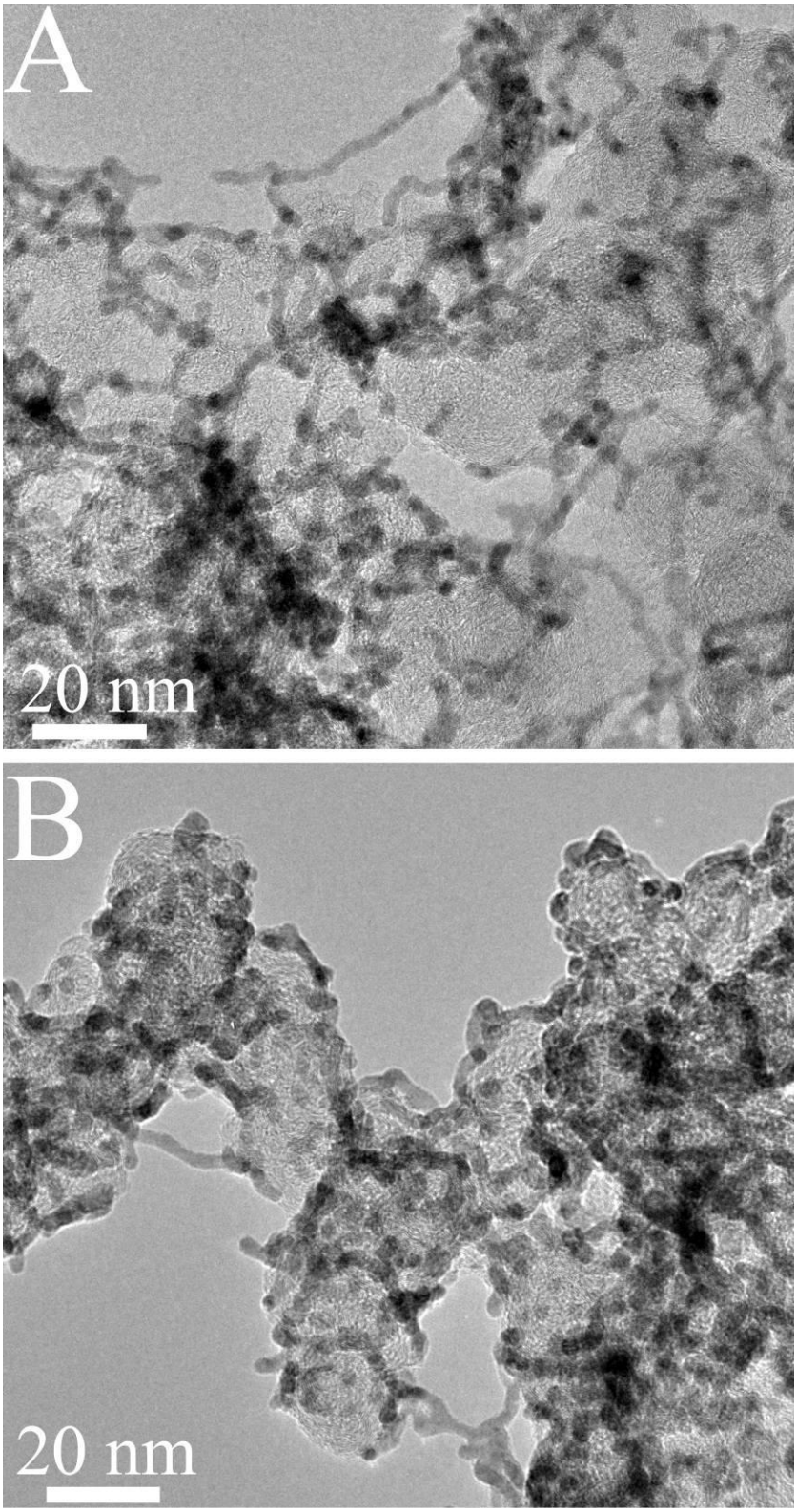

Figure 7.2 Overview TEM images of the Pd_9Au NW/C (A) and Pd (B) NWs highlighting the relatively uniform and ubiquitous net-like distribution of NWs on the surface of the carbon NPs. (Adapted with permission from Ref. 8. Copyright 2012 American Chemical Society)

Subsequently, transmission electron microscopy (TEM) was employed to examine the morphology, crystallinity, and uniformity of the as-prepared $Pd_{1-x}Au_x$ NW/C composites. In particular, we have focused our analysis on the Pd_9Au, Pd_8Au_2, and Pd_7Au_3 NWs, as these are expected to be the most active towards ORR.[12] Utilizing Pd_9Au NWs as a representative example, the overview TEM images (Figure 7.2A) highlight the highly uniform anisotropic 1D structure of the NWs and confirm that only a minimal number of NPs (~5%) are present. It is also apparent that the as-prepared NWs are reasonably well-dispersed, and hence, maintain a uniform spatial distribution on the carbon substrate. The Pd_9Au NWs possess an ultrathin diameter of 2.1 ± 0.5 nm with lengths of up to ~30 nm extending over the carbon substrate. A similar analysis of the Pd (Figure 7.2B), Pd_8Au_2, and Pd_7Au_3 NW/C composites reveals that there is no significant difference in either the NW dimensions, dispersibility of the NWs on the carbon surface, or the crystalline texture of the individual NWs. In fact, the diameters of the various Pd_9Au, Pd_8Au_2, and Pd_7Au_3 NWs are collectively 2.0 ± 0.5 nm, which highlights the uniformity of the samples over a broad range of compositions. The homogeneity of the samples over the entire composition regime emphasizes the importance of chemical composition as the key factor in determining electrocatalytic performance.

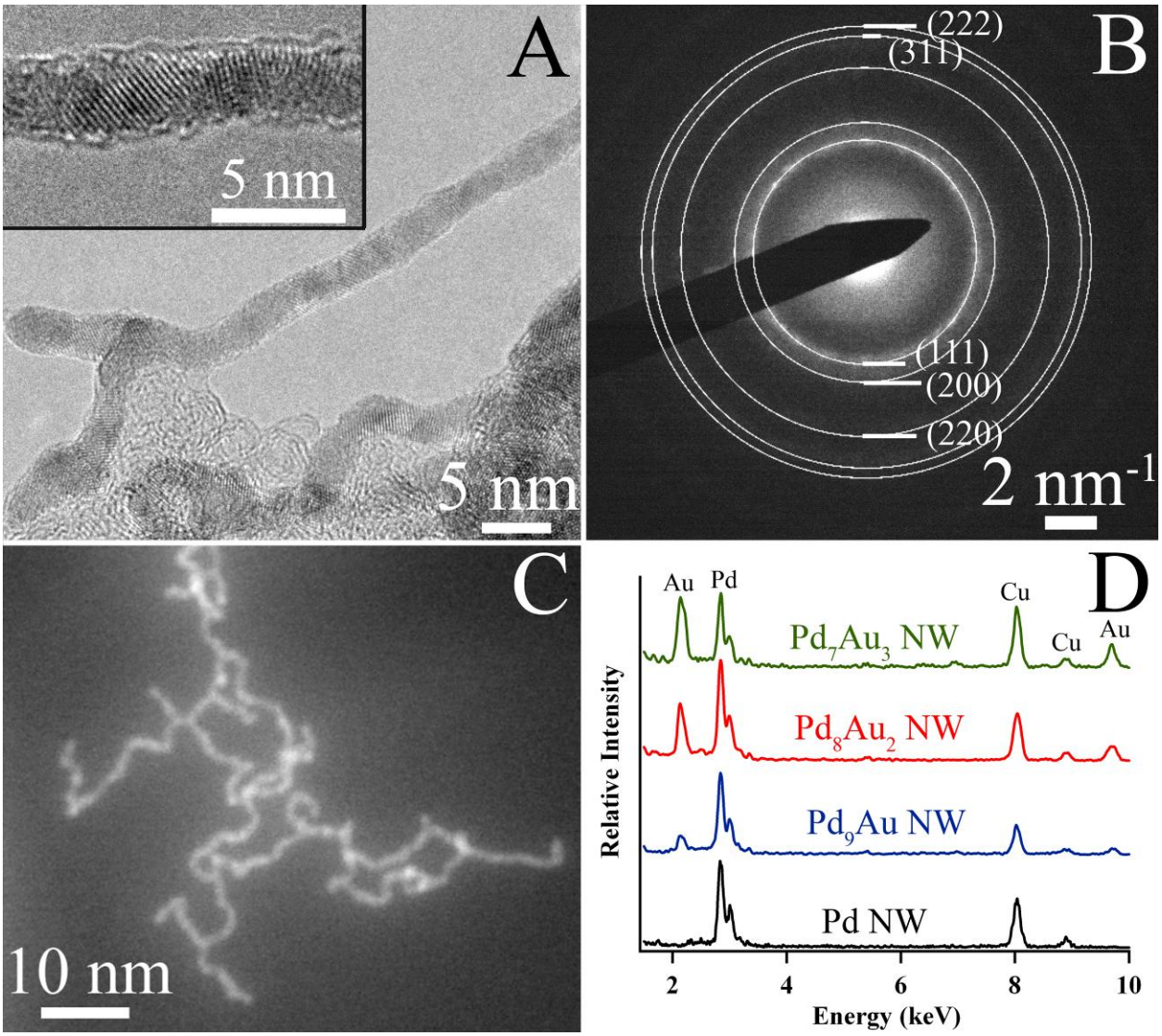

Figure 7.3 Structural characterization of ultrathin $Pd_{1-x}Au_x$ NW/C. Representative TEM image (A) of Pd_9Au NWs supported on Vulcan XC-72R carbon support. The inset to panel A shows a typical high resolution TEM image, highlighting the segmented nature of the individual NWs. The SAED pattern (B) obtained from a collection of NWs is highlighted. The concentric rings of a simulated diffraction pattern for FCC Pd_9Au are shown as an overlay to the experimentally determined SAED pattern. An HAADF image (C) taken from a representative collection of Pd_8Au_2 NWs is also shown. Characteristic EDAX spectra (D) in STEM mode collected from various $Pd_{1-x}Au_x$ NW/C composites. (Reprinted with permission from Ref. 8. Copyright 2012 American Chemical Society)

A high resolution TEM (HRTEM) image of a single Pd_9Au NW, shown as an inset to Figure 7.3A, confirms that the NWs are composed of multiple extended single crystalline segments oriented along the long axis of the NW. The segmented nature of the NWs is also apparent in the selected area electron diffraction (SAED) pattern (Figure 7.3B), since discrete diffraction spots are present within the continuous rings.[6,9] The diffraction rings present within the SAED can be readily indexed to the (111), (200), (220), (222), and (331) reflections, calculated for the FCC Pd_9Au alloy structure, which is shown as an overlay to the experimentally determined SAED pattern. On the basis of the diffraction pattern, the Pd_9Au, Pd_8Au_2, and Pd_7Au_3 NWs were determined to maintain lattice parameters of 3.923 Å, 3.934 Å, and 3.948 Å, respectively, which is in excellent agreement with the calculated values of 3.909 Å, 3.928 Å, and 3.947 Å for the respective FCC alloys. Thus, the TEM diffraction results are in agreement with the XRD data and further confirm that the NWs possess a homogeneous alloy-type structure.

In addition to examining the uniformity of the NWs in terms of morphology and crystallinity, the homogeneity of the composition and distribution of the elements is also a crucial element in examining the overall quality of the bimetallic NWs. We accomplished this task through collection of EDAX data in scanning TEM mode. Figure 7.3C shows a high angle annular dark field (HAADF) image collected from a representative collection of Pd_8Au_2 NWs. The largely uniform contrast (sensitive to *Z*) over the NW sample indicates that the chemical composition of the NWs is relatively homogeneous. It is apparent in the image that there are some spherical areas of brighter contrast, which may be attributed to either a higher density of material (*e.g.* overlapping of NWs) or to an enrichment of gold in these regions. Similar HAADF results have been observed in the case of the Pd_9Au and Pd_7Au_3 NWs.

To examine the possibility of gold enriched zones existing in the NWs, EDAX spectra and corresponding atomic compositions were obtained in several locations amongst various collections of NWs. The average compositions for the Pd_9Au, Pd_8Au_2, and Pd_7Au_3 NWs were determined to be $Pd_{0.904}Au_{0.096}$ (± 0.006), $Pd_{0.77}Au_{0.22}$ (± 0.02), and $Pd_{0.65}Au_{0.35}$ (± 0.01). The relatively low standard deviation observed in the measured chemical compositions confirms that the gold content is highly uniform throughout the NWs, which suggests that the regions of brighter contrast are not likely a result of gold-enriched zones. In addition, it is crucial to highlight that the measured compositions and the trends in the gold and palladium EDAX signals shown in Figure 7.3D are in good agreement with the results obtained from SEM-EDAX. Thus, the TEM and SEM-EDAX measurements together confirm that there is a high degree of correlation between the actual chemical composition of the precursor solution and the corresponding composition of the resulting NWs.

Previously, Teng et al. examined the fine structure and atomic distribution of analogously prepared $Pt_{1-x}Au_x$ NWs, utilizing the same synthetic method, and have observed similar results.[10,13] In that case, it was found that at moderate to high levels of platinum content in the precursor solution, the formation of alloy type NWs with a homogeneous distribution of the metal atoms throughout the wire diameter was favored. Similar results indicating the presence of a single FCC alloy phase have also been observed in more complex, so-called trimetallic and quadrimetallic NWs, prepared utilizing the same synthetic technique as with PtAu.[11] It was suggested in these reports that the homogeneous distribution results from a competition between several different synthetic parameters, including the relative reduction potentials of the precursors, the interaction of the metal atoms with the ODA surfactant, and the relative free surface energies of the various metals. On the basis of the combined of HAADF images, XRD,

HRTEM images, SAED patterns, and prior insights into the growth mechanism, we believe that our as-prepared $Pd_{1-x}Au_x$ NWs herein maintain relatively uniform, homogeneous alloy compositions without measurable segregation of the constituent elements.

7.3.2. Electrochemical Properties and ORR Performance of $Pd_{1-x}Au_x$ NWs

Our as-prepared $Pd_{1-x}Au_x$ NWs represent an exciting platform for the deposition of Pt_{ML} shells since the influence of the chemical composition of the core NW on the electrocatalytic performance of the Pt_{ML}~$Pd_{1-x}Au_x$ structure towards ORR can be examined. Prior to Pt_{ML} deposition, the electrochemical properties and performance of the as-prepared NWs were studied. In Chapter 4, a treatment protocol was developed for the removal of residual organic impurities from the surfaces of analogous Pd NW/C composites, wherein a UV-ozone atmosphere pre-treatment was combined with a selective CO adsorption process.[6] However, in this particular case, the surfaces of the alloy $Pd_{1-x}Au_x$ NWs could be suitably purified by employing the selective CO adsorption process without requiring the UV-ozone pretreatment. This interesting observation can likely be explained by a significant weakening of the interaction with the NW surface as a result of the addition of gold.[13] Hence, the need for less rigorous pretreatment processing in the case of the bimetallic NWs is a significant step towards increasing the practicality of these composites as potentially viable electrocatalysts. After purification, the quality and electrochemical performance of our as prepared $Pd_{1-x}Au_x$ NWs were obtained by the thin-layer RDE method.[14]

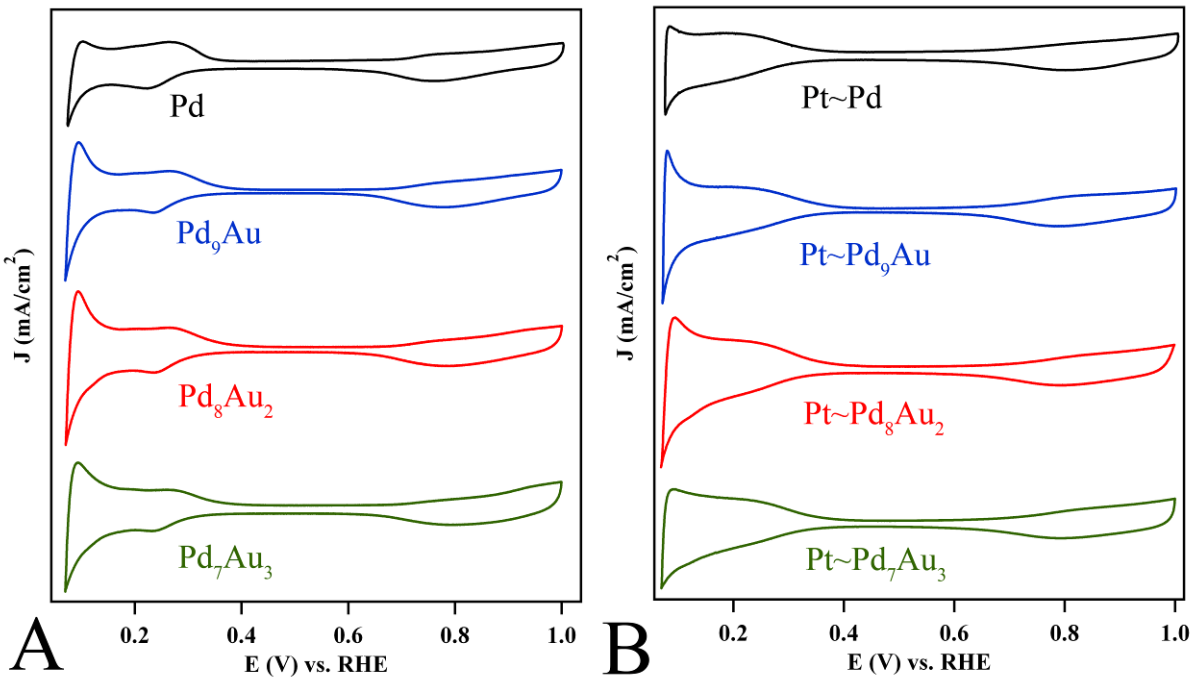

Figure 7.4 Cyclic voltammograms obtained from purified, ultrathin $Pd_{1-x}Au_x$ NW/C composites (x = 0.1, 0.2 and 0.3) by comparison with elemental Pd NW/C before (A) and after (B) the deposition of a Pt_{ML} on the NW surface. (Reprinted with permission from Ref. 8. Copyright 2012 American Chemical Society)

Cyclic voltammograms (CVs) collected from the Pd_9Au, Pd_8Au_2, and Pd_7Au_3 NWs shown in Figure 7.4A display prominent features in the 0 – 0.4 V and the 0.6 – 1.0 V regions, characteristic of H_{ads} processes and the corresponding formation of surface oxide species, respectively. The H_{ads} features in the case of the $Pd_{1-x}Au_x$ NWs are smoother and more reversible than that of the analogous Pd NWs. Analogous results were obtained in the case of the 45 nm Pd_9Au NWs, which also displayed a similar H_{ads} profile that is distinctive from that of elemental Pd but is suggestive of a more active surface.[1] A more profound effect of chemical composition upon the resulting CVs is apparent in the oxide reduction peak, which shifts linearly to higher potentials (*i.e.* 0.7626 V to 0.8006 V) as the gold content is correspondingly increased from 0 to 30%.

Given the uniformity of the NWs in terms of dimension, crystallinity, surface texture, and homogeneity of the various $Pd_{1-x}Au_x$ NW samples, the role of NW composition is highlighted as the primary origin for the trend in the oxide reduction peak potential. The measured shift in the oxide reduction potential is readily explained by the effect of gold in the $Pd_{1-x}Au_x$ ultrathin alloy NWs, which has been shown in the case of analogous PtAu NWs to impart electron density onto the *d*-states of the Pt, thereby making it in essence more noble.[12,13] On this basis of this argument, the strength of the interaction with adsorbed oxygen species should be significantly weakened, as the gold content is increased and cause the discernible shift in the position of the oxide reduction peak.[12,15-17]

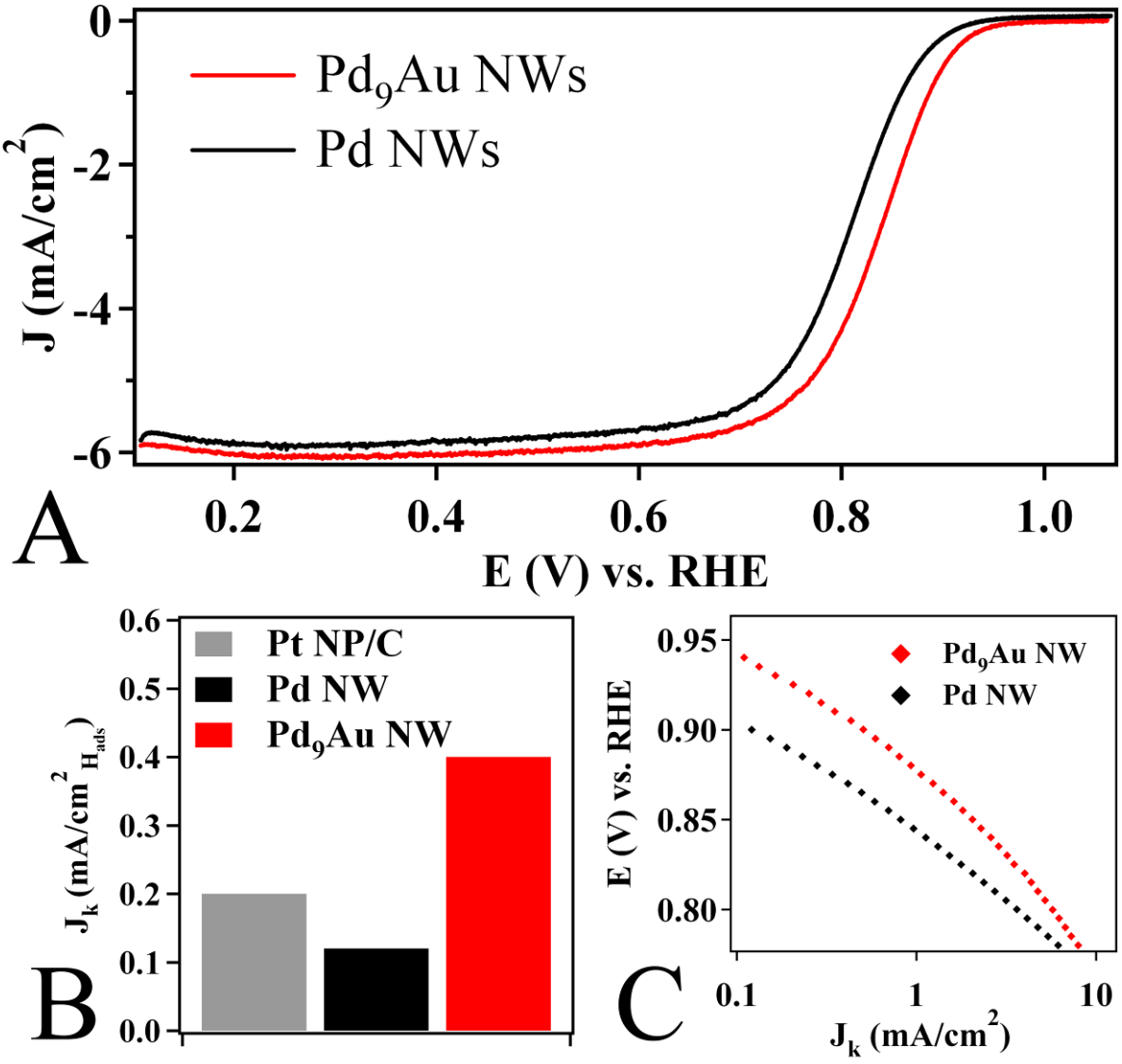

Figure 7.5 The significance of chemical composition on the electrocatalytic performance of $Pd_{1-x}Au_x$ NW/C toward ORR. Representative polarization curves (A) obtained from Pd_9Au NWs in comparison with elemental Pd NWs. Experimentally calculated area-normalized kinetic current densities (J_K, mA/cm^2) measured at 0.9 V are shown in (B) for the Pd_9Au and Pd NWs, with commercial Pt NP/C serving as a reference. *E* vs. J_K plots for the Pd_9Au and elemental Pd NWs are presented in (C). (Reprinted with permission from Ref. 8. Copyright 2012 American Chemical Society)

To demonstrate the high quality of the purified $Pd_{1-x}Au_x$ NW/C, the cathodic ORR kinetics were explored in the case of the Pd_9Au NW/C composites. In essence, we have specifically selected to examine the Pd_9Au NW/C composites, since these structures are anticipated to maintain the highest performance.[6,12] On the basis of the polarization curves obtained in an oxygen saturated electrolyte (Figure 7.5A), the Pd_9Au NWs maintain significantly enhanced performance as compared with analogous elemental Pd NWs. The measured specific activities obtained from Pd_9Au NW/C, Pd NW/C, and commercial Pt NP/C are summarized in Figure 7.5B. It is apparent that the Pd active sites in the Pd_9Au NW/C composites yield a high specific activity of 0.40 mA/cm^2, which represents a four-fold and two-fold enhancement with respect to that the value measured for elemental Pd NW/C (0.12 mA/cm^2) and for Pt NP/C (0.20 mA/cm^2), respectively. In fact, the potential vs. specific activity (E vs. J_K) plot (Figure 7.5C) reveals that the consistently enhanced performance of the Pd_9Au NWs is maintained with respect to that of the Pd NW/C over a broad range of plausible fuel cell potentials. Hence, the Pd_9Au NW/C composites with essentially no measurable platinum content possess outstanding capabilities that surpass even commercial Pt NP/C, thereby confirming the overall quality of our NWs.

Although some studies suggest that the origin of enhanced activity particularly in the case of alcohol oxidation arises from the mutual presence of Pd-Au pair sites at the catalytic interface,[18-20] we have demonstrated in Chapter 6 that the enhanced ORR performance in the case of bimetallic $Pd_{1-x}Au_x$ nanostructures largely arises from their homogeneous alloy type-structure, while the presence of Pd-Au surface pair sites does not necessarily promote significant enhancement.[1]

7.3.3. Composition-Dependent ORR Performance in Core-Shell Pt_{ML}~$Pd_{1-x}Au_x$ NWs

Given the high performance of the $Pd_{1-x}Au_x$ system, our as-prepared $Pd_{1-x}Au_x$ NWs were employed as high quality, 1D substrates for the deposition of a Pt_{ML} shell, thereby forming desired Pt_{ML}~$Pd_{1-x}Au_x$ NW/C composites. The deposition of the Pt_{ML} shell was confirmed by the CVs obtained from the Pt_{ML}~$Pd_{1-x}Au_x$ NW/C composites after the Cu UPD/galvanic displacement process shown in Figure 7.4B. Polarization curves (Figure 7.6A) obtained from Pt_{ML}~Pd_9Au NW/C and Pt_{ML}~Pd NW/C display a significantly enhanced ORR performance of the alloyed NWs, even when compared with elemental Pt_{ML}~Pd NW/C analogues. To explore the dependence of chemical composition upon ORR activity, specific activities and Pt mass activities were measured at 0.9 V for the Pt_{ML}~$Pd_{1-x}Au_x$ NW/C (x = 0, 0.1, 0.2, & 0.3) composites and the results are summarized in Figure 7.6B. Interestingly, the measured activities and the E vs. J_K curves (inset to Figure 7.6A) reveal that there is a distinct "volcano-type" dependence of the measured ORR activity with respect to the composition of the NWs. The maximum specific (0.98 mA/cm^2) and platinum mass activities (2.54 A/mg_{Pt}) are achieved in the Pt_{ML}~Pd_9Au NW/C composite, which represents an outstanding enhancement as compared with Pt NP/C (0.20 mA/cm^2, 0.10 A/mg_{Pt}), serving as a commercial standard.

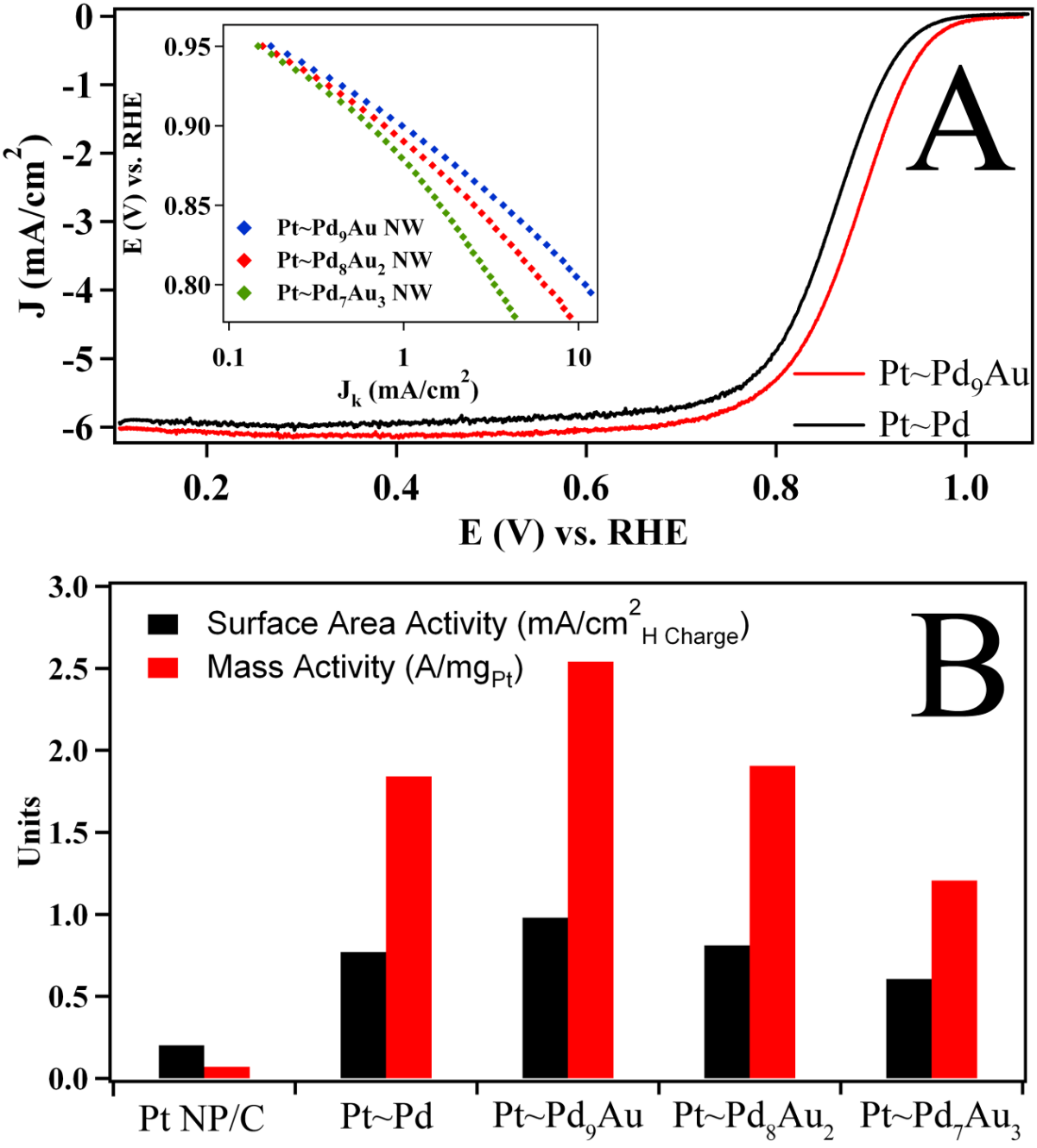

Figure 7.6 Composition-dependent performance in hierarchical Pt_{ML}~$Pd_{1-x}Au_x$ NW/C composites toward ORR. Representative polarization curves (A) obtained from the Pt_{ML}~Pd_9Au NW/C composites with the analogous Pd NW/C composites serving as a comparison. An *E* vs. J_K plot for the various Pt_{ML}~$Pd_{1-x}Au_x$ NW/C composites is shown as an inset to (A). Experimentally determined kinetic currents at 0.9 V normalized to the measured ESA and the platinum mass are shown (B) for the Pt_{ML}~$Pd_{1-x}Au_x$ NW/C and commercial Pt NP/C samples, respectively. (Reprinted with permission from Ref. 8. Copyright 2012 American Chemical Society)

In terms of catalyst morphology, the volcano-type dependence in the case of the NWs is in excellent agreement with results previously obtained on Pt_{ML}~$Pd_{1-x}Au_x$ NP/C systems.[12,15] These data also demonstrate an optimal peak performance in the case of Pt_{ML}~Pd_9Au. Hence, the presence of a similar composition-dependent performance in the case of both Pt_{ML}~Pd_9Au NPs and NWs is a clear indication that the gold dopant and homogeneous alloy-type composition play a crucial role in modifying the electrocatalytic properties of the bimetallic alloy. In this particular case, however, it is apparent that the one-dimensional NW structural motif results in a significantly enhanced performance as compared with the corresponding Pt_{ML}~Pd_9Au NP/C. Specifically, the Pt_{ML}~Pd_9Au NWs (0.98 mA/cm^2) in this report maintain a nearly two-fold higher specific activity as compared with the analogous value for Pt_{ML}~Pd_9Au NPs (0.5 mA/cm^2) obtained in a previous report under MEA conditions.

The origin of the measured volcano-type dependence as a function of chemical composition represents an interesting question, since it is related to the nature of the bimetallic heterostructured NWs. Specifically, the explanation for the electrocatalytic performance of Pt_{ML} catalysts has been largely attributed to a combination of (i) a structural effect wherein the core atoms impart a strain-induced contraction of the Pt_{ML} and (ii) an electronic effect as a result of the coupling between the core and shell atoms.[21] These complementary effects are thought to mutually contribute to a favorable downshift in the *d*-band center of the Pt_{ML} and a corresponding weakening of the interaction with oxygen adsorbates in the case of Pt_{ML}~Pd. This combination of factors has been previously predicted by Nørskov and co-workers to result in improved ORR kinetics.[22,23]

Taking into account these considerations, we can separately examine the effect of the gold composition upon the structural and electronic interactions between the Pt_{ML} shell and the

$Pd_{1-x}Au_x$ core. First, increasing gold content has been shown to promote unique electronic properties, wherein the reconfiguration of the charge distribution results in an increased electron density on the Pd atoms.[13,24,25] Recently, EXAFS data obtained from Pt_{ML}~Pd_9Au NPs/C by Adzic and co-workers has demonstrated that the formation of Pd-O is greatly suppressed at potentials of up to ~0.9 V, suggesting that the gold additive significantly stabilizes palladium towards oxidation and dissolution. In this case, the stabilizing effect of the gold additive is manifested in the CVs obtained from as-prepared $Pd_{1-x}Au_x$ (Figure 7.4A), which display significantly weakened interactions with oxygen adsorbates, as the gold content is increased. Importantly, a similar shift from 0.7816 V to 0.7926 V in the oxide reduction peak potential is observed after Pt_{ML} deposition (Figure 7.4B), as the gold content is increased from 10% to 30%, which confirms that the electronic properties of the core are imparted upon the Pt_{ML} shell.

Second, we consider the relationship between the gold content of the core NW with respect to the structural interaction between the NW core and the Pt_{ML} shell. Based upon the HRTEM and XRD results herein, it is apparent that the lattice parameter of the alloy is notably increased, as the content of gold is increased within the $Pd_{1-x}Au_x$ NW. Thus, the compressive strain induced by the lattice mismatch between the Pt_{ML} and the $Pd_{1-x}Au_x$ core is expected to decrease as the gold content is increased.[12,21] Interestingly, the measured potential of Pt_{ML}~Pd NWs (0.7987 V) is significantly shifted to higher potentials as compared with the alloy-type structures. This result points toward a sizeable strain-induced effect in the case of the elemental Pd NW cores, as compared with the analogous $Pd_{1-x}Au_x$ NW cores.

From all of these results, it is clear that the structural and electronic interactions between the Pt_{ML} and the $Pd_{1-x}Au_x$ NW core are strongly dependent upon chemical composition and these factors trend in opposite fashion with chemical composition. Therefore, we believe that the

observed volcano type trend in activity likely results from the competition between the structural and electronic effects, as gold content is increased in the NW core. Essentially, the peak of the composition curve, *e.g.* the Pt_{ML}~Pd_9Au NWs, represents an optimum composition wherein a favorable synergistic effect is observed between the structural and electronic effect at that specific composition, thereby leading to a maximized optimum activity. In addition, recent reports have also demonstrated that segregation of the gold and palladium components may occur at the relatively high potentials required for ORR, a factor which may also contribute to the observed correlation between chemical composition and electrochemical performance.[26-28] Although significant insights are presented herein, a more exhaustive examination of the electronic and structural properties of these bimetallic Pd-Au NWs, using advanced spectroscopy techniques, would be required in order to more fully determine the precise interplay and relationship between morphology, composition, and electrocatalytic performance..

7.3.4. Size-Dependent ORR Performance in Core-Shell Pt_{ML}~$Pd_{1-x}Au_x$ NWs

To complement our analysis of the composition-dependent behavior in the ultrathin Pt_{ML}~Pd_9Au NWs, the size-dependent performance was also evaluated by comparing the cathodic ORR kinetics of our ultrathin 2 nm Pt_{ML}~Pd_9Au NW/C with that of larger single crystalline analogues with diameters of 45 nm.[1] The size-dependent performance is highlighted in Figure 7.7, which shows a comparison of the specific, platinum, and PGM activities in the 2 nm and 50 nm NWs. The specific activities were determined to be 0.98 mA/cm^2 and 0.95 mA/cm^2 for the 2 nm and 45 nm NWs, respectively, and interestingly, these values *did not* show significant size dependence. By contrast, in Chapters 3 – 6, a considerable correlation between NW diameter and the inherent ORR activity of Pt, Pd, and Pt_{ML}~Pd NWs has been observed with

greatly enhanced performance achieved, as the NW diameter was decreased to the ultrathin (~2 nm) scale. This phenomenon has been ascribed by our group and others to a corresponding size-induced contraction of the NW surface.[6,7,9]

In the current study, the absence of a size dependence in the specific activity is of significant interest and is attributed to an overshadowing of any inherent size-induced structural effects observed in elemental systems by the complex structural and electronic effects imparted by the PdAu alloy core onto the Pt_{ML} shell. Specifically, the addition of gold into the ultrathin NWs has been shown to significantly expand the lattice of the PdAu alloy as compared with that of the elemental wire, as demonstrated by both XRD and HRTEM data. Therefore, the prominent absence of any size-dependent enhancement in specific activity can be readily explained by the mitigation of the size-induced contraction of the NW surface in the case of elemental NWs (*e.g.* Pt, Pd, & Pt_{ML}~Pd NWs),[7,9] as a result of the presence of gold.

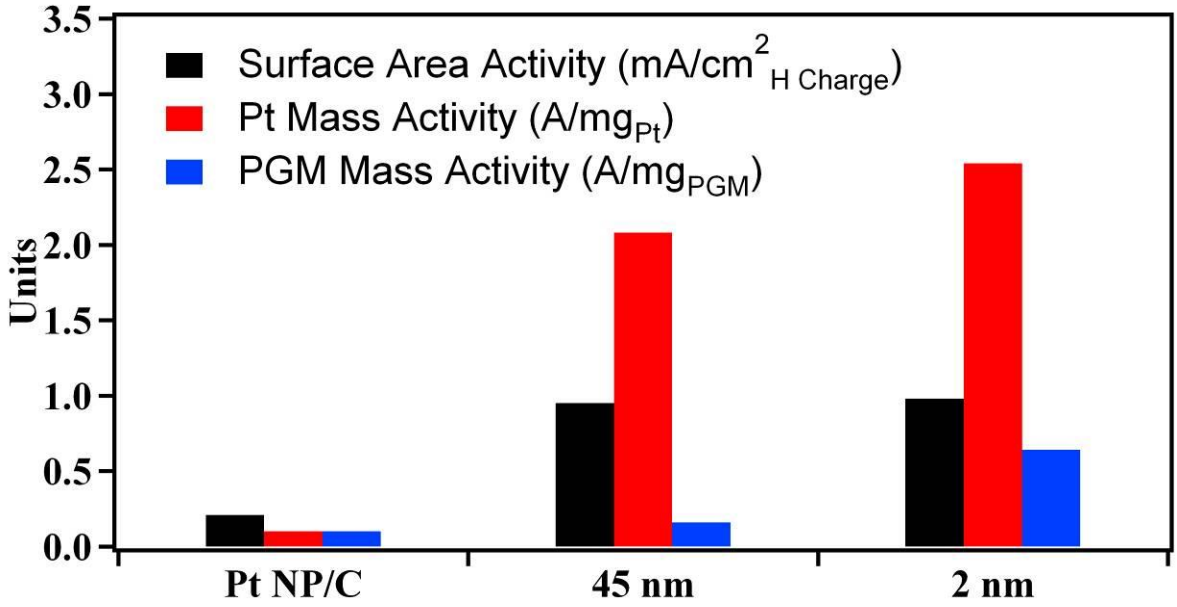

Figure 7.7 Size-dependent performance in hierarchical Pt_{ML}~$Pd_{1-x}Au_x$ NW/C composites toward ORR. Experimentally determined specific (black), platinum mass (red) and platinum group metal mass (blue) kinetic current densities measured from Pt_{ML}~Pd_9Au NWs with diameters of 45 and 2 nm, respectively. The analogous data from commercial Pt NP/C are shown as a comparative standard. (Reprinted with permission from Ref. 8. Copyright 2012 American Chemical Society)

Although the specific activity represents an important element in understanding the intrinsic activity of ORR catalysts, the mass activity data provide a far more useful insight into the effectiveness of the catalyst in terms of both viability and cost, given the significant expense of PGMs. On the basis of the platinum and PGM mass activities, it is apparent that a significant size-dependence is observed in the performance of the Pt_{ML}~Pd_9Au NWs. Specifically, the ultrathin 2 nm NWs maintain significantly enhanced activities of 2.54 A/mg_{Pt} and 0.64 A/mg_{PGM}, as compared with the 50 nm NWs (2.08 A/mg_{Pt}, 0.16 A/mg_{PGM}). These tangible improvements in the mass normalized performance achieved in the ultrathin NWs can be readily attributed to not only improved catalyst utilization but also better dispersion of these catalysts as a result of the ultrathin diameter and the carbon support. It is also clear from these results that the Pt_{ML}~Pd_9Au NWs can outperform analogous Pt_{ML}~Pd NWs (0.55 A/mg_{PGM}), an observation which provides for further evidence that the composition plays a key role in the overall performance. Furthermore, the high PGM activity observed in the case of the ultrathin NWs is more than triple the activity of 0.1 – 0.2 A/mg_{PGM} typically observed with commercial Pt NP/C. Thus, these results confirm the striking advantages of simultaneously optimizing size and composition, since measureable and significant improvements in the ORR performance can be achieved with significantly lower quantities of PGM.

7.3.5. Scaled Up Synthesis of Pt_{ML}~Pd_9Au NWs and Preliminary Membrane Electrode Assembly Testing

Given the promising results obtained under half-cell conditions, we have initiated the process of examining these highly active Pt_{ML}~Pd_9Au NW/C composites under realistic MEA conditions. Toward this goal, we have successfully scaled up the synthetic protocol to produce

near gram-scale quantities of Pt_{ML}~Pd_9Au NWs and the corresponding characterization of the as-synthesized NWs confirms that there are no declines in either purity, homogeneity, or dispersion. This finding highlights the importance of developing room-temperature, solution-based protocols, since the scalability can be easily realized in comparison with other more complex or rigorous synthetic schemes. The mass-produced Pt_{ML}~Pd_9Au NW/C composites rendered into a catalyst ink solution were spray-coated directly onto gas diffusion media with a loading to 0.150 mg/cm^2, forming a functional cathode for an MEA. In a preliminary test, the specific and mass normalized ORR activities were determined to be 0.72 mA/cm^2 and 1.7 A/mg_{Pt}, respectively, under the conditions described by the U.S. DOE for testing cathode electrocatalysts under MEA conditions.[5] Although considerable optimization is necessary in terms of the electrode preparation and MEA assembly, the preliminary activities determined herein are highly promising and demonstrate that activities significantly beyond that of Pt NP/C can be achieved under MEA conditions. Further research and development are expected to lead to results considerably closer to those measured under RDE conditions.

7.4 Conclusions

Recently, much of the focus in developing highly active 1D materials has been on creating novel complex bimetallic and even multimetallic formulations involving Pt and Pd. However, it is apparent from the shortfalls in the performance of these catalysts that developing a more complete understanding of the electrocatalytic properties in these multimetallic catalysts is crucial if they are ever to be used as practical catalysts in realistic systems. In this case, we have demonstrated for the first time that remarkable enhancements can be made in a bimetallic catalyst by systematically tailoring their morphology, dimensions, and chemical composition in

order to maximize the performance of the PdAu alloy. Examination of these structure and composition dependent properties requires the development of flexible synthetic methods to enable simultaneous control over a variety of synthetic parameters. In this case, high quality, ultrathin $Pd_{1-x}Au_x$ NWs have been prepared by an ambient, facile, environmentally sustainable, solution-based method that readily allows for control over composition. Characterization of the as-prepared NWs confirms that they are homogeneous alloys with uniform chemical composition with the composition of NWs predictably controlled from the ratio of the precursors used in the reaction. The electrochemical performance of the Pd_9Au NW has been examined and measurable enhancements in specific and mass activities have been observed by comparison with elemental Pd NWs and more importantly, commercial Pt NP/C.

The influence of composition and size upon the electrocatalytic reduction of oxygen has been separately examined in novel, hierarchical Pt_{ML}~$Pd_{1-x}Au_x$ 1D systems. An optimum performance has been observed in the case of the ultrathin Pt_{ML}~Pd_9Au NWs, which display outstanding specific, platinum mass, and PGM mass activities of 0.98 mA/cm^2, 2.54 A/mg_{Pt}, and 0.64 A/mg_{PGM}, respectively. The measured activity represents a significant and promising step forward, since the platinum and corresponding PGM mass activity are several times higher than the analogous activity values typically measured for Pt NP/C. On the basis of a preponderance of evidence from our structural characterization and electrochemical measurements, the observed enhancement in these NWs can most likely be attributed not only to the unique composition-dependent structural and electronic properties associated with the $Pd_{1-x}Au_x$ alloy type nanostructures but also to their ultrathin diameters.

A more thorough examination of the electronic and structural properties of these bimetallic, anisotropic nanostructures is beyond the scope of this report, but may lead to a more

comprehensive understanding of the roles of both chemical composition and size in determining the resulting electrocatalytic performance. Nonetheless, the clearly measurable enhancements in the Pt_{ML}~Pd_9Au NWs achieved thus far render this class of bimetallic catalysts as both exciting and highly effective.

7.5 References

(1) Koenigsmann, C.; Sutter, E.; Chiesa, T. A.; Adzic, R. R.; Wong, S. S. *Nano Lett.* **2012**, *12*, 2013-2020.
(2) Koenigsmann, C.; Wong, S. S. *ACS Catal.* **2013**, ASAP.
(3) *Fuel Cell Catalysts*; Koper, M. T. M., Ed.; Wiley Interscience: Hoboken, NJ, 2009.
(4) Gewirth, A. A.; Thorum, M. S. *Inorg. Chem.* **2010**, *49*, 3557-3566.
(5) *Multi-Year Research, Development and Demonstration Plan: Planned Program Activities for 2005-2015*, Department of Energy, 2009.
(6) Koenigsmann, C.; Santulli, A. C.; Gong, K.; Vukmirovic, M. B.; Zhou, W.-p.; Sutter, E.; Wong, S. S.; Adzic, R. R. *J. Am. Chem. Soc.* **2011**, *133*, 9783-9795.
(7) Koenigsmann, C.; Santulli, A. C.; Sutter, E.; Wong, S. S. *ACS Nano* **2011**, *5*, 7471-7487.
(8) Koenigsmann, C.; Sutter, E.; Adzic, R. R.; Wong, S. S. *J. Phys. Chem. C* **2012**, *116*, 15297-15306.
(9) Koenigsmann, C.; Zhou, W.-p.; Adzic, R. R.; Sutter, E.; Wong, S. S. *Nano Lett.* **2010**, *10*, 2806-2811.
(10) Teng, X.; Han, W.; Ku, W.; Hucker, M. *Angew. Chem. Int. Ed.* **2008**, *47*, 2055-2058.
(11) Wei-Qiang, H.; Dong, S.; Lijun, W.; Toshihiro, A.; Yimei, Z. *Nanotechnology* **2009**, *20*, 495605.
(12) Xing, Y.; Cai, Y.; Vukmirovic, M. B.; Zhou, W.-P.; Karan, H.; Wang, J. X.; Adzic, R. R. *J. Phys. Chem. Lett.* **2010**, *1*, 3238-3242.
(13) Teng, X.; Feygenson, M.; Wang, Q.; He, J.; Du, W.; Frenkel, A. I.; Han, W.; Aronson, M. *Nano Lett.* **2009**, *9*, 3177-3184.
(14) Garsany, Y.; Baturina, O. A.; Swider-Lyons, K. E.; Kocha, S. S. *Anal. Chem.* **2010**, *82*, 6321-6328.
(15) Sasaki, K.; Naohara, H.; Cai, Y.; Choi, Y. M.; Liu, P.; Vukmirovic, M. B.; Wang, J. X.; Adzic, R. R. *Angew. Chem. Int. Ed.* **2010**, *49*, 8602-8607.
(16) Cheng, F.; Dai, X.; Wang, H.; Jiang, S. P.; Zhang, M.; Xu, C. *Electrochim. Acta* **2010**, *55*, 2295-2298.
(17) Sarapuu, A.; Kasikov, A.; Wong, N.; Lucas, C. A.; Sedghi, G.; Nichols, R. J.; Tammeveski, K. *Electrochim. Acta* **2010**, *55*, 6768-6774.
(18) Cui, C.-H.; Yu, J.-W.; Li, H.-H.; Gao, M.-R.; Liang, H.-W.; Yu, S.-H. *ACS Nano* **2011**, *5*, 4211-4218.
(19) Venkatachalam, S.; Jacob, T. *PCCP* **2009**, *11*, 3263-3270.
(20) Chen, M.; Kumar, D.; Yi, C.-W.; Goodman, D. W. *Science* **2005**, *310*, 291-293.

(21) Adzic, R.; Zhang, J.; Sasaki, K.; Vukmirovic, M.; Shao, M.; Wang, J.; Nilekar, A.; Mavrikakis, M.; Valerio, J.; Uribe, F. *Top. Catal.* **2007**, *46*, 249-262.
(22) Nørskov, J. K.; Rossmeisl, J.; Logadottir, A.; Lindqvist, L.; Kitchin, J. R.; Bligaard, T.; Jonsson, H. *J. Phys. Chem. B* **2004**, *108*, 17886-17892.
(23) Greeley, J.; Nørskov, J. K. *J. Phys. Chem. C* **2009**, *113*, 4932-4939.
(24) Damjanovic, A.; Brusić, V. *Electrochim. Acta* **1967**, *12*, 1171-1184.
(25) Damjanovic, A.; Brusic, V.; Bockris, J. O. M. *J. Phys. Chem.* **1967**, *71*, 2741-2742.
(26) Mayrhofer, K. J. J.; Juhart, V.; Hartl, K.; Hanzlik, M.; Arenz, M. *Angew. Chem. Int. Ed.* **2009**, *48*, 3529-3531.
(27) Mayrhofer, K. J. J.; Hartl, K.; Juhart, V.; Arenz, M. *J. Am. Chem. Soc.* **2009**, *131*, 16348-16349.
(28) Jirkovský, J. S.; Panas, I.; Romani, S.; Ahlberg, E.; Schiffrin, D. J. *J. Phys. Chem. Lett.* **2012**, *3*, 315-321.

Chapter 8. Summary & Outlook

One-dimensional nanostructures represent an exciting structural paradigm in the continuing search for high-performance ORR electrocatalysts, particularly because of their inherent structural anisotropy. Despite the growing interest in preparing, synthesizing, and using robust 1D catalysts in practical applications, there has been a surprising lack of effort placed on cogently scrutinizing and correlating the influence of various physicochemical properties of 1D electrocatalysts (*e.g.* chemical composition, particle dimensions, and structural geometry, all of which can be controlled experimentally) with their intrinsic electrochemical performance and durability. Hence, the lack of fundamental insights into the structural properties of these catalysts may provide, in part, an explanation for the continuing challenge of consistently achieving enhanced mass activities in 1D architectures in excess of those measured with their 0D NP analogues.

Therefore, in this Dissertation, we have sought to focus on understanding the key structure-activity correlations, such as the specific roles of particle size and chemical composition, in dictating the electrocatalytic properties of 1D materials, so as to provide a useful foundation for generating highly effective and practical catalysts. Toward this goal, we have made several tangible advances in synthesis, nanomaterial purification, structural characterization, and catalyst design, with the objective of achieving the necessary degree of quality and purity in as synthesized 1D nanostructures. In terms of synthesis, we have developed two solution-based approaches with an emphasis on efficiently producing high-quality 1D nanostructures under ambient conditions, while minimizing the need for toxic reagents and complex synthetic processes. In the context of our template-based, U-tube approach, we have overcome the need for many of the technologically challenging aspects associated with template-

mediated electrodeposition, while producing well-defined 1D nanostructures, in some cases with better quality and reproducibility. Alternatively, we have sought out a more practical and scalable synthetic route for the production of ultrathin noble metal NWs with the emphasis placed on achieving control over chemical composition, batch-to-batch homogeneity and the potential for producing sufficient quantities for testing catalyst performance in functional devices. In terms of deliverables, we have prepared a portfolio of elemental (Pt, Pd, Au, & Ru), bimetallic ($Pd_{1-x}Au_x$ & $Pd_{1-x}Pt_x$), segmented (Pd/Pt & Pd/Au), and core-shell (Pt_{ML}~Pd, Pt_{ML}~$Pd_{1-x}Au_x$, & Pt~Ru) 1D nanostructures. More importantly, we have thoroughly characterized their structure, homogeneity, chemical composition, and growth processes in order to provide a foundation for understanding structure-property correlations in electrocatalysis.

Our efforts have also focused on the very practical challenge of purifying nanostructured materials to optimize their catalytic performance. Although highly advantageous for electrocatalysis, the production of anisotropic structures of noble metals in solution necessarily requires the use of shape-directing agents to overcome the thermodynamic tendency towards isotropic growth. Therefore, the removal of these shape-directing agents represents a very real obstacle toward the sustainable and practical use of as-synthesized 1D nanostructures as realistic electrocatalysts, in the existing literature. Herein, we have sought to overcome this intrinsic synthetic challenge by developing two simple post-processing methods, so as to remove residual impurities and even activate the surfaces of the noble metal NWs by etching defect sites and low-coordination atoms. In addition, our findings point toward the importance of coupling post-processing methods with analytical techniques such as spectroscopy and gravimetric analysis to enable predictable control over the purity and quality of as-synthesized 1D electrocatalysts. The key and fundamental point we demonstrate in this dissertation is that the systematic combination

of green, ambient synthesis with effective post-processing techniques enables essentially a limitless range of achievable synthetic targets in terms of chemical-composition, particle size and crystallinity.

In going beyond mere synthesis, we have deployed our novel class of electrocatalysts to examine the structure-activity correlations in 1D architectures In Chapter 3 – 5, an interesting size-dependent enhancement is observed when the diameters of 1D nanowire electrocatalysts (*i.e.* Pt, Pd, and Pt_{ML}~Pd) are decreased into the ultrathin size regime. At the core of this finding is the notion that 1D nanostructures maintain entirely distinctive structure-activity correlations, by comparison with traditional 0D nanoparticulate motifs. Considering the high costs and low abundance associated with the precious metals, we are able to achieve similar or even better performance as compared with conventional catalysts, but with the use of reduced precious metal content, due to the size and morphological advantages of our 1D systems.

In Chapter 6, we considered the more complex challenge of developing electrocatalysts for DMFCs, which require significant advances in both anode and cathode catalyst design to achieve practical performance for commercialization. The complexity of the challenges associated with MOR and methanol crossover necessitate that effective catalysts be tailored not only in terms of size but also, and more importantly, in terms of their chemical composition and the spatial distribution of elements within discrete, individual catalyst nanostructures. Towards this goal, we have undertaken an examination of composition-dependent trends in high-quality bimetallic $Pd_{1-x}Au_x$ and $Pd_{1-x}Pt_x$ NWs in terms of their ORR activity, methanol tolerant ORR behavior, and MOR performance, respectively. Collectively, our results reveal that the widely held trends between chemical composition and electrocatalytic performance associated with traditional 0D electrocatalysts do not hold in the context of the patently unique anisotropic

structure of 1D nanostructured catalysts. Drawing upon our extensive findings, we have confirmed that significant enhancements in performance can be achieved by tuning the chemical composition of NWs, so as to maximize the size-dependent structural and electronic properties observed in these anisotropic systems.

As a culmination of our efforts, we have sought in Chapter 7 to couple these design principles to produce a fully optimized bimetallic electrocatalysts based upon the promising $Pd_{1-x}Au_x$ alloy system in terms of size, structure, and chemical composition. The resulting Pt_{ML} shell supported on ultrathin (*i.e.* 2 nm) Pd_9Au NW/C core catalysts evinced outstanding Pt mass and PGM activity values of 2.54 A/mg_{Pt} and 0.64 A/mg_{PGM}, respectively, representing a ten-fold enhancement over analogous data for commercial Pt NP/C. Recent preliminary results have demonstrated that the excellent performance is conserved when tested under realistic MEA conditions. Collectively, it is evident that tailoring structure, morphology, and composition at the nanoscale particularly in the case of 1D noble metal nanostructures is a key and promising route toward overcoming the technological challenges associated with PEMFCs and many other devices.

Nonetheless, several key issues remain in the practical progression and incorporation of 1D catalysts in true fuel cell applications. *First*, a crucial prerequisite for effectively examining structure-activity trends in 1D systems necessitates that these catalysts possess similar and consistent crystallinity, purity, surface texture, morphology, and homogeneity, so as to isolate either the particle composition or dimension as the major parameter responsible for defining performance. From a rational design perspective, such a synthetic need requires the continued development of protocols that are both reasonably flexible and robust in terms of tailoring the size and composition of as-prepared catalysts, while also maintaining a high degree of

consistency. This goal is further complicated by the need for these processes to adhere to relatively high standards of sustainability, efficiency, and scalability, in terms of reagent use, energy consumption, and life-cycle considerations, in order to gain any measure of commercial relevance and acceptance, moving forward. The point is that pure, relatively benign catalytic nanomaterials need to be produced relatively easily and cheaply in high yield and large quantities with minimal amounts of byproducts. Thus, continued research into so-called "green techniques" is essential for the reliable and scalable production of 1D nanoscale electrocatalysts.

Second, the emerging literature on 1D electrocatalysts has established that significant enhancements can be garnered by moving towards complex structural motifs (*e.g.* including but not limited to core-shell, axial segmented, and 3D hierarchical architectures). This growing degree of structural complexity and sophistication inevitably requires a concurrent and parallel push for a broad range of effective characterization techniques in order to effectively probe the structure of the material and the accompanying catalytic interface within. Currently, traditional *ex-situ* methods such as electron microscopy, spatially resolved elemental analysis, and electrochemical techniques have become ubiquitous in accurately probing the structure and properties of these interesting systems and their corresponding active sites.

However, these *ex situ* techniques are significantly limited in their ability to probe structure and function within the relatively complex architecture of functional PEMFC devices. Thus, effective *in situ* characterization of materials under realistic operating conditions will necessitate the corresponding development and general use of a broader spectrum of arguably more advanced characterization techniques. For instance, synchrotron X-ray absorption spectroscopy (XAS)-based techniques represent an exciting platform with which to examine the nature of the electronic properties, bonding, and structure of the interface of 1D catalysts under

standard operating electrochemical conditions. It is likely that the fundamental insights gained into the performance of 1D electrocatalysts using these tools will likely guide future research in terms of defining new directions for substantially improving durability and stability, for example.

Third, theoretical and first-principles methods such as DFT have already been invaluable in terms of correlating the physicochemical properties of 1D architectures with their corresponding performance. For example, first-principles calculations have played a key role in elucidating the origin of enhanced performance in ultrathin Pt, Pd, and Pt_{ML}~Pd NWs. However, the recent development of multi-metallic 1D electrocatalysts poses a particularly interesting problem, since the activity in these systems appears to be related not only to size and structure but also to chemical composition in unforeseen ways. This situation is further complicated by the uniqueness of 1D nanostructures in terms of their structural and electronic effects, arising from their anisotropy. Therefore, a key step in constructing a plausible rationale for understanding the structure-activity correlations in these complex systems will be to deploy the predictive power of DFT to systematically probe and correlate the role of composition with catalytic activity in these 1D architectures. Without doubt, the successful integration of viable synthetic methodologies with effective first-principles approaches should provide an excellent framework for routinely preparing high-quality catalysts, essentially from scratch, and subsequently targeting their optimal chemical composition and morphology for enhanced performance with minimum PGM content.

Collectively, the future development of 1D electrocatalysts requires a rigorous effort towards understanding their inherent structural individuality, which differentiates their behavior from that of their conventional, broadly commercialized nanoparticulate brethren. Hence, as the development of these 1D catalysts continues to advance, it is clear that a coherent optimization

of size, composition, and structure will allow for significant improvements in terms of their cost-effectiveness and practicality as potential replacements for existing 0D catalysts. In so doing, a bright and promising future exists for the broader inclusion and use of 1D catalysts as key components of future, commercial PEMFCs.

Chapter 9. References
In Order of Appearance

(1) Patete, J. M.; Peng, X.; Koenigsmann, C.; Xu, Y.; Karn, B.; Wong, S. S. *Green Chem.* **2011**, *13*, 482-519.
(2) Tiano, A. L.; Koenigsmann, C.; Santulli, A. C.; Wong, S. S. *Chem. Commun.* **2010**, *46*, 8093-8130.
(3) Xia, Y.; Yang, P.; Sun, Y.; Wu, Y.; Mayers, B.; Gates, G.; Yin, Y.; Kim, F.; Yan, H. *Adv. Mater.* **2003**, *15*, 353-389.
(4) Xiong, Y.; Xia, Y. *Adv. Mater.* **2007**, *19*, 3385-3391.
(5) Sau, T. K.; Rogach, A. L. *Adv. Mater.* **2010**, *22*, 1781-1804.
(6) Mao, Y.; Kanungo, M.; Hemraj-Benny, T.; Wong, S. S. *J. Phys. Chem. B* **2006**, *110*, 702-710.
(7) Mao, Y.; Park, T.-J.; Zhang, F.; Zhou, H.; Wong, S. S. *Small* **2007**, *3*, 1122-1139.
(8) Mao, Y.; Park, T.-J.; Wong, S. S. *Chem. Commun.* **2005**, 5721-5735.
(9) Murphy, C. J.; Sau, T. K.; Gole, A. M.; Orendorff, C. J.; Gao, J.; Gou, L.; Hunyadi, S. E.; Li, T. *J. Phys. Chem. B* **2005**, *109*, 13857-13870.
(10) Chen, J.; Wiley, B. J.; Xia, Y. *Langmuir* **2007**, *23*, 4120-4129.
(11) Koenigsmann, C.; Scofield, M. E.; Liu, H.; Wong, S. S. *J. Phys. Chem. Lett.* **2012**, *3*, 3385-3398.
(12) Koenigsmann, C.; Wong, S. S. *Energy Environ. Sci.* **2011**, *4*, 1161 - 1176.
(13) Kline, T. R.; Tian, M.; Wang, J.; Sen, A.; Chan, M. W. H.; Mallouk, T. E. *Inorg. Chem.* **2006**, *45*, 7555-7565.
(14) Armand, M.; Tarascon, J. M. *Nature* **2008**, *451*, 652-657.
(15) Steele, B. C. H.; Heinzel, A. *Nature* **2001**, *414*, 345-352.
(16) Zhao, X.; Sanchez, B. M.; Dobson, P. J.; Grant, P. S. *Nanoscale* **2011**, *3*, 839-855.
(17) Bruce, P. G.; Scrosati, B.; Tarascon, J.-M. *Angew. Chem. Int. Ed.* **2008**, *47*, 2930-2946.
(18) Slaoui, A.; Collins, R. T. *MRS Bull.* **2007**, *32*, 211-218.
(19) Hubbell, J. A.; Chilkoti, A. *Science* **2012**, *337*, 303-305.
(20) Parmon, V. *Mater. Res. Innovations* **2008**, *12*, 60-61.
(21) Hartnig, C.; Jorissen, L.; Lehnert, W.; Scholta, J. In *Materials for Fuel Cells*; Gasik, M., Ed.; Woodhead Publishing: Oxford, UK, 2008, p 185-208.
(22) Lamy, C. In *Carbons for Electrochemical Energy Storage and Conversion Systems* 1ed.; Beguin, F., Frackowiak, E., Eds.; CRC Press: Boca Raton, Fl, 2010, p 377-409.
(23) Narayan, S. R.; Valdez, T. I. *Electrochem. Soc. Interface* **2008**, *17*, 40-45.
(24) Shukla, A. K.; Ravikumar, M. K.; Gandhi, K. S. *J. Solid State Electrochem.* **1998**, *2*, 117-122.
(25) Wasmus, S.; Küver, A. *J. Electroanal. Chem.* **1999**, *461*, 14-31.
(26) Koenigsmann, C.; Santulli, A. C.; Gong, K.; Vukmirovic, M. B.; Zhou, W.-p.; Sutter, E.; Wong, S. S.; Adzic, R. R. *J. Am. Chem. Soc.* **2011**, *133*, 9783-9795.
(27) Koenigsmann, C.; Santulli, A. C.; Sutter, E.; Wong, S. S. *ACS Nano* **2011**, *5*, 7471-7487.
(28) Koenigsmann, C.; Semple, D. B.; Sutter, E.; Tobierre, S. E.; Wong, S. S. *ACS Appl. Mater. Interfaces* **2013**, *5*, 5518-5530.
(29) Koenigsmann, C.; Sutter, E.; Adzic, R. R.; Wong, S. S. *J. Phys. Chem. C* **2012**, *116*, 15297-15306.

(30) Koenigsmann, C.; Sutter, E.; Chiesa, T. A.; Adzic, R. R.; Wong, S. S. *Nano Lett.* **2012**, *12*, 2013-2020.
(31) Koenigsmann, C.; Tan, Z.; Peng, H.; Sutter, E.; Jacobskind, J.; Wong, S. S. *Isr. J. Chem.* **2012**, *52*, 1090-1103.
(32) Koenigsmann, C.; Wong, S. S. *ACS Catal.* **2013**, ASAP.
(33) Koenigsmann, C.; Zhou, W.-p.; Adzic, R. R.; Sutter, E.; Wong, S. S. *Nano Lett.* **2010**, *10*, 2806-2811.
(34) Zhou, W.-P.; Li, M.; Koenigsmann, C.; Ma, C.; Wong, S. S.; Adzic, R. R. *Electrochim. Acta* **2011**, *56*, 9824-9830.
(35) Chalk, S. G.; Miller, J. F. *J. Power Sources* **2006**, *159*, 73-80.
(36) *Fuel Cell Catalysts*; Koper, M. T. M., Ed.; Wiley Interscience: Hoboken, NJ, 2009.
(37) Williams, M. C. *Fuel Cells* **2001**, *1*, 87-91.
(38) He, C.; Desai, S.; Brown, G.; Bollepalli, S. *Electrochem. Soc. Interface* **2005**, *14*, 41-44.
(39) Simon, P.; Gogotsi, Y. *Nat Mater* **2008**, *7*, 845-854.
(40) Adams, T. A.; Nease, J.; Tucker, D.; Barton, P. I. *Ind. Eng. Chem. Res.* **2012**, *52*, 3089-3111.
(41) Cowin, P. I.; Petit, C. T. G.; Lan, R.; Irvine, J. T. S.; Tao, S. *Adv. Energy Mater.* **2011**, *1*, 314-332.
(42) Wang, Y.; Chen, K. S.; Mishler, J.; Cho, S. C.; Adroher, X. C. *Applied Energy* **2011**, *88*, 981-1007.
(43) Kordesch, K. V.; Simader, G. R. *Chem. Rev.* **1995**, *95*, 191-207.
(44) Bolton, J. R. *Solar Energy* **1996**, *57*, 37-50.
(45) Ni, M.; Leung, M. K. H.; Leung, D. Y. C.; Sumathy, K. *Renewable Sustainable Energy Rev.* **2007**, *11*, 401-425.
(46) Choi, W. C.; Jeon, M. K.; Kim, Y. J.; Woo, S. I.; Hong, W. H. *Catal. Today* **2004**, *93-95*, 517-522.
(47) Aricò, A. S.; Srinivasan, S.; Antonucci, V. *Fuel Cells* **2001**, *1*, 133-161.
(48) Xuan, J.; Leung, M. K. H.; Leung, D. Y. C.; Ni, M. *Renewable Sustainable Energy Rev.* **2009**, *13*, 1301-1313.
(49) Nonaka, H.; Matsumura, Y. *J. Electroanal. Chem.* **2002**, *520*, 101-110.
(50) *EFOY Comfort Series Fuel Cells: Technical Specifications*, Smart Fuel Cells Inc., 2013.
(51) *Multi-Year Research, Development and Demonstration Plan: Planned Program Activities for 2005-2015*, Department of Energy, 2009.
(52) *Platinum Availability and Economics for PEMFC Commercialization*, Tiax LLC & United States Department of Energy, 2003.
(53) Sinha, J.; Marcinkoski, J.; Randolph, K.; Benjamin, T. G. *Cost Analysis of Fuel Cell Stacks/Systems*, DOE Hydrogen Program Review, 2009.
(54) Scott, K.; Argyropoulos, P. *J. Power Sources* **2004**, *137*, 228-238.
(55) Wang, C.-Y. *Chem. Rev.* **2004**, *104*, 4727-4766.
(56) Wee, J.-H.; Lee, K.-Y. *J. Power Sources* **2006**, *157*, 128-135.
(57) Hamnett, A. In *Interfacial Electrochemistry: Theory, Experiment and Applications*; Wieckowski, A., Ed.; Marcel Dekker: New York, NY, 1999, p 843-879.
(58) Wang, H.; Alden, L. R.; DiSalvo, F. J.; Abruña, H. c. D. *Langmuir* **2009**, *25*, 7725-7735.
(59) Zhao, X.; Yin, M.; Ma, L.; Liang, L.; Liu, C.; Liao, J.; Lu, T.; Xing, W. *Energy Environ. Sci.* **2011**, *4*, 2736-2753.
(60) Yu, X.; Ye, S. *J. Power Sources* **2007**, *172*, 145-154.

(61) Shao, Y.; Yin, G.; Gao, Y. *J. Power Sources* **2007**, *171*, 558-566.
(62) Liu, H.; Song, C.; Zhang, L.; Zhang, J.; Wang, H.; Wilkinson, D. P. *J. Power Sources* **2006**, *155*, 95-110.
(63) Zhao, T. S.; Chen, R.; Yang, W. W.; Xu, C. *J. Power Sources* **2009**, *191*, 185-202.
(64) Joo, S. H.; Choi, S. J.; Oh, I.; Kwak, J.; Liu, Z.; Terasaki, O.; Ryoo, R. *Nature* **2001**, *412*, 169-172.
(65) Antolini, E.; Salgado, J. R. C.; Gonzalez, E. R. *Appl. Catal., B* **2006**, *63*, 137-149.
(66) Adzic, R.; Zhang, J.; Sasaki, K.; Vukmirovic, M.; Shao, M.; Wang, J.; Nilekar, A.; Mavrikakis, M.; Valerio, J.; Uribe, F. *Top. Catal.* **2007**, *46*, 249-262.
(67) Zhang, J.; Vukmirovic, M. B.; Xu, Y.; Mavrikakis, M.; Adzic, R. R. *Angew. Chem. Int. Ed.* **2005**, *44*, 2132-2135.
(68) Zhang, J.; Vukmirovic, M. B.; Sasaki, K.; Nilekar, A. U.; Mavrikakis, M.; Adzic, R. R. *J. Am. Chem. Soc.* **2005**, *127*, 12480-12481.
(69) Shukla, A. K.; Raman, R. K. *Ann. Rev. Mater. Res.* **2003**, *33*, 155-168.
(70) Nørskov, J. K.; Bligaard, T.; Rossmeisl, J.; Christensen, C. H. *Nat. Chem.* **2009**, *1*, 37-46.
(71) Nørskov, J. K.; Rossmeisl, J.; Logadottir, A.; Lindqvist, L.; Kitchin, J. R.; Bligaard, T.; Jonsson, H. *J. Phys. Chem. B* **2004**, *108*, 17886-17892.
(72) Greeley, J.; Nørskov, J. K. *J. Phys. Chem. C* **2009**, *113*, 4932-4939.
(73) Feibelman, P. J.; Hammer, B.; Nørskov, J. K.; Wagner, F.; Scheffler, M.; Stumpf, R.; Watwe, R.; Dumesic, J. *J. Phys. Chem. B* **2000**, *105*, 4018-4025.
(74) Adzic, R. R.; Wang, J. X. *J. Phys. Chem. B* **1998**, *102*, 8988-8993.
(75) Adzic, R. R.; Wang, J. X. *J. Phys. Chem. B* **2000**, *104*, 869-872.
(76) Markovic, N. M.; Schmidt, T. J.; Stamenkovi, V.; Ross, P. N. *Fuel Cells* **2001**, *1*, 105-116.
(77) Mavrikakis, M.; Hammer, B.; Nørskov, J. K. *Phys. Rev. Lett.* **1998**, *81*, 2819.
(78) Mayrhofer, K. J. J.; Blizanac, B. B.; Arenz, M.; Stamenkovic, V. R.; Ross, P. N.; Markovic, N. M. *J. Phys. Chem. B* **2005**, *109*, 14433-14440.
(79) Mukerjee, S.; McBreen, J. *J. Electroanal. Chem.* **1998**, *448*, 163-171.
(80) Shao, M.; Peles, A.; Shoemaker, K. *Nano Lett.* **2011**, *11*, 3714-3719.
(81) Tritsaris, G.; Greeley, J.; Rossmeisl, J.; Nørskov, J. *Catal. Lett.* **2011**, *141*, 909-913.
(82) Tsou, Y. M.; Cao, L.; Castro, E. D. *ECS Transactions* **2008**, *13*, 67-84.
(83) Shao-Horn, Y.; Sheng, W.; Chen, S.; Ferreira, P.; Holby, E.; Morgan, D. *Top. Catal.* **2007**, *46*, 285-305.
(84) *Monthly Average Commercial Price of Platinum*, Johnson & Matthey, February 2013.
(85) Lim, B.; Jiang, M.; Camargo, P. H. C.; Cho, E. C.; Tao, J.; Lu, X.; Zhu, Y.; Xia, Y. *Science* **2009**, *324*, 1302-1305.
(86) Shao, M.; Yu, T.; Odell, J. H.; Jin, M.; Xia, Y. *Chem. Commun.* **2011**, *47*, 6566-6568.
(87) Wang, C.; Daimon, H.; Onodera, T.; Koda, T.; Sun, S. *Angew. Chem. Int. Ed.* **2008**, *47*, 3588-3591.
(88) Wang, Q.; Geng, B.; Tao, B. *J. Power Sources* **2011**, *196*, 191-195.
(89) Zhang, J.; Lima, F. H. B.; Shao, M. H.; Sasaki, K.; Wang, J. X.; Hanson, J.; Adzic, R. R. *J. Phys. Chem. B* **2005**, *109*, 22701-22704.
(90) Zhang, J.; Mo, Y.; Vukmirovic, M. B.; Klie, R.; Sasaki, K.; Adzic, R. R. *J. Phys. Chem. B* **2004**, *108*, 10955-10964.
(91) Mazumder, V.; Lee, Y.; Sun, S. *Adv. Funct. Mater.* **2010**, *20*, 1224-1231.
(92) Shao, M.; Liu, P.; Zhang, J.; Adzic, R. *J. Phys. Chem. B* **2007**, *111*, 6772-6775.

(93) Wang, D.; Li, Y. *Adv. Mater.* **2011**, *23*, 1044-1060.
(94) Stamenkovic, V. R.; Markovic, N. M. In *Handbook of Fuel Cells*; John Wiley & Sons Ltd.: 2009; Vol. 5, p 18-29.
(95) Yang, H. *Angew. Chem. Int. Ed.* **2011**, *50*, 2674-2676.
(96) Heinzel, A.; Barragán, V. M. *J. Power Sources* **1999**, *84*, 70-74.
(97) Antolini, E.; Lopes, T.; Gonzalez, E. R. *J. Alloys Compd.* **2008**, *461*, 253-262.
(98) DeLuca, N. W.; Elabd, Y. A. *J. Polym. Sci., Part B: Polym. Phys.* **2006**, *44*, 2201-2225.
(99) Batista, E. A.; Hoster, H.; Iwasita, T. *J. Electroanal. Chem.* **2003**, *554-555*, 265-271.
(100) Shiroishi, H.; Ayato, Y.; Kunimatsu, K.; Okada, T. *J. Electroanal. Chem.* **2005**, *581*, 132-138.
(101) Kunimatsu, K.; Hanawa, H.; Uchida, H.; Watanabe, M. *J. Electroanal. Chem.* **2009**, *632*, 109-119.
(102) Shao, M. H.; Adzic, R. R. *Electrochim. Acta* **2005**, *50*, 2415-2422.
(103) Shao, M. H.; Warren, J.; Marinkovic, N. S.; Faguy, P. W.; Adzic, R. R. *Electrochem. Commun.* **2005**, *7*, 459-465.
(104) Housmans, T. H. M.; Koper, M. T. M. *J. Phys. Chem. B* **2003**, *107*, 8557-8567.
(105) Liu, P.; Nørskov, J. K. *Fuel Cells* **2001**, *1*, 192-201.
(106) Basnayake, R.; Li, Z.; Katar, S.; Zhou, W.; Rivera, H.; Smotkin, E. S.; Casadonte, D. J.; Korzeniewski, C. *Langmuir* **2006**, *22*, 10446-10450.
(107) Chu, D.; Gilman, S. *J. Electrochem. Soc.* **1996**, *143*, 1685-1690.
(108) Hu, J.; Odom, T. W.; Lieber, C. M. *Acc. Chem. Res.* **1999**, *32*, 435-445.
(109) Lieber, C. M. *Solid State Commun.* **1998**, *107*, 607-616.
(110) Kuchibhatla, S.; Karakoti, A. S.; Bera, D.; Seal, S. *Prog. Mater Sci.* **2007**, *52*, 699-913.
(111) Morozan, A.; Jousselme, B.; Palacin, S. *Energy Environ. Sci.* **2011**, *4*, 1238-1254.
(112) Antolini, E.; Perez, J. *J. Mater. Sci.* **2011**, *46*, 1-23.
(113) Li, H.-H.; Cui, C.-H.; Yu, S.-H. *ChemCatChem* **2013**, *5*, 1693-1695.
(114) Cademartiri, L.; Ozin, G. A. *Adv. Mater.* **2009**, *21*, 1013-1020.
(115) Subhramannia, M.; Pillai, V. K. *J. Mater. Chem.* **2008**, *18*, 5858-5870.
(116) Wang, S.; Jiang, S. P.; Wang, X.; Guo, J. *Electrochim. Acta* **2011**, *56*, 1563-1569.
(117) Yu, X.; Ye, S. *J. Power Sources* **2007**, *172*, 133-144.
(118) Chen, Z.; Waje, M.; Li, W.; Yan, Y. *Angew. Chem. Int. Ed.* **2007**, *46*, 4060-4063.
(119) Garbarino, S.; Ponrouch, A.; Pronovost, S.; Gaudet, J.; Guay, D. *Electrochem. Commun.* **2009**, *11*, 1924-1927.
(120) Wang, C.; Waje, M.; Wang, X.; Tang, J. M.; Haddon, R. C.; Yan *Nano Lett.* **2003**, *4*, 345-348.
(121) Tian, M.; Kumar, N.; Xu, S.; Wang, J.; Kurtz, J. S.; Chan, M. H. W. *Phys. Rev. Lett.* **2005**, *95*, 076802.
(122) Zhiyong, Z.; Li, M.; Wu, Z.; Li, W. *Nanotechnology* **2011**, *22*, 015602.
(123) Kamat, P. V. *J. Phys. Chem. Lett.* **2012**, *3*, 3404-3404.
(124) Vukmirovic, M. B.; Bliznakov, S. T.; Sasaki, K.; Wang, J. X.; Adzic, R. R. *Electrochem. Soc. Interface* **2011**, *20*, 33-40.
(125) Schneider, C. A.; Rasband, W. S.; Eliceiri, K. W. *Nat. Methods* **2012**, *9*, 671-675.
(126) Garsany, Y.; Baturina, O. A.; Swider-Lyons, K. E.; Kocha, S. S. *Anal. Chem.* **2010**, *82*, 6321-6328.
(127) Watanabe, M.; Igarashi, H.; Yosioka, K. *Electrochim. Acta* **1995**, *40*, 329-334.

(128) Zecevic, S. K.; Wainright, J. S.; Litt, M. H.; Gojkovic, S. L.; Savinell, R. F. *J. Electrochem. Soc.* **1997**, *144*, 2973-2982.
(129) Strmcnik, D.; Tripkovic, D.; van der Vliet, D.; Stamenkovic, V.; Markovic, N. M. *Electrochem. Commun.* **2008**, *10*, 1602-1605.
(130) Wang, J. X.; Markovic, N. M.; Adzic, R. R. *J. Phys. Chem. B* **2004**, *108*, 4127-4133.
(131) Kobayashi, H.; Yamauchi, M.; Kitagawa, H.; Kubota, Y.; Kato, K.; Takata, M. *J. Am. Chem. Soc.* **2008**, *130*, 1828-1829.
(132) Vidakovic, T.; Christov, M.; Sundmacher, K. *Electrochim. Acta* **2007**, *52*, 5606-5613.
(133) Brankovic, S. R.; Wang, J. X.; Adzic, R. R. *Surf. Sci.* **2001**, *474*, L173-L179.
(134) Wang, J. X.; Inada, H.; Wu, L.; Zhu, Y.; Choi, Y.; Liu, P.; Zhou, W.-P.; Adzic, R. R. *J. Am. Chem. Soc.* **2009**, *131*, 17298-17302.
(135) Adzic, R. R.; Strbac, S.; Anastasijevic, N. *Mater. Chem. Phys.* **1989**, *22*, 349-375.
(136) Xiao, L.; Zhuang, L.; Liu, Y.; Lu, J.; Abruña, H. c. D. *J. Am. Chem. Soc.* **2008**, *131*, 602-608.
(137) Zhou, H.; Zhou, W.-p.; Adzic, R. R.; Wong, S. S. *J. Phys. Chem. C* **2009**, *113*, 5460-5466.
(138) Liang, H.-W.; Cao, X.; Zhou, F.; Cui, C.-H.; Zhang, W.-J.; Yu, S.-H. *Adv. Mater.* **2011**, *23*, 1467-1471.
(139) Alia, S. M.; Zhang, G.; Kisailus, D.; Li, D.; Gu, S.; Jensen, K.; Yan, Y. *Adv. Funct. Mater.* **2010**, *20*, 3742-3746.
(140) Xiao, Q.; Cai, M.; Balogh, M.; Tessema, M.; Lu, Y. *Nano Res.* **2012**, *5*, 145-151.
(141) Sun, S.; Jaouen, F.; Dodelet, J.-P. *Adv. Mater.* **2008**, *20*, 3900-3904.
(142) Górzny, M. Ł.; Walton, A. S.; Evans, S. D. *Adv. Funct. Mater.* **2010**, *20*, 1295-1300.
(143) Uota, M.; Hayashi, Y.; Ohyama, K.; Takemoto, H.; Iriki, R.; Kishishita, T.; Shimoda, M.; Yoshimura, T.; Kawasaki, H.; Sakai, G.; Kijima, T. *J. Nanosci. Nanotechnol.* **2010**, *10*, 5790-5795.
(144) Fiorentini, V.; Methfessel, M.; Scheffler, M. *Phys. Rev. Lett.* **1993**, *71*, 1051-1054.
(145) van Beurden, P.; Kramer, G. J. *J. Chem. Phys.* **2004**, *121*, 2317-2325.
(146) Haftel, M. I.; Gall, K. *Phys. Rev. B: Condens. Matter* **2006**, *74*, 035420-035412.
(147) Rossmeisl, J.; Nørskov, J. K. *Surf. Sci.* **2008**, *602*, 2337-2338.
(148) Wong, S. S.; Koenigsmann, C. Nanostructures Having Enhanced Catalytic Performance and Method for Preparing the Same.U.S. Patent Application 20120088656, 2012.
(149) Shen, Z.; Yamada, M.; Miyake, M. *Chem. Commun.* **2007**, 245-247.
(150) Teranishi, T.; Kurita, R.; Miyake, M. *J. Inorg. Organomet. Polym.* **2000**, *10*, 145-156.
(151) Ranpura, H. M.; Butler, D. H.; Chang, L. H.; Tracy, C. J.; Beaudoin, S. P. *J. Electrochem. Soc.* **1999**, *146*, 3114-3118.
(152) Dean, J. A. *Lange's Handbook of Chemistry*; 14th ed.; MacGraw Hill: New York, NY, 1992.
(153) Xu, S.; Tang, B.; Zheng, X.; Zhou, J.; An, J.; Ning, X.; Xu, W. *Nanotechnology* **2009**, *20*, 415601.
(154) Lide, D. R. *CRC Handbook of Chemistry & Physics*; 75 ed.; CRC Press: Boca Raton, FL, 1994.
(155) Anastasijevic, N. A.; Vesovic, V.; Adzic, R. R. *J. Electroanal. Chem.* **1987**, *229*, 317-325.
(156) Stamenkovic, V.; Schmidt, T. J.; Ross, P. N.; Markovic, N. M. *J. Phys. Chem. B* **2002**, *106*, 11970-11979.

(157) Kondo, Y.; Takayanagi, K. *Phys. Rev. Lett.* **1997**, *79*, 3455.
(158) Kondo, Y.; Takayanagi, K. *Science* **2000**, *289*, 606-608.
(159) Matanović, I.; Kent, P. R. C.; Garzon, F. H.; Henson, N. J. *J. Phys. Chem. C* **2012**, *116*, 16499-16510.
(160) Matanović, I.; Kent, P. R. C.; Garzon, F. H.; Henson, N. J. *J. Electrochem. Soc.* **2013**, *160*, F548-F553.
(161) Antolini, E. *Energy Environ. Sci.* **2009**, *2*, 915-931.
(162) *Monthly Average Commercial Price of Palladium*, Johnson & Matthey, February 2013.
(163) Wang, X.; Kariuki, N.; Vaughey, J. T.; Goodpaster, J.; Kumar, R.; Myers, D. J. *J. Electrochem. Soc.* **2008**, *155*, B602-B609.
(164) Xu, C.; Zhang, Y.; Wang, L.; Xu, L.; Bian, X.; Ma, H.; Ding, Y. *Chem. Mater.* **2009**, *21*, 3110-3116.
(165) Li, B.; Greeley, J.; Prakash, J. *ECS Transactions* **2009**, *19*, 109-116.
(166) Gibbs, D.; Ocko, B. M.; Zehner, D. M.; Mochrie, S. G. J. *Phys. Rev. B: Condens. Matter* **1988**, *38*, 7303.
(167) Hansen, H. A.; Rossmeisl, J.; Nørskov, J. K. *PCCP* **2008**, *10*, 3722-3730.
(168) Adzic, R. R.; Gong, K.; Cai, Y.; Wong, S. S.; Koenigsmann, C. Method for Removing Strongly Adsorbed Surfactants and Capping Agents from Metal to Facilitate their Catalytic Applications.U.S. Patent Application 20130178357, 2013.
(169) Teng, X.; Han, W.; Ku, W.; Hucker, M. *Angew. Chem. Int. Ed.* **2008**, *47*, 2055-2058.
(170) Mazumder, V.; Sun, S. *J. Am. Chem. Soc.* **2009**, *131*, 4588-4589.
(171) Dicks, A. L. *J. Power Sources* **2006**, *156*, 128-141.
(172) Wang, C.; Daimon, H.; Onodera, T.; Koda, T.; Sun, S. *Angew. Chem. Int. Ed.* **2008**, *47*, 3588-3591.
(173) Gonzalez, S.; Illas, F. *Surf. Sci.* **2005**, *598*, 144-155.
(174) Kato, H. S.; Okuyama, H.; Yoshinobu, J.; Kawai, M. *Surf. Sci.* **2002**, *513*, 239-248.
(175) Li, Y.; El-Sayed, M. A. *J. Phys. Chem. B* **2001**, *105*, 8938-8943.
(176) Aliaga, C.; Park, J. Y.; Yamada, Y.; Lee, H. S.; Tsung, C.-K.; Yang, P.; Somorjai, G. A. *J. Phys. Chem. C* **2009**, *113*, 6150-6155.
(177) Pang, S.; Kurosawa, Y.; Kondo, T.; Kawai, T. *Chem. Lett.* **2005**, *34*, 544-545.
(178) Tanuma, T.; Terazono, S. *J. Power Sources* **2008**, *181*, 287-291.
(179) Prabhuram, J.; Wang, X.; Hui, C. L.; Hsing, I. M. *J. Phys. Chem. B* **2003**, *107*, 11057-11064.
(180) Park, J.; Aliaga, C.; Renzas, J.; Lee, H.; Somorjai, G. *Catal. Lett.* **2009**, *129*, 1-6.
(181) Chen, W.; Kim, J.; Sun, S.; Chen, S. *PCCP* **2006**, *8*, 2779-2786.
(182) Liu, Z.; Shamsuzzoha, M.; Ada, E. T.; Reichert, W. M.; Nikles, D. E. *J. Power Sources* **2007**, *164*, 472-480.
(183) Martín, A. J.; Chaparro, A. M.; Folgado, M. A.; Rubio, J.; Daza, L. *Electrochim. Acta* **2009**, *54*, 2209-2217.
(184) Kondo, S.; Nakamura, M.; Maki, N.; Hoshi, N. *J. Phys. Chem. C* **2009**, *113*, 12625-12628.
(185) Teng, X.; Yang, H. *Nano Lett.* **2005**, *5*, 885-891.
(186) Gong, K.; Chen, W.-F.; Sasaki, K.; Su, D.; Vukmirovic, M. B.; Zhou, W.; Izzo, E. L.; Perez-Acosta, C.; Hirunsit, P.; Balbuena, P. B.; Adzic, R. R. *J. Electroanal. Chem.* **2010**, *649*, 232-237.

(187) Ghosh, T.; Vukmirovic, M. B.; DiSalvo, F. J.; Adzic, R. R. *J. Am. Chem. Soc.* **2010**, *132*, 906-907.
(188) Knupp, S.; Vukmirovic, M.; Haldar, P.; Herron, J.; Mavrikakis, M.; Adzic, R. *Electrocatalysis* **2010**, *1*, 213-223.
(189) Sasaki, K.; Naohara, H.; Cai, Y.; Choi, Y. M.; Liu, P.; Vukmirovic, M. B.; Wang, J. X.; Adzic, R. R. *Angew. Chem. Int. Ed.* **2010**, *49*, 8602-8607.
(190) Song, Y.; Garcia, R. M.; Dorin, R. M.; Wang, H.; Qiu, Y.; Coker, E. N.; Steen, W. A.; Miller, J. E.; Shelnutt, J. A. *Nano Lett.* **2007**, *7*, 3650-3655.
(191) Ksar, F. a.; Surendran, G.; Ramos, L.; Keita, B.; Nadjo, L.; Prouzet, E.; Beaunier, P.; Hagège, A. s.; Audonnet, F.; Remita, H. *Chem. Mater.* **2009**, *21*, 1612-1617.
(192) Caihong, F.; Zhang, R.; Yin, P.; Li, L.; Guo, L.; Shen, Z. *Nanotechnology* **2008**, *19*, 305601.
(193) Yuan, Q.; Zhou, Z.; Zhuang, J.; Wang, X. *Chem. Mater.* **2010**, *22*, 2395-2402.
(194) Yuan, Q.; Zhuang, J.; Wang, X. *Chem. Commun.* **2009**, 6613-6615.
(195) Liang, H.-W.; Liu, S.; Gong, J.-Y.; Wang, S.-B.; Wang, L.; Yu, S.-H. *Adv. Mater.* **2009**, *21*, 1850-1854.
(196) Huang, X.; Zheng, N. *J. Am. Chem. Soc.* **2009**, *131*, 4602-4603.
(197) Lu, Y.; Wang, Y.; Chen, W. *J. Power Sources* **2011**, *196*, 3033-3038.
(198) Teng, X.; Feygenson, M.; Wang, Q.; He, J.; Du, W.; Frenkel, A. I.; Han, W.; Aronson, M. *Nano Lett.* **2009**, *9*, 3177-3184.
(199) Sun, Y.; Zhang, L.; Zhou, H.; Zhu, Y.; Sutter, E.; Ji, Y.; Rafailovich, M. H.; Sokolov, J. C. *Chem. Mater.* **2007**, *19*, 2065-2070.
(200) Hurst, S. J.; Payne, E. K.; Qin, L.; Mirkin, C. A. *Angew. Chem. Int. Ed.* **2006**, *45*, 2672-2692.
(201) Liang, H.-W.; Liu, S.; Yu, S.-H. *Adv. Mater.* **2010**, *22*, 3925-3937.
(202) Perry, J. L.; Martin, C. R.; Stewart, J. D. *Chem-Eur. J.* **2011**, *17*, 6296-6302.
(203) Chen, A.; Holt-Hindle, P. *Chem. Rev.* **2010**, *110*, 3767-3804.
(204) Wang, Z.-j.; Xie, Y.; Liu, C.-j. *J. Phys. Chem. C* **2008**, *112*, 19818-19824.
(205) Azulai, D.; Belenkova, T.; Gilon, H.; Barkay, Z.; Markovich, G. *Nano Lett.* **2009**, *9*, 4246-4249.
(206) Kijima, T.; Yoshimura, T.; Uota, M.; Ikeda, T.; Fujikawa, D.; Mouri, S.; Uoyama, S. *Angew. Chem. Int. Ed.* **2004**, *43*, 228-232.
(207) Xu, Z.; Shen, C.; Sun, S.; Gao, H. J. *J. Phys. Chem. C* **2009**, *113*, 15196-15200.
(208) Zhang, J.; Liu, H.; Wang, Z.; Ming, N. *Adv. Funct. Mater.* **2007**, *17*, 3295-3303.
(209) Tsukamoto, R.; Muraoka, M.; Seki, M.; Tabata, H.; Yamashita, I. *Chem. Mater.* **2007**, *19*, 2389-2391.
(210) Wang, H.; Xu, C.; Cheng, F.; Jiang, S. *Electrochem. Commun.* **2007**, *9*, 1212-1216.
(211) Zhang, F.; Yiu, Y.; Aronson, M. C.; Wong, S. S. *J. Phys. Chem. C* **2008**, *112*, 14816-14824.
(212) Zhang, F.; Wong, S. S. *ACS Nano* **2009**, *4*, 99-112.
(213) Zhang, F.; Wong, S. S. *Chem. Mater.* **2009**, *21*, 4541-4554.
(214) Zhang, F.; Sfeir, M. Y.; Misewich, J. A.; Wong, S. S. *Chem. Mater.* **2008**, *20*, 5500-5512.
(215) Zhang, F.; Mao, Y.; Park, T.-J.; Wong, S. S. *Adv. Funct. Mater.* **2008**, *18*, 103-112.
(216) Mao, Y.; Zhang, F.; Wong, S. *Adv. Mater.* **2006**, *18*, 1895-1899.
(217) Mao, Y.; Wong, S. S. *J. Am. Chem. Soc.* **2004**, *126*, 15245-15252.

(218) Wong, S. S.; Koenigsmann, C. Surfactantless Metallic Nanostructures and Methods for Synthesizing Same.U.S. Patent Application 20130084210, 2013.
(219) Schönenberger, C.; van der Zande, B. M. I.; Fokkink, L. G. J.; Henny, M.; Schmid, C.; Krüger, M.; Bachtold, A.; Huber, R.; Birk, H.; Staufer, U. *J. Phys. Chem. B* **1997**, *101*, 5497-5505.
(220) Favier, F.; Walter, E. C.; Zach, M. P.; Benter, T.; Penner, R. M. *Science* **2001**, *293*, 2227-2231.
(221) Yun, M.; Myung, N. V.; Vasquez, R. P.; Lee, C.; Menke, E.; Penner, R. M. *Nano Lett.* **2004**, *4*, 419-422.
(222) Cheng, F.; Wang, H.; Sun, Z.; Ning, M.; Cai, Z.; Zhang, M. *Electrochem. Commun.* **2008**, *10*, 798-801.
(223) Kartopu, G.; Habouti, S.; Es-Souni, M. *Mater. Chem. Phys.* **2008**, *107*, 226-230.
(224) Sharabani, R.; Reuveni, S.; Noy, G.; Shapira, E.; Sadeh, S.; Selzer, Y. *Nano Lett.* **2008**, *8*, 1169-1173.
(225) Cui, S. T. *J. Chem. Phys.* **2005**, *123*, 054706-054704.
(226) Crank, J. *The Mathematics of Diffusion*; Oxford University Press: Oxford, UK, 1975.
(227) Keating, C. D.; Natan, M. J. *Adv. Mater.* **2003**, *15*, 451-454.
(228) Stoermer, R. L.; Cederquist, K. B.; McFarland, S. K.; Sha, M. Y.; Penn, S. G.; Keating, C. D. *J. Am. Chem. Soc.* **2006**, *128*, 16892-16903.
(229) Brunker, S. E.; Cederquist, K. B.; Keating, C. D. *Nanomedicine* **2007**, *2*, 695.
(230) Reich, D. H.; Tanase, M.; Hultgren, A.; Bauer, L. A.; Chen, C. S.; Meyer, G. J. *J. Appl. Phys.* **2003**, *93*, 7275.
(231) Kline, T. R.; Paxton, W. F.; Mallouk, T. E.; Sen, A. *Angew. Chem. Int. Ed.* **2005**, *44*, 744-746.
(232) Ibele, M. E.; Wang, Y.; Kline, T. R.; Mallouk, T. E.; Sen, A. *J. Am. Chem. Soc.* **2007**, *129*, 7762-7763.
(233) Paxton, W. F.; Sundararajan, S.; Mallouk, T. E.; Sen, A. *Angew. Chem. Int. Ed.* **2006**, *45*, 5420-5429.
(234) Dhar, P.; Fischer, T. M.; Wang, Y.; Mallouk, T. E.; Paxton, W. F.; Sen, A. *Nano Lett.* **2006**, *6*, 66-72.
(235) Hong, Y.; Blackman, N. M. K.; Kopp, N. D.; Sen, A.; Velegol, D. *Phys. Rev. Lett.* **2007**, *99*, 178103.
(236) Hong, Y.; Velegol, D.; Chaturvedi, N.; Sen, A. *PCCP* **2010**, *12*, 1423-1435.
(237) Ibele, M.; Mallouk, T. E.; Sen, A. *Angew. Chem. Int. Ed.* **2009**, *48*, 3308-3312.
(238) Paxton, W. F.; Sen, A.; Mallouk, T. E. *Chem. Eur. J.* **2005**, *11*, 6462-6470.
(239) Wang, Y.; Hernandez, R. M.; Bartlett, D. J., Jr.; Bingham, J. M.; Kline, T. R.; Sen, A.; Mallouk, T. E. *Langmuir* **2006**, *22*, 10451-10456.
(240) Sundararajan, S.; Lammert, P. E.; Zudans, A. W.; Crespi, V. H.; Sen, A. *Nano Lett.* **2008**, *8*, 1271-1276.
(241) Wang, J. *ChemPhysChem* **2009**, *10*, 1748-1755.
(242) Liu, F.; Lee, J.; Zhou, W. *Small* **2006**, *2*, 121-128.
(243) Liu, F.; Lee, J. Y.; Zhou, W. *J. Electrochem. Soc.* **2006**, *153*, A2133-A2138.
(244) Liu, F.; Lee, J. Y.; Zhou, W. J. *Adv. Funct. Mater.* **2005**, *15*, 1459-1464.
(245) Shaijumon, M. M.; Ou, F. S.; Ci, L.; Ajayan, P. M. *Chem. Commun.* **2008**, 2373-2375.
(246) Maillard, F.; Savinova, E. R.; Stimming, U. *J. Electroanal. Chem.* **2007**, *599*, 221-232.

(247) Maillard, F.; Eikerling, M.; Cherstiouk, O. V.; Schreier, S.; Savinova, E.; Stimming, U. *Faraday Discuss.* **2004**, *125*, 357-377.
(248) Hara, M.; Linke, U.; Wandlowski, T. *Electrochim. Acta* **2007**, *52*, 5733-5748.
(249) Rabis, A.; Rodriguez, P.; Schmidt, T. J. *ACS Catal.* **2012**, *2*, 864-890.
(250) Watanabe, M.; Tryk, D. A.; Wakisaka, M.; Yano, H.; Uchida, H. *Electrochim. Acta* **2012**, *84*, 187-201.
(251) Shui, J.-l.; Chen, C.; Li, J. C. M. *Adv. Funct. Mater.* **2011**, *21*, 3357-3362.
(252) Guo, S.; Li, D.; Zhu, H.; Zhang, S.; Markovic, N. M.; Stamenkovic, V. R.; Sun, S. *Angew. Chem. Int. Ed.* **2013**, *52*, 3465-3468.
(253) Liu, C.-W.; Wei, Y.-C.; Liu, C.-C.; Wang, K.-W. *J. Mater. Chem.* **2012**, *22*, 4641-4644.
(254) Tan, Y.; Fan, J.; Chen, G.; Zheng, N.; Xie, Q. *Chem. Commun.* **2011**, *47*, 11624-11626.
(255) Liao, H.; Hou, Y. *Chem. Mater.* **2013**, *25*, 457-465.
(256) Chuan-Jian, Z.; Jin, L.; Bin, F.; Bridgid, N. W.; Peter, N. N.; Rameshwori, L.; Jun, Y. *Nanotechnology* **2010**, *21*, 062001.
(257) Sarapuu, A.; Kasikov, A.; Wong, N.; Lucas, C. A.; Sedghi, G.; Nichols, R. J.; Tammeveski, K. *Electrochim. Acta* **2010**, *55*, 6768-6774.
(258) Damjanovic, A.; Brusić, V. *Electrochim. Acta* **1967**, *12*, 1171-1184.
(259) Xing, Y.; Cai, Y.; Vukmirovic, M. B.; Zhou, W.-P.; Karan, H.; Wang, J. X.; Adzic, R. R. *J. Phys. Chem. Lett.* **2010**, *1*, 3238-3242.
(260) Cui, C.-H.; Yu, J.-W.; Li, H.-H.; Gao, M.-R.; Liang, H.-W.; Yu, S.-H. *ACS Nano* **2011**, *5*, 4211-4218.
(261) Zhu, C.; Guo, S.; Dong, S. *Adv. Mater.* **2012**, *24*, 2326-2331.
(262) He, W.; Liu, J.; Qiao, Y.; Zou, Z.; Zhang, X.; Akins, D. L.; Yang, H. *J. Power Sources* **2010**, *195*, 1046-1050.
(263) Lee, C.-L.; Chiou, H.-P. *Appl. Catal., B* **2012**, *117–118*, 204-211.
(264) Lee, C.-L.; Chiou, H.-P.; Wu, S.-C.; Wu, C.-C. *Electrochim. Acta* **2010**, *56*, 687-692.
(265) Wang, W. M.; Li, Z. L.; Zou, Z.; Yang, H.; Feng, S. *ECS Transactions* **2008**, *16*, 613-619.
(266) Yang, J.; Zhou, W.; Cheng, C. H.; Lee, J. Y.; Liu, Z. *ACS Appl. Mater. Interfaces* **2009**, *2*, 119-126.
(267) Rauber, M.; Alber, I.; Müller, S.; Neumann, R.; Picht, O.; Roth, C.; Schökel, A.; Toimil-Molares, M. E.; Ensinger, W. *Nano Lett.* **2011**, *11*, 2304-2310.
(268) Wang, S.; Wang, X.; Jiang, S. P. *Nanotechnology* **2008**, *19*, 455602.
(269) Maksimuk, S.; Yang, S.; Peng, Z.; Yang, H. *J. Am. Chem. Soc.* **2007**, *129*, 8684-8685.
(270) Guo, S.; Zhang, S.; Sun, X.; Sun, S. *J. Am. Chem. Soc.* **2011**, *133*, 15354-15357.
(271) Niu, Z.; Wang, D.; Yu, R.; Peng, Q.; Li, Y. *Chemical Science* **2012**, *3*, 1925-1929.
(272) Zhang, J.; Sasaki, K.; Sutter, E.; Adzic, R. R. *Science* **2007**, *315*, 220-222.
(273) Tiano, A. L.; Santulli, A. C.; Koenigsmann, C.; Feygenson, M.; Aronson, M. C.; Harrington, R.; Parise, J. B.; Wong, S. S. *Chem. Mater.* **2011**, *23*, 3277-3288.
(274) Cheng, F.; Dai, X.; Wang, H.; Jiang, S. P.; Zhang, M.; Xu, C. *Electrochim. Acta* **2010**, *55*, 2295-2298.
(275) Damjanovic, A.; Brusic, V.; Bockris, J. O. M. *J. Phys. Chem.* **1967**, *71*, 2741-2742.
(276) Greeley, J.; Norskov, J. K. *J. Phys. Chem. C* **2009**, *113*, 4932-4939.
(277) Li, H.; Sun, G.; Li, N.; Sun, S.; Su, D.; Xin, Q. *J. Phys. Chem. C* **2007**, *111*, 5605-5617.
(278) Mott, D.; Luo, J.; Njoki, P. N.; Lin, Y.; Wang, L.; Zhong, C.-J. *Catal. Today* **2007**, *122*, 378-385.

(279) Luo, J.; Njoki, P. N.; Lin, Y.; Mott, D.; Wang; Zhong, C.-J. *Langmuir* **2006**, *22*, 2892-2898.
(280) Yang, L.; Yang, W.; Cai, Q. *J. Phys. Chem. C* **2007**, *111*, 16613-16617.
(281) Liu, Y.; Chi, M.; Mazumder, V.; More, K. L.; Soled, S.; Henao, J. D.; Sun, S. *Chem. Mater.* **2011**, *23*, 4199-4203.
(282) Choi, J.-H.; Park, K.-W.; Park, I.-S.; Kim, K.; Lee, J.-S.; Sung, Y.-E. *J. Electrochem. Soc.* **2006**, *153*, A1812-A1817.
(283) Yin, M.; Huang, Y.; Liang, L.; Liao, J.; Liu, C.; Xing, W. *Chem. Commun.* **2011**, *47*, 8172-8174.
(284) Zhong, W.; Liu, Y.; Zhang, D. *J. Phys. Chem. C* **2012**, *116*, 2994-3000.
(285) Yuan, D.; Gong, X.; Wu, R. *J. Chem. Phys.* **2008**, *128*, 064706-064705.
(286) Cui, C.-H.; Li, H.-H.; Cong, H.-P.; Yu, S.-H.; Tao, F. *Chem. Commun.* **2012**, *48*, 12062-12064.
(287) Zhang, S.; Shao, Y.; Liao, H.-g.; Liu, J.; Aksay, I. A.; Yin, G.; Lin, Y. *Chem. Mater.* **2011**, *23*, 1079-1081.
(288) Vidal-Iglesias, F. J.; Solla-Gullón, J.; Herrero, E.; Aldaz, A.; Feliu, J. M. *Angew. Chem. Int. Ed.* **2010**, *49*, 6998-7001.
(289) Gewirth, A. A.; Thorum, M. S. *Inorg. Chem.* **2010**, *49*, 3557-3566.
(290) Wei-Qiang, H.; Dong, S.; Lijun, W.; Toshihiro, A.; Yimei, Z. *Nanotechnology* **2009**, *20*, 495605.
(291) Venkatachalam, S.; Jacob, T. *PCCP* **2009**, *11*, 3263-3270.
(292) Chen, M.; Kumar, D.; Yi, C.-W.; Goodman, D. W. *Science* **2005**, *310*, 291-293.
(293) Mayrhofer, K. J. J.; Juhart, V.; Hartl, K.; Hanzlik, M.; Arenz, M. *Angew. Chem. Int. Ed.* **2009**, *48*, 3529-3531.
(294) Mayrhofer, K. J. J.; Hartl, K.; Juhart, V.; Arenz, M. *J. Am. Chem. Soc.* **2009**, *131*, 16348-16349.
(295) Jirkovský, J. S.; Panas, I.; Romani, S.; Ahlberg, E.; Schiffrin, D. J. *J. Phys. Chem. Lett.* **2012**, *3*, 315-321.